Novel metal-metal oxide thick film heating elements produced by the dual-stage flame spray processing of a gas atomised Ni-Cr-Fe alloy

By

Mark Duffield

Thesis submitted in accordance with the requirements of the University of Liverpool for the degree of Doctor in Philosophy

January 2017

Preface

This dissertation is submitted for the degree of Doctor of Philosophy at the University of Liverpool. The work undertaken and described herein was carried out under the supervision of Professor Gordon J. Tatlock in the School of Engineering and Material Science, at the Centre for Materials and Structures, University of Liverpool, between September 2012 and December 2016.

This work is original except where acknowledgement and references are made to the previous work. Neither this nor any substantially similar dissertation has been or is being submitted for a degree, diploma or other qualification at any other university.

Mark Duffield

…….

Date: 01/2017

Acknowledgements

I must begin by thanking my supervisor Professor Gordon J. Tatlock for his tremendous support, encouragement and guidance throughout the course of my studies. I am extremely grateful for the many valuable technical discussions and his patience during the write-up! I also wish to thank my secondary supervisor Dr Peter Fox for the interest shown in my work, and his useful contributions.

I gratefully acknowledge the staff at the Nanoinvestigation Centre at Liverpool (NiCaL) including Dr. Simon Romani, Dr. Karl Dawson, Dr. Tobias Heil, Dr. Kerry Abrams, Ms. Lynn Allan and Mr. Alan Tidbury. Special thanks are due to Dr. Karl Dawson for FIB specimen production and operation of the STEM microscope. The other University staff I would also like to thank are Mr. David Atkinson and Mrs. Margaret Robinshaw.

At the SuperSTEM facility in Daresbury, Dr David Henandez-Maldonado is kindly thanked for his microscopy and EELS analysis.

This work has been supported by the European Regional Development Fund/Centre for Global Eco-Innovation, whose maintenance grant is gratefully recognised. Special thanks are due to 2DHeat Ltd for their supply of the thick film heating elements studied during this project. In particular, I wish to thank my main contacts at the company, Mr. John Lewis and Dr. Marcus Rutherford.

A special thanks to Dr. Thomas Boegelien, and my officemates Keith Arnold and Kiriakos Moustoukas for their comradery and useful technical discussions over the course of my studies.

Finally, I would like to express my deepest gratitude to my parents, brothers and sister, whose love and encouragement has proven invaluable throughout this experience.

Abstract

2DHeat Ltd have developed a novel thick film technology for the manufacture of energy efficient, electric heating elements. Their two-step procedure employs existing flame spray technology to partially oxidise a powdered Ni-Cr-Fe alloy (approximately 75wt% Ni, 15wt% Cr, 10wt% Fe) and subsequently deposit it upon an enamelled substrate. Due to a more efficient transfer of heat, these films can achieve the same performance (e.g. for cooking or drying) as traditional coiled wire elements while operating at considerably lower temperatures.

In order to assess phase formation and microstructural during the manufacturing process, a range of optical, structural and chemical characterisation techniques have been used to examine the materials produced at different stages of the production process. To monitor the possible changes occurring during heating element operation, the flame sprayed thick films have also been examined following heat treatment at temperatures ranging from 400˚C -800˚C.

Characterisation of the initial gas atomised Ni-Cr-Fe alloy, indicated its composition and crystal structure were largely consistent with Inconel 600 from which it was produced. Particle size distribution, determined by means of image analysis, indicated that particle diameter ranged from 4-51µm, with a mean value of 25µm.

After flame spraying the powdered alloy, a combination of X-ray diffraction and SEM-EDS indicated the presence of high percentage of Cr and Fe doped NiO, alongside smaller quantities of the original alloy, low alloyed Ni and a spinel phase. Particle size distribution, again determined by image analysis, suggested that particle diameter ranged from 1-76µm, with a mean value of 36µm. High resolution TEM/STEM analysis of the oxidised powder particles revealed that numerous spinel particles had grown topotactically within the Cr and Fe doped NiO.

Flame spray deposition of the partially oxidised powder, produced a thick film consisting of approximately 62% oxide, 17% metal and 21% porosity according to image analysis. X-ray diffraction patterns suggested that the phases detected in the partially oxidised powder remained present after the second flame spray procedure. However, an increase in the intensity of the metallic peaks suggested that the metallic material accumulated preferential during deposition. High resolution TEM/STEM analysis of the Cr and Fe doped grains within the thick film, revealed variations in the degree of spinel precipitation. While some grains had a homogenous single-phase structure, other grains contained arrays of coherent particles, similar to those observed within the oxidised powder.

Decomposition of the Cr and Fe doped NiO within the thick films was induced by heating specimens for 66h at 800˚C. Combined XRD and SEM analyses confirmed a widespread increase in the spinel phase throughout the specimens. During TEM/STEM analysis, arrays of coherent spinel precipitates were noted throughout the oxide grains. In contrast to the precipitates within the oxidised powder and as-deposited thick film, TEM used in conjunction with EELS elemental mapping indicated that these particles were of octahedral morphology, and bound by the {111} planes. Site occupancy within the precipitates was studied at an atomic scale using the EELS technique.

Contents

Publications and conference contributions

Journal article

Mark E Duffield; Gordon J Tatlock; John F Lewis (2017). High temperature decomposition of Fe and Cr doped NiO produced by a novel flame spray technique. *Approved for publication in Oxidation of Metals.*

Conference poster

Mark E Duffield; Gordon J Tatlock; John F Lewis (2015). Novel eco-friendly metal-metal oxide thick film heating elements. Gordon Research Conference on High Temperature Corrosion, Colby-Sawyer College, New London, NH (USA), July 2015

Oral presentations

Mark E Duffield; Gordon J Tatlock; John F Lewis (2015). Novel eco-friendly metal-metal oxide thick film heating elements. National Student Conference in Metallic Materials (2015), Manchester Conference Centre, Manchester (UK), June 2015

Gordon J Tatlock; Mark E Duffield; John F Lewis (2016). High temperature decomposition of Fe and Cr doped NiO produced by a novel flame spray technique. International Symposium on High-Temperature Corrosion and Protection of Materials, Les Embiez (France), May 2016.

Nomenclature

ADF	Annular dark field
APS	Atmospheric plasma spray
BF	Bright field
BSE	Backscattered electron
CBED	Convergent-beam electron diffraction
CCD	Charge-couple device
CDF	Centred dark field
CFSE	Crystal field stabilisation energy
CN	Coordination number
CVD	Chemical vapour deposition
EDS	Energy dispersive X-ray spectroscopy
EELS	Electron energy-loss spectrometry
EPMA	Electron-probe microanalyzer
FEG	Field-emission gun
FFT	Fast Fourier transform
FIB	Focused ion beam
HAADF	High angle annular dark field
HVOF	High-velocity oxygen fuel
MFC	Mass flow controller
MSA	Multivariate statistical analysis
PCA	Principal component analysis
SAD(P)	Selected-area diffraction (pattern)
SDD	Silicon-drift detector
SEM	Scanning electron microscope/microscopy
SE	Secondary electron

STEM	Scanning transmission electron microscope/microscopy
TEM	Transmission electron microscope/microscopy
TDS	Thermal diffuse scattering
VPS	Vacuum plasma spray
VSM	Vibrating sample magnetometer
XRD	X-ray diffraction
XRF	X-ray fluorescence
ZAF	atomic number/absorption/fluorescence correction

Chapter 1

Introduction

1.1 Thick film electric heating elements

1.1.1 Introduction

2DHeat Ltd has developed a novel thick film technology for the manufacture of energy efficient, electric heating elements. During their production process, a gas atomised Ni-Fe-Cr alloy (approximately 75wt% Ni, 15wt% Cr, 10wt% Fe) is converted into mixed metal-metal oxide thick film, through the application of existing flame spray technology. When an electrical current is passed through the material, thermal energy is generated due to resistive heating.

By transferring heat more efficiently, the thick films are able to achieve the same performance (e.g. for cooking or drying) as traditional coiled wire elements while operating at considerably lower temperatures. The associated energy savings make the thick film heating elements a potentially interesting alternative for any manufacturer employing current coiled wire technology.

An example of a heating element designed for use within tumble dryer is displayed in figure 1.1.

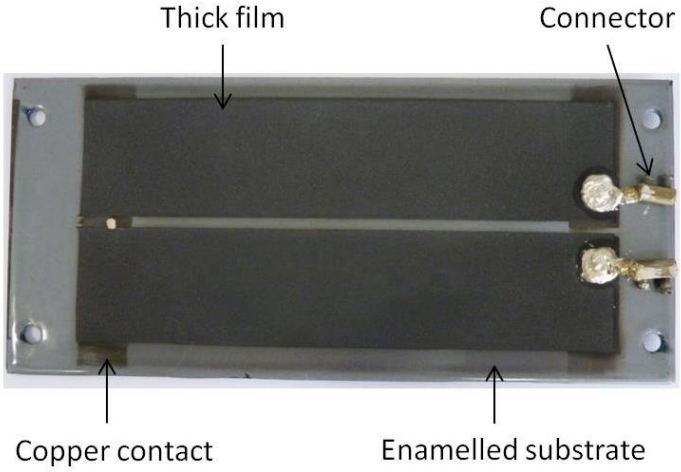

***Figure 1.1**: Thick film heating element deposited on enamelled substrate measuring approximately 20 x 9cm.*

1.1.2 Manufacture

During the first stage of manufacture a gas atomised Ni-Cr-Fe alloy is oxidised by passing it through an oxyacetylene flame (see figure 1.2). The particles are cooled rapidly from high temperature by directing the spray into a quenching bath filled with water. In the second stage of the production process, the partially oxidised powder is deposited by another flame spray gun onto an enamelled substrate. Electrical Cu contacts strips may be flame-sprayed in appropriate positions either before or after this second stage.

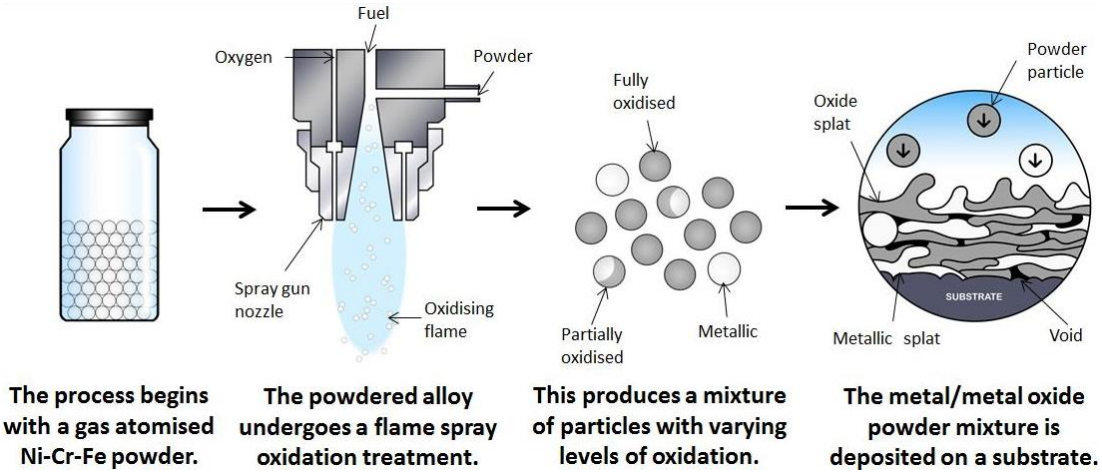

***Figure 1.2**: Manufacture of the thick film heating elements.*

1.2 Project aims

The primary objective of this project has been to evaluate the phase formation and microstructural evolution that occurs during the flame spray processing of a gas atomised Ni-Cr-Fe alloy. Material has been examined using combination of optical, structural and chemical characterisation techniques, at the various stages of the manufacturing procedure. To assess possible phase changes occurring during the heating element operation, specimens of the thick film were examined using the same analytical procedures following a range of heat treatments.

1.3 Report structure

Following the introduction, the thesis consists of an additional 8 chapters. Background information is presented alongside a review of the relevant literature in Chapter 2. The materials and experiment techniques employed during the current study are detailed in Chapter 3. Results obtained from the original and partially oxidised powders, the as-deposited thick film and the heat treated thick film are presented in Chapters 4, 5 and 6 respectively. The data collected in the results chapters is discussed more thoroughly in chapter 7. The key findings of this work are then summarised in Chapter 8, while possible suggestions for future work are provided in Chapter 9.

Chapter 2

Literature review and background

2.1 Thermal spraying

2.1.1 Introduction

The concept of thermal spraying was supposedly conceived as Swiss inventor Max Schoop observed his children playing with a toy cannon. Noticing the deformation of lead pellets discharged against a brick wall, Schoop realised propelled metal particles could be used to produce a surface coating.

Developed at the start of the 20th century, Schoop's earliest thermal spray technique drew upon early experiments in which molten metal was inserted into a high velocity gas stream. His initial setup comprised of a compressor that supplied air to a high temperature helical tube. The resulting flow of heated air was used to pressurise a container filled with molten metal and expel it as a fine spray towards a substrate. This early system, while unwieldy and inefficient, did serve as a useful proof of concept.

Discontinuing the work with molten metal spray, Schoop and his colleagues developed the first instrument for spraying solid metal wire in 1912. This relatively simple device operated by feeding a wire rod into a high temperature flame where it was melted, atomized and propelled towards the substrate by stream of compressed gas (see figure 2.1). Initially this combustion based process was referred to as metallization, now it is more commonly known as flame spraying [1].

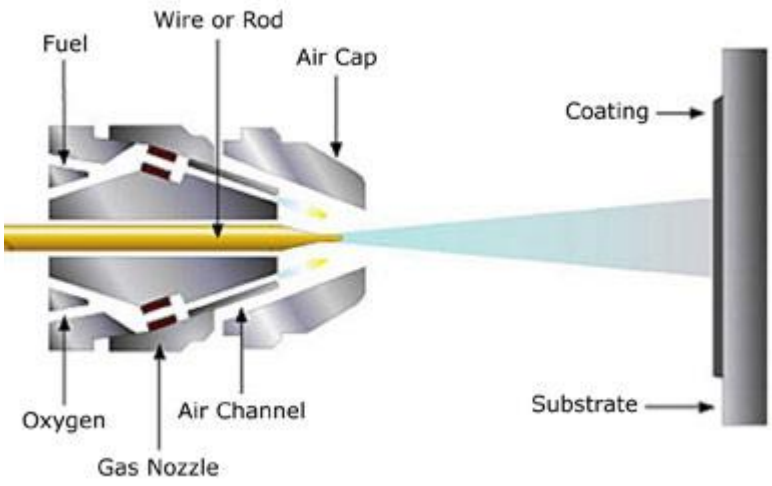

***Figure 2.1**: Schematic showing flame spraying using a wire feedstock [2].*

Since the conception of the process, technological advances have seen a growth in the number thermal spray techniques (see figure 2.1). Refinements to the original flame spray procedure have been accompanied by the development of high velocity oxy-fuel (HVOF), detonation gun (D-gun), electric arc and plasma arc processes.

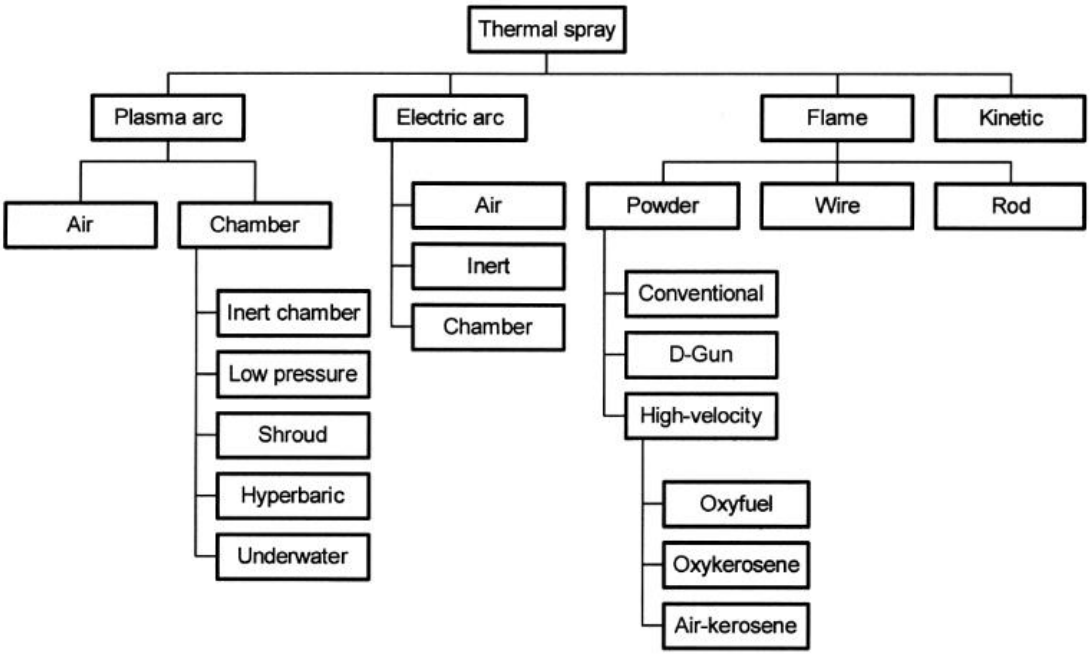

***Figure 2.2**: Thermal spray application methods [3].*

Flame powder spraying

The thermal spray method employed during the current project is known as flame powder spraying. This technique was first developed by Schori in the early 1930s. In this process a powder feedstock is fed from a hopper into an oxy-fuel flame where it melts and is transported by a mixture of flame and carrier gases to the substrate. Particles travel at a relatively low velocity (<100m/s) and as a result cohesion between the particles and bond strength with the work piece are generally low; additionally, flame sprayed coatings are often high in porosity [3].

2.1.2 Oxidation of metals during thermal spraying

Depending upon the working environment, coatings may be applied to alter thermal conductivity [4], reduce susceptibility to wear [5] or improve resistance to oxidation and corrosion [6]. The degree to which a metallic coating enhances performance is partially dependent upon the level of oxidation experienced during thermal spraying. In corrosive environments oxides disrupt chemical uniformity and provide lower resistant pathways through which corrosion can proceed [7]. During temperature cycling thermal barrier coatings may suffer cracking and spalling due differences between oxide and metal thermal coefficients of expansion [8].

For reasons such as those alluded to, oxide formation during thermal spraying has attracted a significant amount of research. In contrast to this project, most of these investigations seek to limit or (as near as possible) eradicate oxidation during the deposition process. However, despite the conflicting goals, the mechanisms of thermal spray oxidation are still of common interest.

Stages of oxidation

During thermal spraying, oxidation can be split into inflight and post-impact oxidation. In their HVOF investigation, Hackett and Settles [9] further divided this into three separate oxidation regions (see figure 2.3). In region I, which spans from the point of particle injection to the end of the jet core, oxidation occurs due to free oxygen in the combustion products. In region II (between the end of the jet core and the point of impact) inflight oxidation results from the entrainment of the local

atmosphere into the flame. Finally, in region III post-impact oxidation occurs as freshly formed splats are exposed to the atmosphere prior to deposition of the next layer [10].

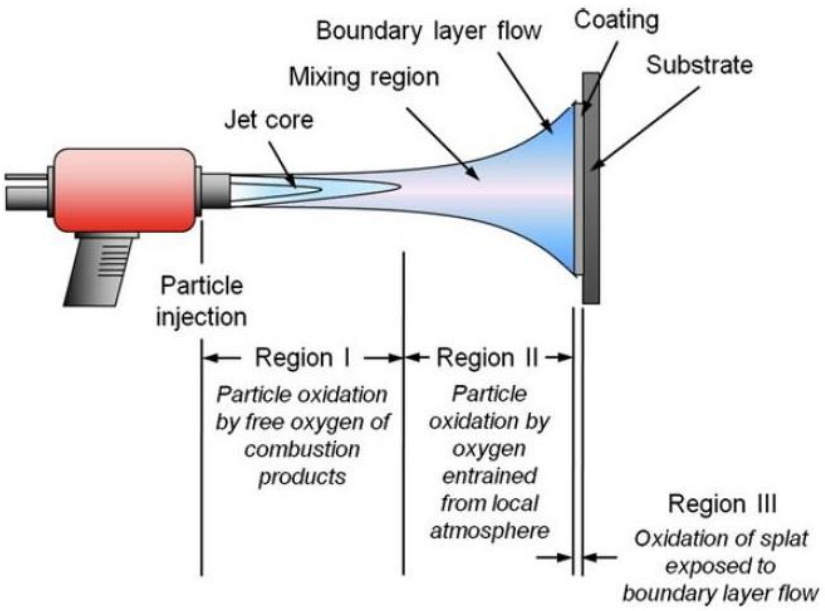

***Figure 2.3**: Schematic showing potential regions of oxidation during a generic thermal spray procedure [10].*

Similarly to Hackett and Settles, Vardelle et al divided the plasma spray procedure into three different oxidation stages: the first occurring as particles approach their melting temperature, the second as molten particles react with entrained gases and the third after deposition on the substrate [11].

Mechanisms of inflight oxidation

During thermal spray processing, entrained particles react with the surrounding environment by either diffusion or convection. Diffusion is the prevailing mechanism when the partial pressure of the reactive gases surrounding the particle reaches a specific value. At this critical pressure the flux of reactive gases towards the surface of the molten particle is greater than the counter flux of feedstock vapour and an oxide will begin to form at the metal – gas interface [12].

Diffusion controlled oxidation commonly manifests in the form of a thin oxide shell. Under the extreme thermal spray conditions, the integrity of this shell is particularly susceptible to any expansion mismatch between the newly formed oxide and the

unreacted particle core. Irregularities in the oxide scale enables diffusion controlled reactions to proceed at faster rates than otherwise expected.

Convection becomes the dominant mechanism when velocity differences between a liquefied particle and the surrounding gases promote a convection motion within the particle. Reported in HVOF, plasma and wire-arc spraying [13], this phenomenon can oxidise material at a much greater rate than diffusion controlled reactions [14].

The convective motion within a liquid particle may be represented using a spherical hill vortex. This is a model that describes fluid motion or vortex distribution within a sphere [15]. As part of their plasma spray investigation Espie et al [16] used the model to describe the formation of iron oxide nodules within pure iron particles (see figure 2.4). They proposed that internal circulation disturbs the outer oxide and deposits fragments within the particle while simultaneously moving fresh liquid to the surface. The immiscibility of the liquid FeO (T_m = 1370˚C) and liquid iron (T_m = 1538˚C) was attributed to differences in surface tensions [10].

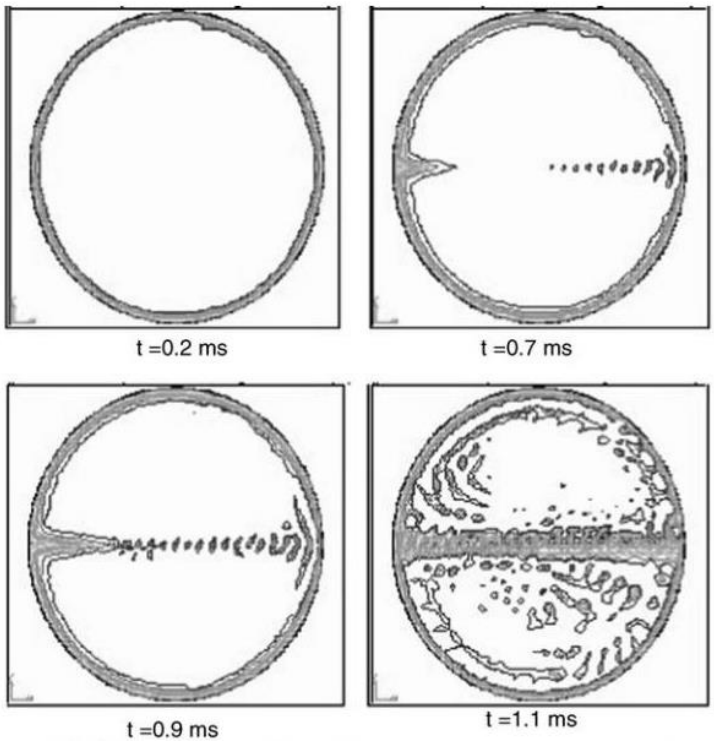

***Figure 2.4**: Model of internal convection and oxide penetration by Hill vortex mechanism [16].*

The presence of internal oxides has been confirmed by other researchers such as Deshpande et al [13], Wei et al [17], Syed et al [18]. Nodular oxides have also been observed after flame spraying a gas atomised Ni-Cr-Fe alloy during the current project (see figure 4.18).

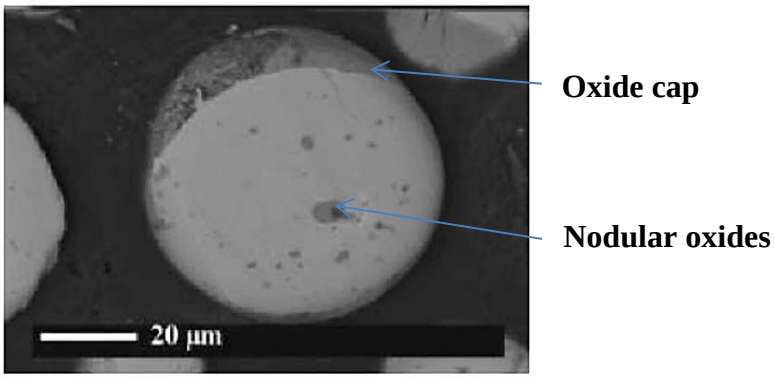

Figure 2.5*: SE image displaying nodular oxides in a 316 stainless steel powder particle [18].*

The accumulation of oxide at one end of plasma sprayed particles has been reported by Ageorges and Fauchais [19], as well as Syed et al [18]. It is proposed that oxide cap formation occurs as a light oxide on the surface of the molten metal is pushed towards the rear of the traveling particle, when the velocity of the gas becomes slower than that of the particle in the plume of the plasma jet.

Post-impact oxidation

When a molten particle impacts the substrate, the surface of the newly formed splat is exposed to the surrounding environment, until the arrival of another molten droplet. During this time period, the surface of the splat may be oxidised by the impinging gas jet, causing post-impact oxidation [10]. The time lag between two successive splats influences the length of time over which post-impact oxidation occurs. The extent of this time lag is affected by the powder feed rate, torch traverse speed and deposition efficiency of the procedure [13]. For this reason, post-impact oxidation has been the source of conflicting opinions.

Studying the oxidation of Fe during plasma spraying, Espie et al [20] suggested that splat oxidation was negligible due to the short time period (10-20µs) between

successive splats. The post impact increase in oxygen content was attributed to the hot gases sweeping the coating surface during the seconds between two successive passes of the spray gun. Conversely, Deshpande et al [13] reported the formation of thin oxide layers on the top surfaces of splats, following the plasma spraying of a Ni-5wt% Al coating.

Influences on oxidation

1. *Thermal spray technique*

The degree of oxidation that occurs during thermal spraying is governed by a number of factors, one of which is the characteristics of the spray technique. As figure 2.6 demonstrates, a metal may experience a wide range of different temperatures and velocities depending upon the chosen method of deposition. This was demonstrated by Deshpande et al [13] who compared the oxide content within Ni-5wt%Al coatings deposited using the air plasma spray (APS), wire arc spray and high velocity oxy-fuel (HVOF) techniques. They found that the wire arc spray and APS coatings contained substantially more oxidation and porosity than those produced using HVOF. This was attributed to the longer periods of high temperature air exposure associated with the wire spray and APS procedures. A similar study, comparing CoNiCrAlY coatings deposited by HVOF and plasma spray techniques has also been conducted by Scrivani et al [21].

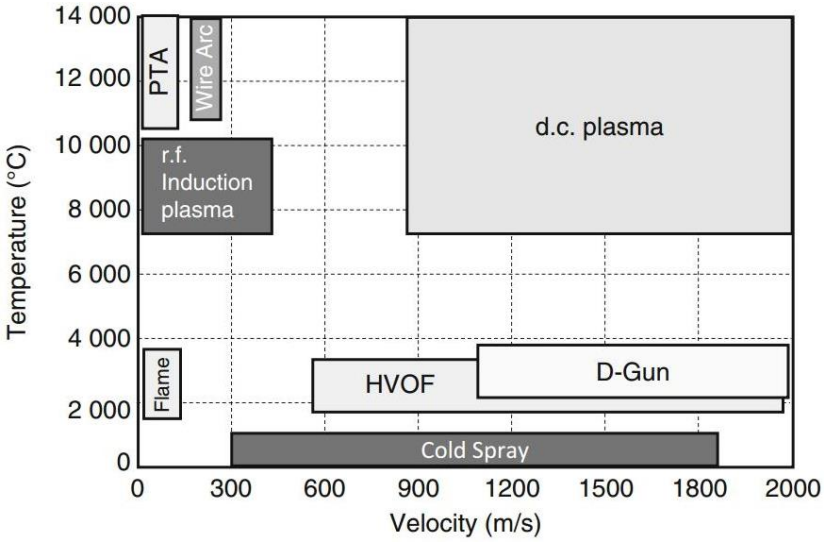

***Figure 2.6**: The range of temperatures and velocities associated with different thermal spray procedures [22].*

2. *Oxygen/fuel ratio*

In thermal spray processes that use a combustion flame, the oxygen/fuel ratio plays an important role in determining flame temperature. When the quantity of oxidising agent exceeds the stoichiometric requirements, the excess oxidising agent makes no contribution to the combustion reaction, but absorbs some of the produced heat. Therefore a fuel-lean flame will burn at a lower temperature than that obtained with a stoichiometric mixture. Likewise, when the quantity of fuel exceeds the stoichiometric requirements, the excess fuel is heated by the reaction without participating in it, thereby lowering the flame temperature below that produced by the stoichiometric mixture [23]. During thermal spray processes the temperature at which the feedstock metal is deposited influences the oxygen content of the coating.

It has been suggested by Hackett and Settles [24] that the lower temperatures associated with an increase in the oxygen/fuel ratio, restrict oxidation during HVOF spraying. Conversely, when Moskowitz and Lindley [25] used the HVOF technique to apply stainless steel coatings they found that decreasing the oxygen/fuel ratio minimised oxidisation during processing.

During a study conducted by Dobler et al [26], the spray parameters of two HVOF systems were varied in order to assess their influence upon oxidation. In both systems a relatively low particle temperature was maintained by selecting non-stoichiometric mixtures of oxygen and fuel. To achieve low oxide content, a high oxygen/fuel ratio was selected for one system, while a low oxygen/fuel ratio was selected for the other system.

3. *Controlled atmosphere and gas shroud oxidation protection*

Most thermal spray processes take place in air where oxygen can become entrained in the jet and react with the sprayed materials. Oxidation may be greatly reduced if the spraying takes place in vacuum or a controlled environment. This has been demonstrated by Scrivani et al [21], who found that CoNiCrAlY coatings produced using vaccum plasma spray (VPS) displayed much lower oxidation that those manufactured using axial plasma spray (AxPS) or HVOF.

As the equipment used to produce the vacuum or controlled environment is expensive, gas shrouding has also been employed as a cheaper alternative. Researchers have experimented with both combustible and inert gases as shrouding gases. Employing nitrogen as a shroud gas, Wang et al [27] deposited stainless steel using the wire arc spray process. It was reported that oxidation in the inert gas sprayed coating was less than in the air sprayed coating. On the other hand, Volenik et al [28] used acetylene as a shrouding gas, and found it better at reducing oxide contents than more conventional nitrogen-hydrogen shrouding during the plasma spraying of stainless steel. The effectiveness of the acetylene shrouding was attributed to the gas displacing air and also reducing oxygen availability in the plume by combining with it during the combustion reaction.

4. *Spray distance*

The distance between the substrate and the nozzle of the spray gun is another factor that can affect the oxide content of a coating. Li and Li [29] found that the consequences of varying the spray distance changed depending upon which oxidation process was dominate. When in-flight oxidation was controlling, shortening the spray distance reduced oxide content as particles spent less exposed to the process. However, when post-impact oxidation dominated, lengthening the spray distance reduced oxide content, as the newly deposited material was further away from the heat source.

Investigating the oxidation behaviour of Fe and Ni-Cr based alloys during air-plasma spraying, Zeng et al [30] found that the oxygen content of the coatings rose with increasing spray distance. This suggests that in-flight oxidation was the dominant oxidation process during these experiments.

5. *Particle size*

Studies have shown that particle size influences the degree of oxidation within a thermally sprayed coating. Typically, when in-flight oxidation dominates, researchers such as Seo et al [31], and Sobolev and Guilemany [32] have reported that oxide content within the coatings becomes greater as particle size decreases. This has been attributed to the greater surface area of the finer powder particles.

When Li and Li [29] produced coatings with particles sizes of <50μm they also found oxide content increased as the particle size became smaller. However, for particle sizes >50μm, oxygen content remained relatively stable in spite of changes to the particle size. It was proposed that for the finer particles in-flight oxidation was dominant, and for the larger particles, post-impact oxidation was the controlling mechanism. A transient particle size range was suggested over which the dominant oxidation mechanism changed.

2.1.3 Thermal spraying of Ni-Cr alloys

Ni-Cr alloys are commonly used at high temperatures, in environments requiring resistance from oxidising and corrosive agents, and for anti-wear performance. When subjected to heat, Ni-Cr alloys with high Cr contents form passivating oxide layers which help protect the alloy from further degradation. In addition to corrosion and oxidation resistance, Ni-Cr based superalloys, such as Inconel 600, offer high temperature strength due to either solid solution strengthening or precipitation strengthening.

Thermal spraying of Ni-Cr alloys onto less expensive materials enables oxidation and corrosion resistant components to be manufactured at a significantly lower cost than the bulk material equivalent. Ni-Cr coatings of high Cr content have found numerous applications in the chemical and petrochemical industries as well as in the production of gas turbines. However, in spite of their successful implementation, there still exists a performance gap between the Ni-Cr coated components and their bulk material counterparts.

Ahmed and colleagues investigated the effects of microstructural features on the corrosion resistance of bulk and HVOF sprayed Inconel 625 [33]. Potentiodynamic tests in an acidic electrolyte showed that the corrosion performance of the thermally sprayed material was inferior to that of the bulk material. While the porosity of the coatings was considered a contributing factor, galvanic corrosion between Cr-depleted resolidified regions and unmelted material was regarded the main reason for the coating's poorer corrosion resistance. In a subsequent study by Bakare et al, the performance gap between wrought and HVOF sprayed Inconel 625 was again

demonstrated by conducting potentiodynamic scans in sulphuric acid [34]. The poorer corrosion resistance of the thermally sprayed coating was attributed to the formation of the non-protective $Ni(OH)_2$. Growth of the oxide was considered a consequence of the localised regions of different composition formed by partial oxidation during the deposition process.

To address the performance difference between the bulk and thermally sprayed materials, researchers have subjected Ni-Cr based coatings to different surface melting techniques. Following laser re-melting, Tuominan et al reported significant improvements in the wet corrosion and high temperature oxidation performance of a HVOF sprayed Inconel 625 coating [35]. This was attributed to the homogenisation of the coating's microstructure and the elimination of interconnected porosity. Liu et al demonstrated the importance of selecting the correct processing parameters during their examination of laser re-melted, HVOF sprayed, WC-Inconel 625 coatings [36]. Experimenting with different laser powers and scanning velocities, optimal operating windows were established, outside of which the coatings were more prone to cracking. González et al compared the wear resistance and microstructural integrity of flame sprayed Ni-Cr-B-Si coatings after laser and oxyacetylene flame re-melting procedures [37]. While tribological evaluation of the laser and flame modified surfaces revealed no significant difference in wear behaviour, microstructural examination showed that the flame treated coatings suffered from incomplete melting. This was attributed to the imprecision of the oxyacetylene flame process.

Ni-Cr-B based metallic glasses have drawn considerable interest by combining attractive properties such as high hardness and wear resistance with an ability to protect against aqueous corrosion. Formation of these amorphous alloys requires rapid rates of cooling (in the order of 10^6 Ks^{-1} [38]) to prevent the nucleation and growth of the crystalline phases. As thermal spray processing involves the rapid solidification of molten particles, researchers have attempted to employ this technique in the production of amorphous coatings. Dent et al HVOF sprayed a Ni-Cr-Mo-B alloy onto mild steel substrates, producing coatings with a mixture of amorphous and crystalline phases [38]. The presence of the crystalline material was attributed to the transformation of amorphous material during successive spray gun passes and heterogeneous nucleation on oxide inclusions. Lee and Min similarly

reported a mixture of amorphous and crystalline phases during their examination of a HVOF sprayed Ni-Cr-W-Mo-B coating [39].

2.2 NiO

2.2.1 Crystal structure and general characteristics

Above its Néel temperature at 250˚C, NiO has a NaCl crystal structure consisting of two interlocking FCC sublattices. These sublattices are offset by [0.5,0,0], with one containing Ni^{2+} ions and the other containing O^{2-} ions (see figure 2.7). Below 250˚C, the NiO undergoes a rhombohedral distortion as a result of antiferromagnetic ordering [40].

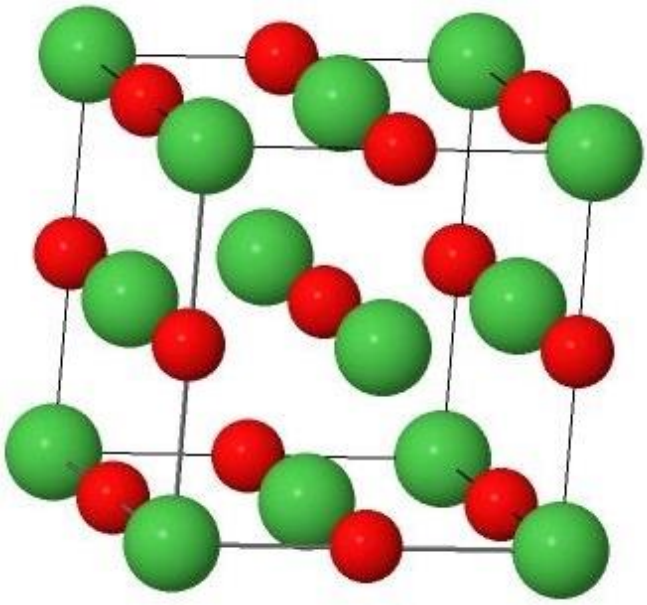

Figure 2.7*: Schematic diagram of the NiO unit cell, with O anions appearing green and Ni cations appearing red.*

NiO displays deviations from stoichiometry which may be represented by the formula $Ni_{1-x}O$. Even at high temperatures, the non-stoichiometry of this oxide remains very low, not exceeding 10^{-1} [41]. As x is decreased from this upper limit towards zero, the changes in stoichiometry cause a transformation in the appearance of the compound. At the upper limit of x, NiO is a black, opaque material. As x decreases and the material becomes increasingly stoichiometric, the NiO becomes green and translucent [42].

Studies have established that stoichiometric nickel oxide is an excellent insulator with a band gap of 4.0eV and a resistivity at room temperature of approximately $10^{13}\Omega$cm [43]. However, in non-stoichiometric NiO, the presence of microstructural defects such as Ni^{2+} vacancies causes the NiO to exhibit p-type semiconducting behaviour [44]. Within the literature there is confusion as to whether conduction occurs due to thermal excitation of holes from shallow acceptor levels, or because of thermal excitation of mobility (small polaron hopping) [45].

2.2.2 Nickel Oxide Formation

Oxidation of nickel proceeds by the outwards migration of cations and electrons from the metal-metal oxide interface to the metal oxide-gas interface. Correspondingly cation vacancies (singly or doubly charged) move in the opposite direction [46]. Under ideal conditions NiO growth occurs according to the parabolic rate law with the rate limiting factor being the diffusion of Ni cations through the oxide layer by a vacancy mechanism [47].

At temperatures over 1000˚C, results within literature generally conform to this model of oxide growth. One such example is the work conducted by Mrowec and Grzesik between the temperatures of 1100 -1400˚C. Here, good agreement was found between the calculated and the experimentally determined parabolic rate constants for nickel oxidation. It was also confirmed, through the positioning of markers at the metal-metal oxide interface that Ni cations were diffusing outwards through the oxide scale [41].

At temperatures below 1000˚C, the mechanisms governing the oxidation of nickel start to become more complicated. Oxidation no longer adheres as strictly to Wagner's theory of oxidation [48] in some cases proceeding between $10^4 - 10^7$ times faster than predicted [47]. This behaviour has been attributed to the influence of a variety of short circuit paths including grain boundaries and dislocations [49]. An example of this break from the parabolic law is documented by Atkinson et al [47]. Using Ni^{63} and O^{18} tracers, transportation processes within growing NiO scales were investigated over the temperature range 500-1300˚C. At temperatures below 800˚C, it was reported that the principal mechanism of scale growth was short-circuit

diffusion of Ni through grain boundaries in the NiO. Likewise, when Herchl et al [50] studied Ni oxidation at temperatures between 500˚C and 800˚C, they also found NiO growth did not adhere to the parabolic law. This was again attributed to grain boundary diffusion supplementing the diffusion occurring through the NiO lattice.

At lower temperatures (23˚C-450˚C) and pressures ($7x10^{-8}$ – $8x10^{-4}$ Torr) Graham and Cohen [51] studied the oxidation behaviour of polycrystalline nickel. At temperatures below 300˚C, rather than parabolic growth, they observed logarithmic kinetics with oxide layers reaching a limiting thickness that varied with oxidation temperature [52]. Due to uncertainties regarding the pressure dependence of oxide growth and the effects of electric fields on thin film growth Graham and Cohen found it difficult to identify the rate-determining step. Nevertheless, ionic transport and chemisorption at the outer surface layer were suggested as possibilities.

2.2.3 Fe doped NiO

Fe-Ni-O pseudo-binary section of Fe_2O_3-NiO in air

As the Fe-Ni-O system is of great significance in the manufacture of corrosion-resistant and high-temperature steels, the Fe-Ni-O system has attracted substantial attention from researchers such as Rhamdhani et al [53], Luoma [54] and Schneider and Schmalzried [55].

Rhamdhani et al studied the phase equilibria of Fe-Ni-O in air experimentally, at temperatures ranging from 800˚C to 1600˚C. Data was presented in the form of a phase diagram (see figure 2.8), alongside computed predictions and the results of Schneider and Schmalried [55]. Over the range of compositions studied, the formation of (Fe,Ni)O-bunsenite, spinel and hematite phases was observed. Generally the results of the investigation agreed with the computed values, and the data collected by previous researchers. However, Rhamdhani et al [53] did measure a substantial increase in the solubility of Fe in (Fe,Ni)O-bunsenite. This was accredited to improvements made in their experimental technique.

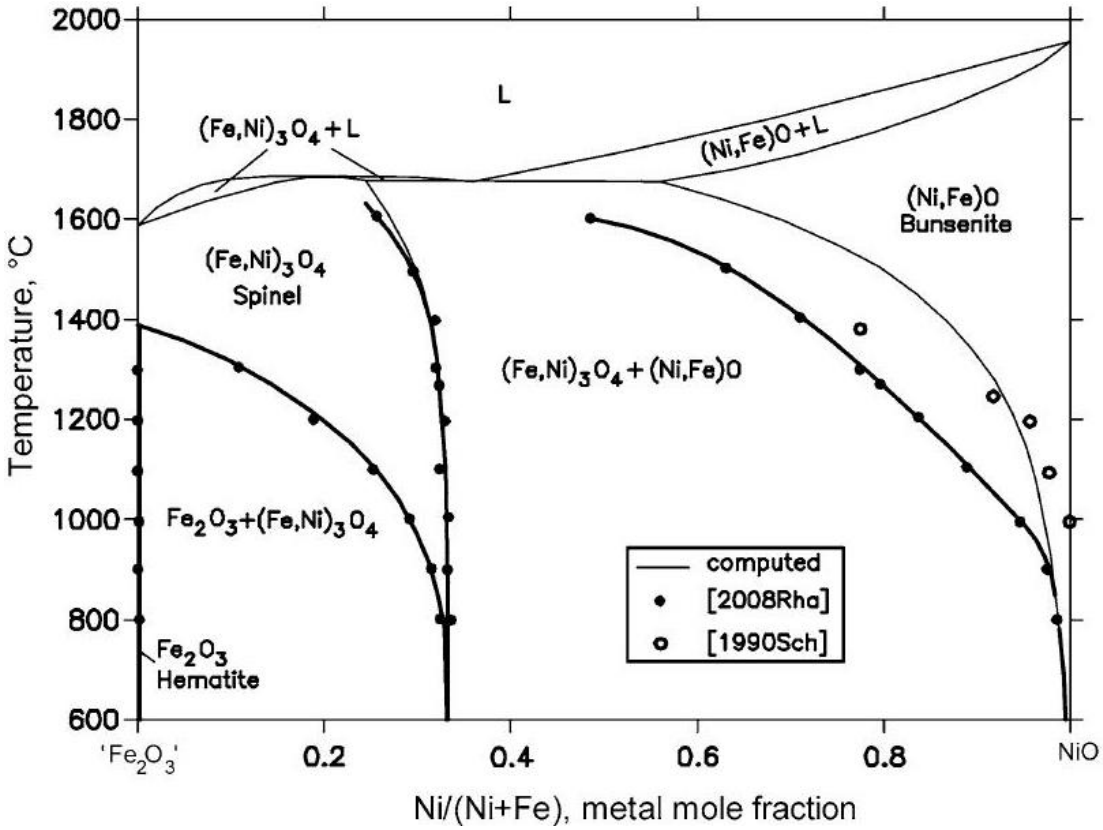

***Figure 2.8**: Fe-Ni-O pseudo-binary phase diagram of Fe_2O_3-NiO in air [56].*

In the current study, the right side of the Fe-Ni-O pseudo binary has been of particular interest, suggesting that the NiO lattice structure accepts significant quantities of Fe dopant at high temperature.

Structural analysis of Fe doped NiO

A variety of Fe doped NiO nanostructures have been prepared using the electrospinning [57, 58], chemical co-precipitation [59] and hydrothermal [60] techniques. Kim et al [61] have also produced Fe-doped hollow spheres with shell thickness of ~12nm using a process which involved: application of Fe-precursors to Ni spheres, partially oxidation of the sphere's surfaces, dissolution of the Ni cores and a final heat treatment.

During these studies, while Fe dopant levels remained below 3at%, XRD analysis detected no alteration in the lattice parameter of the cubic, NiO phase. Manna et al substantiated the findings of their XRD analysis by using lattice resolution images to calculate d-spacings consistent with pure NiO [60].

The stability of the NiO lattice parameter with increasing Fe content was attributed to the similar ionic radii of the Ni and Fe ions. At the coordination number (CN) of 6, the Fe^{2+} and Fe^{3+} atomic radii are 0.78Å and 0.65Å respectively, which are close to the Ni^{2+} atomic radii of 0.69Å [62]. It was therefore proposed that the Fe ions may substitute Ni ions without significantly altering the NiO lattice parameter.

Mallick et al [63], who used XRD to examine Fe doped NiO particles produced by chemical co-precipitation, also found that the NiO lattice parameter remained constant up to dopant levels of 3at%. However, when Fe concentration was increased to 5at%, a slight increase in NiO lattice parameter was noted, indicating that strain had become sufficient to induce a detectable change.

Similarly to Mallick et al, Mishra and colleagues [59] also produced Fe doped NiO nanoparticles using the co-precipitation method. Comparing diffractograms obtained from Fe doped with non-doped NiO specimens, a broadening was noted the peaks of the former. Using the Debye-Scherrer equation, a drastically reduced grain size was calculated in the Fe doped specimens. This restriction in grain growth was attributed to strain evolution in the matrix.

2.2.4 Cr doped NiO

Cr-Ni-O pseudo-binary phase diagram

The Ni-Cr binary system forms the base of some of the most important heat resistance alloys. Therefore, the Cr-Ni-O ternary system, which describes the influence of oxygen upon these alloys, has attracted significant interest. Experimental work carried out by researchers has formed the basis for thermodynamic analyses conducted by Taylor and Dinsdale [64] and Kjellqvist et al [65].

In Taylor and Dinsdale's assessment of the system, good agreement was generally found with the experimental results. However, this model was found to produce an unwanted miscibility gap in the liquid phase. Using the same experimental results in a subsequent study, Kjellqvist et al reassessed the liquid phase, eliminating the miscibility gap. Due to the reassessment of the liquid phase, the calculated $NiCr_2O_4$

melting point was changed from 2138˚C to 2083˚C. A Cr-Ni-O pseudo-binary in air, constructed by Kjellqvist et al, compares the two assessments of the system (see figure 2.9).

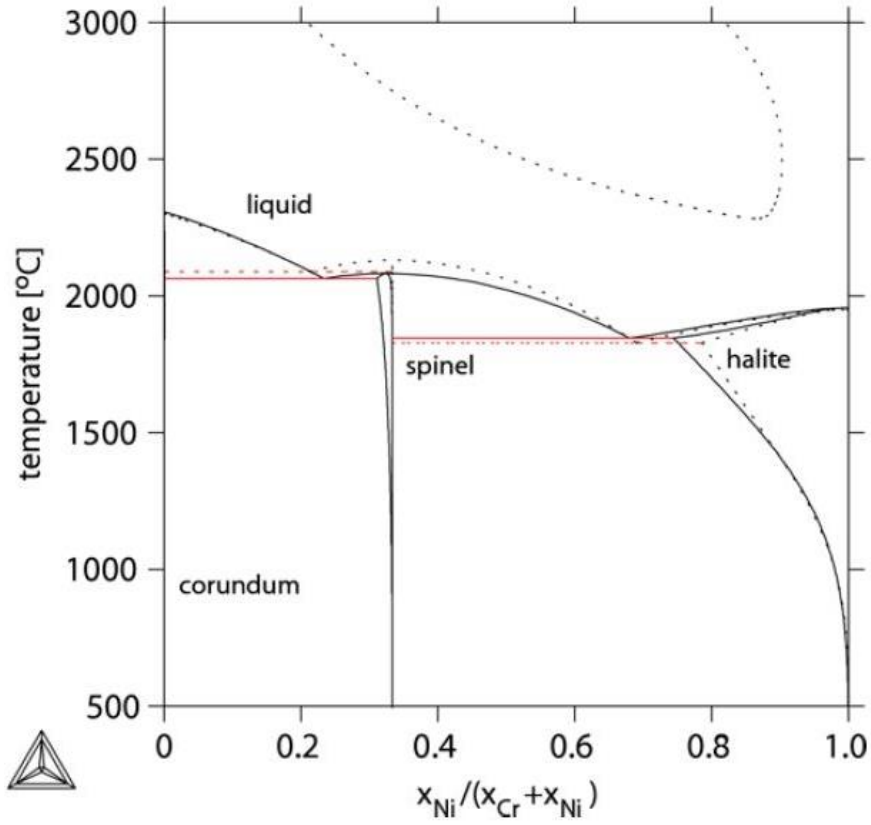

Figure 2.9*: Calculated Cr-Ni-O pseudo-binary in air at 1 atm. The solid lines and dashed lines signify the work of Kjellqvist et al [65] and Taylor and Dinsdale [64] respectively.*

In a similar fashion to the Fe-Ni-O pseudo-binary, the right side of the Cr-Ni-O phase diagram suggests that a significant quantity of Cr may substitute into the NiO lattice at high temperature.

Structural analysis of Cr doped NiO

Cr doped NiO has attracted attention as a potential sensing electrode for the detection of harmful pollutants such xylene, toluene and NO_2. Subsequently, sensors of varying scales and morphologies have been produced using a solvothermal reaction [66], electrostatic spraying [67], and the thermal decomposition of nitrates [68]. During these investigations, the newly formed doped NiO sensors were examined

using X-ray diffraction to determine whether a solid solution had formed and whether any secondary phases were present.

In XRD experiments conducted by Kim et al [66] and Cao et al [67], pure NiO specimens were compared with doped samples containing up to 2.56 at% Cr. Both studies reported that the Cr doping caused no significant difference to the cubic structure of the NiO. Conversely, when Elumalai et al [68] compared diffraction patterns obtained from pure and 3 at% Cr doped NiO specimens, it was noted that the peaks in the doped sample had shifted to a slightly higher angle. Estimated lattice parameters of 4.154Å and 4.141Å were calculated for the pure and doped NiO specimens respectively.

At the coordination number (CN) of 6 the ionic size of the Cr^{3+} (0.615Å) is smaller than that of the Ni^{2+} (0.69Å). Elumalai et al proposed that this size difference was responsible for the reduction in the size of the doped NiO lattice parameter.

2.3 Spinel

2.3.1 Introduction

As noted previously with NiO, the crystal structure of spinel also features an O sublattice. The spinel unit cell consists of 32 O anions and 24 cations. Of the 24 cations, 16 occupy one half of the octahedral sites, while the other 8 occupy one eighth of the tetrahedral sites (see figure 2.10).

In a normal spinel such as $NiCr_2O_4$ [69], the divalent ions (Ni^{2+}) are located on the tetrahedral sites and the trivalent ions (Cr^{3+}) are positioned on the octahedral sites. Conversely, in an inverse spinel such as $NiFe_2O_4$ [70], half the trivalent ions (Fe^{3+}) are located on the tetrahedral sites, while the divalent ions (Ni^{2+}) and the remaining half of the trivalent ions (Fe^{3+}) occupy the octahedral sites. Additionally, there are also mixed spinel [71], which are intermediate between the normal and inverse spinel structures.

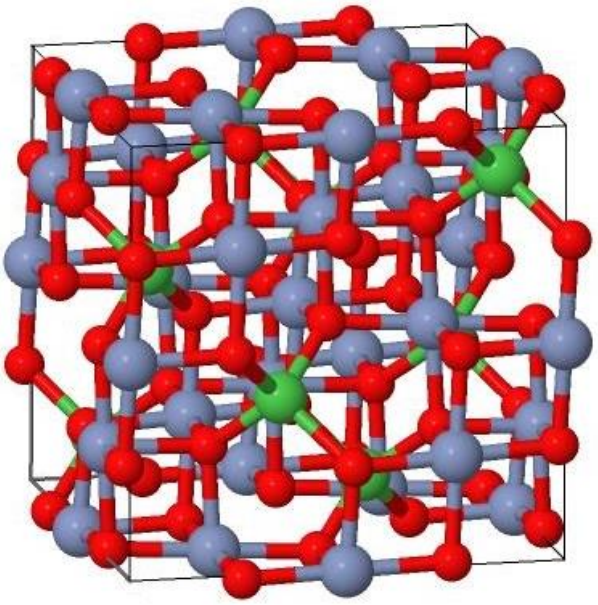

***Figure 2.10**: Schematic diagram of the spinel unit cell. Cations positioned on octahedral and tetrahedral sites appear purple and green respectively, while O anions appear red.*

2.3.2 Cr-substituted nickel ferrites

The electrical, magnetic and structural properties of a spinel oxide may be altered by adjusting the site and valance distributions through metallic doping. Substituted nickel ferrites have been widely employed as magnetic materials due to their high electrical resistivity, low eddying current and dielectric losses [72].

The substitution of Fe^{3+} with Cr^{3+} ions in the $NiFe_2O_4$ crystal structure has received attention from a number of researchers [72, 73, 74, 75, 76, 77]. This work is of particular interest to the current project, as composition of the studied spinel is believed to lie between the extremities of the $NiFe_2O_4$ - $NiCr_2O_4$ binary.

Structural properties

The influence of Cr^{3+} substitution on the crystal structure of $NiFe_2O_4$, has been examined using the X-ray and neutron diffraction techniques [66, 67, 68, 69, 70]. Results have shown that the lattice parameter of the $NiCr_xFe_{2-x}O_4$ decreases linearly with increasing Cr^{3+} concentration over the range $0 \leq x \leq 1.4$. This has been

accredited to the ionic radius of the 6-fold-coordinated Cr^{3+} (0.615Å) being smaller than that of the 6-fold coordinated Fe^{3+} (0.67Å) [62].

Considering the intensity ratios of planes $I_{(200)/I(400)}$, $I_{(400)/(440)}$ and $I_{(422)/I(400)}$ sensitive to cation distribution, Singhal and Chandra used intensities calculated from X-ray diffraction patterns to determine the arrangement of Ni^{2+}, Cr^{3+} and Fe^{3+} ions in $NiCr_xFe_{2-x}O_4$ [72]. The results suggested that Cr^{3+} favoured octahedral sites while $x<0.8$, then began occupying both tetrahedral and octahedral sites at $x=0.8$.

In contrast to the aforementioned XRD studies, Ziemniak et al [71], and Allen et al [77], examined $NiCr_xFe_{2-x}O_4$ across the entire compositional range, reporting a non-linear relationship between lattice parameter and increasing Cr content. These researchers reported that the lattice parameter of $NiCr_xFe_{2-x}O_4$ decreased with rising Cr content until approximately $x = 1$. After this point, further increases in Cr concentration then caused the lattice parameter to grow. First considering crystal field stabilisation energy (CFSE) values, Allen et al ranked cations in order of their preference for the octahedral sites: Cr^{3+}, Ni^{2+}, Fe^{3+}. Until $x = 1$ ($Ni(CrFe)O_4$), it was proposed that the smaller Cr^{3+} ions would replace the Fe^{3+} ions on the octahedral sites, leading to a reduction in lattice parameter. Once all the Fe^{3+} ions at the octahedral sites had been replaced, further Cr^{3+} additions ($1 < x \leq 2$) were expected to replacing Ni^{2+} at the octahedral sites due to their greater preference for the octahedral sites. These displaced Ni^{2+} ions would then, in effect, replace smaller Fe^{3+} in the tetrahedral sites causing the observed increase in lattice parameter.

Magnetic properties

The influence of Cr^{3+} doping on the magnetic properties of $NiCr_xFe_{2-x}O_4$ was also investigated by Singhal and Chandra [72], using a vibrating sample magnetometer (VSM). Results indicated that the saturation magnetization decreased linearly as the Cr concentration increased. This was attributed to a weakening of the exchange interactions in the octahedral sublattice by non-magnetic Cr^{3+} ions which favour the octahedral sites. While saturation magnetization decreased, coercivity was found to increase slowly up to $x = 0.8$, after which it increased steeply. This was ascribed to Cr^{3+} ions on the tetrahedral sites, causing a negative trigonal field to be superimposed on the octahedral Cr^{3+} ions. Due to this, a 2-fold degeneracy of the

orbital ground state caused an unquenched orbital angular momentum and a large anisotropy. Similar behaviour was noted by Gabal and Angari [73] who studied $NiCr_xFe_{2-x}O_4$ over the range $0 \leq x \leq 1$.

A Mössbauer study conducted by Singhal and Chandra [72], examined $NiCr_xFe_{2-x}O_4$ specimens with compositions of between x = 0 and x = 1.2. The spectra collected from all the specimens exhibited two Zeeman sextets, due to Fe^{3+} ions at the octahedral and tetrahedral sites, indicating the material was ferrimagnetic. At room temperature, hyperfine magnetic field values for both forms of lattice site decreased as the Cr concentration increased. This was reported to occur because the replacement of Fe^{3+} ions by Cr^{3+} ions affects the hyperfine field of the closest Fe^{3+}sites by means of super transferred hyperfine fields. The intensity of the octahedral site was found to decrease up to x = 0.8 and then increase with additional Cr doping. Singhal and Chandra attributed this to coercivity behaviour, formerly encountered at this composition during VSM experimentation.

Electrical conduction

The electrical conductivity of $NiCr_xFe_{2-x}O_4$ specimens has been reported to rise with increasing temperature, in a fashion similar to most semiconducting materials [73, 76, 75]. At low temperatures these specimens exhibited a clear frequency dependency, which decreased with rising temperature, until the specimens became frequency independent. The specific temperature at which the specimens became frequency independent was identified as the Curie temperature.

Studying $NiCr_xFe_{2-x}O_4$ over the range $0 \leq x \leq 1$, Gabal and Angari [73] found that conductivity decreased with the increase in Cr concentrations. Assuming that conduction was due to electron transfer by cations situated on the octahedral sites, it was proposed that the observed conductivity decrease was due to Cr^{3+} ions replacing Fe^{3+} on the octahedral sites. Here, it was suggested, that the Cr^{3+} ions would restrict the Fe^{2+} to Fe^{3+} conduction that occurs due to the small polaron hopping mechanism. Similar reductions in conductivity were reported by Lee et al [76], and Fayek and Ata-Allah [75], in studies examining $NiCr_xFe_{2-x}O_4$ between $0 \leq x \leq 0.6$ and $0 \leq x \leq 1$ respectively.

Between x=0 and x=1, Gabal and Angari reported that the activation energy for conduction rose with increasing Cr concentrations. Conversely, Fayek and Ata-Allah, who studied $NiCr_xFe_{2-x}O_4$ over the same range of compositions, found that activation energies increased up to x=0.6 and then decreased upon further Cr addition.

2.3.3 Immiscibility in the $NiFe_2O_4$ and $NiCr_2O_4$

Ziemniak and colleagues [71] investigated spinel immiscibility by air annealing a series of $NiCr_xFe_{2-x}O_4$ single-phase solid solutions ($0 \leq x \leq 2$) at 600˚C. After 1 year at this temperature, XRD scans revealed evidence of partial phase separation in the spinel of composition x = 1. This composition was further investigated by growing crystals of $Ni(CrFe)O_4$ in a molten salt process, at temperatures between 400˚C and 900˚C. Chemical analyses performed by EDS and electron microprobe analyser (EMPA) revealed composition variations consistent with phase separation. The solvus determined using these results is displayed in figure 2.11.

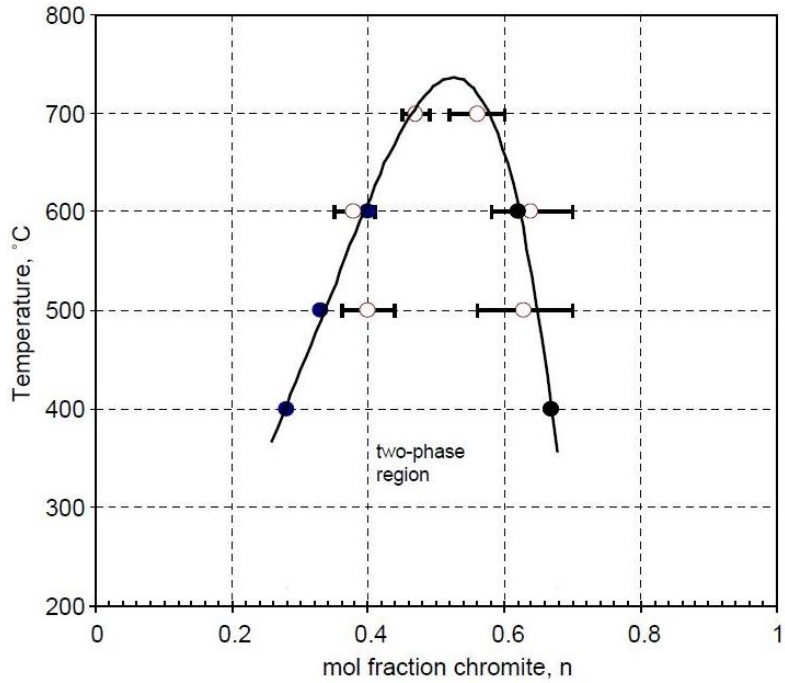

***Figure 2.11**: Measured solvus in the $NiCr_xFe_{2-x}O_4$ spinel binary. EDS and EMPA results are represented by open circles and filled circles respectively [71].*

As figure 2.11 demonstrates, a consolute solution temperature of approximately 750˚C appears in the $NiFe_2O_4$ – $NiCr_2O_4$ spinel binary. This is consistent with the work of Allen et al [77], who reported complete mixing in this system at 950˚C.

Spinel formation during the current study typically occurred above the consolute solution temperature at 800˚C. However, even during the lower temperatures heat treatments (400˚C - 500˚C), it is unlikely that phase separation occurs, as the spinel within the thick films has a Cr-rich composition, which situates it within the single-phase region.

2.4 Spinel precipitation within a NiO matrix

2.4.1 Nucleation

The process of phase transformation may be divided into nucleation and a growth stages. Nucleation involves the grouping of atoms into small metastable clusters of the new phase (embryos), which then grow to become stable (nuclei). In the growth stage, these nuclei then increase in size at the expense of the parent material.

There are two types of nucleation: homogeneous and heterogeneous. During homogeneous nucleation, the new phase nucleates uniformly throughout the parent phase. Conversely, for heterogeneous nucleation, the nuclei develop preferentially at sites like grain boundaries, dislocations and container surfaces.

Homogenous nucleation

Consider the solidification of a material from γ to α phase at a temperature where both are of the same composition. It is assumed that the α phase forms spherical nuclei, each of which have a radius of r [78].

The overall free energy change accompanying this phase transformation consists of two terms. One of these relates to the volume of the precipitate and the other to the interface between the precipitate and the parent material.

The first of the term is the free energy difference between the α and γ phases, or volume free energy $\Delta G_{v,}$ multiplied by the volume of the spherical nucleus

$(4/3\,\pi r^3)$. ΔG_v becomes negative when the temperature is below the equilibrium temperature at which the α phase forms.

The second term consists of the surface free energy σ, which is positive, multiplied by the surface area of the nucleus ($4\pi r^2$).

Finally, the overall free energy due to the formation of precipitate of radius r is the sum of these terms.

$$\Delta G = \frac{4}{3}\pi r^3 \Delta G_v + 4\pi r^2 \sigma \qquad \textit{equation 2.1}$$

Figure 2.8 displays the volume, surface and overall free energy contributions plotted against the precipitate radius. Because the volume increases with as the radius cubed, the surface energy term dominates when the precipitate is small and the volume free energy dominates when the precipitate is large. As figure 2.12 demonstrates, the precipitate free energy increases initially, before passing through a maximum and declining.

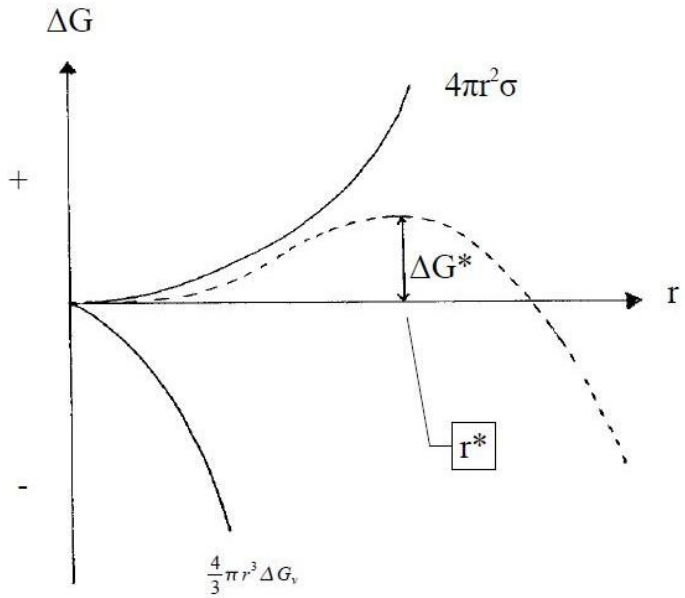

Figure 2.12*: Graphical plot showing the free energy change with precipitate radius.*

Particles with radii less than critical radius r* are unstable and termed embryos, while particles with radii exceeding the critical radius are stable, and described as nuclei. The free energy value that corresponds to the critical radius is termed the critical free energy (barrier) ΔG*, and is the free energy required for the formation of a stable nucleus.

To calculate r*, the ΔG equation is differentiated with respect to r, and the resulting expression set equal to zero. After solving for r, the following equation is obtained:

$$r^* = \frac{2\sigma}{\Delta G_v} \qquad \textit{equation 2.2}$$

By substituting the expression for r* into equation 2.1, it may be shown that:

$$\Delta G^* = \frac{16\pi\sigma^3}{3(\Delta G_v)^2} \qquad \textit{equation 2.3}$$

Heterogeneous nucleation

While the degree of undercooling required for homogenous nucleation can be significant, in most situations only a low level of undercooling is required. This is because the critical free energy barrier for nucleation (ΔG*) is reduced when the nuclei develop upon pre-existing interfaces, as the surface free energy lessens [78].

This process may be understood by considering the nucleation of a solid from a liquid phase, on a flat surface (see figure 2.13). At the two-phase boundary, three interfacial energies are found: the solid-surface (σ_{SI}), solid-liquid (σ_{SL}), and liquid-surface (σ_{LI}) interfacial energies.

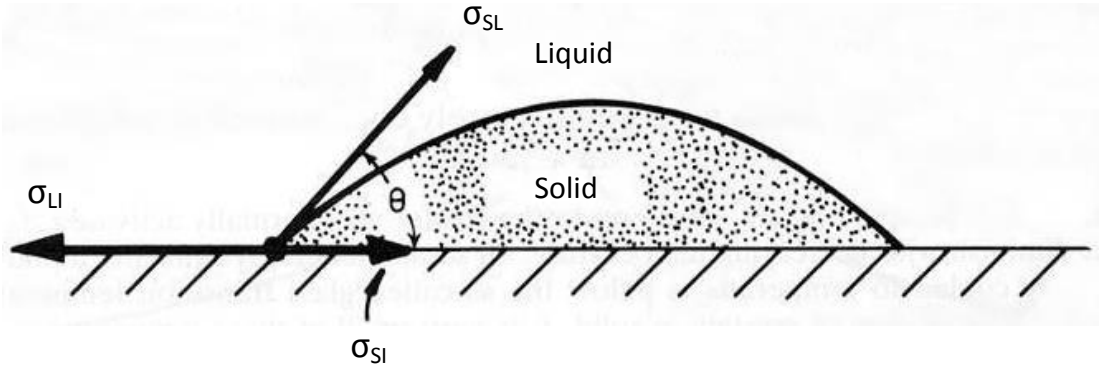

***Figure 2.13**: Heterogeneous nucleation of spherical cap on a flat surface.*

Balancing the interfacial tensions in the plane of the flat surface gives the following expression, where the angle between the σ_{SI} and σ_{SL} vectors is the wetting angle.

$$\sigma_{LI} = \sigma_{SI} + \sigma_{SL}\cos\theta \qquad \textit{equation 2.4}$$

The formation of the nucleus produces the following change in Gibbs free energy:

$$\Delta G = V_S\Delta G_V + A_{SI}\sigma_{SI} + A_{SL}\sigma_{SL} - A_{SL}\sigma_{LI} \qquad \textit{equation 2.5}$$

Where $V_s\Delta G_v$ is the free energy change associated with the precipitation of the solid. The $A_{SI}\sigma_{SI}$ and $A_{SL}\sigma_{SL}$ terms are free energy necessary for the interface around the precipitate. And, the negative $A_{SL}\sigma_{LI}$ term is the free energy reduction that occurs as the interface between the liquid and flat surface is removed during the precipitation of the solid.

It may be shown that:

$$\Delta G_{het} = \left(\frac{4}{3}\pi r^3 \Delta G_v + 4\pi r^2 \sigma_{SL}\right) S(\theta) = \Delta G_{hom} S(\theta) \qquad \textit{equation 2.6}$$

Where S(θ) is a function of the wetting angle θ and has a numerical value of between zero and one.

By differentiating equation 2.6 with respect to r, and setting the resulting expression equal to zero, the critical radius r* may be calculated. Its value is the same as the critical radius for homogeneous nucleation (equation 2.2).

$$r^* = \frac{2\sigma}{\Delta G_v} \qquad \textit{equation 2.7}$$

By substituting the expression for r* into equation 2.6, it may be shown that:

$$\Delta G^* = \frac{16\pi\sigma^3}{3(\Delta G_v)^2} S(\theta) \qquad \textit{equation 2.8}$$

From equation 2.8 it is clear that the critical free energy barrier for heterogeneous nucleation is smaller than that for homogeneous nucleation (equation 2.3) by an amount corresponding to S(θ).

2.4.2 Cation vacancies

Assuming the spinel and doped NiO phases share an O sublattice, the precipitation of spinel particles would seem only to require the rearrangement of cations. However, as spinel contains trivalent cations, charge balance in the spinel phase will require a lower number of cations per O anion than the doped NiO. Therefore, vacancies are also needed for the precipitation of the spinel within a doped NiO [79].

The formation of a spinel requires some divalent cations to be replaced by vacancies and trivalent cations. For one unit cell of spinel to replace the equivalent volume of 8 NiO unit cells (spinel lattice parameter is almost exactly twice that of the NiO lattice parameter) 16 trivalent cations and 8 vacancies must be substituted for 24 divalent cations.

Changes to both the temperature and O activity influence the valance state of the Fe and Cr dopant atoms. This affects the vacancy concentration within the doped NiO, which must adjust to preserve charge neutrality. As environmental conditions cause the divalent cations to adopt a trivalent state, the additional positive charge is balanced by a cation vacancy. Therefore, assuming the vacancy concentration is in equilibrium with the local atmosphere, the concentration of vacancies will be half that of the trivalent cations.

While investigating the thermodynamics of the Ni-Fe-O system, Schneider and Schmalzreid [55] used coulometric titration to measure vacancy concentration in Fe-doped NiO. During the study, samples doped with 1-10 at% Fe were held at temperatures of between 900 and 1030˚C, at a variety of O partial pressures. Results showed that vacancy concentration rose with increasing Fe concentrations, decreasing temperatures or a reduction in oxygen partial pressure. For each of the compositions tested, measurements suggested that all Fe in the doped NiO had become trivalent before spinel precipitation began.

Another study conducted by Greskovich [80], suggests that the Cr within Cr-doped NiO exists predominantly in a trivalent state when heated in air between the temperatures of 1330˚C and 1580˚C. During this research single crystals of NiO were heated in contact with Cr_2O_3 tablets in order to examine the kinetics of $NiCr_2O_4$ formation in NiO. Subsequent XRD measurements indicated that the NiO lattice parameter decreased following the heat treatment as smaller Cr^{3+} ions substituted for the larger Ni^{2+} ions. These results were in agreement with previous investigations carried out by Hauffe [81] and Wagner and Zimens [48].

2.4.3 Modes of spinel precipitation

The precipitation of a spinel within a (A,B)O solid solution has been shown to occur by the local reordering of cations and pre-existing cation vacancies. Additional, it may also occur by internal oxidation, which requires the long-ranged diffusion of vacancies from the surface.

These contrasting modes of precipitation can attributed to a difference in the valence state of the dopant atoms before nucleation. Investigating spinel precipitation within the Ni-Fe-O system, Summerfelt and Carter [82] slowly cooled doped NiO to just above the solvus temperature, enabling the majority of the Fe to form Fe^{3+} as vacancy concentration reached equilibrium. With continued cooling, spinel precipitation then occurred through the local rearrangement of cations and cation vacancies. This widespread precipitation has also been reported in the $NiCr_2O_4$/NiO system by Chen et al [83].

In contrast to the aforementioned studies, Ostyn et al [84] held a Fe-doped NiO at low oxygen partial pressure, where dopant cations were predominantly in a divalent state. Then at temperatures of 900˚C-1200˚C, spinel precipitation was induced by a rapid increase in oxygen activity. During this process vacancies diffused from the surface, enabling the divalent Fe cations to form trivalent Fe cations and spinel to precipitate topotactically within the NiO matrix. Measurements suggested that the two phase NiO-spinel layer thickness varied parabolically with time, indicating that the diffusion of vacancies from the surface was a rate limiting factor.

Similar internal oxidation experiments have been carried out in (MgFe)O solid solutions by Luecke and Kohlstedt [85]. After annealing specimens at a low oxygen partial pressure, they heated specimens in air to temperatures between 873˚C and 1076˚C, and observed the inward growth of a two-phase region. The growth rate of this internally oxidised region was found to obey a parabolic law. Ricoult and Schmalzried [86], who also examined internal oxidation within (MgFe)O solid solutions, reported a break from this parabolic dependency when the two-phase region had grown sufficiently thick.

2.4.4 Morphology of spinel precipitates

During the examination of the $NiFe_2O_4$/NiO and $NiCr_2O_4$/NiO systems, a variety of different precipitate morphologies have been reported. Octahedrons bound by the {111} planes have been observed in the $NiFe_2O_4$/NiO system [82], while faceted particles of an undetermined shape have been reported in the $NiCr_2O_4$/NiO system [83]. Dendritic precipitates, with arms extended in the <100> directions, were common to both systems [87, 83], whereas coherent ellipsoids are only documented in the $NiCr_2O_4$ system [83]. As a variety of morphologies may occur within each system, it appears that the kinetics of nucleation and growth play an important role in determining precipitate shape.

Summerfelt and Carter [82] examined the influence of nucleation rate on spinel morphology while investigating the $NiFe_2O_4$/NiO system. To achieve high rates of nucleation a Fe doped NiO specimen was held at 792˚C (158˚C below the solvus temperature) for 40 minutes. Subsequent TEM examination revealed that arrays of coherent, octahedron-shaped particles had precipitated within the specimen. To produce lower nucleation rates, a further sample was cooled slowly from above the solvus temperature into the two-phase region. Under these conditions, larger coherent precipitates formed with a dendritic appearance

In the $NiCr_2O_4$/NiO system, Chen et al [83] also examined how contrasting rates of nucleation could affect precipitate morphology. When nucleation rates in the Cr doped NiO were low, due to the slow cooling from above the solvus temperature, dendritic precipitates developed. However, when a specimen was held at 950˚C and greater undercooling produced higher rates of nucleation, arrays of coherent, spherical precipitates initially formed. Continued aging caused the precipitates to develop faceted and then ellipsoidal morphologies, after 1 day and 9 days respectively. The ellipsoidal plates were identified as the system's minimum energy shape.

The changes in spinel morphology with nucleation rate may be explained by considering the conditions necessary for solid-state dendrite formation. These requirements have been summarised by Doherty [88] as follows:

1. Low mismatch between the precipitate and matrix phases.

2. A low rate of solute diffusion within the precipitate.

3. Almost isotropic surface energy.

4. A wide spacing between precipitates.

When the nucleation rates were slow, all the requirements for dendritic growth in the $NiFe_2O_4$/NiO and $NiCr_2O_4$/NiO systems appeared to have been fulfilled. However, at higher rates of nucleation this was no longer true. As greater nucleation rates increase the density of the spinel particles, a reduction in the spacing of the precipitates likely causes the difference in morphology.

During a further study conducted by Summerfelt and Carter [87], Fe doped NiO (~2at%Fe) was cooled slowly (100˚C/h) from above the solvus temperature to room temperature, causing the formation of dendritic precipitates. Subsequently the specimen was heated to 850˚C and studied intermittently using TEM over a 35h time period. Over the course of the heat treatment, the dendritic particles were found to transform into octahedrons. As misfit between the spinel and NiO phases is small (approximately 0.3% at 850˚C) shape transformation was considered to occur primarily to reduce interface energy. The stability of the transformed precipitates during further heat treatments suggested the octahedron was the minimum-energy shape.

In the $MgFe_2O_4$/NiO system, coherent octahedrons bound by {111} planes [89] and coherent dendrites with arms extending in the <100> directions have likewise been observed [90]. The growth of dendrite arms in the <100> direction has been attributed to the minimum elastic modulus in the <100> directions of the MgO crystal structure [86]. A similar assertion was made by Summerfelt and Carter during their examination of dendritic $NiFe_2O_4$ precipitates within a NiO matrix [82].

2.4.5 Grain boundary denuded zones

Upon the heat treatment of NiO doped with either Cr [83] or Fe [91], studies have reported the development of precipitate free zones adjacent to the grain boundaries. The formation of denuded zones such as these may be attributed to either vacancy depletion or solute depletion. While considering Guinier-Preston zone precipitation

during the aging of Al alloys, Jacob and Pashley [92] discussed these two possibilities.

Vacancy-depleted denuded zones

As figure 2.14 shows, Jacob and Pashley defined a maximum temperature (T_C) at which homogeneous nucleation can occur, when no excess vacancies are present. Once temperatures exceed this value homogenous nucleation does not take place due to an insufficient solute supersaturation. Jacob and Pashley hypothesized that above this temperature nucleation may occur with a critical excess-vacancy concentration $(C_V)_C$ up to a maximum temperature T'_C. The production of such a vacancy excess occurs when a sample is quenched from high temperature. During subsequently aging above T_C, these excess vacancies affect precipitation by either aiding the diffusivity of the solute, or by producing vacancy aggregates where the new phase may nucleate [93].

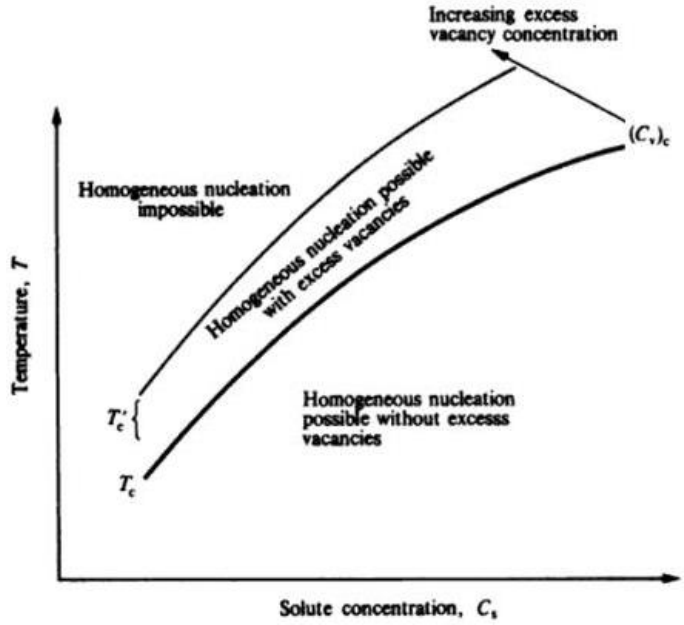

***Figure 2.14**:Graph displaying the variation of T_C and T'_C with solute concentration [94].*

After quenching to the aging temperature T_A, an excess-vacancy profile develops next to the grain boundary (see figure 2.15). This occurs because grain boundaries act as vacancy sinks. The shape of the excess-vacancy profile will depend upon the temperature the material was quenched from and the rate at which cooling

proceeded. As figure 2.15 illustrates, this produces changes in the width of the denuded regions.

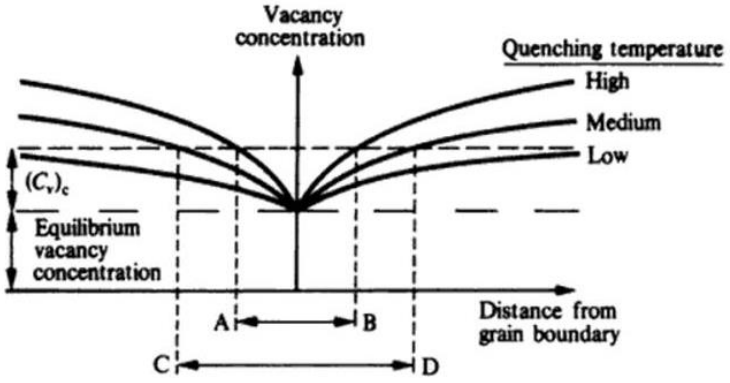

***Figure 2.15**: Schematic showing the excess vacancy profiles near the grain boundary after quenching [94].*

Using the model of Jacob and Pashley, when $T_A < T_C$ nucleation will take place right up to the grain boundary; however, when $T_A > T_C$ nucleation may only occur in areas of the sample where the excess-vacancy concentration exceeds the critical value $(C_V)_C$. Therefore, in figure 2.15, homogeneous nucleation will not happen in the vacancy-depleted region defined by AB.

Solute-depleted denuded zones

During quenching, precipitate free zones develop when solute is lost to the grain boundary due to heterogeneous nucleation of precipitates, or the preferential segregation of solute at the boundary. Both of these scenarios result in a solute-concentration profile similar to that displayed in figure 2.16. Reference to this diagram shows that at an aging temperature (T_A) with a specific excess vacancy concentration, there is a critical solute concentration (C_S) necessary for nucleation to occur. The C_S values for different aging temperatures are displayed in figure 2.16 as a series of horizontal lines. Intersections between these lines and the solute-concentration profile give the width of the solute-depleted denuded zone. Figure 2.16 illustrates that only solute-depleted precipitate free regions may form when the aging temperature is below T_C [93].

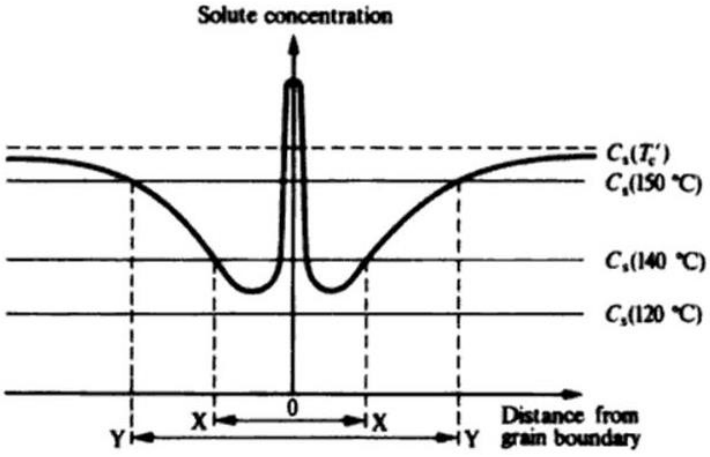

***Figure 2.16**: Schematic of the solute concentration profile following quenching [94].*

2.5 Summary

As the production of oxide during flame spray processing is integral to success of the heating elements, the chapter begins by reviewing other reported instances of metal oxidation during thermal spraying. In contrast with the current work, the majority of this research seeks to limit metal oxidation during the deposition process. However, despite this difference, the factors that affect oxidation while employing these techniques are of common interest.

During the current study, flame spray oxidation of the gas atomised Ni-Cr-Fe alloy produces a metastable Fe and Cr doped NiO. As the author is unaware of any previous examination of a similarly doped NiO, the published work concerning NiO single-doped with Fe or Cr is discussed. Of particular interest were the Cr-Ni-O and Fe-Ni-O pseudo binaries which helped predict the behaviour of the Fe and Cr doped NiO during heat treatment.

When heated at a suitable temperature, the Fe and Cr doped NiO decomposed to form more energetically favourable NiO and spinel phases. As the spinel that formed lay between the extremities of the $NiFe_2O_4$ – $NiCr_2O_4$ binary, literature examining Cr-substituted nickel ferrites was reviewed. Work concerning the mechanisms and morphologies of spinel precipitation within a NiO matrix was then discussed at the conclusion of the chapter.

Chapter 3

Materials and experimental techniques

This chapter begins by introducing the starting material (a gas atomised Ni-Cr-Fe alloy) and the flame spray processing used to convert it into thick film heating elements (3.1-3.2). The subsequent sections (3.3-3.9) then detail the experimental methods used to prepare and analyse the materials produced at the different stages of manufacture.

3.1 ECKA 500 powder

Produced by ECKA granules, ECKA 500 is a nitrogen gas atomised Ni-Cr-Fe alloy manufactured from Inconel 600 (one of a family of austenitic Ni-Cr based superalloys [95]). The specific composition of the powder along with the particle size distribution is presented in the tables below (data courtesy of ECKA granules). Chemical analysis of the material was determined using XRF while a sieve system was used to measure the particle size distribution.

***Table 3.1**: Chemical composition of ECKA 500 Powder*

Element	Ni	Cr	Fe	Si	Cu	Mn	C
wt%	Bal.	14.9	8.6	0.55	0.3	0.13	0.06

***Table 3.2**: Particle size distribution within ECKA 500 Powder*

Sieve Size (µm)	+38	+31	+26	+22	+18	+16	<16
Percent (%)	9.16	23.51	23.11	19.40	12.30	8.82	3.70

3.2 Manufacture

3.2.1 Oxidation of ECKA 500

In the first stage of manufacture ECKA 500 is oxidised by passing it through an oxyacetylene flame. During this process a powder feed rate of approximately 8g/min is maintained using a Sulzer Metco 4MP powder feeder. The N carrier gas, which

passes through the powder feed unit, is kept a pressure of 1 to 1.1bar by a WESCOL two stage regulator. Meanwhile O_2 and C_2H_2 gas flow rates are set at 30L/min and 12L/min respectively (stoichiometric ratio of 2.5:1) using two Brooks mass flow controllers (model 5851S for O_2 and model 5850S for C_2H_2). These MFCs are operated using a two channel Brooks Instrument's 0152 electronic read out and control unit.

Rather than employing a commercial gun, powder is oxidised using a custom made "spray block" connected to a modified oxyacetylene welding nozzle. This spray block is simply a machined piece of stainless steel into which four threaded holes have been bored. Powder is fed through the block's top hole, while the combustion gases enter through orifices on the side. The combined gas and powder flows exit the spray block through the nozzle attached to the bottom hole.

To cool the high temperature powder particles, the spray is directed into a 500mm (W) x 500mm (W) x 200mm (H) aluminium quenching bath, filled to 120mm with water. During the oxidation procedure, evaporated water is replaced after liquid depth drops by approximately 5mm. To change the severity of the oxidation treatment, the quenching bath supports are used to adjust spray path length. In the current study, the ECKA 500 powder was oxidised over a spray path length of 600mm.

3.2.2 Deposition of metal-metal oxide powder

The second stage of production involves the deposition of the partially oxidised ECKA 500 onto a substrate surface. During this process the spray nozzle travels at 300mm/s back and forth across the target material, advancing 5mm forward at the end of each pass. For maximum deposition efficiency, the nozzle is positioned 112mm above the surface of the substrate. As the most concentrated deposition falls within a 12mm diameter circle, plenty of overlap occurs between each successive line. The aim of this overlap is to keep the element thickness as consistent as possible so as resistance, and by extension, heat generation is as uniform as possible.

As the nozzles changes direction at the end of each pass, it must decelerate before laying down a new line of material. Since the deposition rate remains constant, this

results in a build-up of material near the edges of the element. To combat this problem, the perimeter of the substrate is masked, and the spray gun is programed to overshoot the edges of the targeted region (see figure 3.1). Any excess deposition due to variation in nozzle velocity then takes place on the surface of the mask rather than the substrate.

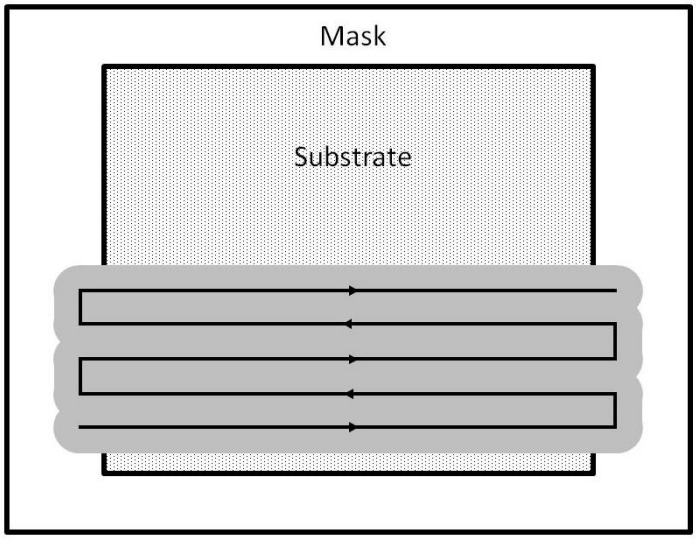

Figure 3.1*: Illustration showing the spray pattern relative to the substrate and mask. By overshooting the targeted area, material build-ups associated with the change in nozzle direction do not occur on the substrate surface.*

While spraying the heating elements a powder feed rate of approximately 2g/min is sustained using a Sulzer Metco 4MP powder feeder. The N carrier gas, passing through the powder feed unit, is kept a pressure of 1 to 1.1bar by a WESCOL two stage regulator. The C_2H_2 flowrate is set at 40L/min, and that of the O_2 at 15L/min (stoichiometric ratio of 2.5:1). The gas flow is regulated using two Brooks MFCs (model 5851S for O_2 and model 5850S for C_2H_2) which are operated using a two channel Brooks Instrument's 0152 electronic read out and control unit.

A deposition efficiency of approximately 11% has been calculated by measuring the mass gain of the substrate following the spray procedure. The main sources of powder wastage are "bounce-off" from the target surface and deposition on the masked area. To reduce powder wastage the non-deposited material is recycled during the spraying of subsequent heating elements.

3.3 Sample preparation

3.3.1 Optical microscopy and SEM

Preparation of thick film specimens

Thick film samples were mounted in phenolic thermosetting resin and then polished to a 1µm finish using standard metallographic procedure. Surface integrity was further improved by using an alumina suspension on a napped cotton cloth to achieve a 0.5µm finish.

Preparation of powder specimens

Prior to hot compression mounting, powders (~0.2g of ECKA 500 or ~0.1g of oxidised powder) were mixed with ~6g of finely ground phenolic resin. This mixture was then poured into the mounting press and topped off with an additional 12g of mounting resin. Polishing of the mounted powders then proceeded in the same manner as described previously.

3.3.2 FIB TEM sample preparation

As traditional methods of sample preparation would have proven difficult due to the brittle, porous nature of the material, TEM specimens were prepared using a focused gallium ion beam (FIB).

Focused Ion Beam (FIB)

Focused ion beam (FIB) instruments, as the name suggests, use a finely focused ion beam (typically Ga^{+}) to interact with materials. While operating at low beam currents, very little material is sputtered and the ion beam may be used to generate secondary electron images in a similar manner to the scanning electron microscope (SEM). At higher beam currents, sputtering yields are much greater allowing for site-specific micromachining.

A basic, single beam FIB system consists of an ion source, an ion beam column and a vacuum working chamber. The ion beam is produced by applying a strong

electrical field to a liquid metal ion source (LMIS). An accelerating voltage then propels the ions down the ion beam column. Here, electrostatic lenses focus the beam, apertures define beam current and diameter, stigmation poles keep the beam profile circular and separate sets of deflection plates are used to raster and blank the beam. Within the vacuum working chamber, the beam impacts the surface of the sample set upon a motorised stage. Typically, gas delivery sources are attached to the chamber enable FIB-assisted chemical vapour deposition (CVD) of a variety of metal species [96].

When an ion beam hits the surface of sample, energy is transferred to the material though both elastic and inelastic collisions. During inelastic collisions ion energy is transferred to electrons within the sample causing the ionization of atoms and the emission of electrons and electromagnetic radiation. In elastic collisions, ion energy is transferred to the impacted atom as translational energy. This may cause sample atoms to be displaced from their original lattice site or ejected from the surface of the specimen. Given sufficient energy an incident ion atom can displace many surface atoms in an event known as a collision cascade (see figure 3.2). The formation of multiple interstitial-vacancy pairs in a crystalline material, along with ion implantation can result in surface amorphisation [97].

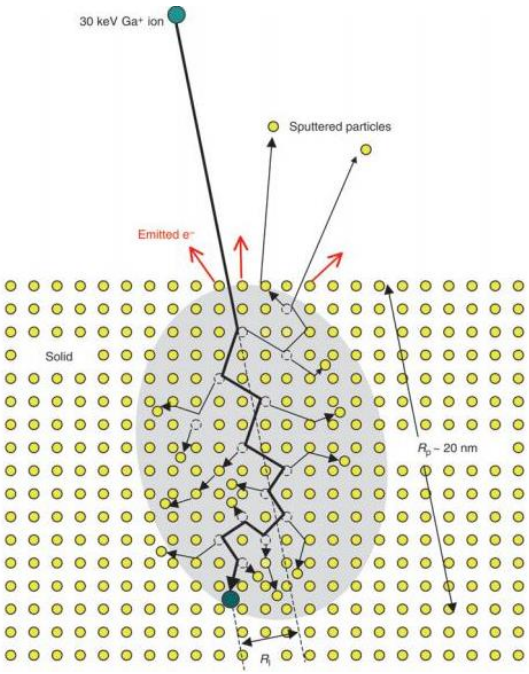

***Figure 3.2**: Diagram showing a collision cascade produced by a high energy ion upon impact with a crystalline lattice [97].*

Instrument

The instrument used for this task was an FEI Helios NanoLab 600i DualBeam FIB/SEM. This microscope employs a Ga ion gun and electron gun at a 52˚ angular separation, for combined imaging and micromachining. To manoeuvre specimens, the Omniprobe 100.7 micro-manipulator was used in combination with a gas injection system that enabled Pt deposition.

TEM foil prepared from thick film

The film's rough surface finish (a characteristic property of many thermally sprayed coatings [98]) proved inhibitive to FIB sample preparation, so before inserting into the instrument, the surface was polished to a 1μm finish. After this, TEM foils were then prepared by an in situ lift-out technique similar to that described by Gianuzzi [99] and Tomus [100]. This method started with the deposition of a protective Pt strip over the area of interest. Trenches were then milled on either side of the strip, isolating a thin lamella from the bulk material (Figure 3.3a). For these early milling stages an acceleration voltage of 30kV and high beam current (21 to 65nA) were selected to enable faster rates of material removal. After the trenches had been cut, the sample was tilted to >45˚ and incisions were made around the edges of the lamella, releasing it from the bulk material. The specimen was then transported, by means of an Omniprobe manipulator, to a Cu support grid where it was attached using ion beam deposited Pt (Figure 3.3b). Here, the sample was tilted to ± 2° and the lamella was thinned to electron transparency (~100nm) using a 30kV Ga ion beam with a reduced beam current (80pA to 2.5nA). Finally, the specimen received a low kV (2 to 8kV) polish in order to help remove material damaged during the earlier stages of thinning [101].

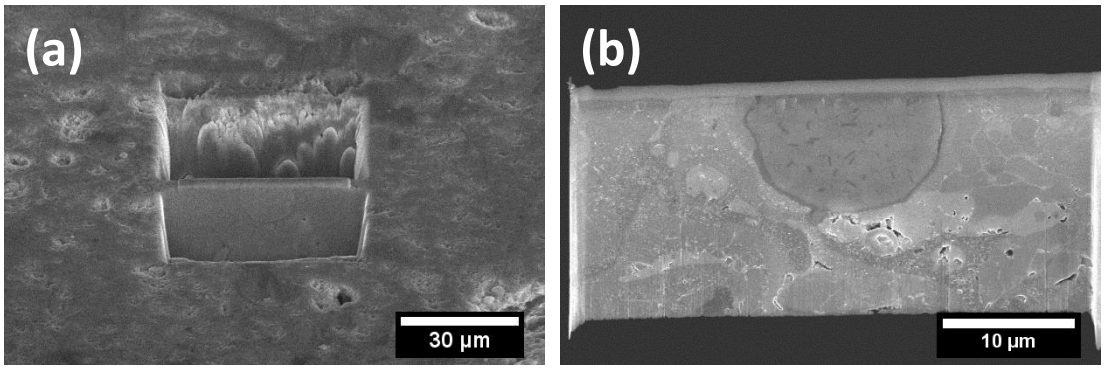

Figure 3.3*: SE images showing: (a) two trenches sputtered either side of the area of interest. (b) the TEM foil after extraction from the excavation site.*

TEM foil prepared from powder particle

Thin lamella TEM specimens were also produced from powder using the FIB instrument. At the beginning of this process, a particle of interest was picked up using the Omniprobe needle and transported to a Cu support grid where it was attached using ion beam deposited Pt. After securing the particle, initial thinning was conducted using an accelerating voltage of 30kV and a beam current of 21nA. Beam current was then dropped to between 80pA and 2.4nA as the lamella approached a target thickness of ~100nm. To clean the surface of the specimen, a final low energy polish was carried out at an accelerating voltage of 2kV.

3.3.3 Preparation of samples for XRD

Thick film specimens

Prior to testing, samples were prepared to fit within the internal dimensions of the diffractometer specimen holders (24mm diameter, 2mm depth). To achieve this, the film was first detached from the substrate (vitreous enamelled low carbon steel) by a simple flexing procedure. It was then ground to an appropriate shape using rotating, 1200 grit, SiC discs.

Finely ground thick film/oxidised powder

To ensure the random orientation of crystallites within the test specimens, samples of both the thick film and oxidised powder were finely ground using a quartz mortar

and pestle. The powder was then sprinkled on top of a petroleum jelly coated glass slide, positioned level with the top of the diffractometer specimen holder.

3.4 Heat treatments

Typically, the thick film electric heating elements operate at average surface temperatures of between 400˚C and 500˚C. However, due to the inhomogeneity of the material (and the associated variation in resistance), it is not unusual to observe millimetre scale, high temperature spots glowing red on the element's surface. To investigate the behaviour of the material at these higher temperatures, specimens were subjected to isothermal heat treatments in an open-air tube furnace. Annealing times ranged 5mins to 66h, and were conducted at temperatures of between 400˚C and 800˚C.

3.5 Optical microscopy

Optical images were collected from Bakelite mounted specimens under bright-field illumination. This was achieved using a Nikon Epiphot epi-illumination microscope in conjunction with an Infinity 2 camera system. The Infinity Analysis software enabled the camera to be operated via computer.

The epi-illumination or reflected light microscope illuminates the specimen from the same side as the objective lens making it ideal for studying opaque materials such as metals or ceramics. In this arrangement, the light source is focused upon sample by the objective lens, which acts as both an objective and condenser lens. After striking the sample, reflected light re-enters the objective lens creating an inverted, real image of the sample within the microscope. This image is then magnified by the eyepiece producing an enlarged, virtual image for observation [102].

3.5.1 Measuring the metal/porosity content of the film

The percentage of metal/porosity within the thick film was estimated by image analysis of optical micrographs. These images were obtained from two thick film cross-sections, oriented such that the layered deposits sat at right angles to the

viewing direction. From each cross-section, a set of ten low magnification images (x600) were analysed; the aim being to account for the inhomogeneity of the metal/porosity distribution.

The percentage of metal/porosity within each micrograph was calculated using the Java image processing program ImageJ [103]. To enable use of the program's threshold function, each image was initially converted into greyscale. The bright or dark pixels, which correspond to the metallic and porous areas respectively, were then highlighted by adjusting the threshold limits on pixel intensity. Once the metallic or porous content had been highlighted, (see figure 3.4) ImageJ's "measure" function was used to calculate the percentage of the micrograph occupied.

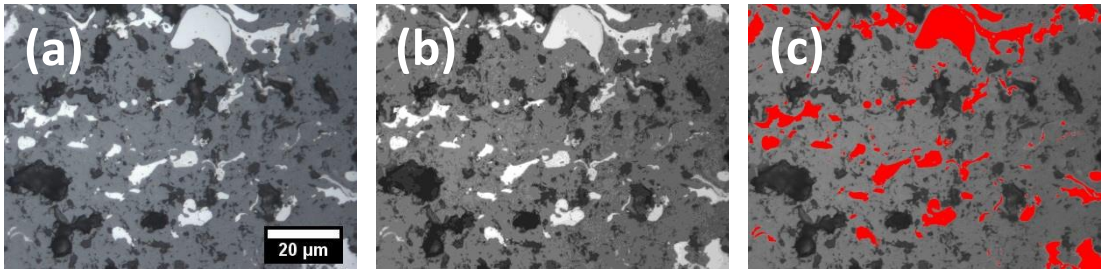

***Figure 3.4**: Optical micrograph (a) is converted into a greyscale image (b) which is then used to measure (c) the percentage of metal.*

3.6 Scanning electron microscopy (SEM)

The scanning electron microscope uses a focused, high energy beam of electrons to examine the surface of a specimen. When the electrons interact with the sample they generate secondary and backscattered electrons which can be used to reveal information about a material's topography, chemical composition, crystal structure and orientation. By using radiation with a much smaller wavelength than visible light, a SEM can resolve much finer details than a traditional light microscope. Additionally, the smaller convergence angle of the beam gives images a much greater depth of field.

A typical SEM is composed of an electron gun, an electron column and working chamber, all held under vacuum. Depending upon the microscope, electrons may be extracted from the source either by heating or through the application of a large

electrical potential. Once emission is achieved, electrons are accelerated down the electron column by an applied potential difference. In the column, electromagnetic lenses focus the beam, apertures establish beam current and diameter, stigmators keep the beam profile circular and deflector plates are used to raster the beam. Upon exiting the column, the electron beam enters the working chamber where it impacts the sample. Detectors inside the chamber then measure the intensity of secondary and backscattered electrons [104].

3.6.1 Secondary electrons (SEs)

SEs are generated during the interaction between the electron beam and the sample material. Upon impact, the incident beam causes electron ejection from the conduction or valence band of the specimen's atoms by means of inelastic scattering events. As little energy is required to free electrons from their parent atoms, the SEs emitted are of low energies (typically <50eV) [105]. For this reason, SEs may only escape from the specimen if they are located near the surface. The sensitivity of SEs to specimen topography makes them the main means of image formation in an SEM.

3.6.2 Backscattered electrons (BSEs)

BSEs are another type of signal produced as the electron beam impacts the surface of a specimen. In contrast to SEs, these electrons are the product of elastic interactions with the nuclei of a sample's atoms and therefore retain much of the incident beam energy. Due to their higher energies, BSE can escape from deeper within the sample than the SEs. Consequently, the information collected isn't quite as surface specific and BSE images suffer from a lower spatial resolution. However, despite the lower resolution, BSE images are a useful way of displaying atomic number contrast. As higher average Z materials reflect a greater percentage of incident electrons, materials with the highest average Z will appear brightest in BSE images.

Another cause of contrast in BSE images is difference in grain orientation. The angle at which a crystal lattice sits relative to the incident beam will affect the depth to which an electron can penetrate the sample before being scattered (see figure 3.5). Crystal orientations which allow deeper penetration of electron will appear darker in

an electron channelling contrast image (ECCI) because less BSEs successfully reach the detector [106].

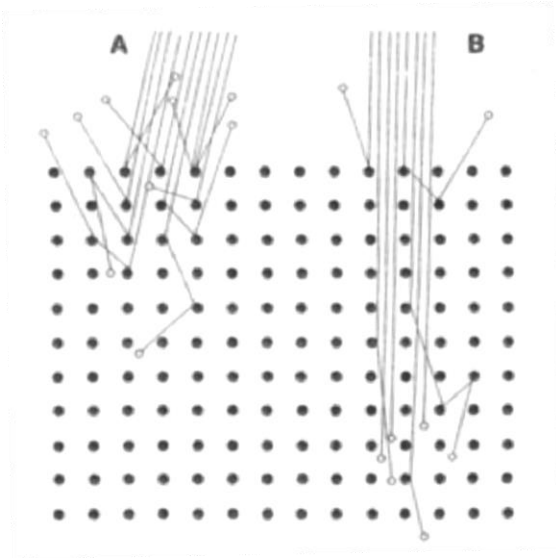

***Figure 3.5**: Illustration showing relative orientation of a crystal lattice to incident electrons, where (a) produces more surface interactions and (b) enables the channelling of electrons between atomic columns [107].*

3.6.3 Instruments

The majority of SEM was performed using a JEOL JSM-7001F field emission scanning electron microscope. Typically the instrument was operated at a 20kV acceleration voltage, using spot size 12 while maintaining the analytical working distance (10mm). To better resolve nanoscale surface features, the accelerating voltage was reduced to 15kV, while spot size and working distance remained the same.

Some low magnification work was also conducted using a JEOL JSM-6610 SEM. This microscope was operated at a 20kV acceleration voltage, using spot size 30 (arbitrary units) while keeping the working distance at 10mm.

3.6.4 Energy dispersive X-ray spectroscopy (EDS)

During the interaction between high energy electrons and specimen, X-rays are produced alongside secondary and backscattered electrons. The wavelengths of some

of these X-rays are indicative of the atoms from which they were emitted. By measuring the energy of each characteristic X-ray it is possible to determine and quantify the elements present in a material. This technique is known as energy dispersive X-ray spectroscopy (EDS).

The generation of characteristic X-rays is associated with the emission of secondary electrons. When an electron is ejected from the inner shell of a specimen atom by an incident electron the resulting hole leaves the atom in an instable state. To rectify this, an electron from the atom's outer shell moves into the inner shell vacancy. In order to balance the difference between the two energy states an X-ray is emitted that is characteristic of the atomic species. The wavelength of this X-ray will vary depending upon the orbital of electron which fills the vacancy.

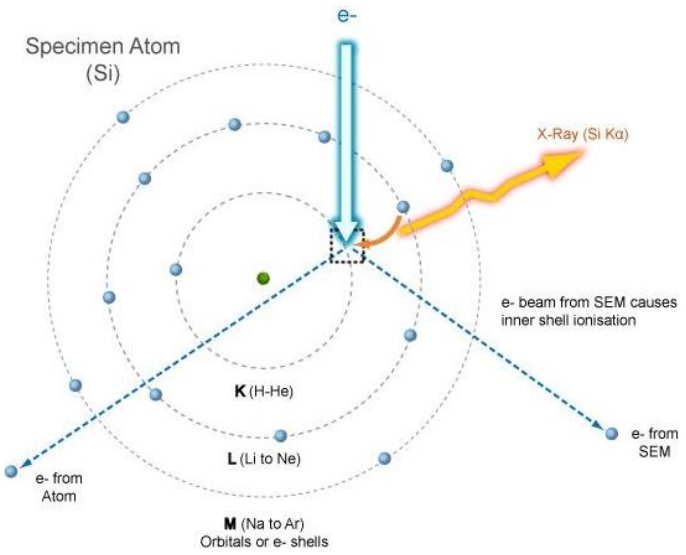

***Figure 3.6**: Illustration showing the generation of characteristic X-ray emission [108].*

To measure X-ray emissions, detectors are placed as close as practically possible to the sample. When an incident X-rays impacts the semiconducting material (typically Si or Ge based) within a detector, electron-hole pairs are created. Subsequent application of a voltage across the semiconductor produces a current proportional to the energy of the X-ray. By measuring the size of the current, the source of the X-ray may be identified.

Although the majority of elements may be successfully detected, those with especially low atomic numbers can pose problems. Windows used to shield detectors from contamination, absorb a significant amount of low energy X-rays making lighter elements more difficult to detect. In the past, Be windows which absorb X-rays with energy <~1eV, made EDS analysis of elements lighter than Na impractical. These days, detectors are fitted with ultrathin windows that extend the analytical range down to B [109].

Instruments

The chemical analysis of powders and thick film specimens was mainly conducted using a JEOL JSM-7001F SEM equipped with an Oxford Instruments X-act detector (model: 51-ADD0001). An acceleration voltage of 20kV was used to ensure the incident beam energy exceeded the critical ionization energy of Ni by a comfortable margin. For good quality spectra, longer processing times were combined with dead times of 30-40% and live times of 60s or greater. During chemical mapping, data was normally collected over several hours. In order to minimise specimen drifting, the site lock function was enabled using the Oxford Instruments INCA microanalysis software.

More minor EDS studies were carried out using the JEOL JSM-6610 SEM. This instrument was equipped with an INCA X-act detector (model: 51-ADD0013) and utilized the same operating software as the 7001F. Acceleration voltages of 20-25kV were employed, while dead times, live times and processing times remained consist with the parameters previously outlined.

The atomic/weight percentage of the specimens' constituent elements was determined semi-quantitatively using the Oxford Instruments microanalysis software. This program converts k-ratios (ratio of element peak intensity in the sample to element peak intensity for the standard) to element concentrations by applying the XPP matrix correction algorithm (a variant of the ZAF procedure [110]). These matrix corrections are based on differences in mean atomic number, absorption of X-rays and X-ray fluorescence.

3.7 Transmission electron microscopy (TEM)

The TEM shares structural similarities with a transmitted light microscope (see figure 3.7) but uses an electron beam to interact with the sample instead of light. As with transmitted light microscopy, information is obtained by the partial transmission of radiation through the material of interest. However, due to smaller wavelength of the high energy electrons, the TEM is capable of imaging at considerably greater resolutions.

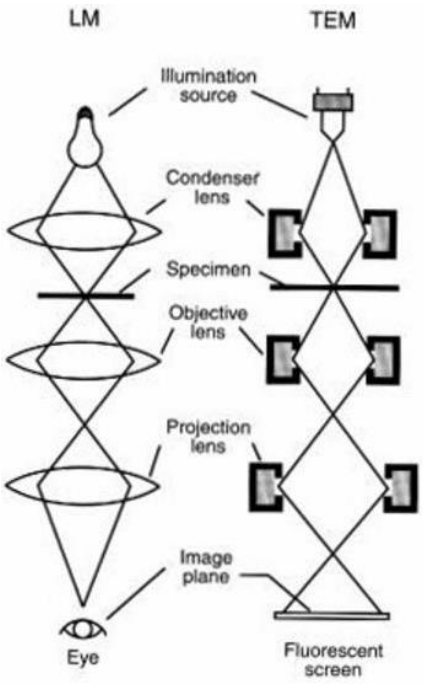

Figure 3.7*: Illustration showing the similarity of optic arrangement in the light microscope and TEM [111].*

Aside from atomic resolution imaging, the TEM's ability to perform electron diffraction enables the analysis of a specimen's atomic structure. When operating in conjunction with EDS and EELs systems, the TEM may also be used to investigate a material's chemical composition and electronic properties respectively.

A typical TEM may be divided into three main systems: the illumination system, the objective lens/sample stage and the projection system. The illumination system is composed of an electron gun, which generates the electrons and the condenser lenses, which transfers them towards the specimen. The sample stage/objective lens system is where the electron beam interacts with the specimen and the image is

created. The projection system consists of several more electromagnetic lenses that magnify the image and focus it upon the viewing screen or detector.

3.7.1 Instruments

Transmission electron microscopy was carried out using JEOL 2000FX and 3010 microscopes operating at 200kV and 300kV acceleration voltages respectively. Both microscopes used thermionic electron guns, with the 2000FX's employing a tungsten filament and 3010's a LaB_6 filament.

In both microscopes, specimens were examined in a double tilt sample holder. To calculate the angle θ between two crystal poles, the following equation [112] was applied:

$$cos\,\theta = cos(Tx_2 - Tx_1) + cos(Ty_2 - Ty_1) - 1 \qquad \textit{Equation 3.1}$$

where, the X-tilt and Y-tilt angles at pole 1 are represented by Tx_1 and Ty_1, and at pole 2 by Tx_2 and Ty_2.

For compositional analysis, the 2000FX employed an EDAX X-ray detection system running in conjunction with EDAX Genesis software. In the 3010, the same analysis was carried out using a Link ISIS Pentafet detector accompanied by Link ISIS software.

3.7.2 Imaging

Specimen imaging was conducted using bright field (BF) and centred dark field (CDF) techniques. In the 2000FX images were recorded on photographic plates while in the 3010 they were recorded digitally by a Gatan model 694 retractable slow-scan CCD camera.

Bright field

During this study the microscopes were most frequently operated using BF imaging conditions. In this mode, the direct beam (which is selected by inserting an aperture into the back focal plane of the objective lens) is used to form the image. Within BF

images, the darkest regions correspond to the areas of the specimen which scatter the electrons most strongly.

Centred dark field

Under DF conditions, an image is formed from one or more diffracted beams selected using the objective aperture. The further the beam's displacement from the optical axis, the greater the effects of aberrations and astigmatism. Therefore, when using microscopes without aberration correction (such as the 2000FX and 3010) it is necessary to tilt the diffracted beam onto optical axis. This technique is known as centred dark field (CDF) imaging [113].

In this work, the CDF technique was employed to image spinel crystal arrays embedded within NiO grains. The diffraction pattern illustrated below demonstrates how this method was employed to form images using the spinel reflections.

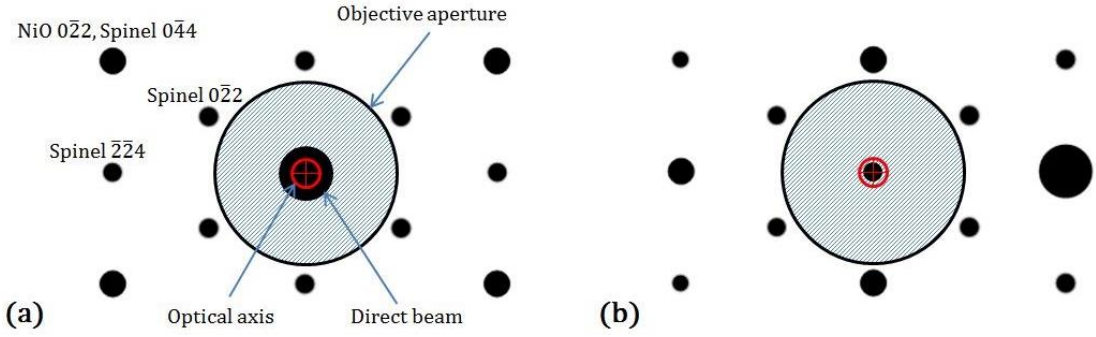

***Figure 3.8**: A schematic showing the diffraction pattern from spinel particles in a NiO matrix on the [111] zone axis. (a) The direct beam is positioned on the optical axis with the objective aperture positioned for BF imaging. (b) For CDF imaging, the objective aperture selects a diffracted beam which is positioned on the zone axis by tilting the incident beam.*

3.7.3 Electron diffraction

When a high energy electron beam encounters a thin film specimen Coulomb interactions cause electron scattering. Depending upon the angle of deflection, waves

of electrons travelling from the sample may combine constructively or destructively. When the Bragg conditions are fulfilled and the constructive interference occurs, diffraction maxima become observable on the viewing screen. Measuring the angles and distances between these high intensity spots can reveal useful information about a material's crystal structure [114].

Selected area diffraction

Selected area diffraction (SAD) is one method by which a diffraction pattern may be obtained from a specific area of a sample. To form a selected area diffraction pattern (SADP), the electron beam is spread (by underfocusing a condenser lens) and an aperture is positioned in the image plane of the objective lens. SAD aperture focus may then be adjusted to until diffraction spots appear sharp.

Prior to the acquisition of a SADP, grains of interest were rotated onto an appropriate zone axis using the double tilt sample holder. Due to the limitations imposed by aperture size (D = 0.5μm), these patterns were typical obtained from microscale metal/oxide grains.

Convergent beam electron diffraction

Another method that may be used to obtain area specific diffraction data is convergent beam diffraction (CBED). As the name suggests, this technique uses a convergent beam of electrons to restrict the volume of material contributing to the diffraction pattern (electron beam may be focused to a diameter of approximately 2nm [115]). While the parallel illumination in SAD produces diffraction spots, CBED results in the formation of diffraction disks.

Convergent beam diffraction was employed to investigate nanoscale crystals that couldn't be isolated using selected area diffraction. Such features included grain boundary precipitates and fine oxide grains.

To increase the accuracy of inter-planar spacing and angle measurements, efforts were made to avoid disc overlap in the CBED patterns. As the angle of convergence is proportional to the diameter of the diffraction disc, non-overlapping discs could be produced by restricting the convergence angle using smaller condenser apertures.

3.7.4 Indexing diffraction patterns

When prior knowledge of the possible phases present limited the number of solutions to a diffraction pattern, the following approach was taken:

1. The 000 spot was identified, then the reciprocal lattice vectors (r_1 and r_2) and the inter-planar angle (ϕ) were measured (see below).

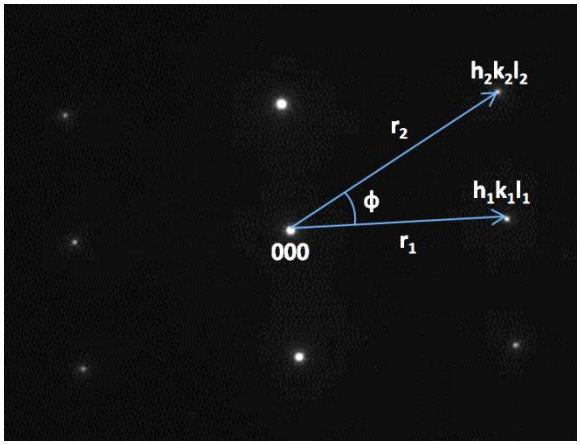

***Figure 3.9**: Selected area diffraction pattern*

2. A table listing the d-spacing ratios of permitted diffraction planes in the most likely crystal structure was prepared.

3. The nearest value to the ratio r_1/r_2 was then located within this table.

4. Once a matching d-spacing ratio was found, the more widely spaced plane was assigned to the shortest r value.

5. The possible angles between the two sets of Miller indices were then calculated using inter-planar angle equations. For cubic structures, which were the work's main focus, equation 3.2 was employed.

$$cos\phi = \frac{h_1h_2+k_1k_2+l_1l_2}{\sqrt{h_1^2+k_1^2+l_1^2}\sqrt{h_2^2+k_2^2+l_2^2}} \qquad \textit{Equation 3.2}$$

6. If the measured angle agreed with one of the calculated angles then the indexing was accepted. If not, then a new pair of possible planes was selected.

7. After a successful match, the rest of the pattern was indexed by means of vector addition.

8. Finally, plane spacings (*d*) corresponding to r_1 and r_2 were calculated using equation 3.3, and compared with values in the FIZ Karlsruhe inorganic crystal structure database (ICSD).

$$d = L\lambda/r \qquad \textit{Equation 3.3}$$

In this equation λ is the wavelength of the electron beam and L is the camera length.

The zone axis, which is approximately parallel to beam direction, is calculated by finding the vector product of the assigned pair of Miller indices.

$$[UVW] = (h_1k_1l_1)(h_2k_2l_2) \qquad \textit{Equation 3.4}$$

To check the consistency of the indexing a final calculation was carried out using the Weiss zone law (see equation 3.5). This confirms that the zone axis is perpendicular to the Miller indices designated to the diffracting planes.

$$[UVW].(hkl) = 0 \qquad \textit{Equation 3.5}$$

3.7.5 TEM-EDS

The TEM's combination of thin film specimens and high acceleration voltages limits the spread of the electron beam within the sample. Consequently, the volume from which characteristic X-rays are emitted is much smaller than that within SEM specimens (see figure 3.10). By equipping a TEM with an EDS detector, chemical analysis may be conducted at higher spatial resolution, enabling the study of nanoscale microstructural features.

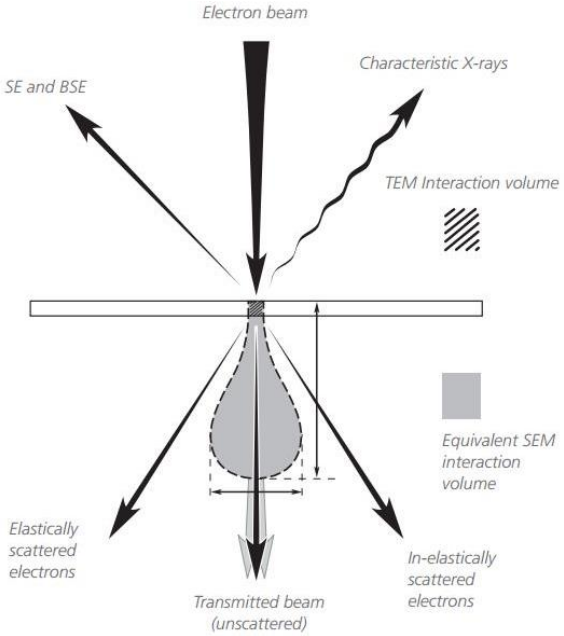

***Figure 3.10**: Comparison between TEM and SEM interaction volumes [116].*

Elemental analysis of TEM cross sections was performed within the JEOL 3010 and 2000FX microscopes. The former was equipped with an Oxford instruments detector (model:6636) and ran Link ISIS software, while the latter used an EDAX detecting system running alongside EDAX genesis software. To improve the quality of the spectra, longer processing times were combined with dead times of 30-40% and live times of 300s.

3.8 Scanning transmission electron microscopy (STEM)

The scanning transmission electron microscope (STEM) operates in a similar fashion to an SEM; raster scanning a focused beam of electrons across a sample's surface while simultaneously collecting a signal for image formation. However, while the SEM is typically used for bulk analysis, the STEM utilizes electron transparent cross-sections for transmission modes of imaging.

Due to similarities between the SEM and STEM, several detectors like the EDS and SE detectors are common to both instruments. It is however, the transmitted electrons which offer the highest spatial resolution. These electrons are collected using the BF, annular dark field (ADF) and high angle annular dark field (HAADF) detectors. Arranged concentrically around the microscope's optical axis, these

detectors collect electrons scattered by angles of up to several hundred milliradians (see figure 3.11). Simultaneously electron collection by the different detectors provides contrasting and complimentary specimen images.

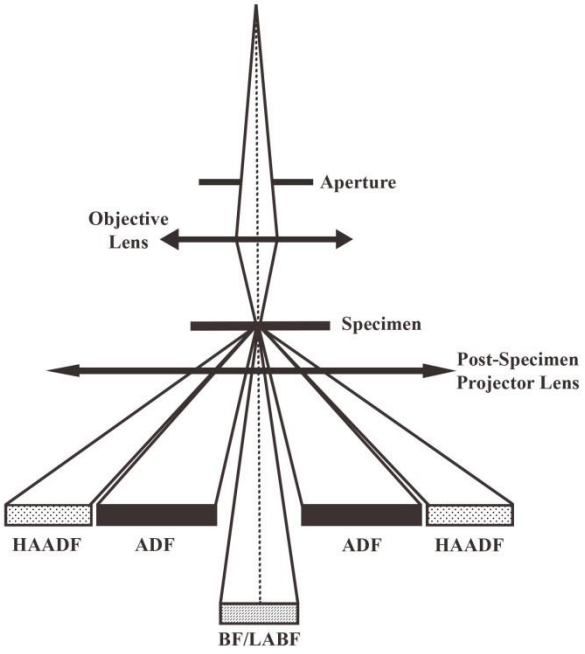

Figure 3.11*: Schematic of STEM showing the positions of the BF, ADF and HAADF detectors.*

3.8.1 Imaging

Bright field

The STEM uses a coherent, converging beam of electrons to illuminate samples, causing diffracted beams to appear as discs on the microscope's detector plane. Near the optical axis, the diffracted beams overlap with the transmitted beam and interference occurs (see figure 3.12). This interaction is equivalent to the interference phenomenon which takes place during lattice imaging in the TEM. To generate the bright field images, a detector is positioned on the microscope's optical axis, where it intercepts the overlapping beams. This detector is of finite size, to increase sensitivity to the fine interference pattern details responsible for phase contrast [117].

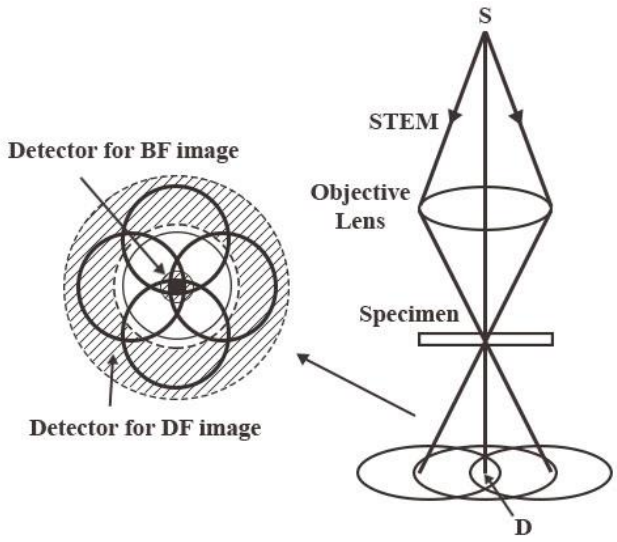

***Figure 3.12**: Overlap of diffraction disks in the detector plane of the STEM.*

Annular dark field (ADF)

The ADF detector surrounds the BF detector, collecting electrons scattered through greater angles. Being much larger than the BF detector, the ADF detector averages over many fringes, and therefore isn't sensitive to the features of the inference pattern. As a result, contrast in the ADF images is based on intensities rather than the phase of the waves (i.e. incoherent imaging). Unlike bright field images, these incoherent ADF images give a true representation of a material's structure enabling easier interpretation of atomic positions.

In addition to detector geometry, ADF image coherency is also influenced by the thermal vibrations of lattice. As electrons propagate through a crystal, phonon interaction causes changes in momentum and energy, preventing interference with other scattered electrons. This process is known as thermal diffuse scattering (TDS).

At high angles, beyond those typical of Bragg scattering, the majority of electrons will have experienced phonon scattering. The intensity of these incoherently scattered electrons is roughly proportional to the square of the atomic number [118]. Therefore, in a HAADF micrograph, heavier atoms will appear brighter than lighter ones. For this reason, images taken using a HAADF detector are often referred to as Z-contrast images.

3.8.2 Electron energy loss spectroscopy (EELS)

As an electron passes through a thin film sample, it may experience inelastic scattering, causing a loss of energy. Using an electron spectrometer, the energy loss may be measured, and the possible source of the energy loss discerned. Potential inelastic interactions include phonon scattering, plasmon scattering, single valence electron excitation and inner shell excitation. The energy losses associated with the latter form of inelastic scattering are characteristic of the atom involved and so provide valuable chemical information.

The spectrum

An electron energy loss spectrum is typically separated into three regions: the zero loss peak, the low loss distribution and the ionization edges. The zero loss peak is formed by electrons that have experienced negligible inelastic scattering during transmission through the sample. The low loss distribution contains electrons that have lost up to 50eV, mainly due to plasmon scattering. Electrons that have interacted with the core-shell electrons produce ionization edges, which are usually found between 100eV and 2000eV. Qualitative analysis may be conducted by identifying edge energies and comparing them with known values for different elements [119].

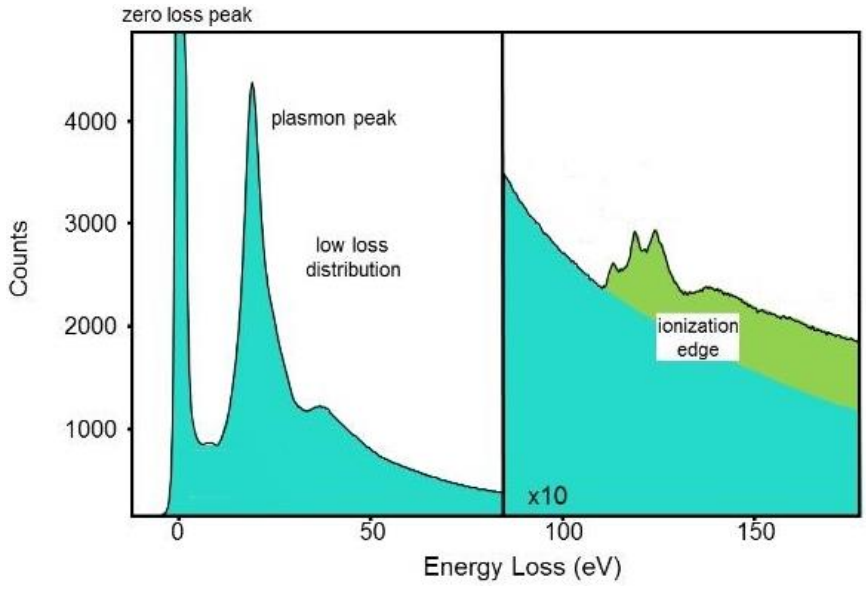

***Figure 3.13**: A diagram displaying the features of a typical electron energy loss spectrum [120].*

Principal component analysis (PCA)

As the ionisation edges are situated on a relatively large background, and a strong decay in intensity occurs with increasing energy loss, good background substitution is important in obtaining accurate results. Because of this, methods such as blind extrapolation, guided extrapolation, multiple least-squares fitting and multivariate statistical analysis (MSA) have been developed in order to isolate the ionisation-loss intensity from the background. The method implemented during the current study was principal component analysis (PCA), which is one of the more common MSA approaches. The general concept of PCA is to reduce the dimensionality of an original large dataset by finding a minimum number of variables that describe the original dataset without losing any significant information [121]. An in-depth discussion of the PCA technique is available in the following sources [121, 122].

3.8.3 Layout of a STEM

The basic arrangement of a STEM is displayed in figure 3.14. Electrons are generated by a FEG, accelerated by an applied potential difference and focused using the condenser and objective lens. The objective aperture defines the beam diameter, while the scanning coils traverse the electron probe across the specimen surface. Detectors positioned above and below the sample, monitor the signals produced during beam-specimen interaction.

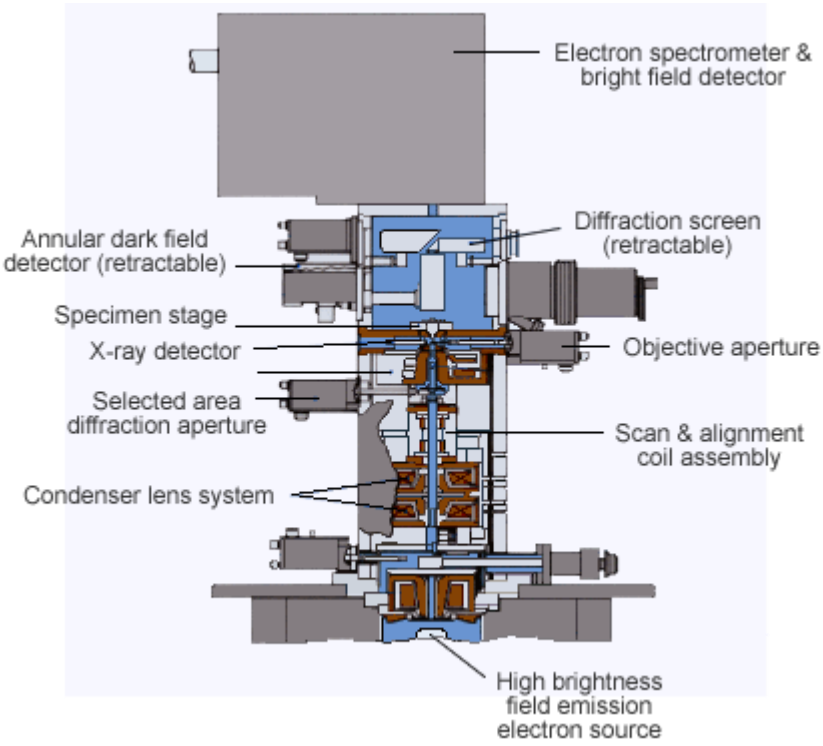

***Figure 3.14**: Illustration showing the basic layout of a STEM [123]*

3.8.4 Instruments

Scanning transmission electron microscopy was mainly conducted using a FEG equipped JEOL 2100FCs operating at an accelerating voltage of 200kV. During the project, images were recorded in both BF and DF illumination conditions. To produce Z-contrast dark field images, a high angle annular dark field (HAADF) detector was used to detect electrons scattered over a semi-angle ranging from 70-90 mrad.

STEM-EELS was carried out using an aberration corrected Nion UltrastemTM 100, operating at an accelerating voltage of 100kV. The convergence semi-angle for the incident probe and the EELS collection semi-angle were 32 mrad and 37 mrad respectively.

3.8.5 STEM-EDS

The chemical analysis of thin foil specimens was performed while running the JEOL 2100FCs in conjunction with an EDAX optima 60 windowless SDD detector. Data was collected and later analysed using the EDAX TEAM software.

During EDS analysis, a larger probe forming aperture and spot size were selected in order to increase characteristic X-ray yield. Elemental maps were typically collected over 2-3h. To minimise specimen drifting, the TEAM software's site lock function was enabled.

3.9 X-ray diffraction (XRD)

The similarity between X-ray wavelength and a solid's atomic spacing enables crystalline materials to diffract X-rays. XRD is an analytical technique that uses this relationship to investigate the arrangement of atoms within solid state matter.

During X-ray diffraction, a monochromatic beam of X-rays interacts with the electrons of the lattice atoms and general scattering occurs. Although most of the scattered radiation is eliminated by destructive interference, in specific directions the X-rays interfere constructively (see figure 3.15). This phenomenon is known as Bragg scattering and can be described by the equation

$$n\lambda = 2d\sin\theta \qquad \textit{Equation 3.6}$$

where, n is an integer, λ is the X-ray wavelength, d is the distance between the atom layers and θ is the angle between the incident X-rays and the crystal surface.

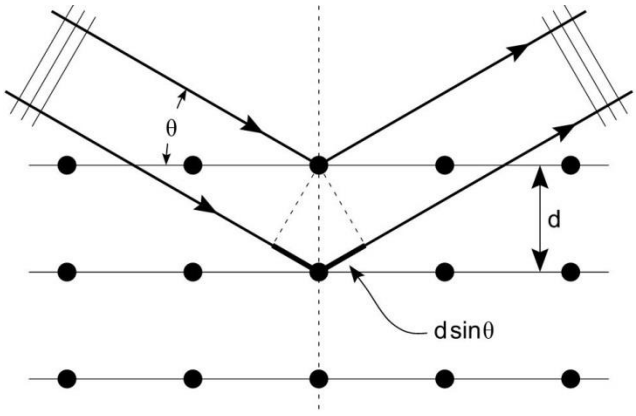

***Figure 3.15**: After reflection the emerging X-rays are in phase and Bragg's Law is fulfilled [124].*

The main components of a typical X-ray diffractometer are an X-ray source, a monochromator, a set of slits, a goniometer and an X-ray detector. Generation of the X-rays takes place within an X-ray tube, where a finely focused beam of electrons induce X-ray emission from a metal target (normally Cu or Mo). A monochromator filters this emission, reducing the amount of white and Kβ radiation. To enhance focusing, a slit collimates the beam before it encounters the sample surface. Following this interaction, the diffracted beam passes through another slit before being collected by a scintillation counter. During experimentation the goniometer rotates, varying the interaction angle between specimen and X-ray beam [125].

3.9.1 Instrument

Both thick film and powder samples were examined using a Riguku Miniflex II desktop diffractometer, in the θ-2θ Bragg-Brentano configuration. This instrument uses an X-ray tube equipped with a Cu target to generate characteristic Kα X-rays of wavelength 1.5406Å.

3.9.2 Diffractometer settings

Typically, survey scans were conducted over a 2θ range of 20-90˚ using a 0.01˚ step size and a dwell time of 1s. Then after the peaks of interest had been identified, data was collected over a 2θ range of 30-50˚, with a step size of 0.01˚ and dwell time of

5s. This slower scan speed was selected in order to obtain a reasonable signal to noise ratio.

Upon completion of the scans, peak search software was used to remove background noise and the Cu Kα2 peak. Phase identification was then conducted by comparing results with standard XRD data obtained from the inorganic crystal structure database (ICSD). Finally, the CMPR software was used to present the diffraction data.

Chapter 4

Characterisation of an oxidised Ni-Cr-Fe alloy powder

During the first stage of thick film manufacture, a powdered Ni-Cr-Fe alloy was oxidised by passing it through an oxyacetylene flame, resulting in the production of a metal-metal oxide powder mixture. As the properties of this powder dictate the behaviour of the thick film heating element, initial work aimed to develop an understanding of the new materials formed. To this end, the changes occurring during heat treatment were investigated using a range of physical and chemical characterization techniques.

In this chapter, section 4.1 investigates the properties of the initial gas atomised alloy, while section 4.2 examines the materials which developed during flame spray oxidation. In both 4.1 and 4.2, results are divided into subsections based upon the three main methods of characterization: SEM, XRD and TEM.

4.1 ECKA 500 powder characterization

The starting material in the manufacturing process is a powdered alloy fabricated using the gas atomization technique. Produced from the ingots of alloy 600, the powder consists of Ni balanced with approximately 15wt% Cr, 10wt% Fe and other minor alloying elements. XRF analysis performed by manufacturer ECKA granules gave the following compositional breakdown.

***Table 4.1**: Chemical composition of ECKA 500 Powder*

Element	Ni	Cr	Fe	Si	Cu	Mn	C
wt%	Bal.	14.9	8.6	0.55	0.3	0.13	0.06

4.1.1 SEM/EDS analysis

Solidification microstructure

Initially the gas atomised powder was examined in the SEM, revealing that the majority of particles had a near-spherical shape. However, as figure 4.1 shows, some of the powder differed from the typical morphology forming either clusters of fused particles or thin flakes.

The conjoined particle clusters typically consisted of a large particle capped by one or more smaller ones. Their formation may be related to differences between the solidification rates of the small and large metallic droplets. Small particles, having solidified first, cross the flight path of larger, slower cooling, molten droplets. Due to the differences in their states, the smaller particle is able to fuse to the surface of the larger one [126].

Conversely, the morphology of the flake-like particles suggests a very different formation history. One possibility is that the liquid particles were quenched against the walls of the gas atomiser. Alternatively, oxide formation on the surface of the scattered liquid metal could also have impeded spheroidisation.

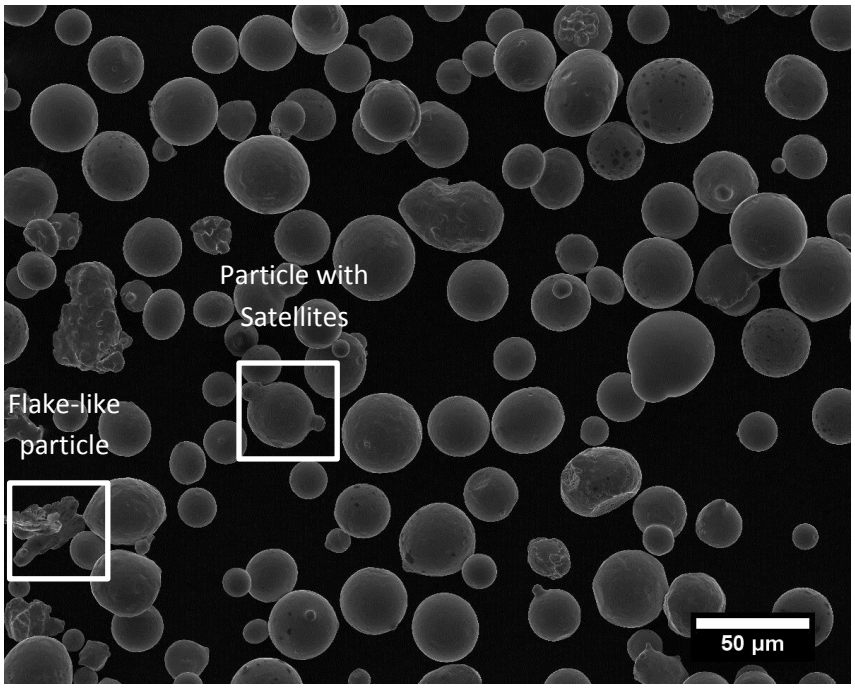

***Figure 4.1**: Morphology of nitrogen gas atomised Inconel 600.*

Particle size distribution

The powder particle size distribution, calculated by image analysis of low magnification SE images, is displayed in the histogram below. Particle diameter was found to range from 4μm to 51μm, with a mean diameter of 25μm.

A comparison with the manufacturer's sieve gradation test showed fair agreement despite the sample size limitations of the image analysis method. The data sheet provided by ECKA granules showed that 78% of the powder particles were between 18μm and 38μm in diameter. Of those powder particles measured by image analysis, 71% were found to fall within the same range.

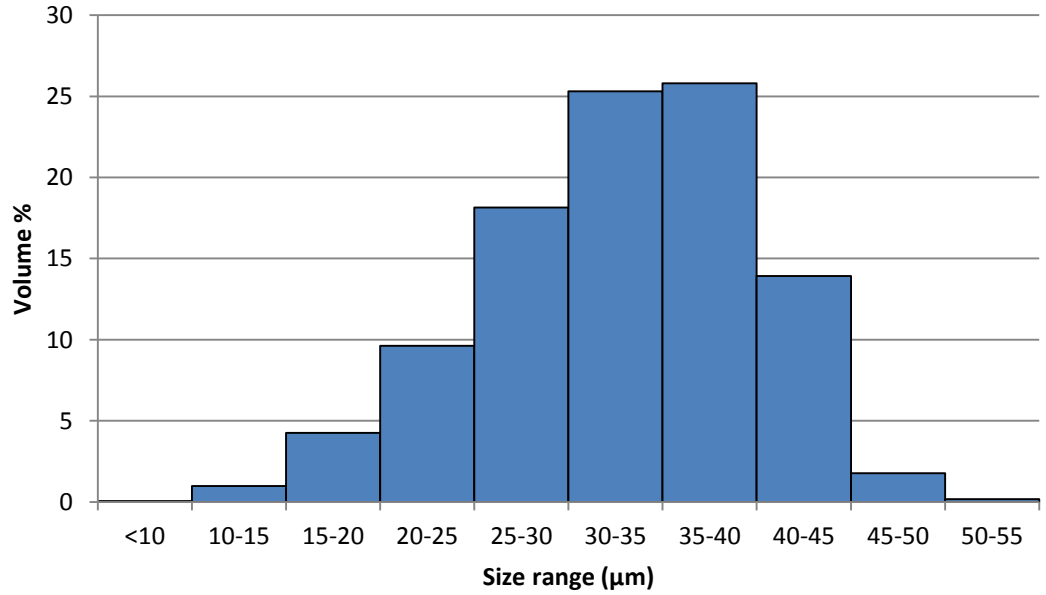

***Figure 4.2**: ECKA 500 particle size distribution histogram produced by means of image analysis.*

Cellular and dendritic particles

Upon inspection at higher magnification, the bulk of spherical particles were found to display surface structures that were either dendritic, cellular (see figure 4.3) or a mixture of the two. These contrasting structures were observable across the 4-51 micron particle size range. Although Inconel 600 powders have received little attention within the literature, similar morphologies have been noted in other gas atomised Ni-based superalloy powders of comparable size distribution. [127].

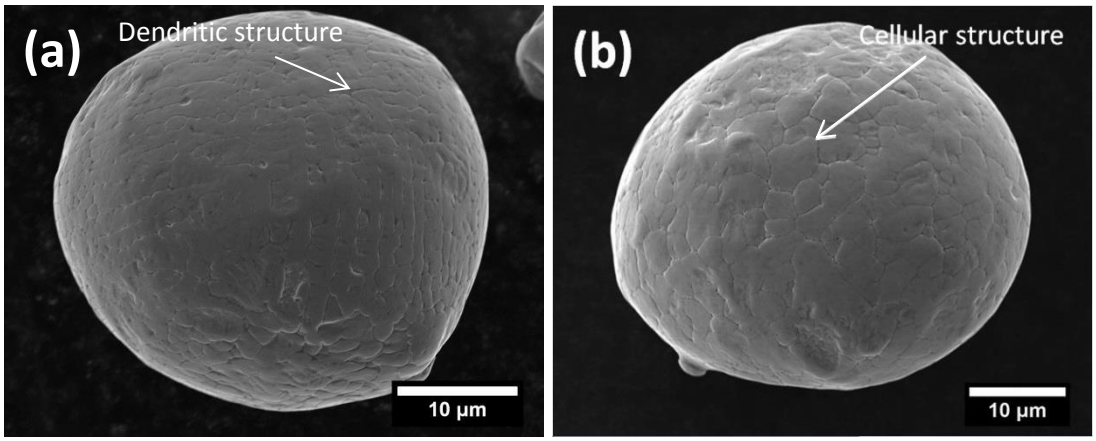

Figure 4.3*: SE images showing evidence of (a) dendritic and (b) cellular crystal growth.*

Following the examination of their external surface, cellular and dendritic particles were examined in cross-section. Despite the variation in microstructure, EDS readings obtained from the two particle types revealed no significant difference in composition (see figure 4.4); though minor alloying elements were undetectable, the ratio of the major constituents was in agreement with the manufacturer's chemical analysis.

The cellular particle, imaged using backscattered electrons, displays a collection of equiaxed grains, developed after multiple nucleation events in the centre of the cooling droplet. Brightness contrast between neighbouring grains highlights their random orientation. In contrast, the dendritic particle solidifies as crystals nucleate and then grow directionally along energetically favourable crystallographic directions. Competing dendrites meet in the centre of the particle, applying stresses which alter crystal orientation, causing brightness differences in the BSE image.

Primarily, the cellular and dendritic particles appeared to be of a single phase; however, BSE imaging did reveal the presence lower z nanoparticles, located on the grain boundaries. The considerable brightness difference between the boundary particles and the surrounding alloy suggests a significant difference in atomic number, making carbide, nitride or oxide precipitates possibilities. Conformation of the nanoscale particles chemical composition was unattainable by EDS analysis due to electron beam spreading within the surrounding alloy.

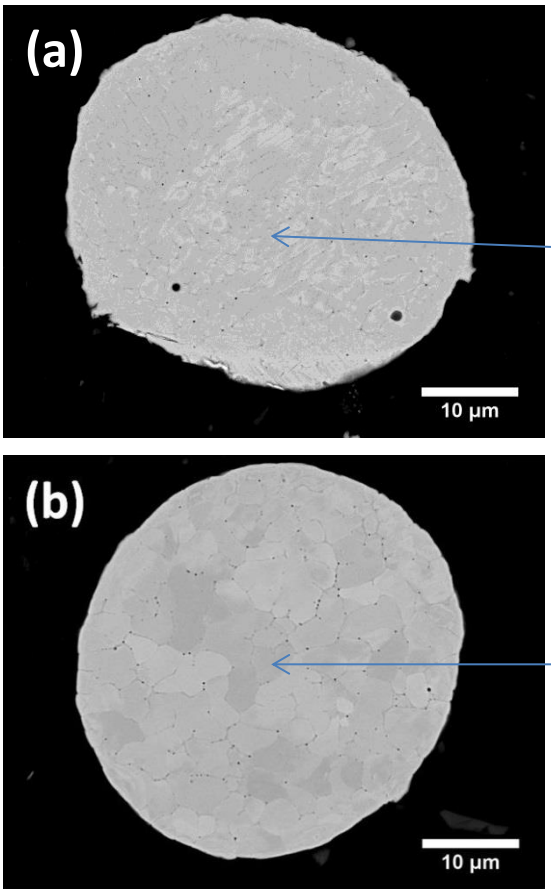

Element	Wt%	At%
Cr K	16	18
Fe K	9	9
Ni K	75	73
Total	100	100

Element	Wt%	At%
Cr K	15	17
Fe K	10	10
Ni K	75	73
Total	100	100

***Figure 4.4**: BSE images of cross-sectioned powder particles displaying (a) dendritic and (b) cellular microstructures.*

Anomalous powder particles

Though the majority of examined particles (approximately 500) appeared to conform to the manufacturer's chemical analysis, SEM-EDS identified a small percentage of particles with a different composition. These particular particles contained elevated levels of Si and Ni, in addition to a reduced amount Fe and Cr (see EDS readings in figure 4.5).

In contrast to the particles of typical composition, those with higher Si contents appeared to have much smoother, more spherical exteriors, displaying no sign of cellular or dendritic formations. Similarly, when the particles were examined in cross-section, the interior displayed no obvious evidence of grain structure, suggesting the material was amorphous. These particles, cooled rapidly during gas atomisation, appear to have frozen in a disordered state before crystals had a chance to form.

Using EDS in combination with SEM image analysis, Si rich particles were identified, and their diameters assessed. Measurements indicated that the average diameter of these Si rich particles was equal to the overall powder average of 25µm. In total, the Si rich material accounted for 4.5% of the total volume of the powder particles tested.

A number of potential explanations exist for this difference in powder composition. One possibility is that Si, added as a fluxing agent to the melt, was not distributed evenly before gas atomisation. Similarly, impurities acquired from either the furnace or recycled metal may have caused localised variation in the melt's composition. Another explanation for the composition difference is manufacturer blending two separate powder batches.

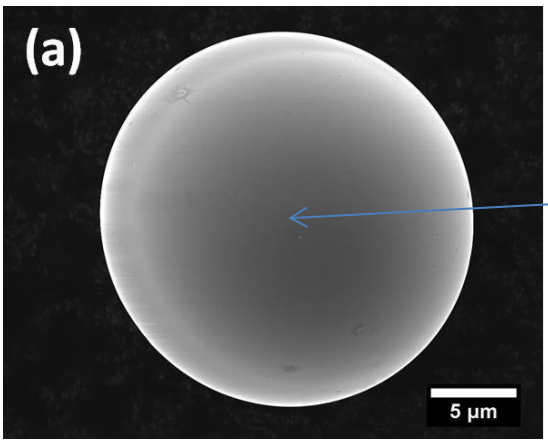

Element	Wt%	At%
Si K	6	11
Cr K	8	8
Fe K	3	3
Ni K	83	78
Total	100	100

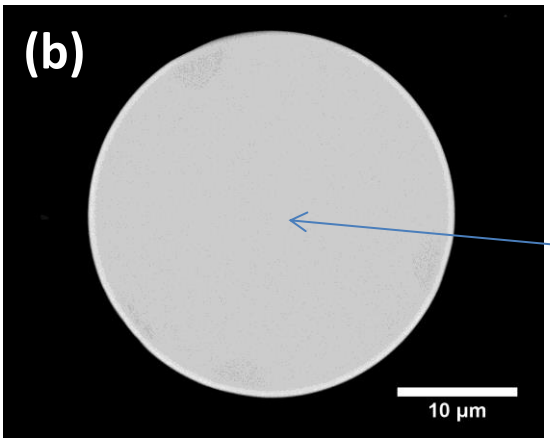

Element	Wt%	At%
Si K	6	11
Cr K	8	8
Fe K	2	3
Ni K	84	78
Total	100	100

***Figure 4.5**: Particles of higher Si content imaged (a) whole using SE and (b) cross-sectioned using BSE.*

The microstructure of these Si rich particles was further examined at high resolution using transmission electron microscopy. The results of this investigation are presented in section 4.1.3.

Contamination of powder particles

During SEM examination of the ECKA 500 powder, surface impurities were observable on a minority of particles (see figure 4.6). EDS analysis, indicated a high atomic percentage of O along with much smaller quantities of Ca, Al and Si. When the powder was viewed in cross-section, some of the particles displayed large intergranular inclusions (>0.5μm) of a lower atomic weight than the surrounding material. EDS readings from these inclusions, detected the presence of the same elements found within the surface impurities. Measurements from the intergranular inclusions are an indicator of the elements which may form the nanoscale boundary particles.

The morphology of the oxide inclusions was typically spherical, indicating that they solidified from a liquid state within the molten alloy. At the surface, elementally similar oxide impurities produced pancakes-like formations, sometimes thin enough to make out the underlying alloy grain structure. These exterior formations appeared in greater quantity than the inclusions.

The preferential formation of exterior oxide may happen during gas atomisation, as the more readily oxidised elements react with O_2 at the particle's surface. The inclusions may then form as convection currents [20] sweep oxide from the surface of the particle into the interior. Another possibility is the oxide forms prior to gas atomisation, either developing on the surface of the melt, or being introduced as contaminate from either recycled metal or an uncleaned furnace. Turbulence within the furnace mixes the molten oxide into melt where, as the spherical oxide inclusions indicate, it remains immiscible with the surrounding alloy. When the liquid mixture is forced through the nozzle, and the molten material is spheriodized, the lower density oxide rises towards the surface before solidifying.

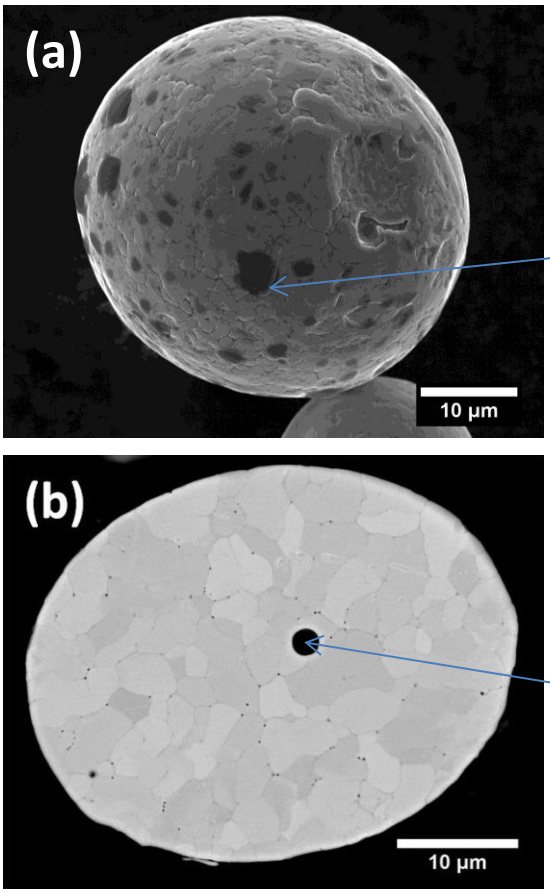

Element	Wt%	At%
O K	35	62
Al K	2	2
Si K	4	4
Ca K	1	1
Cr K	32	18
Fe K	3	2
Ni K	23	11
Total	100	100

Element	Wt%	At%
O K	23	47
Al K	7	8
Si K	3	4
Ca K	7	6
Cr K	17	11
Fe K	5	3
Ni K	38	21
Total	100	100

***Figure 4.6**: (a) SE image showing impurities on a particle surface and (b) BSE image showing a spherical inclusion.*

4.1.2 XRD analysis

When a molten alloy of approximately 76wt% Ni, 15wt% Cr and 9wt% Fe is cooled under equilibrium conditions, the Ni-Cr-Fe ternary phase diagram [128] predicts the formation of a crystalline solid with an FFC crystal structure. This single phase is maintained from the melting point, at approximately 1430˚C, to temperatures as low as 650˚C (see figure 4.7).

Due to the rapid cooling rates associated with gas atomisation, the powdered alloy did not experience equilibrium cooling. To investigate the influence of this processing on phase formation, the powder's crystallography was analysed using XRD.

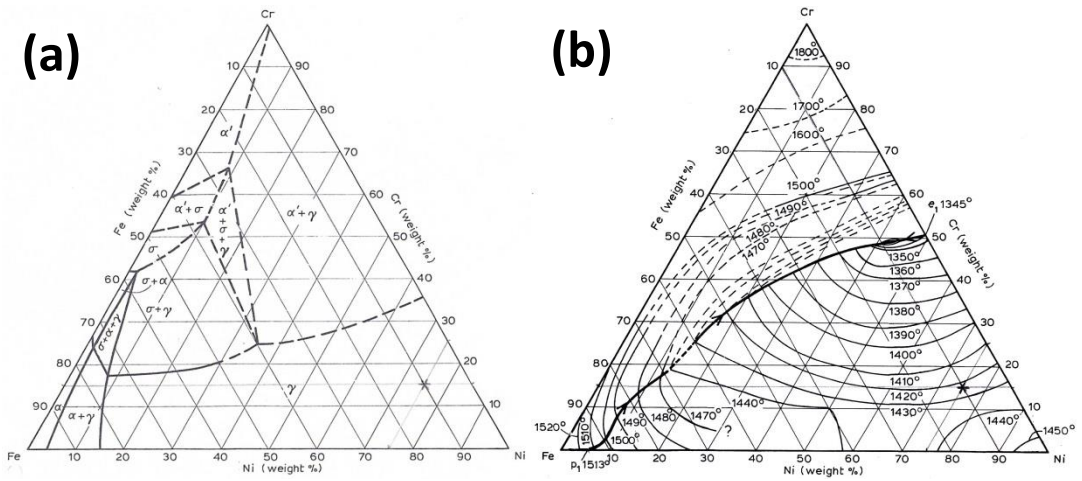

***Figure 4.7**: Ternary Ni-Cr-Fe phase diagrams showing (a) an isothermal section at 650˚C and (b) a liquidus projection [128].*

Despite the non-equilibrium cooling conditions, results of XRD analysis showed the gas atomised powder was primarily composed of a crystalline solid with an FCC crystal structure. Its lattice parameter of 3.56Å was consistent with values reported for the Inconel 600 parent material [129]. When the XRD results were compared with a pure Ni standard (see figure 4.8), it was revealed that the alloying additions had produced a 1.4% increase in the lattice parameter.

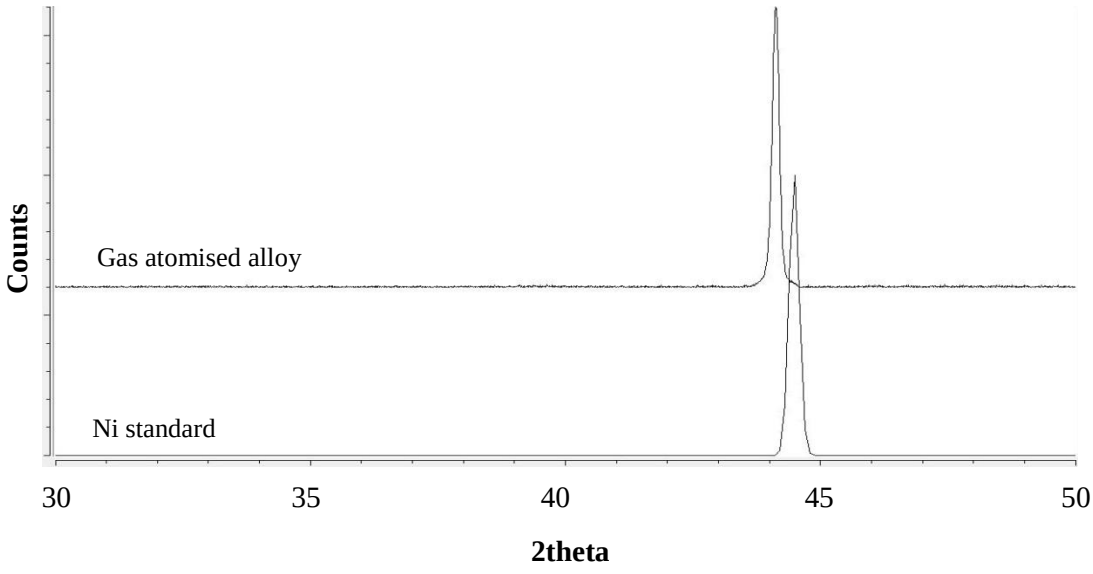

***Figure 4.8**: Comparison between the 111 peaks of the gas atomised alloy and a Ni standard.*

As discussed in 4.1.1, particles of atypical composition, accounting for 4.5vol% of the analysed powder, were detected using SEM-EDS. In an austenitic Ni superalloy,

literature suggests that the measured increases in Si and Ni should produce a detectable decrease in lattice parameter [130], assuming that the detection limit has been exceeded. The lack of evidence within the diffraction pattern may indicate that the anomalous particles are amorphous.

The oxide containing Ca, Al and Si also failed to register within the diffraction pattern, but considering the extremely small quantities of the material, it was unlikely to surpass the detection limits.

4.1.3 TEM analysis

When examining an anomalous particle using TEM, neither imaging nor diffraction techniques could provide any evidence of crystal formation. As figure 4.9 demonstrates, even the higher resolution capabilities of the TEM revealed no grain structure within the particle. This suggests that cooling rates were quick enough to prevent ordering of the atoms during solidification.

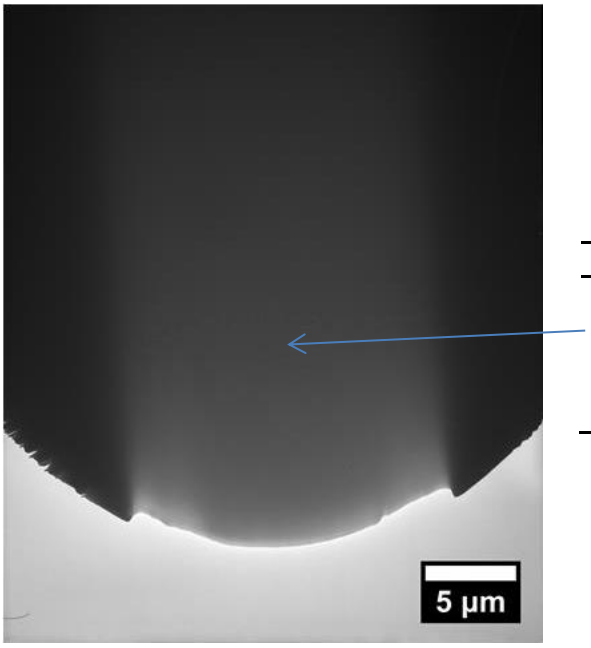

Element	Wt%	At%
Si K	6	11
Cr K	7	8
Fe K	3	3
Ni K	84	78
Total	100	100

***Figure 4.9**: TEM micrograph showing an electron transparent window milled into a particle of atypical composition.*

4.2 Powder characterization following oxidation treatment

Manufacture of the heating elements begins with the flame spray oxidation, and subsequent quenching of a gas atomised Ni alloy. In section 4.2, the effects of this initial production phase are analysed, and contrasted with the results obtained from the original powder.

4.2.1 SEM/EDS analysis

Particle size distribution

Particle size analysis of the flame sprayed powder was again conducted by means of image analysis. The results, displayed alongside those of the gas atomised alloy, are presented in the figure 4.10. This comparison highlighted an increase in the average particle diameter post oxidation treatment. Prior to heat treatment the gas atomised alloy had an average particle diameter of 25μm; following it, this value had risen to 36μm. In addition to the rise in average particle diameter, the flame sprayed powder's particle size range also increased, as evidenced by the rise in standard deviation from 8 to 10.

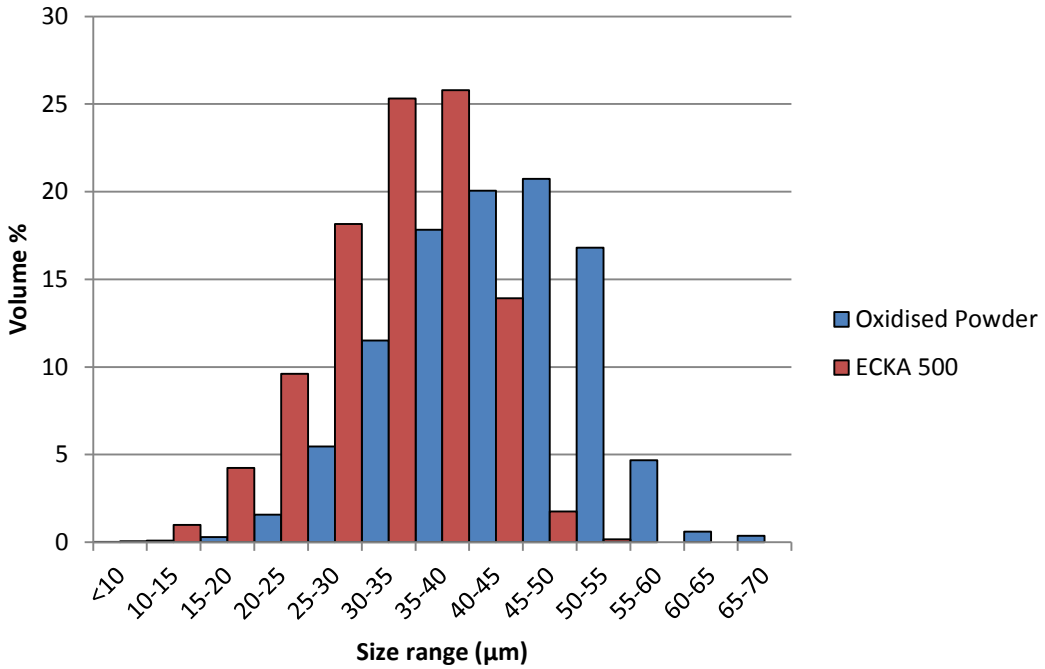

***Figure 4.10**: Histogram comparing the particle size distributions of the ECKA 500 and heat treated powder.*

Cross-sectioned powder

When examined in cross section, the heat treated powder was found to contain particles with varying degrees of oxidation. While the majority were almost entirely oxidised, a small percentage either eluded oxidation or retained a substantial amount of metal. In the BSE image below, the metallic particles appear brighter, due to the greater number of backscattered electrons from the higher atomic number material. EDS measurements acquired from a large number of particles indicated that metallic powder particles accounted for 2.9% of the powder's total volume.

The variation in particle oxidation levels likely resulted from the differing levels of heat exposure experienced during the flame spray heat treatment. Particles that travelled through the hottest region of the oxyacetylene flame (tip of the inner cone) reacted more quickly with the available O_2 and achieved the greatest levels of oxidation. Conversely, those particles that deviated sufficiently from this high temperature zone may have avoided oxidation entirely.

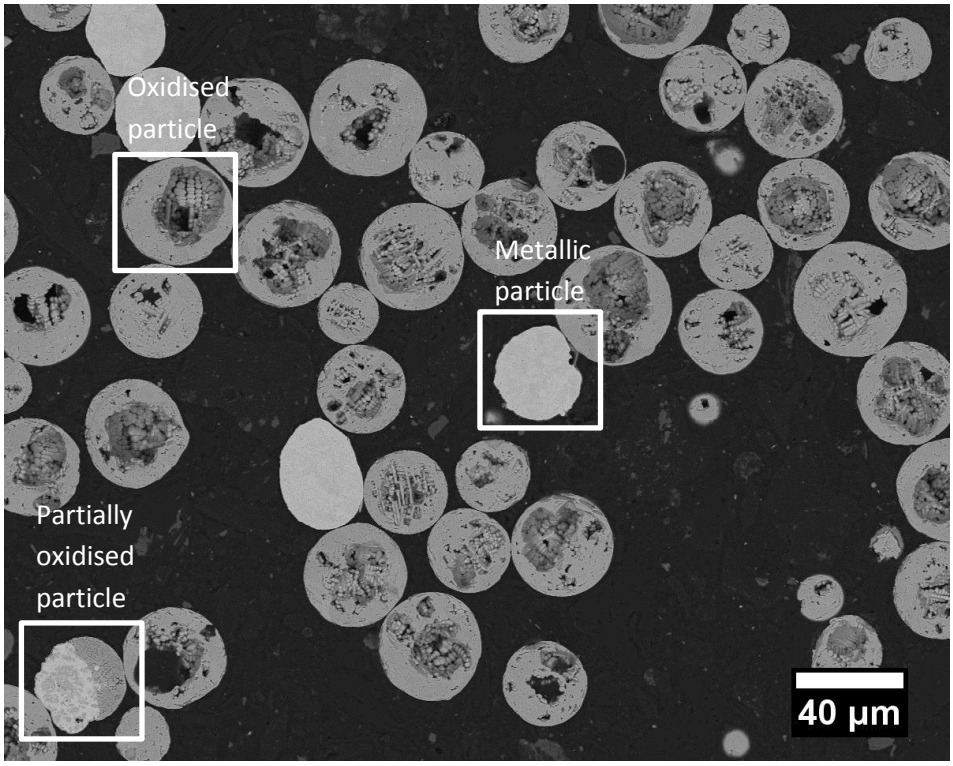

***Figure 4.11**: BSE image of cross-sectioned powder after flame spray oxidation treatment.*

Oxidised particles

While the exterior of the oxidised particles appears relatively dense, cross sectioning revealed the presence of internal porosity. Within these central hollows, dendrite incursions were visible, having grown inwards following surface nucleation (see figure 4.12).

The porosity at the centre of particles may be explained by solidification shrinkage. As solidification front moves inwards, the accompanying volumetric contraction is compensated for by molten material drawn from the particle's centre. As solidification continues this liquid is exhausted resulting in the formation of voids. The development of these pores seems to share similarities with the shrinkage defects that can occur during the casting of metals [131].

A high magnification examination of the oxide seemed to suggest it was composed of a single phase oxide, which EDS readings indicated contained significant amounts of Ni, Cr and Fe. As figure 4.11 shows, the Ni:Cr:Fe ratio remained similar to that observed within the original alloy, while the ratio of metal to O atoms was approximately 1:1.

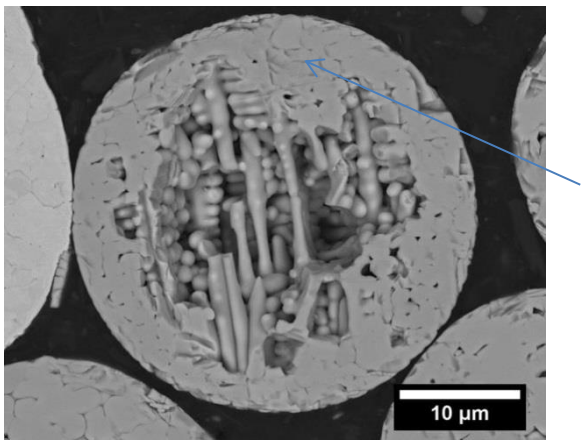

Element	Wt%	At%
O K	23	52
Cr K	13	9
Fe K	6	4
Ni K	58	35
Total	100	100

***Figure 4.12**: BSE image showing dendritic growth within an oxidised powder particle.*

Oxidised particles – elemental mapping

The distribution of the four main constituent elements was investigated using EDS mapping. Within the oxidised particle, the Ni and O concentrations seemed to remain constant; however, as figure 4.13 shows, the Cr and Fe concentrations appeared less

evenly distributed. At the centre of the dendrites Cr dominated, while nearer the edges the elemental mapping suggested Fe accumulated.

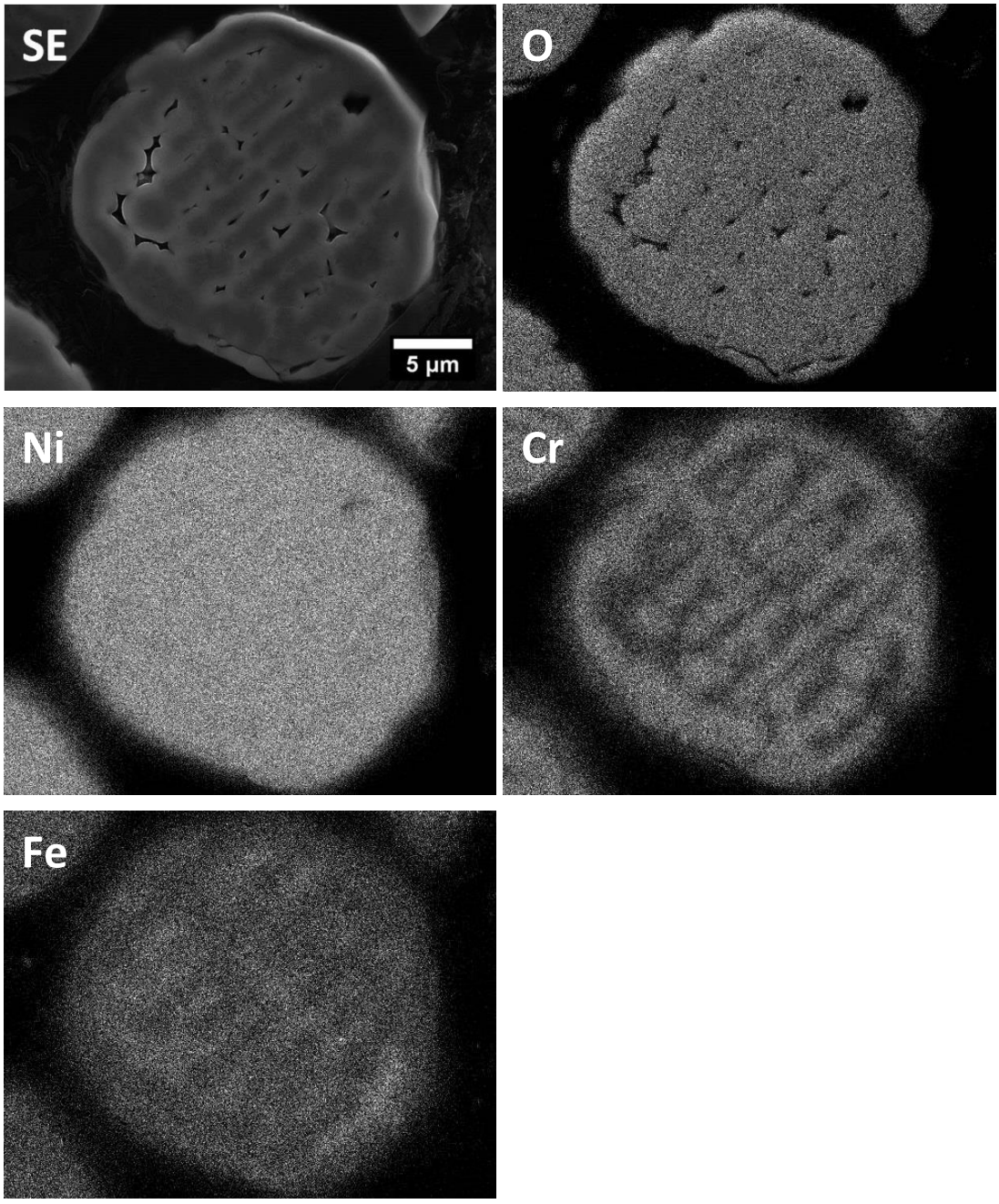

***Figure 4.13**: Elemental maps displaying cored grains within an oxidised particle.*

The development of cored dendrites reflects the non-equilibrium cooling conditions experienced by the material. Cr, having a higher melting point than Fe, enriches the centre of the dendrites, which solidify first as the dendrites branch into the molten oxide. As this Cr rich centre forms, the remaining liquid becomes concentrated in Fe, which later solidifies near the edges of the dendrite.

Oxidised particles - grain boundary Ni

In some of the heavily oxidised particles, material of higher atomic number could be located between the dendritic arms of the oxide (see figure 4.14). When analysed using EDS, the readings indicated almost pure Ni, depleted in the original alloying elements. The formation of these grain boundary deposits may be attributed to Cr and Fe having a greater affinity for O than Ni [132]. As the molten mixture cools, the Cr and Fe react preferentially with O; and in an O deficient atmosphere, the excess Ni is left as metallic particles at the oxide grain boundaries.

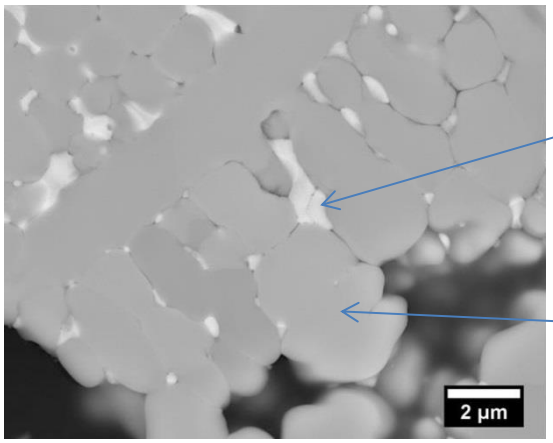

Element	Wt%	At%
O K	6	20
Cr K	3	2
Fe K	4	3
Ni K	87	75
Total	100	100

Element	Wt%	At%
O K	23	52
Cr K	14	9
Fe K	6	4
Ni K	57	35
Total	100	100

***Figure 4.14**: Ni between the arms of the dendritic oxide.*

Oxidised particles – metal and oxide cores

At the centre of the cross sectioned oxidised particles, both metallic and oxide cores were sometimes observable. Their spherical appearance suggests that they solidified from a liquid state. In contrast to the boundary deposits, EDS readings acquired from the metallic cores indicated than the Ni had retained much of the Cr and Fe. As figure 4.15 shows, the composition is very similar to that of the original alloy. When the oxide cores were analysed using EDS, the composition did not appear to differ significantly from the surrounding oxide shell.

The formation of metallic cores within an oxide shell may have proceeded in the following manner. While the particle was in a liquid state, O reacted with the metal near the surface producing a layer of molten oxide surrounding a metallic liquid core. The oxide, having a higher melting point, solidified first forming an oxide shell. As

the particle continued to cool the Ni alloy solidified and the associated reduction in volume caused it to separate from the oxide outer shell.

Further oxidation of the metallic core is one possible explanation for the development of oxide spheres at the centre of some particles. However, in this scenario the oxide would form by a gas/solid reaction, likely producing a layer of oxide of different composition to that of the surrounding shell.

Another possibility is that convection currents are involved in the formation of the oxide cores. After oxidation of the molten metal, the flow of liquid oxide within the particle draws partially solidified material from the surface into the interior. As the particle continues to cool, liquid solidifies around the inclusion while an oxide shell develops at the surface. The shrinkage associated with solidification causes the separation of internal oxide and external shell, resulting in the formation of an oxide core. Having formed concurrently, the core and outer shell could share similar compositions.

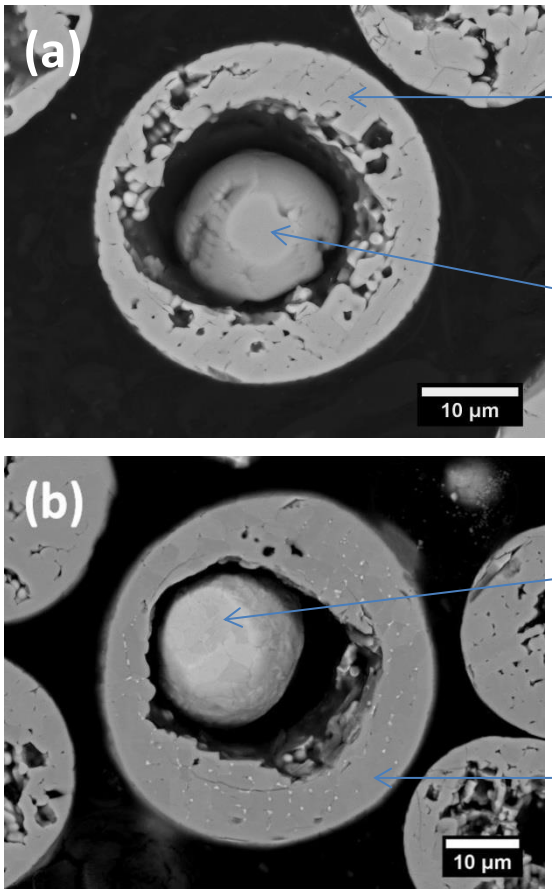

Element	Wt%	At%
O K	24	53
Cr K	12	8
Fe K	6	4
Ni K	58	35
Total	100	100

Element	Wt%	At%
O K	24	53
Cr K	13	9
Fe K	7	4
Ni K	56	34
Total	100	100

Element	Wt%	At%
O K	0	0
Cr K	16	18
Fe K	9	9
Ni K	75	73
Total	100	100

Element	Wt%	At%
O K	24	53
Cr K	12	8
Fe K	7	4
Ni K	57	35
Total	100	100

***Figure 4.15**: BSE images showing particles with (a) oxide and (b) metal cores.*

Oxidised particles – exterior appearance

Typically, the oxidised particles showed evidence on their surfaces of the dendritic growth evident in the cross sections (see figure 4.16 (a)). Sometimes this surface oxide would appear smeared or slightly flattened, as shown in figure 4.16 (b). This could indicate that some of the material is still fairly malleable upon impact with the quenching water.

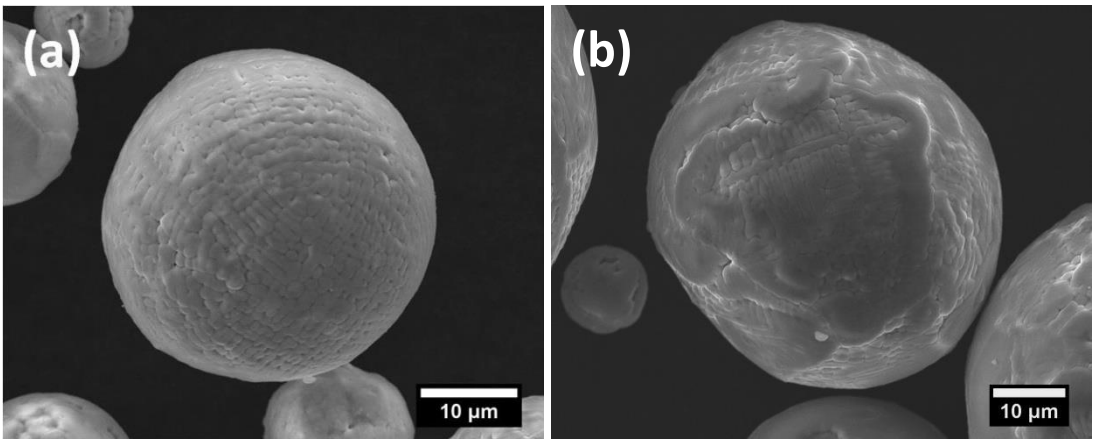

***Figure 4.16**: Oxidised particles imaged using SE showing (a) dendritic surface formations and (b) slight surface flattening.*

Often, solidification appeared to begin at multiple nucleation sites on the surface of the particles. The SE image in figure 4.17 (a), shows how stresses between colliding solidification fronts, could cause the formation of ripples. When these stresses opened up cracks in the outer shell, or the particle otherwise became damaged, it was sometimes possible to see the previously discussed metal/oxide cores. In some cases, as figure 4.17 (b) shows, multiple spheres would form at the centre of the particle.

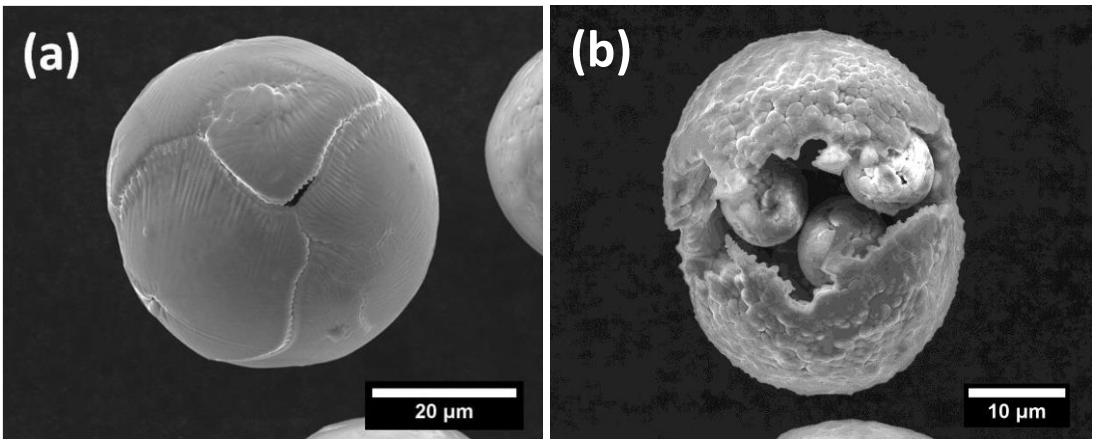

Figure 4.17*: Oxidised particles imaged using SE showing (a) surface ripples at solidification boundaries and (b) central sphere formation.*

Partially oxidised particles

The semi oxidised particles are distinctive in appearance, easily distinguishable from metallic and fully oxidised powder particles. Viewed whole (see figure 4.18 (a)), these particles were mushroom-like in appearance, with a bulbous oxide cap and a stem containing mainly metallic material. EDS readings indicated that the oxide varied compositionally from the fully oxidised particles. Of particular note were the elevated concentrations of Si and O. Examination of the metallic stem revealed Ni, now heavily depleted in the original alloying elements. As observed with the grain boundary deposits within the heavily oxidised particles, Cr and Fe appeared to have reacted preferentially with the available O.

Upon cross-sectioning of the partially oxidised powder particle, BSE imaging revealed low atomic number nodules within the metallic region. Confirmed as oxide by EDS (see figure 4.18 (b)), they may have formed as convection currents within the molten particle drew surface oxide into the centre of the particle [20]. Alternately, they could be incursions from the main oxidised region, appearing as isolated particles due to the angle of cross sectioning.

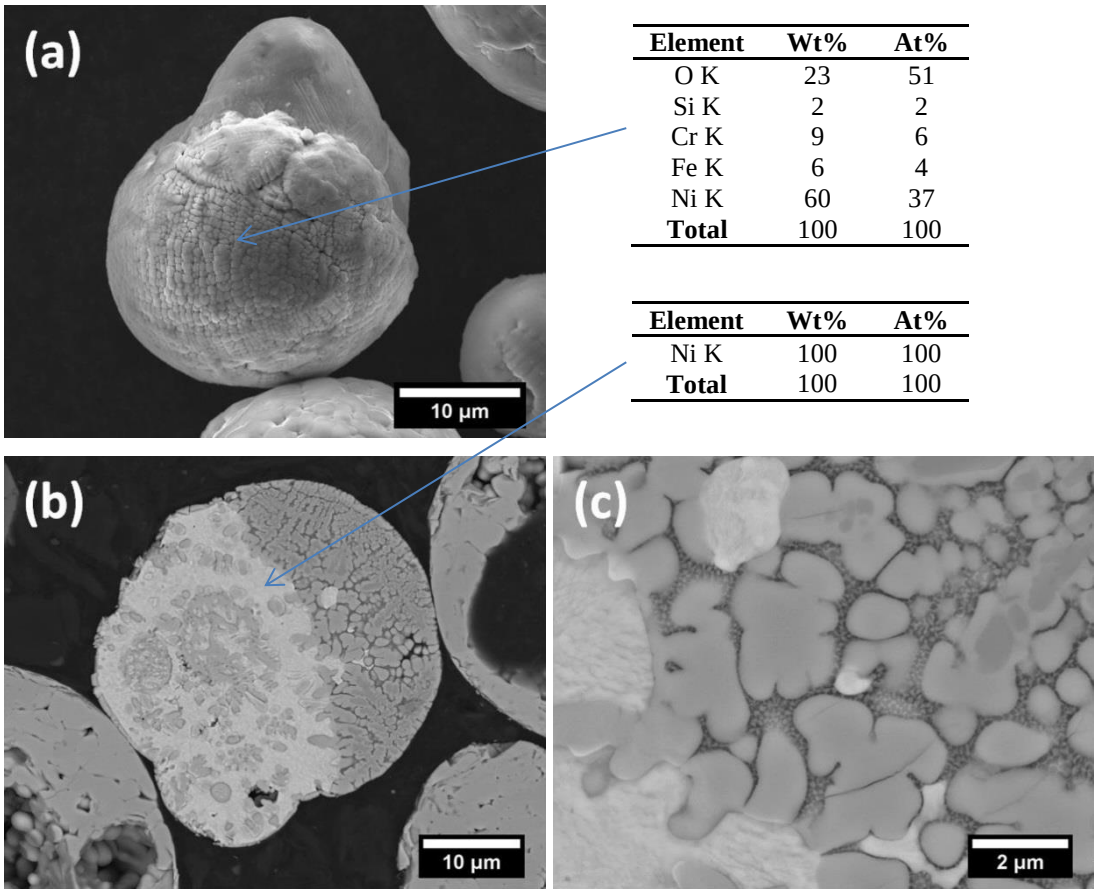

Element	Wt%	At%
O K	23	51
Si K	2	2
Cr K	9	6
Fe K	6	4
Ni K	60	37
Total	100	100

Element	Wt%	At%
Ni K	100	100
Total	100	100

***Figure 4.18**: (a) SE image showing a partially oxidised particle and (b), (c) displaying BSE images of a partially oxidised particle in cross-section.*

Examination of the oxide cap revealed dendritic formations, similar to those observed within the fully oxidised particles. At the centre of these dendrites, BSE imaging displayed darker regions of lower atomic number. A comparison between the elemental distribution maps indicated that Cr was concentrating in these central regions at the expense of Ni (see figure 4.19). The contrast in the BSE images may be explained by a lower average atomic number Cr oxide backscattering fewer electrons than the Ni oxide.

Between the arms of the dendritic structures, BSE imaging identified a two phase region, containing one phase of significantly lower atomic weight. Elemental mapping showed high Si, and slightly lower O concentrations correlated with these interdendritic regions. With Si being substantially lighter than Ni, Fe and Cr, the BSE imaging and the elemental mapping appeared consistent.

The distribution of elements within the oxide cap demonstrates the non-equilibrium cooling conditions experienced during solidification. As observed within the fully oxidised powder, early solidification at the centre of the dendrites was dominated by Cr, which has a higher melting point than other elements present. This enriched the remaining liquid with Ni, some of which then solidified near the edges of the dendrite. Rejection of Si, during this dendrite growth, resulted in its concentration in the interdendritic region. The fine two phase structure that has developed between the dendrites suggests solidification occurred via a eutectic reaction.

The formation of oxide caps during thermal spraying of metallic particles has previously been reported by other researchers such as Syed et al [18], and Ageorges and Fauchais [19]. During the former's work with gas atomised stainless steel, an accumulation of oxide at the tail of particles was noted. These authors explained this by considering the density and surface tension differences between the molten metal and oxide, along with drag forces on the particles.

Three factors that may influence whether a metallic particle becomes partially or completely oxidised are: the degree of heat exposure, oxygen availability and the particle's original composition.

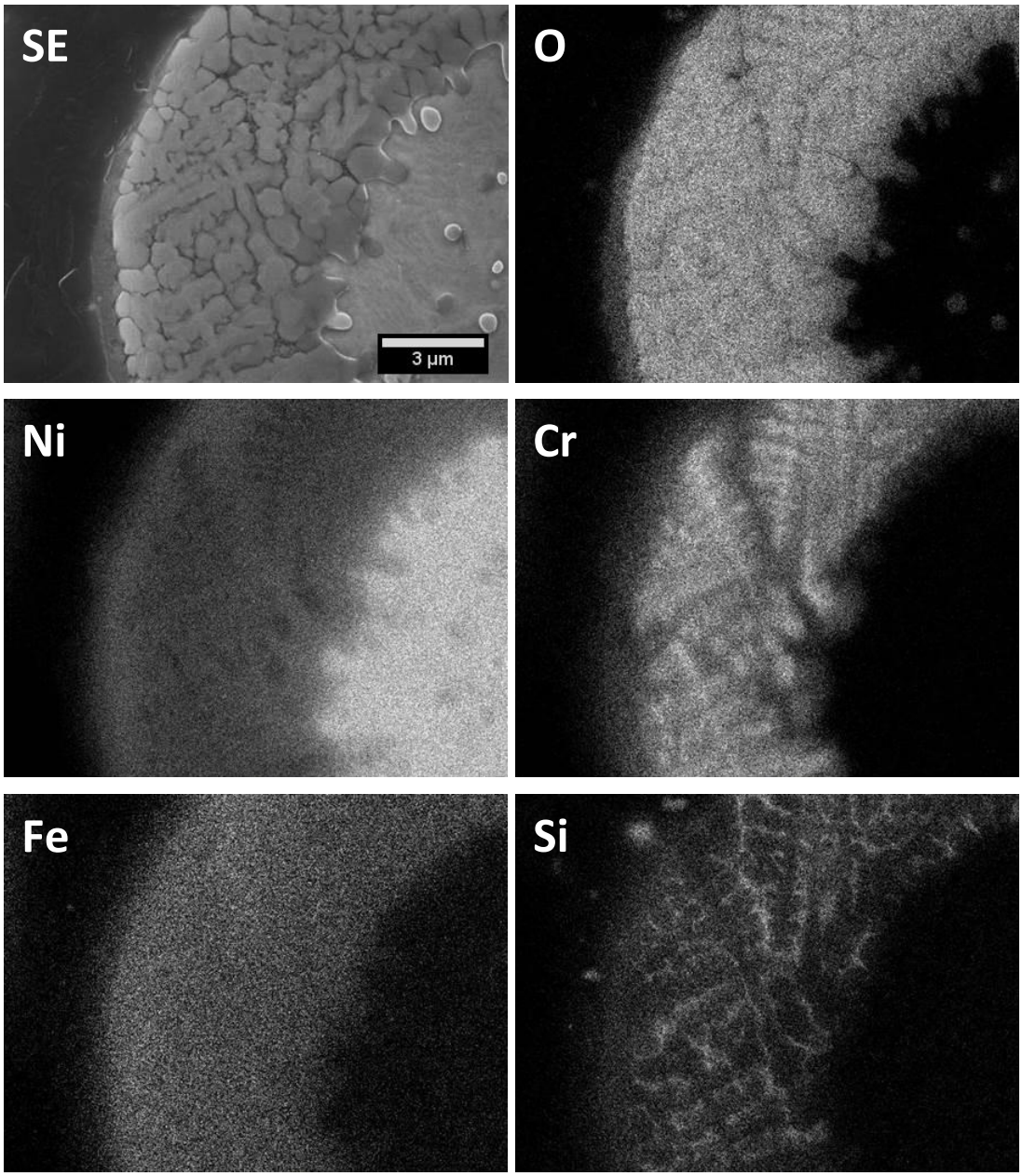

***Figure 4.19**: Elemental maps obtained from partially oxidised powder cross-section.*

Metallic particles

After the heat treatment, EDS measurements made in combination with SEM image analysis indicated that metallic particles accounted for approximately 2.9% of the powder's total volume. As figure 4.20 demonstrates, these particles displayed the same compositional variations observed prior to flame spraying. While some particles conformed to the manufacture's chemical analysis, others showed elevated levels of Si and Ni.

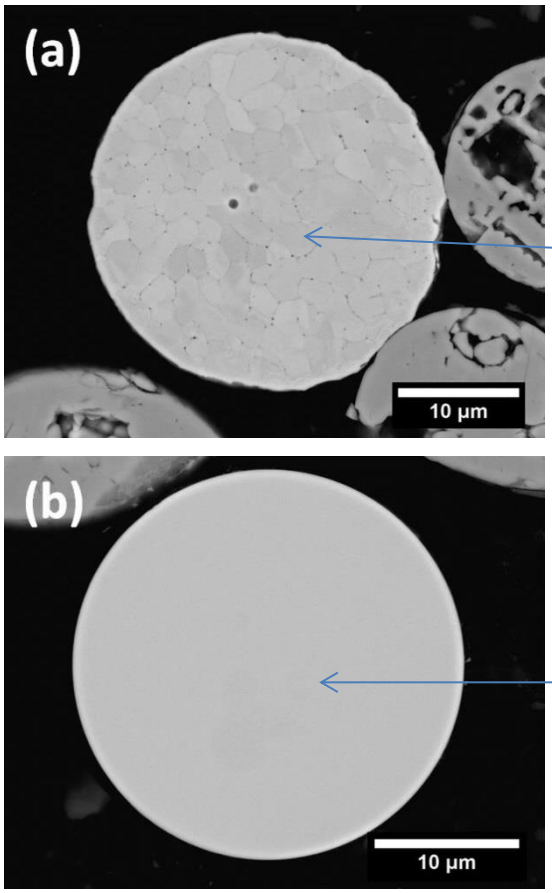

Element	Wt%	At%
Cr K	14	16
Fe K	9	9
Ni K	77	75
Total	100	100

Element	Wt%	At%
Si K	6	12
Cr K	8	8
Fe K	2	2
Ni K	84	78
Total	100	100

***Figure 4.20**: Following flame spray oxidation, the surviving metallic particles remained of varying composition. EDS results obtained from particle (a) were in agreement with the manufacturer's specification, while those obtained from particle (b) indicated a greater concentration of Si.*

Amongst the surviving metallic particles, some appeared to have eluded oxidation, while others had developed thin oxide shells. The distribution of elements within one of these oxide shells was investigated using EDS elemental mapping. In contrast to the fully oxidised powder particles, the oxide forming on the metallic particle's surface appeared to be dominated by Cr (see figure 4.21). This is reminiscent of the scales formed on Ni-Cr-Fe superalloys during lower temperature, solid state oxidation [133].

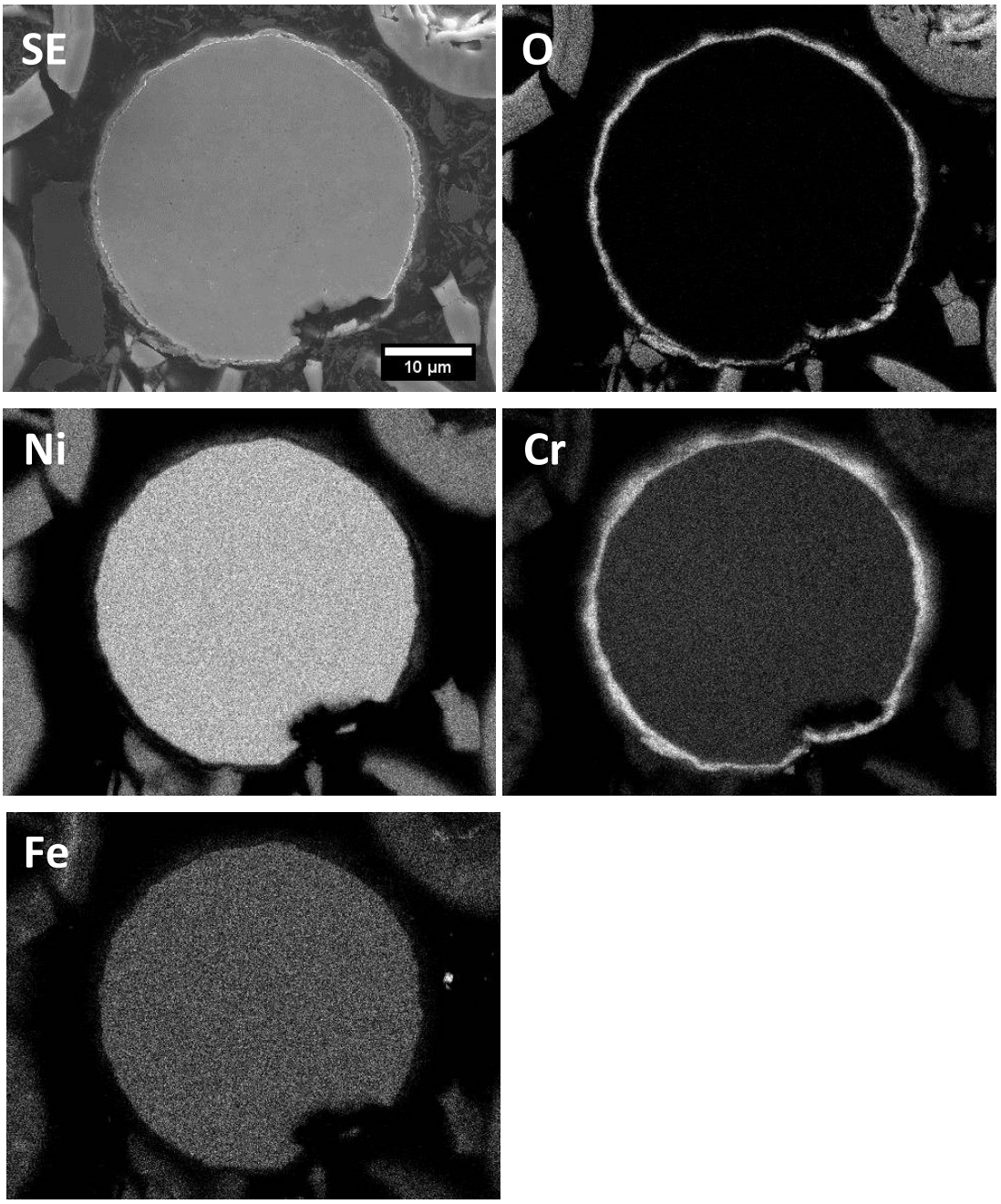

***Figure 4.21**: Elemental maps highlighting the oxide shell surrounding a cross-sectioned metal particle post heat treatment.*

4.2.2 XRD analysis

After the flame spray heat treatment of the gas atomised alloy a number of additional phases became detectable by XRD (see the diffraction pattern in figure 4.22). Within the acquired spectrum, the dominant phase appeared to have a NaCl crystal structure comparable to that of NiO. Its calculated lattice parameter of 4.17Å was just 0.2%

lower than that of the standard NiO data file against which it was being compared [134].

Agreeing with earlier compositional analysis within the SEM, the XRD pattern also indicated the presence of the original gas atomised alloy (lattice parameter 3.56Å) as well as low alloyed Ni (lattice parameter 3.53Å). Though not clearly evident upon SEM inspection, the weak peaks within the XRD pattern also suggested the presence of a small amount of spinel phase (lattice parameter 8.33 Å).

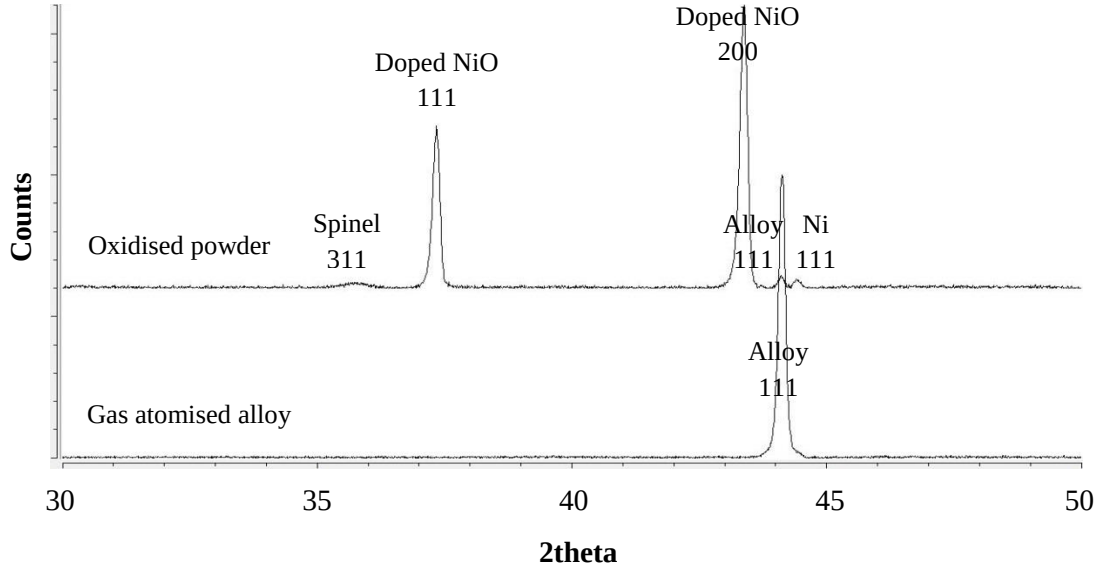

***Figure 4.22**: Diffraction patterns obtained from the powder before and after flame spray oxidation.*

While the XRD results indicated the majority of the powder had a NaCl crystal structure similar to that of NiO, EDS measurements acquired from the bulk oxide suggested the presence of significant quantities of Fe and Cr (see figure 4.12). The most likely explanation for this is the incorporation of Fe and Cr into the NiO lattice structure during the powdered alloy's oxidation (see figure 4.23 (a) and (b)). Since Fe and Cr have similar ionic radii to Ni [62], they may replace Ni atoms in the oxide lattice without significantly altering the lattice parameter.

The limited effect of Fe and Cr dopants on the NiO lattice parameter has been reported elsewhere within the literature. Mallick et al [63] who prepared Fe doped NiO by chemical co-precipitation, found the lattice parameter remained almost unchanged up to 3 at% Fe, before showing a slight increase at 5 at% Fe; while

Elumalai et al [68], who produced NiO doped with 1.5at% Cr by the thermal decomposition of nitrates, measured a minor 0.3% decrease in the lattice parameter.

The pseudo-binary Ni-Fe-O and Ni-Cr-O phase diagrams (see figure 4.23), published by Raghavan [56] and Kjellqvist [65] respectively, suggesting that NiO can integrate appreciable quantities of Fe and Cr at high temperatures (such as those achieved during the oxidation treatment). As the oxidised material undergoes rapid cooling due to the water quench, this metastable high temperature state may be maintained at room temperature where kinetics limit phase transformation.

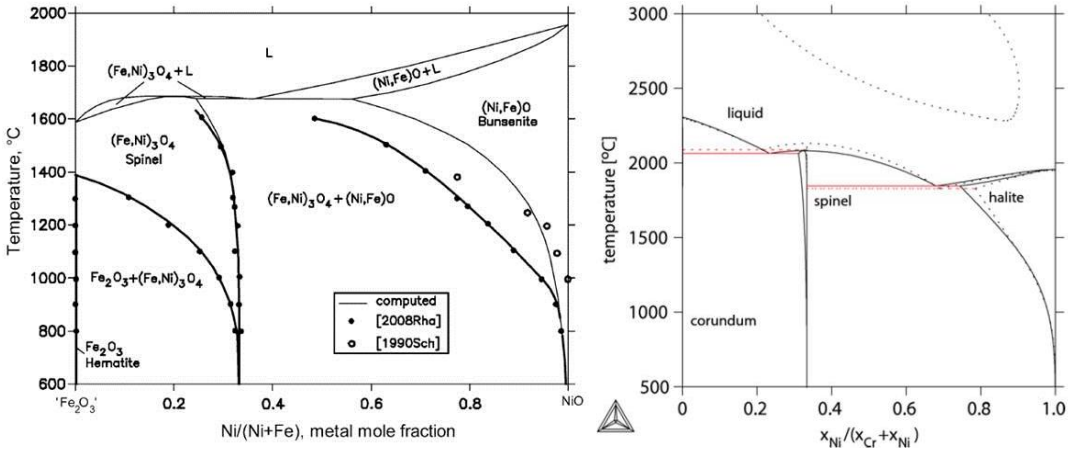

***Figure 4.23**: (a) Fe-Ni-O and (b) Cr-Ni-O pseudo binary phase diagrams.*

4.2.3 TEM analysis

To investigate the relationship between the spinel and doped NiO phases at high resolution, thin foil specimens were prepared with a FIB and analysed using TEM/STEM techniques. One of the TEM specimens produced is displayed in figure 4.24, where it can be seen mounted on a Cu support grid. Due to the porosity at the centre of this particle, gaps are present within cross section where material was lost during FIB processing. The difference in specimen thickness is reflected by the brightness contrast between the top and bottom of the cross section.

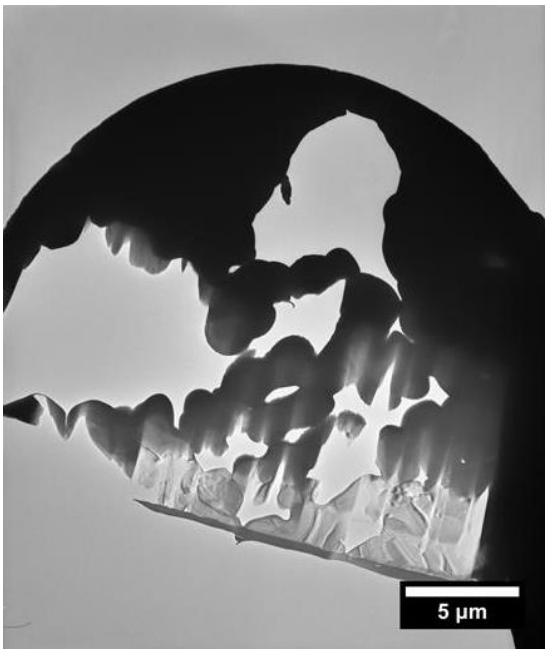

***Figure 4.24**: FIB prepared oxide particle cross-section.*

Oxide grain – EDS analysis

Within the cross sectioned particle, individual oxide grains were found to display the same variations in composition previously noted in the SEM-EDS elemental distribution maps. In the centre of the grain, EDS measurements detected a greater concentration of Cr while nearer the edges there appeared to be greater quantities of Fe (see figure 4.25). Possible reasons for this variation in composition were discussed earlier in section 4.2.1.

On some of these oxide grains, where an edge had been left exposed, layers of material were found to accumulate (see figure 4.25). When compositional analysis was conducted, EDS detected an abnormally high concentration of Ga atoms, suggesting that milled material had been redeposited on the edges of the oxide grains during FIB sample preparation.

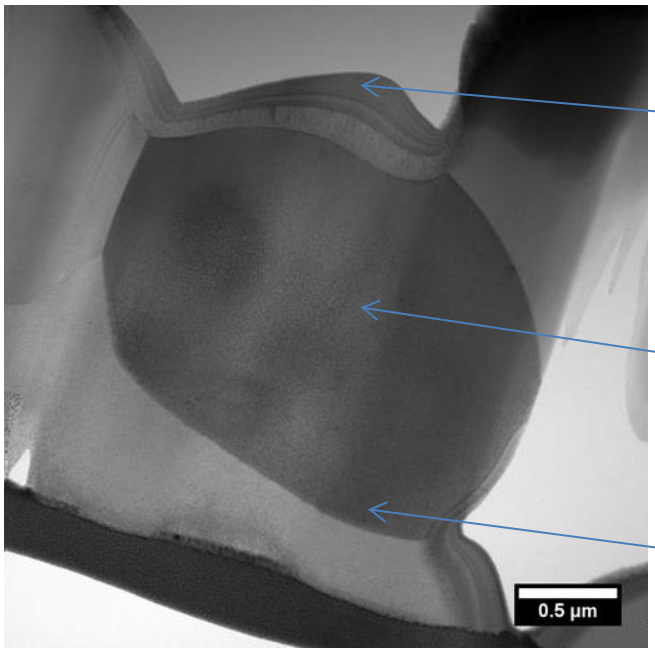

Element	Wt%	At%
O K	14	37
Cr K	12	10
Fe K	5	4
Ni K	52	38
Ga K	17	11
Total	100	100

Element	Wt%	At%
O K	22	49
Cr K	13	10
Fe K	6	4
Ni K	59	37
Total	100	100

Element	Wt%	At%
O K	22	50
Cr K	6	4
Fe K	7	5
Ni K	65	41
Total	100	100

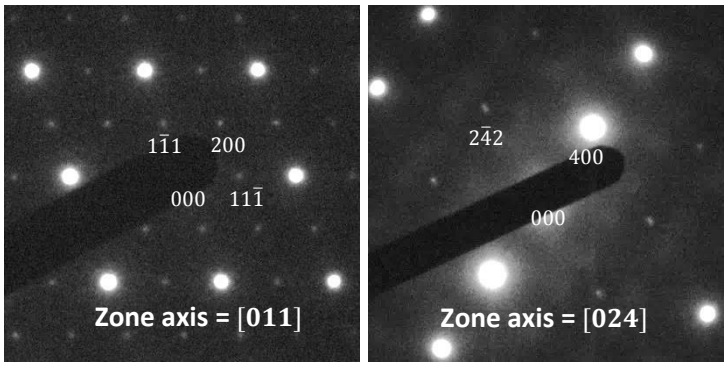

***Figure 4.25**: Bright field image of an oxide grain positioned on zone axis with accompanying diffraction patterns and EDS readings.*

Oxide grain – electron diffraction

As figure 4.25 demonstrates, the SAD diffraction patterns obtained from the oxide grains displayed periodic arrangement of high and low intensity diffraction spots. The angles measured between these reflections were consistent with the cubic structures of both NiO and spinel.

Within these diffraction patterns low intensity spots appeared at half spacings between those of high intensity. Since XRD results indicated that the spinel lattice parameter was approximately half that of the doped NiO (see section 4.2.2), it was hypothesised that the low intensity spots were isolated spinel reflections, while the high intensity were caused by superimposed NiO and spinel reflections. A possible

example of this superposition, would be the overlap of the $(00\bar{2})$ NiO with the $(00\bar{4})$ spinel reflections in figure 4.25 (b).

Using the distances between the low intensity spots, then the distances between the high intensity spots, lattice parameters of approximately 8.4Å and 4.2Å were determined. These values were consistent with those formally calculated for the spinel and doped NiO phases during the XRD examination (see section 4.2.2), suggesting superstition of reflections from two phases was a possibility.

Oxide grain – lattice resolution imaging

A lattice resolution examination, revealed particle arrays of contrasting crystal structure, situated within the oxide grains. As figure 4.26 shows, the double layer superlattice structure of these particles distinguished them from the surrounding matrix. When examined using FFT image analysis, the d-spacing calculated from the particles and the surrounding matrix, were found to correlate with the spinel and NiO values previously obtained through XRD.

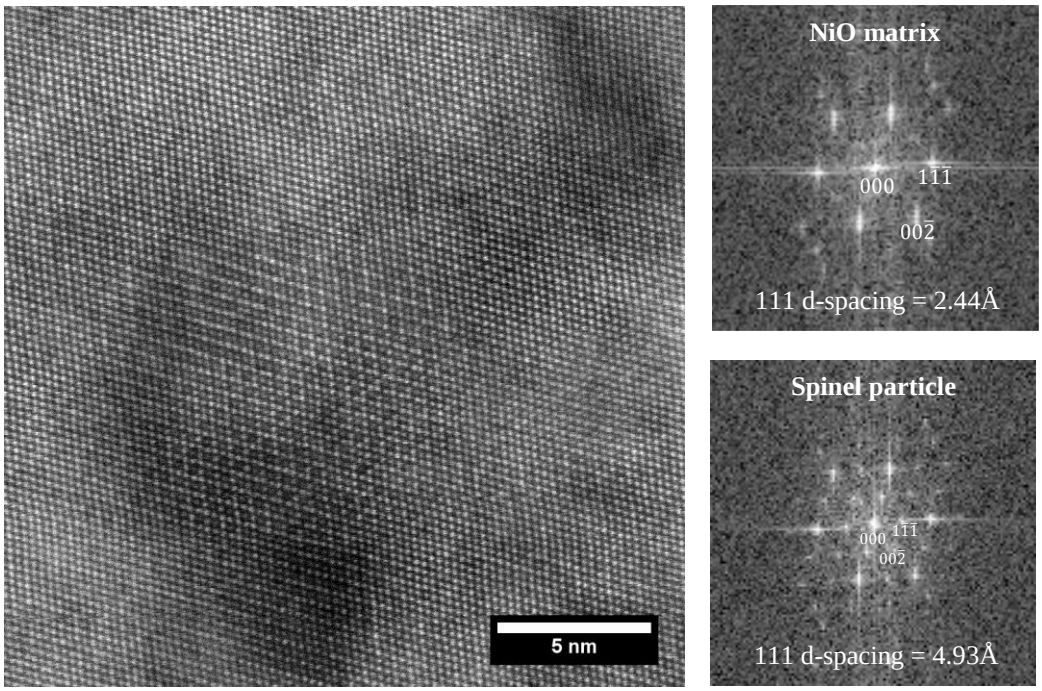

***Figure 4.26**: Spinel particles embedded within a NiO matrix, orientated in the [110] direction.*

FFT image analysis of these micrographs also helped highlight the close relationship that exists between the two structures. As the NiO matrix and the spinel particle are examined in turn, an additional set of diffraction spots appear at half intervals between the NiO spots. These correspond to the spinel 111 d-spacing that is approximately twice that of the 111 NiO d-spacing. The high degree of coherency between the NiO and spinel suggests that the oxygen sublattice is common to both structures and only the cations need to order for spinel precipitates to grow. This close coherency between NiO and spinel precipitates has previously been reported in both Fe doped NiO [87] and Cr doped NiO [83], with reported lattice misfits of 0.2% and 0.4% respectively at room temperature.

Spinel particles – EDS line scan

The variation in composition between the particles and the matrix was confirmed using EDS line scans. One example is displayed in Figure 4.27, where the scan path (represented by a green line) can be seen intersecting two precipitates (appearing dark in the image). As the line scan passes over the particles, the Cr and Fe intensities peak, while the Ni dips and the O remains largely constant. The stability of the O readings across the spinel matrix interface are indicative of shared O sublattice.

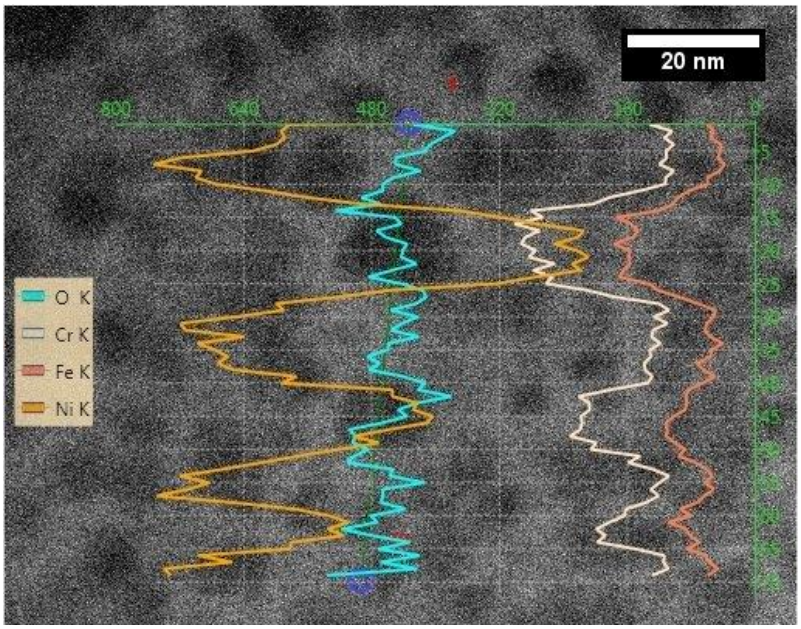

***Figure 4.27**: Elemental scan line (between two blue scan circles) crossing two phase region.*

Chapter 5

Characterisation of the flame sprayed thick film deposit

During the second stage of manufacture, the partially oxidised gas atomised alloy is deposited onto an enamelled substrate, by means of a second flame spray procedure. The resulting flat panel heating elements contain a complex mixture of oxide and metallic phases. To investigate the new phases and microstructures developing during the deposition, the thick film was examined using both physical and chemical characterization techniques. These results were compared with those previously obtained from the partially oxidised powder.

In this chapter, results are divided into sections based upon the method of characterisation. Section 5.1, documents the optical examination, during which the percentages of porosity and metallic material are estimated using image analysis. In section 5.2, results obtained from the thick film are compared with those collected from the partially oxidised power. Section 5.3 uses a combination of SEM and EDS to examine the film in cross section and following fracture. Finally, in section 5.4 the TEM/STEM is used to examine spinel growth within the doped NiO and oxide development around the metallic splats.

5.1 Optical microscopy

After the deposition of the metal-metal oxide powder mixture, a through-thickness cross section was prepared by standard metallographic procedures, before being studied using an optical microscope. This examination revealed a relatively porous film, containing substantial amounts of metallic material embedded within an oxide matrix. The distribution of the different phases is demonstrated in the following optical micrograph (see figure 5.1); here, the relative intensity of the light reflected gives the metallic regions a brighter appearance than the surrounding oxide.

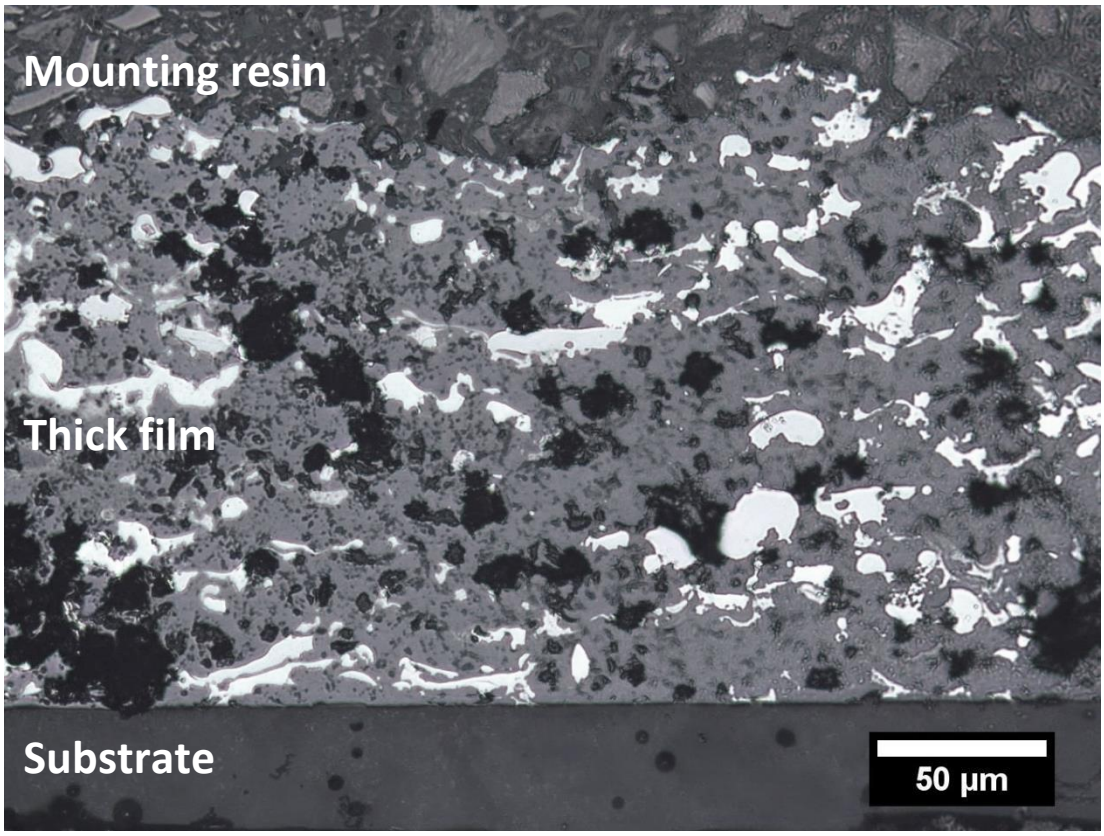

Figure 5.1*: Optical micrograph displaying a through-thickness cross section of the metal-metal oxide thick film.*

As figure 5.1 demonstrates, the impinging metallic particles experienced varying degrees of deformation during flame spray deposition. While some flattened upon impact, others remained much more spherical, due to variations encountered in temperature and velocity. These contrasting conditions are likely related to the dissimilar flightpaths through the oxyacetylene flame. Particles that travel the shortest path lengths to the substrate surface, maintain higher temperatures and velocities, resulting in thinner splat formation. Conversely, those that take longer flight paths, experience greater energy losses, and typically deform less upon collision with the target surface.

Accompanying the alternating layers of oxidised and metallic material, the thick film deposit also exhibited substantial levels of porosity. Formation of these porous areas typically occurs due to imperfect bonding between successive splats, which is exacerbated by the presence of unmelted material [135]. Since the morphology of film's metallic regions indicates some solid state deposition, the same may be assumed of the doped NiO, which has a higher melting temperature. The

incorporation of unmelted material into the thick film may explain the high levels of porosity observed.

5.1.1 Image analysis

To measure the percentage of metallic, non-metallic and porous regions within the thick film, a series of low magnification images were examined using image processing software. As figure 5.2 shows, the high contrast between the three different components enabled them to be easily separated within the optical micrographs.

The results of the image analysis suggested the film was 17% alloyed metal, 62% oxide, and 21% porous. However, the porosity value is likely to be inflated due to difficulties distinguishing pores from voids created during sample preparation. Figures could be further skewed if these voids form through the preferential dislodgement of either the metallic or oxidised material.

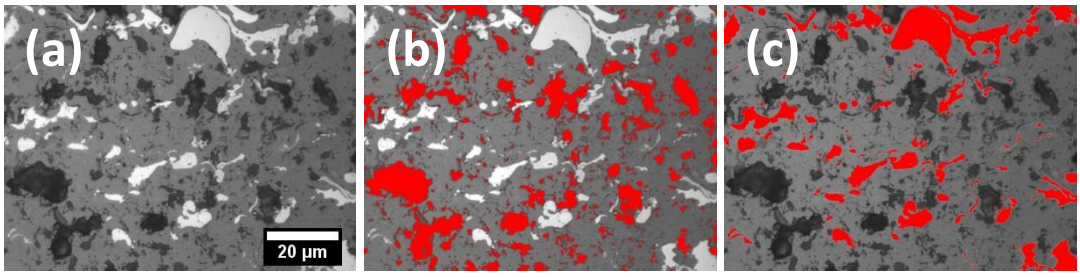

***Figure 5.2**: Thresholding of (a) greyscale image to measure percentage of (b) porosity and (c) metal alloy.*

5.2 XRD analysis of the thermally sprayed thick film

To investigate phase development during the second flame spray procedure a thick film specimen was examined using XRD, following its removal from the substrate. The diffraction patterns obtained from the top and bottom surfaces are displayed alongside the pattern collected from the partially oxidised powder in figure 5.3. A comparison of this data revealed that the same phases were present following the powder's deposition; however, the increased intensity of the metallic diffraction peaks relative to the oxide peaks did indicate the preferential accumulation of

metallic phases. This difference between the metal and oxide deposition rates may be attributed to the disparity in the materials' melting temperatures. A higher proportion of the metal reaches the substrate surface in a molten or softened state, enabling easier deformation and therefore greater bonding efficiency.

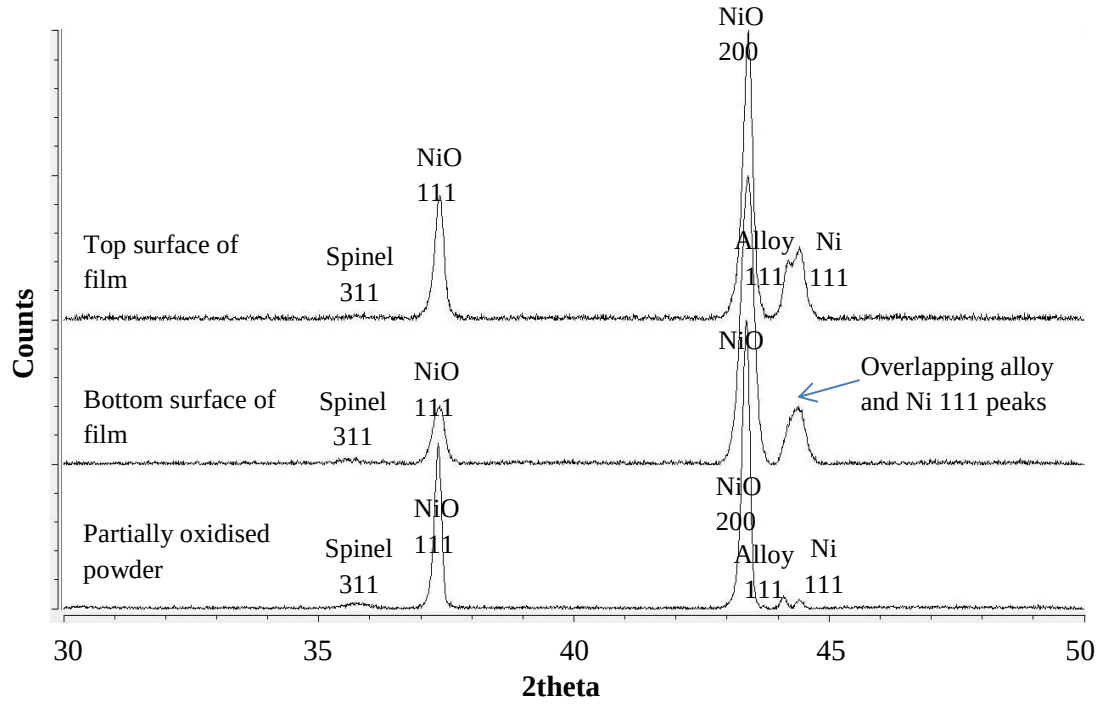

***Figure 5.3**: Diffraction pattern from the partially oxidised powder presented alongside patterns obtained from the top and bottom surfaces of the thick film.*

Also notable in figure 5.3, is how the intensity of the NiO 111 peak relative to the NiO 200 peak changes between the different diffraction patterns. In the pattern obtained from the partially oxidised powder, the NiO peaks intensities are in proportion with ICSD standard [136], suggesting a random orientation of crystals; however, in the thick film diffraction patterns, the increase of NiO 200 peak intensity relative to the NiO 111 peak suggests preferential 200 orientation. Diffraction patterns obtained from the top and bottom surfaces show that the texturing is much stronger near the base of the film, where the material formally sat against the substrate. Seemingly, as material accumulates and surface roughness increases, crystal orientation within the layers deposited later becomes progressively more disordered.

In the diffraction patterns acquired from the thick film, the relative intensity of the spinel 311 peak appeared to decrease. As the NiO and spinel share a close orientation

relationship (see section 4.2.3), the textured growth of the NiO may well influence spinel orientation, resulting in a change to the relative intensity of the spinel 311 peak.

After the film's initial examination, it was ground into a fine powder, and then re-examined using XRD. As figure 5.4 demonstrates, this disrupted the film's texture, giving the NiO crystallites a random orientation comparable with the partially oxidised powder. Also noted, was an increase in the relative intensity of the spinel 311 peak, indicating that the peak's suppression in the thick film diffraction patterns may have been caused by the texture of the material.

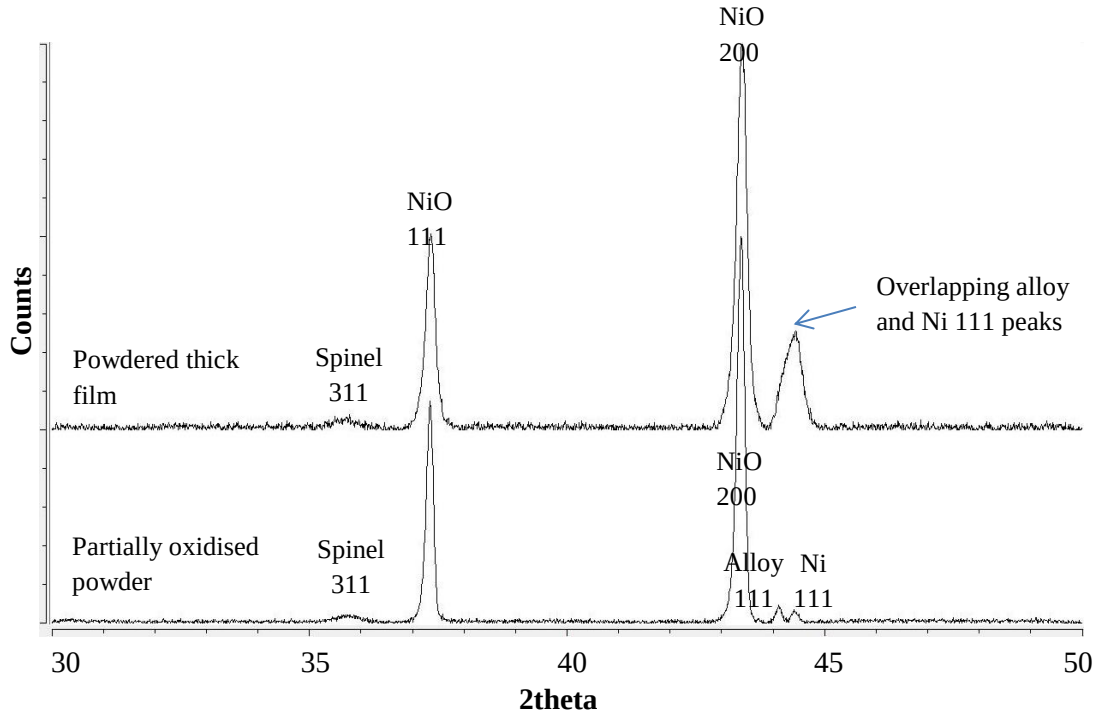

***Figure 5.4**: A comparison of diffraction patterns collected from the partially oxidised powder and the ground thick film.*

5.3 SEM/EDS analysis

5.3.1 Top surface of the film

An SEM examination of the thick film's top surface demonstrated the temperature differences between the impinging particles. Some of the material was spherical, suggesting the particle remained below its melting temperature; while other material

had formed well flattened splats, characteristic of molten state deposition (see SE micrograph in figure 5.5). On the surface of the splats, micro-cracks were visible having likely formed due to thermal stresses (occurring due to differences in the thermal expansivities of the substrate and deposit) and tensile quenching stresses (arising as thermal contraction after solidification becomes restricted by the underlying material) [137]. Scattered across the surface of the film were fine spheroids, a micron or less in diameter, which appeared to have separated from the molten particles during their impact with the surface.

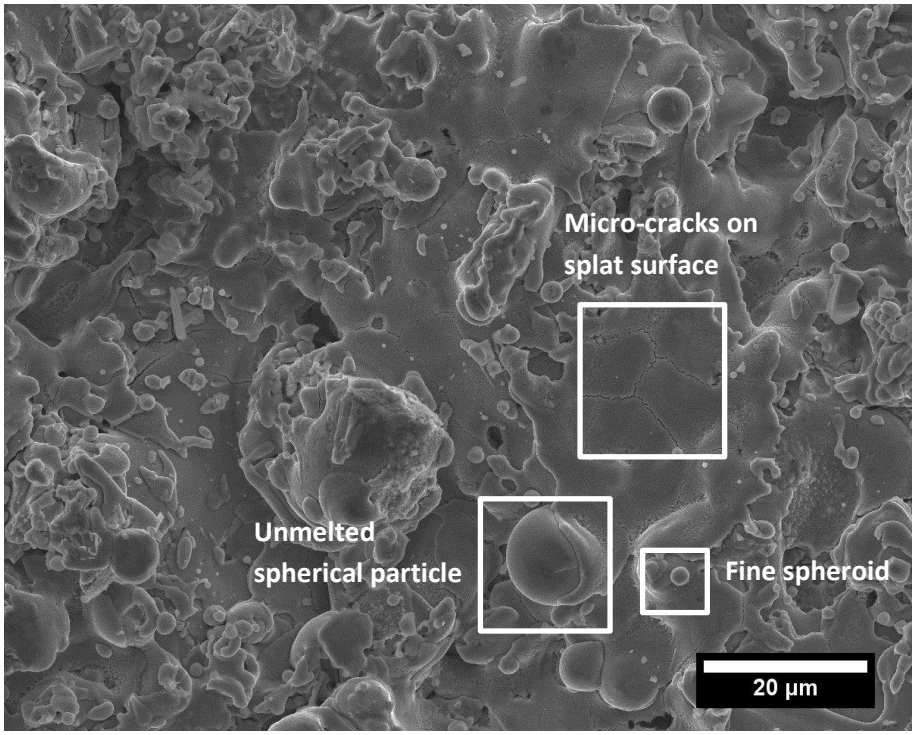

Figure 5.5*: SE micrograph displaying the top surface of the flame sprayed film.*

5.3.2 Fracture surface

The fractured cross section of the thick film displayed evidence of the layered microstructure typically observed within thermally sprayed coatings [135]. As figure 5.6 demonstrates, cracks were found to develop along the splat interfaces, weakening the adhesion between the layers. Separation at the interlamellae boundaries may be caused by gas entrapment during deposition or insufficient wetting of the previously deposited material by the impinging molten particle.

The unmelted spherical particles, observed on the top surface of the film, were also detected within the fracture surface. One such particle, displayed in figure 5.6 (b), can be seen embedded beneath layers of deposited material. At the interfaces between splat and particle, a crack has opened up, suggesting weak adhesion between the melted and unmelted material.

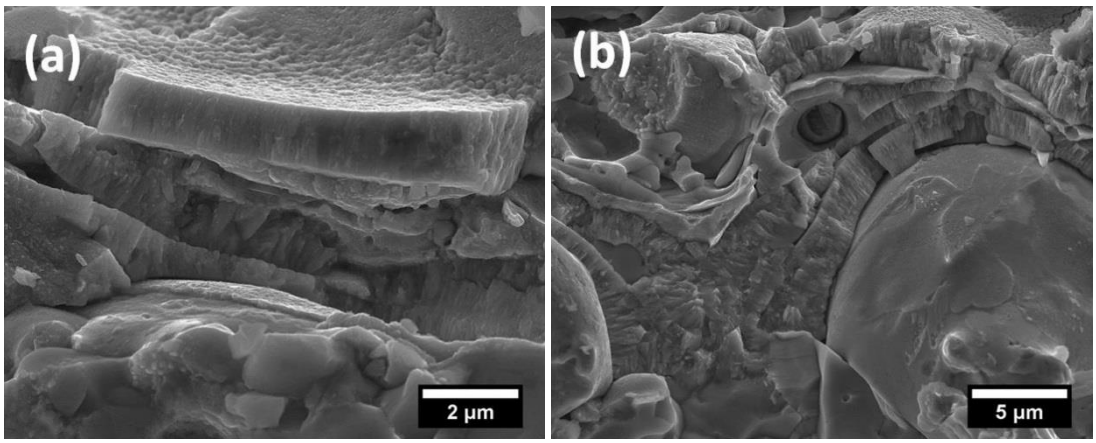

***Figure 5.6**: SE images showing (a) layered deposits and (b) spherical particles embedded within the film.*

Distributed periodically across the fracture surface were C and O rich particles, containing trace amounts of Na, K, Cl and S (see figure 5.7 for EDS measurements). Seemingly formed due to incomplete oxidation of the acetylene gas, these particles would appear to have become entrained in the high temperature gas stream, before being deposited alongside the molten droplets. The presence Na, K, Cl and S within these particles seems likely to have originated from impurities within the acetylene gas.

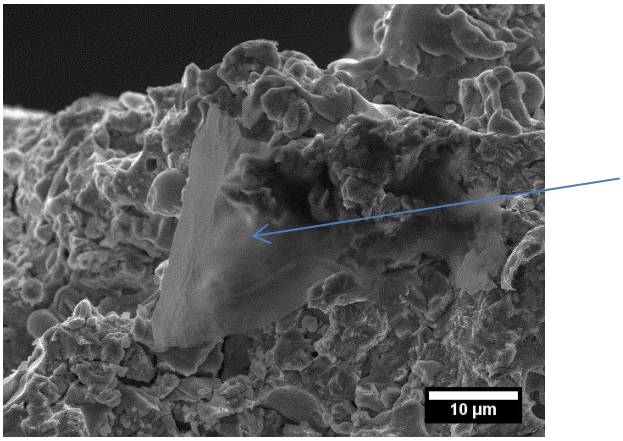

Element	Wt%	At%
C K	46	58
O K	38	35
Na K	3	2
S K	2	1
Cl K	8	3
K K	3	1
Total	100	100

***Figure 5.7**: C and O rich particles discovered within the main body of the thick film.*

5.3.3 Bulk oxide

Another vertical cross section, this time mounted and polished, was next examined using the SEM. Due to the variability in the melting state of the impinging particles, the Cr and Fe doped NiO that formed the bulk of the film, exhibited distinct differences in microstructure. As the micrographs in figure 5.8 (a) and (b) display, the oxide existed in both columnar and equiaxed grain structures.

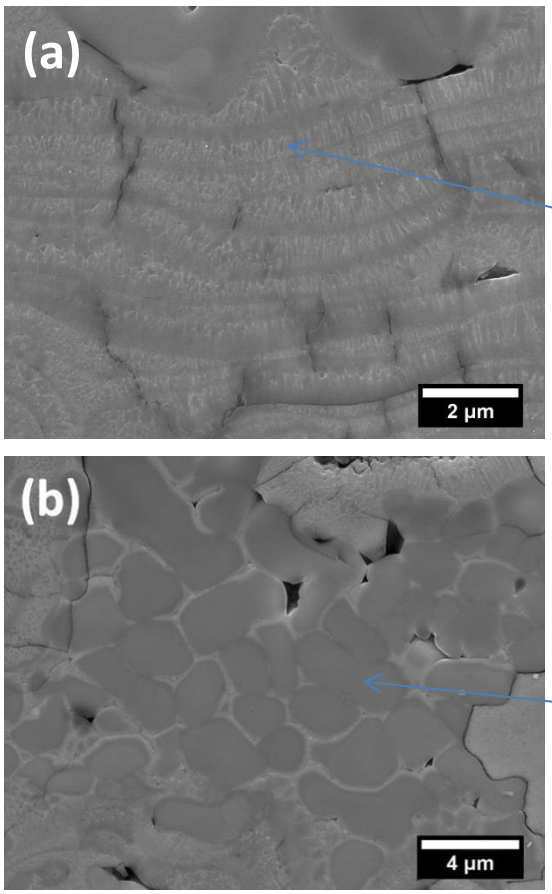

Element	Wt%	At%
O K	21	49
Cr K	14	10
Fe K	8	5
Ni K	57	36
Total	100	100

Element	Wt%	At%
O K	22	51
Cr K	15	10
Fe K	5	4
Ni K	58	35
Total	100	100

***Figure 5.8**: SE images showing oxide of similar chemical composition with (a) columnar and (b) equiaxed grain structures.*

The columnar grain growth, orientated roughly perpendicular to the substrate surface, indicates that oxide particles are liquid during collision with the surface. Upon impact, the molten particle flattens against the surface and nucleation begins heterogeneously at solid-liquid interface. This is followed by the rapid growth of crystals with fast-growth directions orientated parallel to the direction of heat flow [138].

In contrast to the columnar grains, the larger equiaxed grains (typically 1-5μm in width) are grouped in round clusters, indicating much less deformation upon surface contact. This material would appear to have arrived in the solid state and retained some of the characteristics of the oxidised particle grain structure.

Backscattered electron imaging of the contrasting oxide microstructures, revealed particles of higher atomic number, situated on the grain boundaries (see figure 5.9). These particles, which appeared to have precipitated from the surrounding oxide, are discussed further in section 5.4.

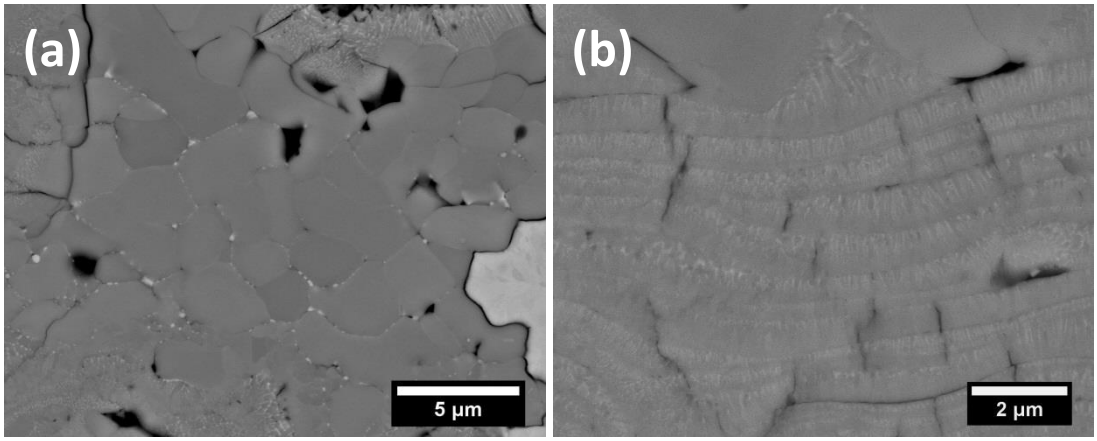

Figure 5.9*: BSE images displaying particles of higher atomic number on the grain boundaries between (a) equiaxed and (b) columnar grains.*

Following the initial examination, the distribution of elements within the dissimilar grain structures was investigated by means of EDS mapping. The maps obtained from an equiaxed region (see figure 5.10), revealed that Ni and O concentrations were relatively constant, while Cr accumulated near the centre of the grains and Fe collected closer to the grain boundaries. The elemental distributions were similar to those acquired from oxidised powder particles, again indicating that this material did not become fully molten during the deposition process. In section 4.2.1, the origins of the elemental concentrations are discussed in further detail.

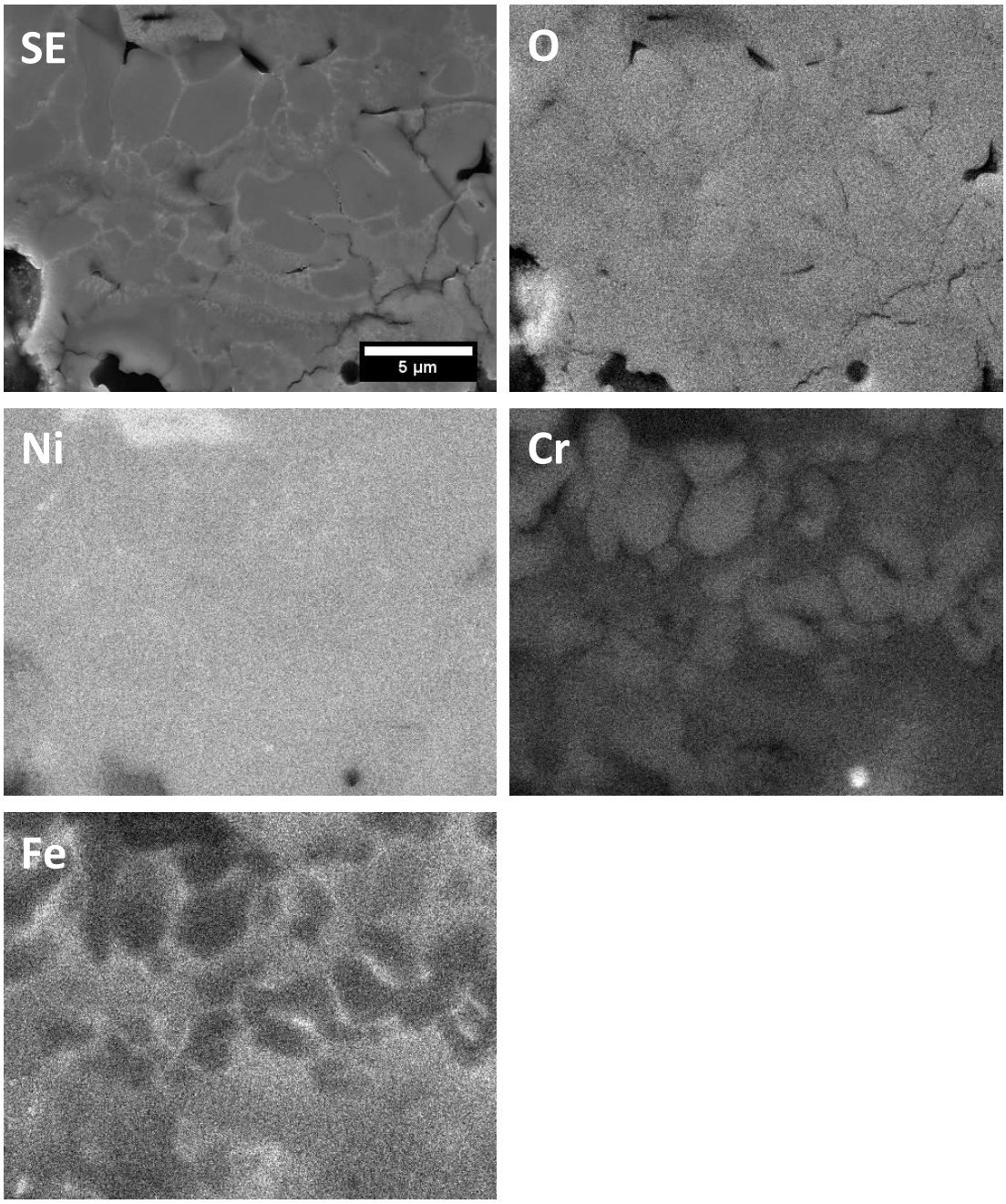

***Figure 5.10**: EDS maps displaying the distribution of elements within the equiaxed grain structure.*

Due to the beam spread within the sample, elemental maps collected from the columnar regions failed to distinguish the finer concentration variations that may have been present within the grains. Consequentially, the elemental maps in figure 5.11 all indicate a relatively uniform distribution of elements across the columnar region.

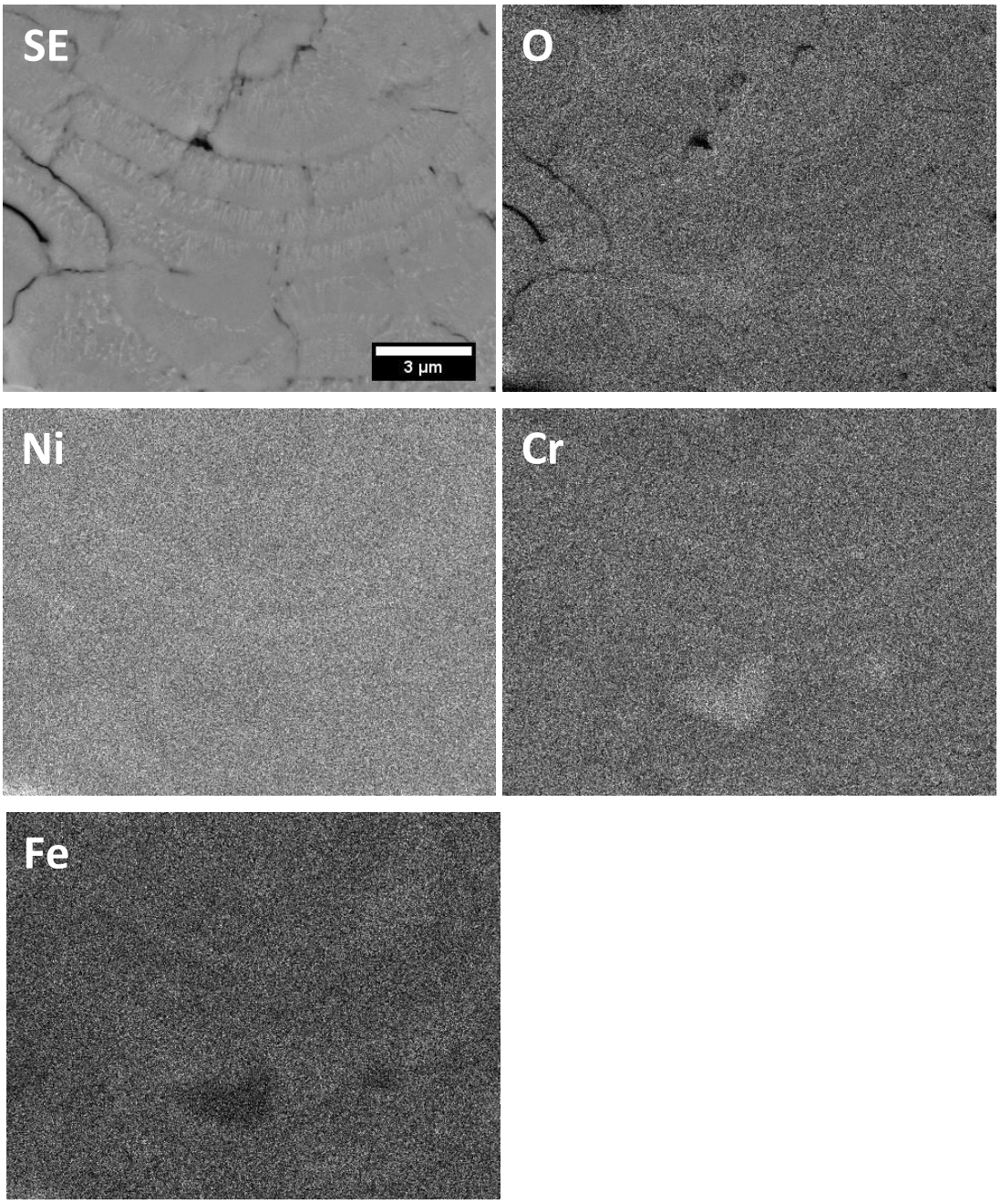

***Figure 5.11**: EDS maps obtained from a columnar grain structure within the thick film.*

Bottom surface

After removing the substrate to expose the base of the thick film, it was possible to examine the material from a bottom-up perspective. When viewed from this angle, the majority of the doped NiO presented the small, equiaxed grains displayed in figure 5.12. This fine grain structure, which is similar to the chill zone at the edge of a casting [139], likely developed as heat loss to the substrate increased the driving

force for nucleation. After the heterogeneous nucleation of these crystals, favourable orientated crystals likely grew parallel to the direction of heat flow, producing the columnar structures observed within the vertical cross section.

The prevalence of the fine grain structure, and apparent absence of the larger equiaxed grains, suggests the successfully deposited doped NiO was in a liquid state during impact. This indicates that the harder, solid state material may have experienced lower adhesion rates when deposited directly onto the enamelled substrate. A higher proportion of molten material solidifying on the substrate may have produced the increase in directional grain growth, detected at the base of the film during XRD examination.

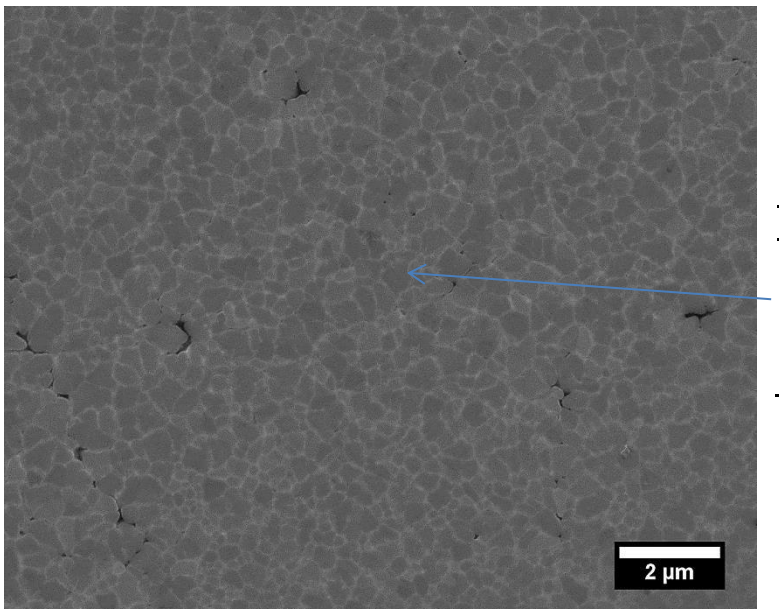

Element	Wt%	At%
O K	22	50
Cr K	15	10
Fe K	5	4
Ni K	58	36
Total	100	100

***Figure 5.12**: Fine, equiaxed grains formed on the bottom surface of the thick film.*

5.3.4 Metallic material

Bonding between metallic particles and oxide matrix

As discussed in section 5.1, the impinging metallic particles experienced varying levels of deformation. Due to variations in temperature and velocity, some particles flattened upon impact while others retained a more spherical appearance. This variation in deposition conditions appeared to influence the strength of bond between the metallic material and the surrounding oxide matrix. As figure 5.13 demonstrates,

the rounder, unmelted particles formed weak bonds, with cracks commonly opening up along the interface between metal and oxide splat. This lack of adhesion may be attributed to a couple of factors: the geometry of the unmelted particle causing poor contacts with the nearby material, and the lower temperature of the metal limiting chemical bond formation.

The molten particles that formed well flattened splats upon impact seemed to form better bonds with the nearby material. The cracking which was prevalent along the perimeter of the more spherical particles was not as noticeable around the edges of the splats. Due to the higher temperatures, these metallic particles reacted more readily with the ambient oxygen, and often developed an accompanying layer of oxide. When imaged using backscattered electrons, this newly formed oxide appeared darker than the doped NiO matrix due to its lower average atomic number (see BSE image presented in figure 5.13).

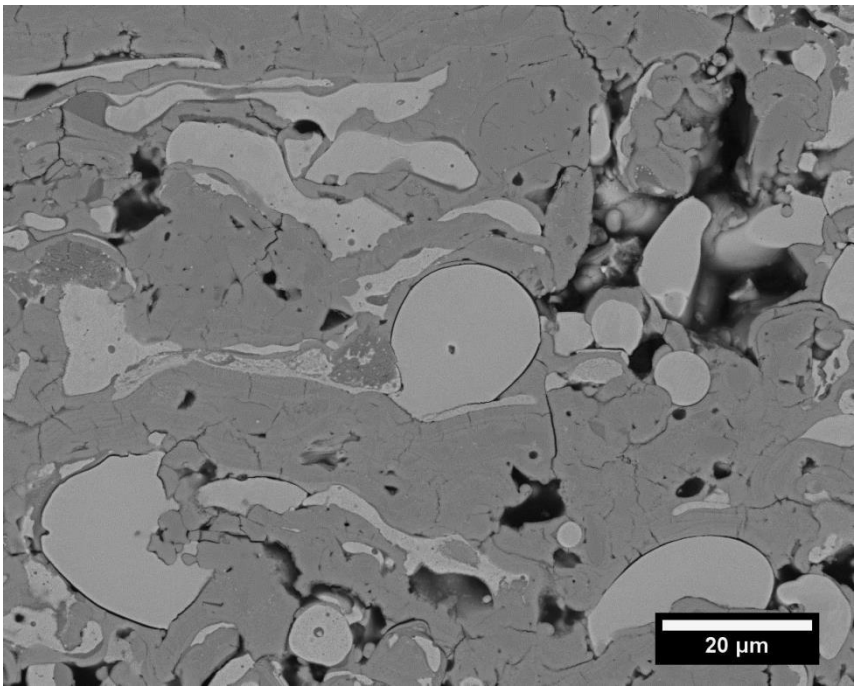

***Figure 5.13**: BSE image showing metallic particles embedded with doped NiO matrix.*

Variability in metallic splat composition

During the optical examination of the film, a slight difference between the colours of the metallic particles was noticed. While the majority appeared white, a few were a

contrasting shade of light grey (see optical micrograph in figure 5.14). To discover whether this difference stemmed from a compositional variation, the same region was analysed using EDS.

The EDS analysis, presented in figure 5.14 (b), confirmed a compositional difference between the dissimilar metallic regions. Readings from the white metallic areas conformed to the manufacturer's chemical analysis, while those from the light grey regions had elevated levels of Si. Not unsurprisingly, the compositional differences identified in the gas atomised alloy (see section 4.1.1) remained present within the thick film.

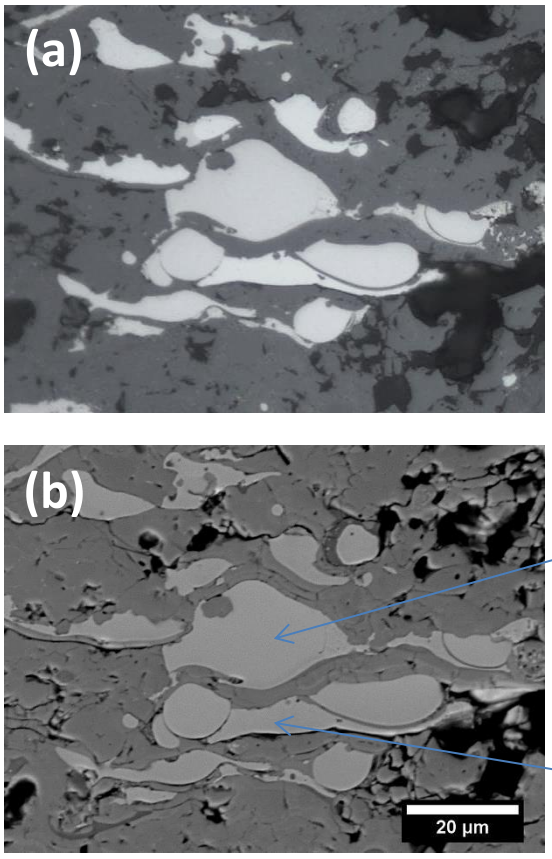

Element	Wt%	At%
Si K	6	11
Cr K	8	8
Fe K	3	3
Ni K	83	78
Total	100	100

Element	Wt%	At%
Cr K	13	15
Fe K	9	9
Ni K	78	76
Total	100	100

***Figure 5.14**: (a) Optical micrograph showing a colour difference between the metallic particles. (b) EDS readings obtained from the same metallic particles.*

Microstructure of metallic splats

The metallic splats, having experienced much higher temperatures than the unmelted particles, reacted with the ambient oxygen and developed more complex microstructures. Two common features of these formations were the lower Z

particles distributed within a metal splat, and higher Z particles dispersed within an outer oxide shell. Figure 5.15 displays an example of this microstructure, imaged using backscattered electrons.

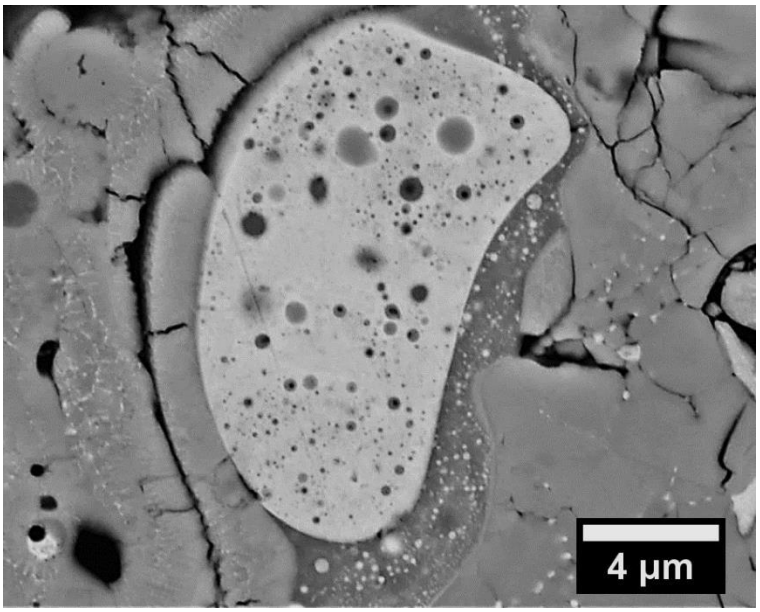

Figure 5.15*: BSE image showing (a) spherical oxide particles within the metal splat and (b) fine metal dispersoids within the oxide outer shell.*

Elemental maps obtained from a metal splat and surrounding oxide, showed that Fe and Cr accumulated within the oxide shell, while Ni was concentrated within the splat (see figure 5.16). This suggests that during deposition the more readily oxidised Fe and Cr [132] diffused from the alloy to react preferentially with available O, causing a depletion of alloying elements within the metal splat.

Due to the beam spreading within the sample, the majority of the submicron dispersoids were undistinguishable in the elemental maps. However, the small number of larger dispersoids that exceeded the detection limits, gave an indication of the elements likely concentrating in the finer particles.

Within the metal splats, the O concentration map showed an accumulation of O within the particles of lower atomic number, suggesting they were oxide particles. The formation of these particles could be attributed to one of the following mechanisms. O dissolved within the molten alloy in-flight before forming oxide phases during cooling as O solubility decreased [140]. Another possibility is that

oxide formed on the molten particle's surface is broken up and redistributed within the particle by convection currents generated through high velocity gas flow [16].

Inside the outer oxide shell, the elemental distribution maps indicated the higher Z particles were rich in Ni and contained significantly less O than the neighbouring oxide. The formation of these dispersoids may occur during the cooling of the surrounding oxide, as the solubility of Ni decreases.

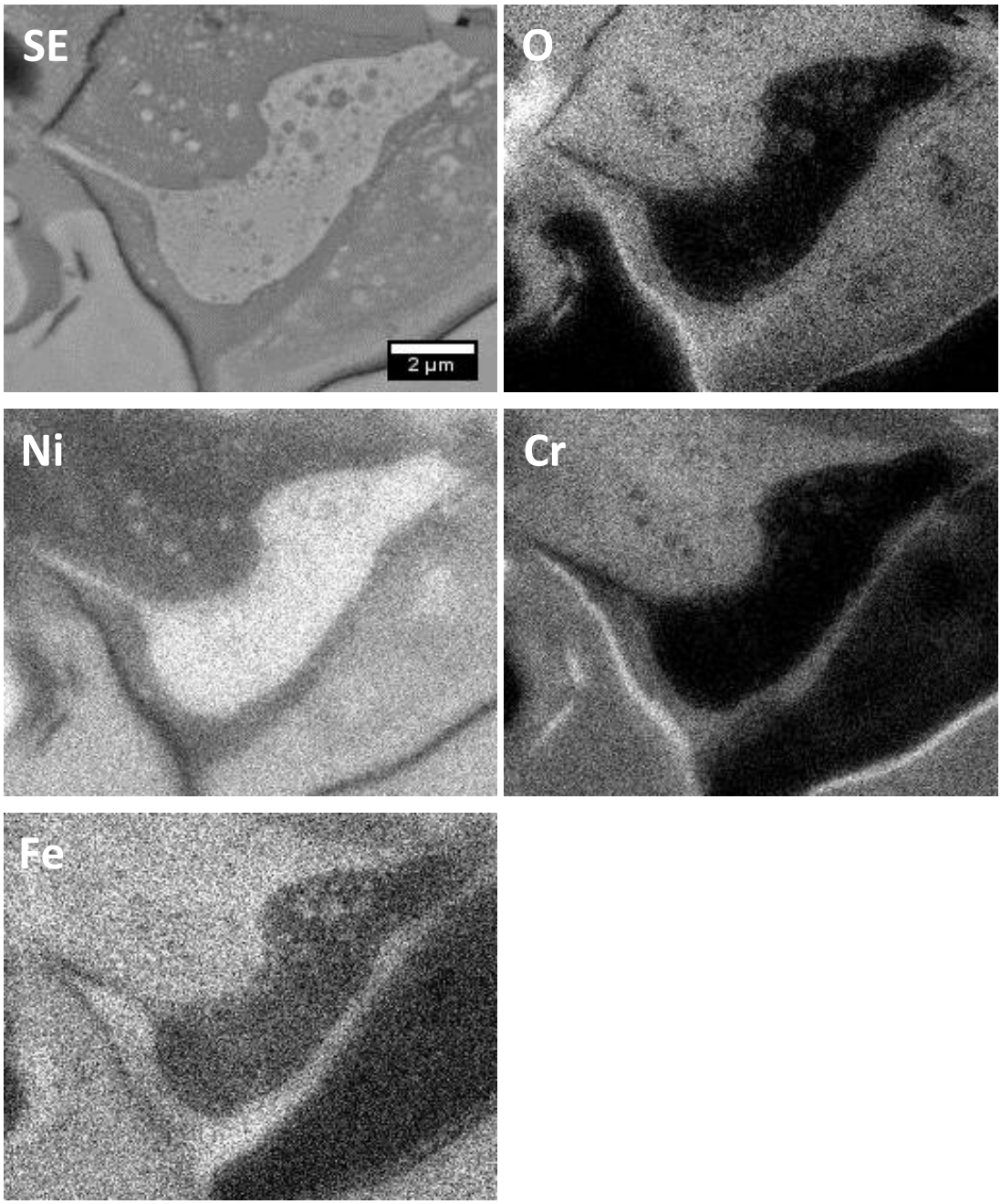

Figure 5.16*: EDS elemental distribution maps obtained from the metallic splat and the accompanying oxide shell.*

On first appearance, the metallic particles within the oxide shells appeared randomly distributed; however, when cross sectioned at the correct angle an ordered structure was observed. As figure 5.17 shows, metallic particles appear to have precipitated at regular intervals between the oxide during solidification. This structured formation which appears to support the previous hypothesis, is discussed in greater detail during the following TEM investigation.

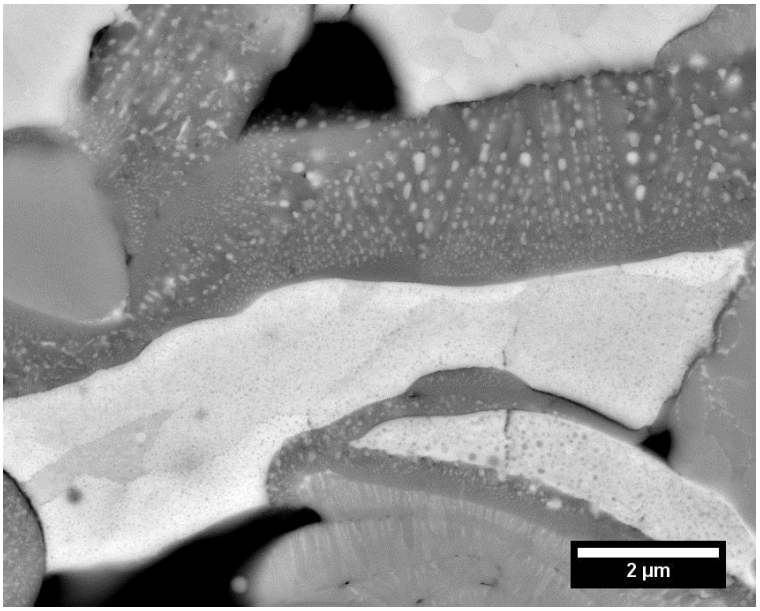

Figure 5.17*: BSE image showing aligned columns of metallic particles within an oxide shell.*

5.4 TEM/STEM analysis

To further examine the new phases and microstructures produced during flame spray deposition, thin foil specimens were prepared for TEM/STEM analysis using a FIB. During the preparation of the initial TEM specimens, the entire FIB extraction was thinned to electron transparency, leaving the samples prone to breakage (see figure 5.18 a). To increase the robustness of the cross sections, subsequent samples were only thinned to electron transparency in select areas of interest; additionally, the specimens were secured to the Cu TEM on two sides rather than just one (see figure 5.18 b).

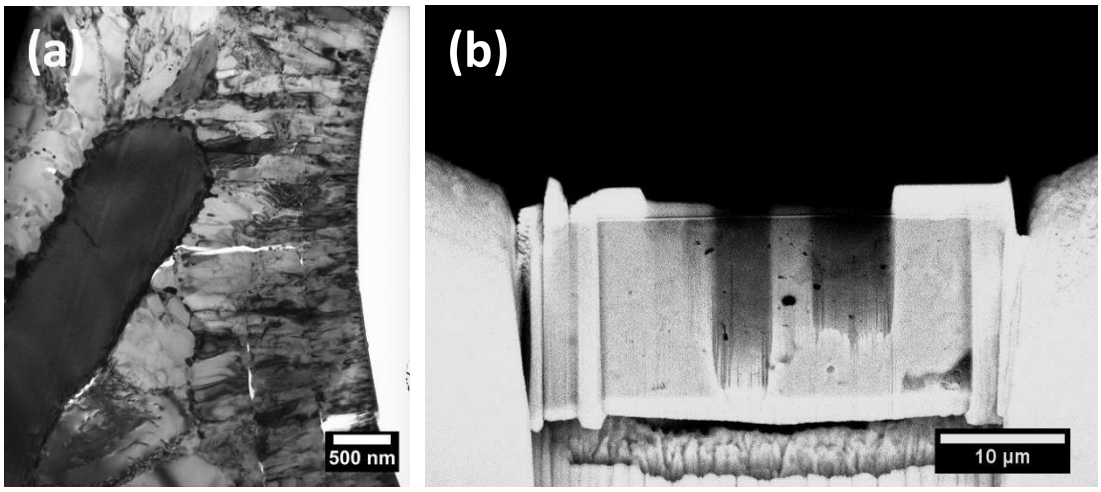

***Figure 5.18**: (a) BF TEM image showing FIB specimen which has fractured along the curved surface. (b) SE image displaying a cross section thinned to electron transparency in two select regions.*

5.4.1 Bulk oxide

As observed in the SEM specimen, the doped NiO within the thin foil specimens exhibited contrasting microstructures. Fully molten material flattened upon impact and developed the fine columnar grain structure displayed in figure 5.19 b, while the solid state material deformed less upon impact and exhibited the larger equiaxed grains shown in figure 5.19 a. As noted during the SEM investigation (see section 5.3.4), particles of higher average atomic number were located along the grain boundaries. Initial EDS spot analysis suggested the particles contained a high concentration of Ni.

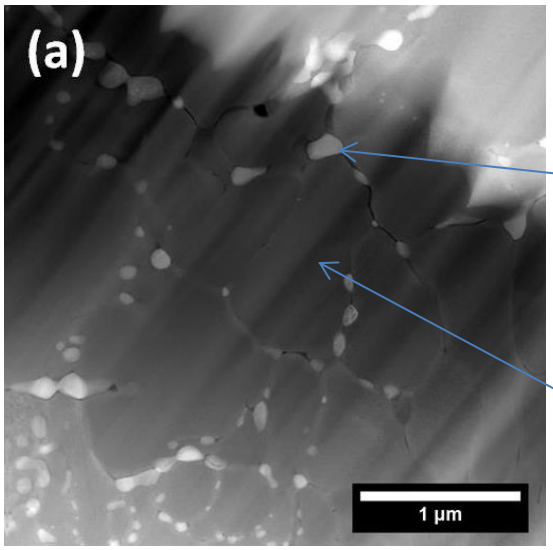

Element	Wt%	At%
O K	5	16
Cr K	1	1
Fe K	2	2
Ni K	92	81
Total	100	100

Element	Wt%	At%
O K	21	49
Cr K	12	9
Fe K	8	5
Ni K	59	37
Total	100	100

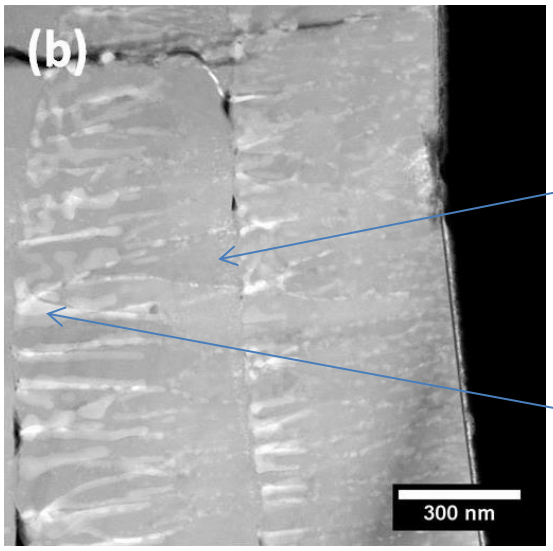

Element	Wt%	At%
O K	21	49
Cr K	14	10
Fe K	8	5
Ni K	57	36
Total	100	100

Element	Wt%	At%
O K	11	31
Cr K	1	1
Fe K	5	4
Ni K	83	64
Total	100	100

***Figure 5.19**: HAADF images displaying (a) equiaxed and (b) columnar grain structures.*

Equiaxed grain structure – EDS analysis

The elemental distribution maps acquired from equiaxed grains within the TEM specimen correlated with those previously obtained from similar structures in the SEM specimen (see section 5.3.4). Within the grains, the Ni and O concentrations were constant, while Cr accumulated at the centres and Fe collected around the grain boundaries (see figure 5.20). As discussed in section 4.2.1, this uneven distribution of Cr and Fe suggests the material was cooled under non-equilibrium conditions. Cr, having higher melting temperature than Fe, enriches the centre of the grains, which

solidify first. The remaining liquid becomes concentrated in Fe, which solidifies later near the edge of the grain.

Agreeing with the initial spot analysis, the elemental distribution maps suggested the boundary particles contained a high concentration of metallic Ni, with depleted levels of alloying elements. These particles may originate from the compositionally similar metallic material, located between the dendritic formations in the oxidised powder (see section 4.2.1).

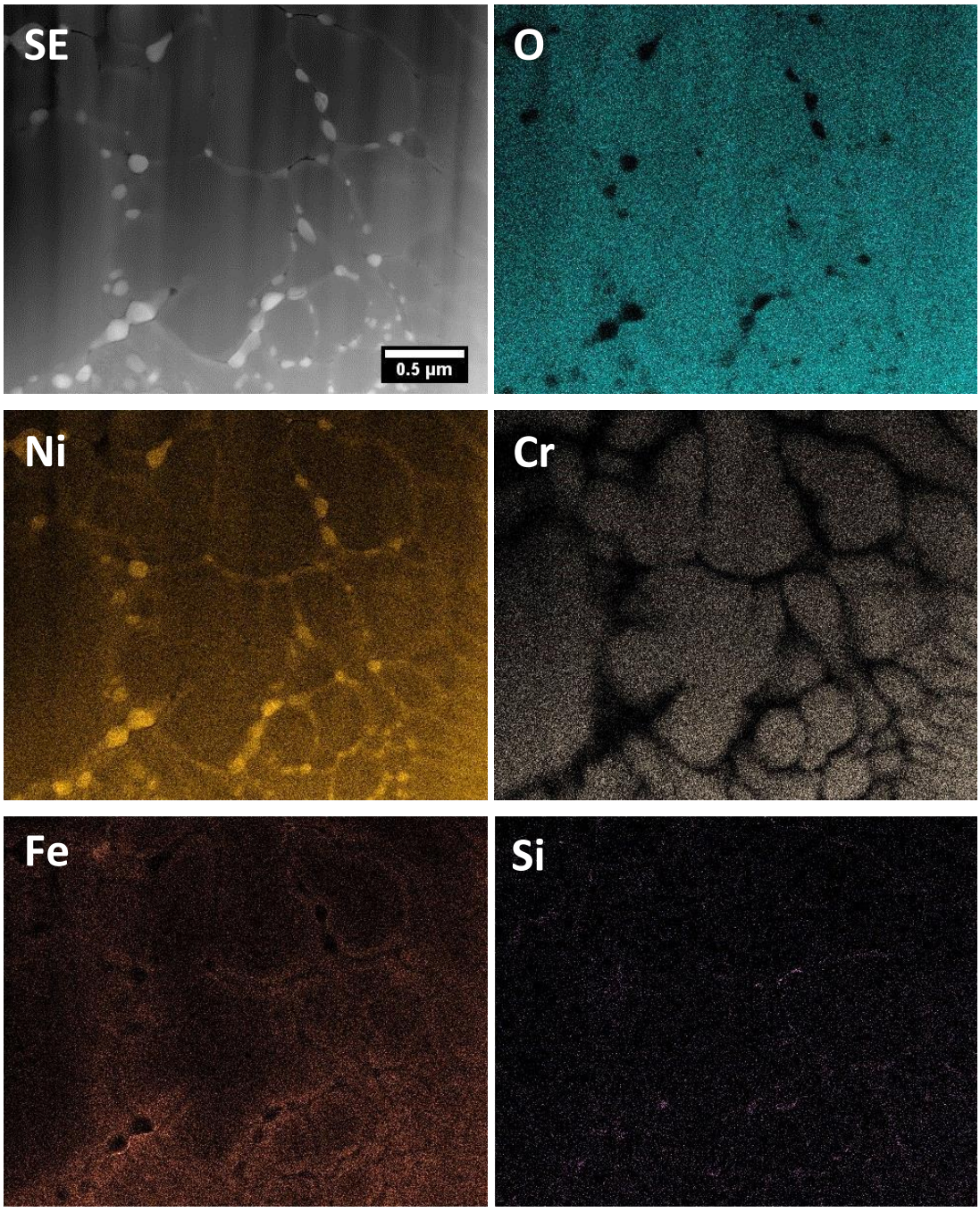

***Figure 5.20**: Elemental maps obtained from equiaxed doped NiO region.*

Equiaxed grain structure – electron diffraction

Analysis of the oxidised powder particle revealed the spinel and NiO phases have complimentary cubic structures, which enables the spinel precipitates to grow topotactically within the NiO. This orientation relationship was reflected by the diffraction patterns obtained from the two phase material, which display a well-defined series of spots as opposed to a set of diffraction rings (see figure 4.24). Since

the lattice parameter of the spinel is approximately twice that of the NiO, the spinel reflections within these patterns have half the spacing of the corresponding NiO reflections.

When equiaxed grains within the thick film specimen were similarly examined, electron diffraction patterns revealed variations in the levels of spinel precipitation. This dissimilarity is demonstrated in figure 5.21 a, which compares contrasting SAD patterns obtained from compositionally similar grains, both orientated on the [114] zone axis. The SAD pattern displayed in figure 5.21 b, shows a combination of spinel and NiO reflections, confirming precipitation has occurred. In contrast, the diffraction pattern presented in figure 5.21 a, shows only NiO reflections, indicating that grain is of single phase.

Spinel precipitation within a doped NiO grain is likely influenced by the heat experienced during the dual flame spray procedures. As material can encounter vastly different temperatures during this process, it is possible that some doped NiO may not experience the temperatures required to induce decomposition. This may cause the inhomogeneity amongst the doped NiO grains.

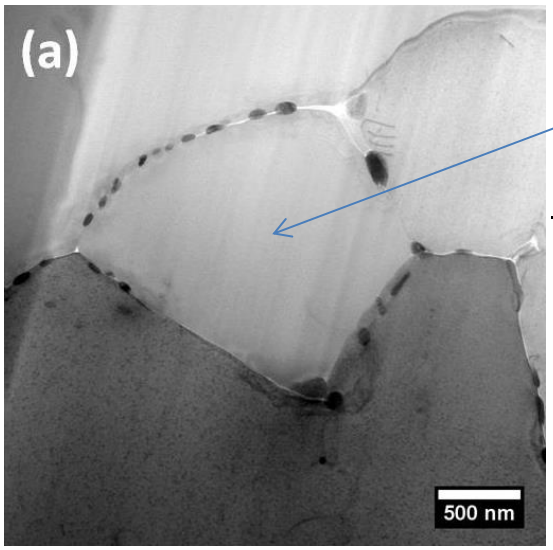

Element	Wt%	At%
O K	23	51
Cr K	14	9
Fe K	6	4
Ni K	57	36
Total	100	100

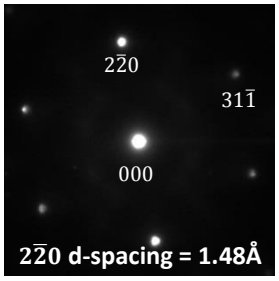

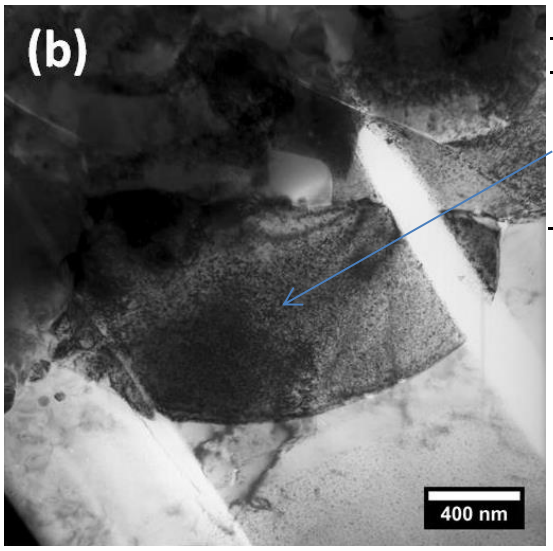

Element	Wt%	At%
O K	21	48
Cr K	16	12
Fe K	5	3
Ni K	58	37
Total	100	100

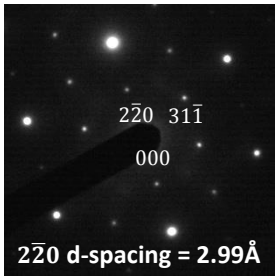

***Figure 5.21**: BF TEM image, with accompanying diffraction pattern and EDS data from (a) a single phase NiO grain and (b) a two phase spinel and NiO grain. Both grains are orientated on the [114] zone axis.*

Equiaxed grains – lattice resolution imaging

Following the electron diffraction analysis, the equiaxed grains were re-examined at high magnification, to enable direct observation of the lattice planes. Supporting the previous findings, the high resolution images revealed structural differences between the equiaxed grains. In some grains, a homogeneous, single phase structure was observed, as figure 5.22 (a) demonstrates. Using FFT image analysis, d-spacings were calculated from these images, which proved consistent with NiO values previously obtained through XRD and electron diffraction. In contrast to this single

phase, other grains were found to contain arrays of particles, with a distinctive double-layer superlattice structure (see figure 5.22 (b)). FFT image analysis, confirmed the d-spacings of the particles and matrix were consistent with previously calculated spinel and NiO values respectively.

The relationship between the adjacent spinel particles in the top left corner of figure 5.22 (b) indicates that spinel particles nucleate randomly within the NiO matrix. Careful inspection of the interface between the particles shows a shifting of the double layered structure during the transition from one particle to the next. This suggests that the particles nucleated on alternate NiO lattice positions.

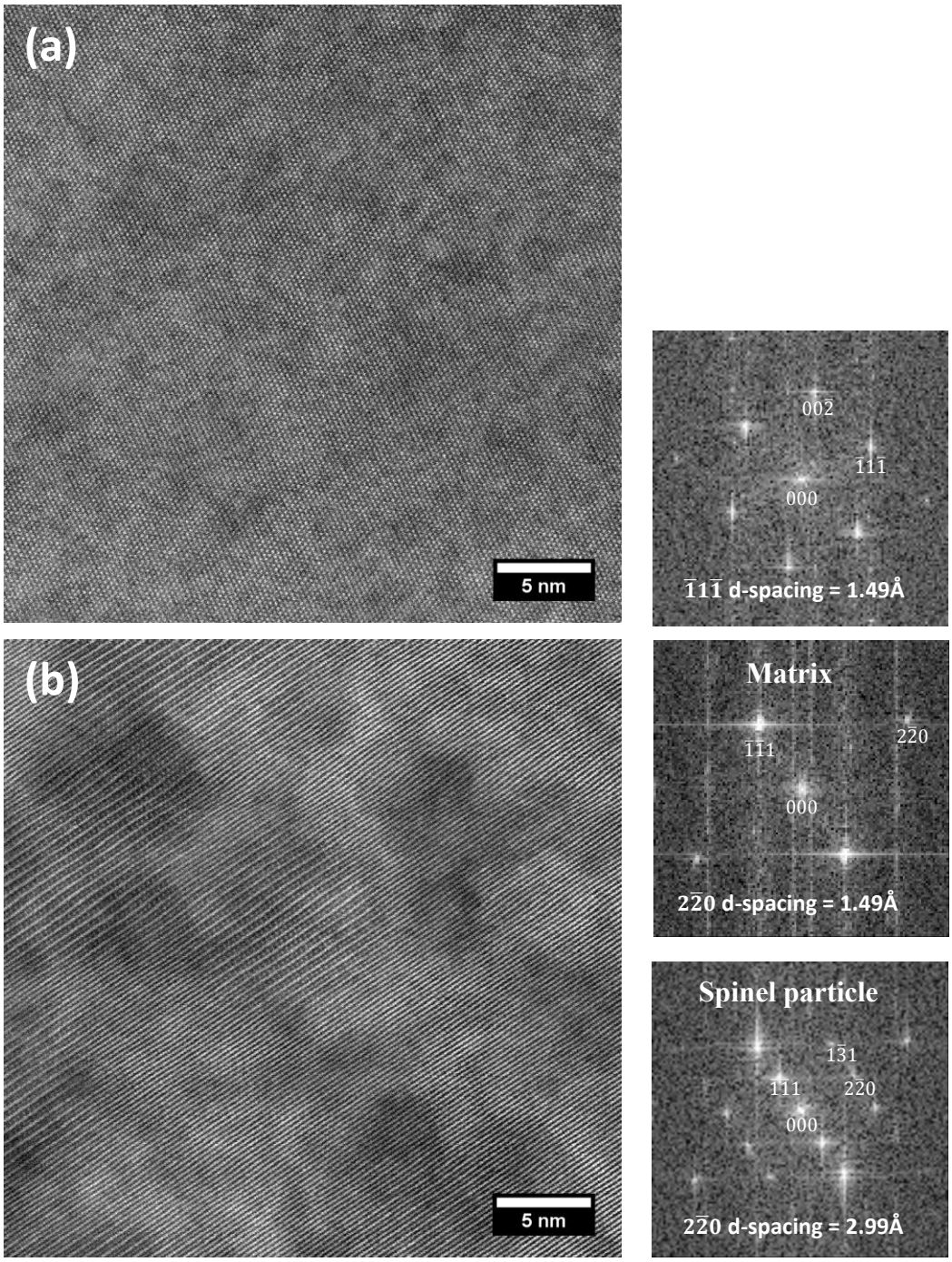

***Figure 5.22**: HAADF images showing (a) a homogeneous single phase NiO orientated in the [110] direction and (b) spinel particles embedded within a NiO matrix, orientated on the [112] zone axis.*

Spinel particles – EDS line scan

The compositional difference between the spinel particles and the surrounding matrix was confirmed using EDS line scans. The results obtained from these scans (figure

5.23) were similar to those previously collected from precipitates in the oxidised powder specimen (see section 4.2.3). Again, as the scan line passed over the spinel particle, Cr and Fe intensities peaked, while Ni fell and O remained fairly constant.

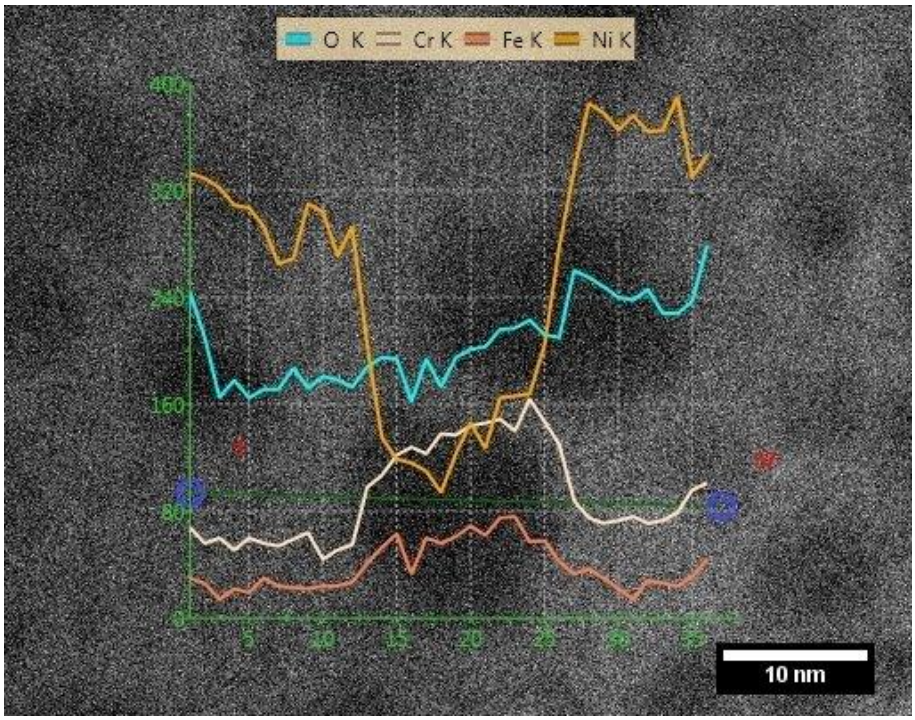

Figure 5.23*: Elemental line scan, represented by the green line intersecting a spinel particle within the doped NiO matrix.*

Equiaxed grain boundary particles – electron diffraction

Typically, the particles decorating the grain boundaries were near-spherical with diameters ranging from 10-100nm. Elemental distribution maps, presented earlier in this section, showed these grain boundary particles contained a high concentration of metallic Ni. When analysed structurally, using convergent beam electron diffraction, the diffraction patterns obtained proved consistent with the FCC crystal structure of lightly alloyed Ni. From the example presented in figure 5.24, a calculated lattice parameter of 3.4Å was calculated, which is within 4% of the value reported for pure Ni [134]. Similarly structured boundary particles would be consistent with the XRD data, which indicated the presence of near pure, FCC Ni within the thick film.

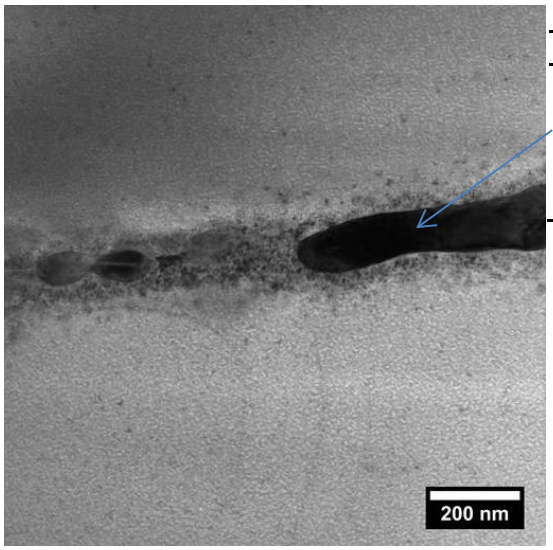

Element	Wt%	At%
O K	1	2
Cr K	1	1
Fe K	2	2
Ni K	96	95
Total	100	100

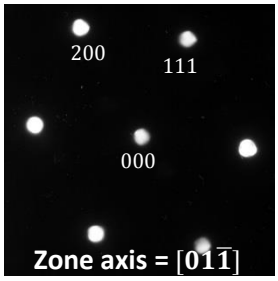

***Figure 5.24**: BF TEM image showing the grain CBED pattern obtained from one of the Ni rich grain boundary particles.*

As figure 5.25 displays, many of the grain boundary particles were intersected by parallel alignments of straight bands. These twinned crystal structures may have occurred due to stresses experienced during the deposition process. On some grain boundaries the twin bands of separate particles appeared to share a common orientation. As twinning takes place on particular planes in specific directions (twinning typically occurs on the {111} planes in the <112> direction in FCC Ni [141]), this suggests that the crystal structures of the particles were also aligned. If correct, this indicates an orientation relationship with the neighbouring oxide, which likely occurred during the particle's formation.

Though the equiaxed regions retained some of the characteristics of the oxidised powder particles, the microstructure is different enough to suggest the material experienced partial melting/softening during deposition. While at these higher temperatures, the doped NiO and Ni rich deposits (located between the dendritic formations [see figure 4.13]) within the oxidised powder particle may mix in a semi-molten state. Subsequently, as the material cools, metal that cannot be incorporated into the NiO crystal structure precipitates at the grain boundaries. Alignment of the particles suggests epitaxial nucleation on the surface of the doped NiO grain.

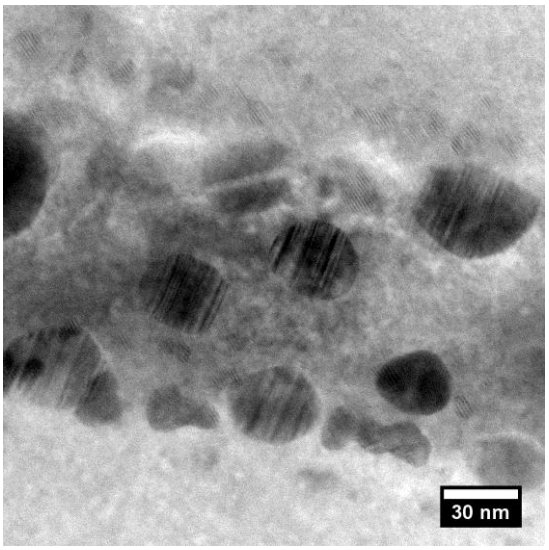

Figure 5.25*: BF STEM micrograph showing twinning within the grain boundary particles. Twin spacings of approximately 0.9-2.1nm were measured.*

Columnar grains – electron diffraction

In contrast to the equiaxed grains, the columnar grain structure formed as completely molten oxide impacting the target surface. Upon this collision the molten material flattened, then nucleation begans heterogeneously at the interface between solid and liquid. This was succeeded by the rapid growth of crystals with fast-growth directions orientated parallel to the direction of heat flow.

The deposition of successive molten particles produced layered formations, as demonstrated by figure 5.26. In the TEM micrograph displayed, three stacked splats are presented in cross section. The interface between the layers is marked by cracks which have opened up along the interlamellae boundaries.

CBED patterns obtained from the columnar grains, proved consistent with the NaCl structure of the doped NiO. The lattice parameters calculated from these patterns agreed with the values formally determined using XRD. In contrast to the equiaxed doped NiO, the grains examined in this particular TEM specimen offered no evidence of spinel precipitation. However, given the small number of grains examined, these results cannot be viewed as representative of the columnar grains in general.

Examination of the layered structure suggested that some columnar grains exhibited a degree of epitaxy with the grains positioned directed below. While collecting diffraction patterns from the grains imaged in figure 5.26 the two adjoining grains displaying high diffraction contrast were observed to have matching orientations. In this case, the grain that nucleated above the first appeared to adopt a similar alignment.

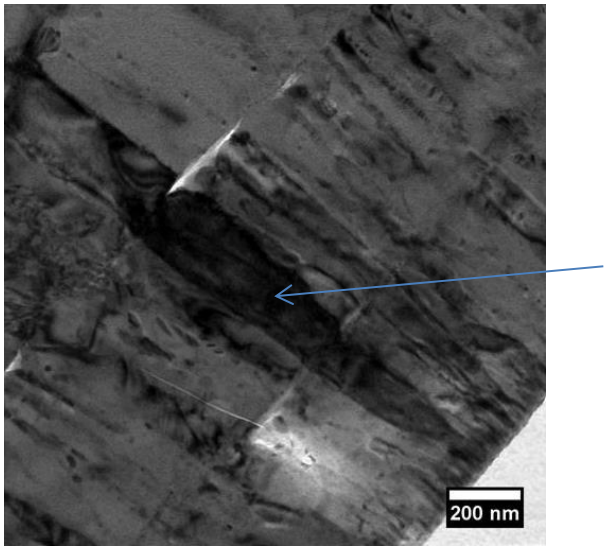

Element	Wt%	At%
O K	21	48
Cr K	12	9
Fe K	8	5
Ni K	59	38
Total	100	100

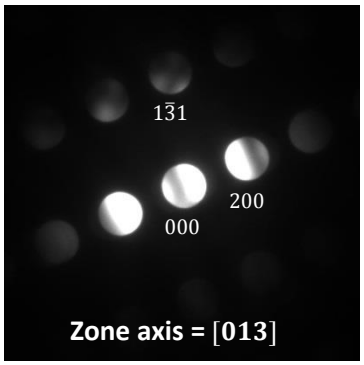

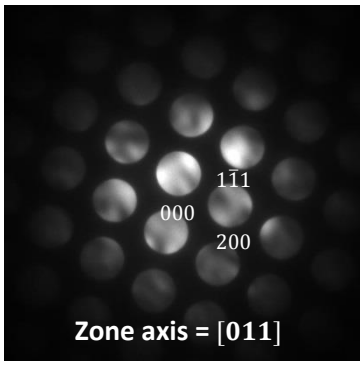

***Figure 5.26**: BF TEM micrograph displaying a columnar grain positioned on zone axis together with diffraction patterns and EDS readings.*

After structural analysis of the columnar grains, the distribution of the main constituent elements was investigated using EDS mapping. As observed within the equiaxed grains, the oxidised regions contained relatively constant levels of Ni and O, while Cr collected at the centre of the grains and Fe accumulated nearer the grain boundaries (see figure 5.27).

As columnar growth progressed towards the top of the splat, the concentration of Fe along the grain boundaries appeared to grow more pronounced. This suggests that as the solidification front advances, Fe concentrates in the liquid before eventually crystallizing near the grain boundaries towards the top of the splat. During this non-equilibrium cooling, the Fe accumulates in the liquid prior to solidification, as it has a lower melting temperature than Cr.

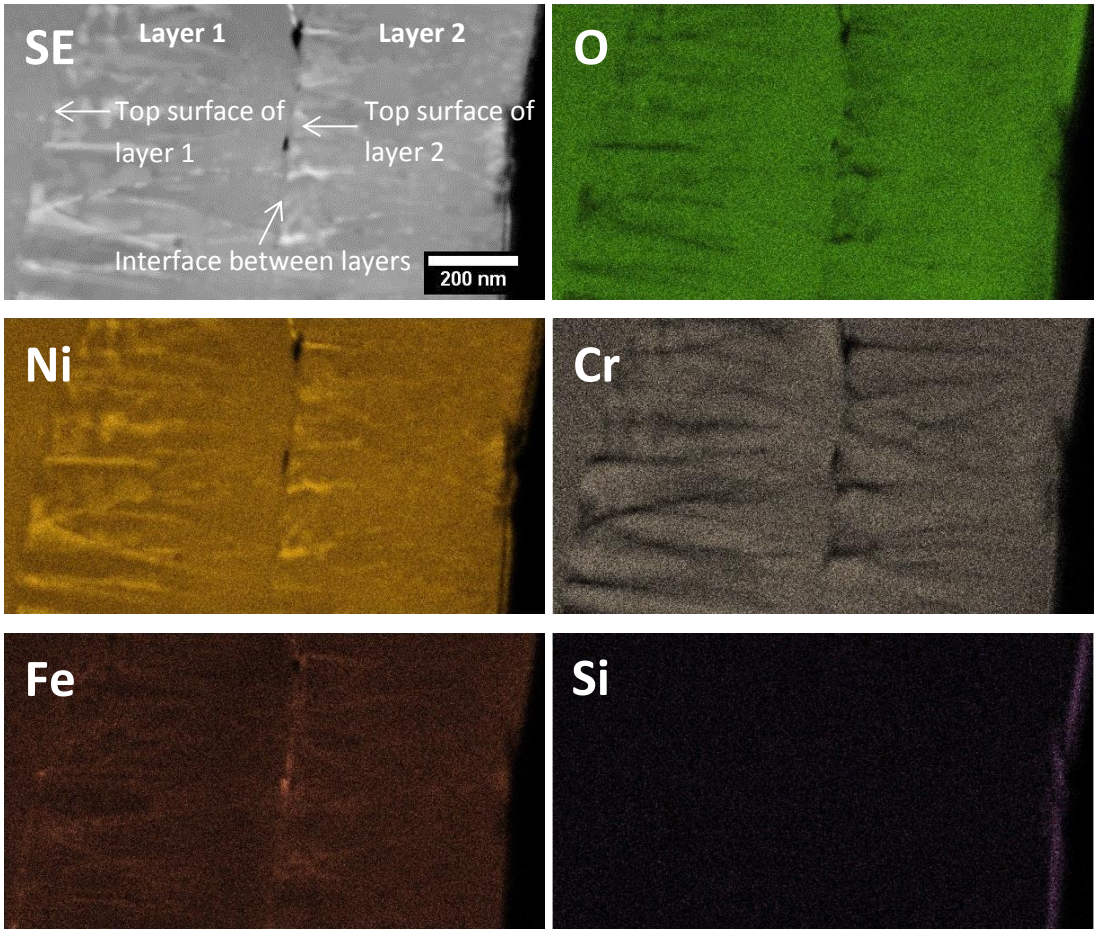

***Figure 5.27**: Elemental concentration maps obtained from the columnar grain formations.*

In addition to the composition variations within the oxide, the elemental distribution maps detected the presence of metallic Ni along the grain boundaries. Behaving in a similar manner to the Fe, the metallic Ni along the grain boundaries increased in concentration towards the top of the splat. This indicates that the molten phase can accommodate more Ni than the solid, causing it to concentrate in liquid ahead of the solidification front. Ultimately as Fe and Cr have a greater affinity for O [132], the Ni precipitates on the grain boundary in the O deficient environment.

5.4.2 Metallic splat microstructure

During the flame spray deposition, the metal powder particles that experienced the higher temperatures reacted with the available O, developing complex microstructures. As the HAADF image below demonstrates, these formations commonly featured lower Z particles dispersed within a metal region, and higher Z particles distributed within the outer oxide shell.

When one of these complex microstructures was mapped using SEM-EDS (see section 5.3.5), the finer details were lost due to electron beam scattering within the bulk sample. STEM-EDS mapping of similar structures within a thin film specimen offered far greater spatial resolution, providing chemical data from the nanoscale features.

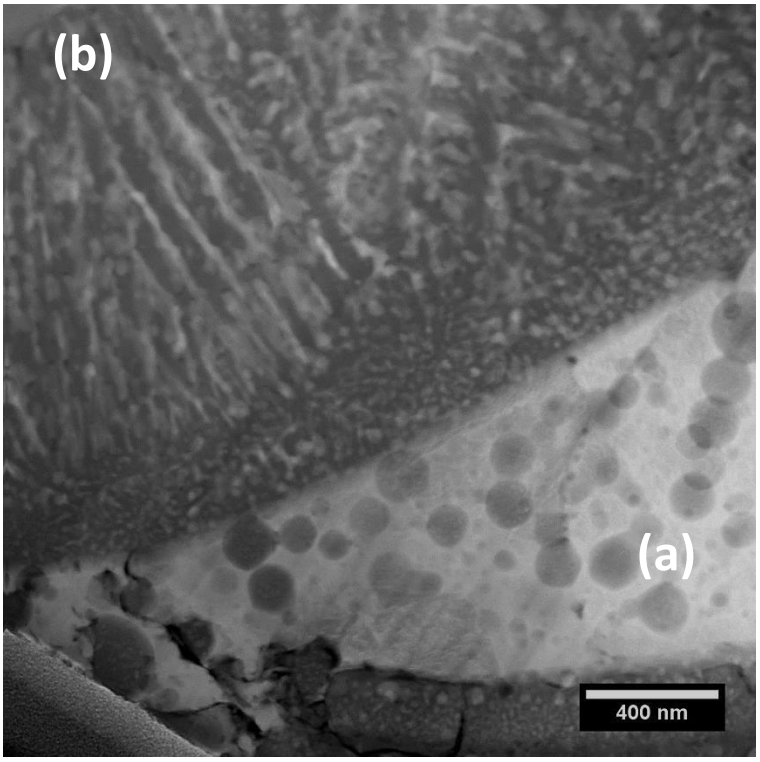

***Figure 5.28**: HAADF image acquired at the interface between (a) a metallic region containing lower Z particles and (b) an oxide shell holding higher Z formations.*

The elemental concentration maps, collected at the interface between the metal splat and outer oxide shell, are displayed in figure 5.29. Within the Ni dominated metallic region, EDS mapping confirmed the presence of oxide particles, containing concentrations of Fe and Cr. Similarly, the elemental distribution maps showed that

Fe and Cr had also accumulated within the oxide of the outer shell. Appearing at regular intervals amongst this oxide were deposits of metallic Ni. These seemed to have precipitated from the molten mixture during cooling as the Fe and Cr reacted preferentially with the available O.

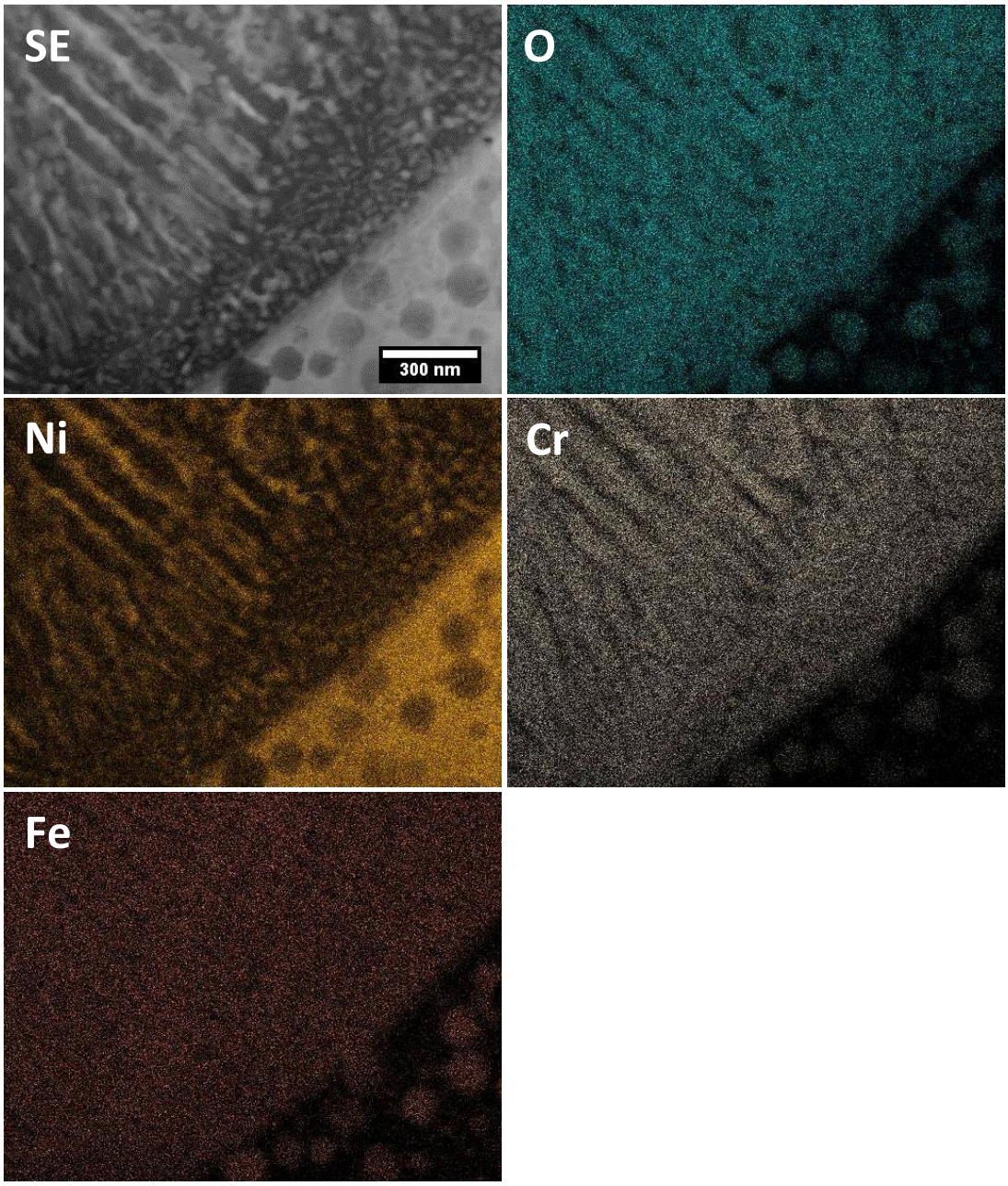

***Figure 5.29**: Chemical concentration maps obtained from the interface between the metallic splat and its oxide shell.*

Possible mechanisms that may have contributed to the formation of these complex microstructures are further discussed in section 4.3.5.

Oxide shell – electron diffraction

The alternating layers of oxide and metallic Ni, which characterised the metal splat's outer shell, were further examined using electron beam diffraction. This examination revealed that the seemingly individual layers were grouped in colonies, with distinct orientations. This is demonstrated by figure 5.30, which shows one such colony positioned on zone axis, displaying much greater diffraction contrast than the surrounding grains.

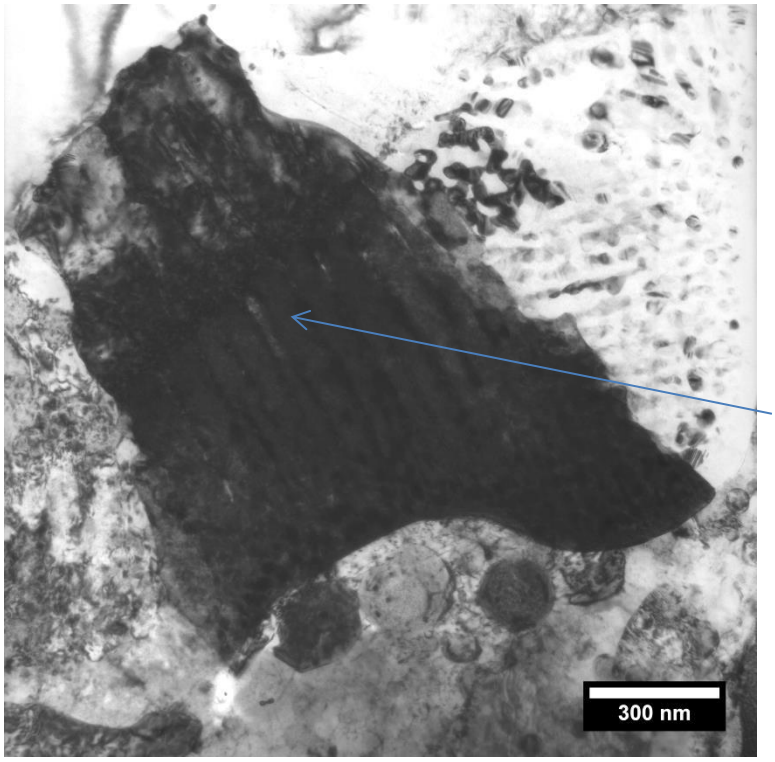

EDS reading from oxide layer

Element	Wt%	At%
O K	32	62
Cr K	32	19
Fe K	11	6
Ni K	25	13
Total	100	100

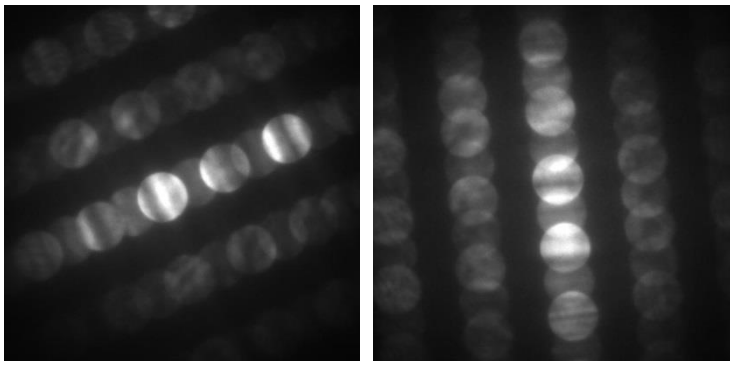

***Figure 5.30**: BF TEM micrograph displaying the mixed metal-metal oxide structure positioned on zone axis together with diffraction patterns and EDS readings.*

Attempts were made to acquire convergent beam diffraction patterns from both the metallic and oxide layers. However, diffraction patterns acquired from the metallic

regions were not discernibly different from those obtained from the oxide region. This could indicate that the metallic layers are extremely fine, and that when the electron beam was focused on these regions a high proportion of the surrounding oxide was being sampled.

Convergent beam diffraction patterns obtained from one of the oxide layers are presented in figure 5.30. EDS readings acquired from this region indicated a ratio of elements consistent with $(CrNiFe)_2O_3$ corundum. However, the diffraction data proved a poor fit with standards in the Karlsruhe chemical database, and so currently these diffraction patterns remain unresolved.

The apparent interconnectivity of the lamellae suggests that this mixed metal-metal oxide structure may form in a similar manner to pearlite [142]. In this scenario, the molten material cools to a eutectic point and Ni begins to nucleate on grain boundaries. During the growth of this phase, the adjacent liquid becomes depleted in Ni and solidifies to form the oxide. Since Ni has lower solubility within the oxide, it is expelled from this region, and enriches the nearby liquid. As a result, another Ni layer nucleates and grows next to the oxide layer. This two phase structure may then grow outwards from the original nucleation point, as Ni diffuses from the growing oxide into to the adjacent Ni platelets.

Chapter 6

High temperature heat treatment of Cr and Fe doped NiO

After exposure to an operating voltage of ~230V AC, the heating elements experience permanent time and temperature dependent resistance changes that caused reductions in the energy efficiency. Following instillation within a tumble dryer, the initial drying cycles (approximately 15mins long) would cause incremental increases to the heating element's resistance before reaching a plateau after about 20 cycles. Measurements obtained by 2DHeat indicated total resistance increases of up to 30% during these initial tumble dryer runs. To investigate the possible causes of this behaviour, samples of the thick film were subjected to a variety of heat treatments before being examined using a range a characterization techniques. This chapter documents how these heat treatments affected the Cr and Fe doped NiO that accounts for the bulk of the thick film.

In this chapter, section 6.1 presents the results obtained from combined XRD and SEM analysis of the thick film, while section 6.2 documents the initial STEM/TEM investigation. Subsequent EELs analysis, examining atomic position of the elements within the NiO and spinel structures, is presented in section 6.3.

6.1 XRD and SEM analysis

6.1.1 Decomposition of Fe and Cr doped NiO

The pseudo-binary Ni-Fe-O and Ni-Cr-O phase diagrams (see figure 6.1), suggest that a metastable Cr and Fe doped NiO should decompose to form more energetically favourable NiO and spinel phases when given the correct heat treatment. In order to induce this effect, specimens of the thick film were subjected to long heat treatments at temperatures (66h at 800˚C) beyond those typically experienced during tumble dryer operation. XRD and SEM were then employed to search for evidence of phase change.

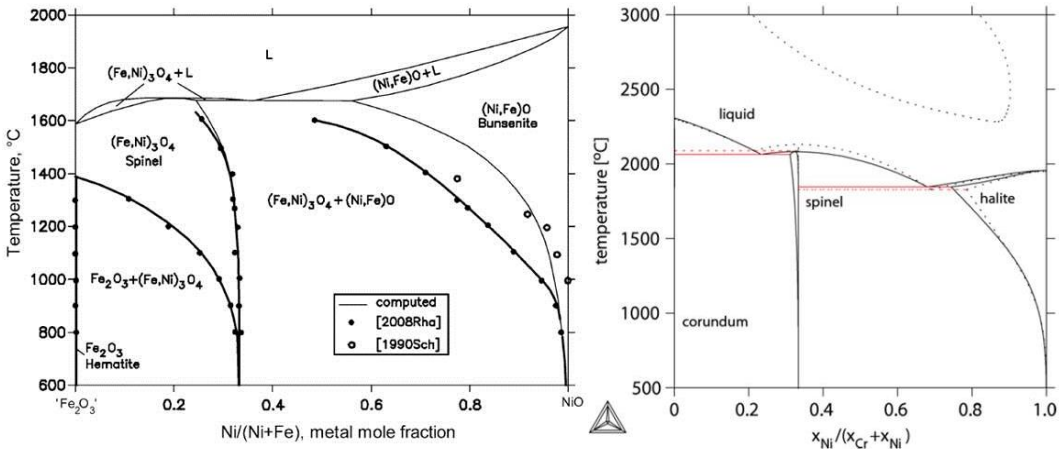

***Figure 6.1**: (a) Fe-Ni-O [56] and (b) Cr-Ni-O [65] pseudo binary phase diagrams.*

Diffraction patterns obtained before and after the 66hr 800˚C heat treatment indicated that the doped NiO was decomposing. Prior to heat treatment the spinel 311 peak was scarcely distinguishable above the background noise; however, following the heat treatment, the height of the spinel 311 peak relative to the NiO 111 and 200 peaks increased notably (see figure 6.2).

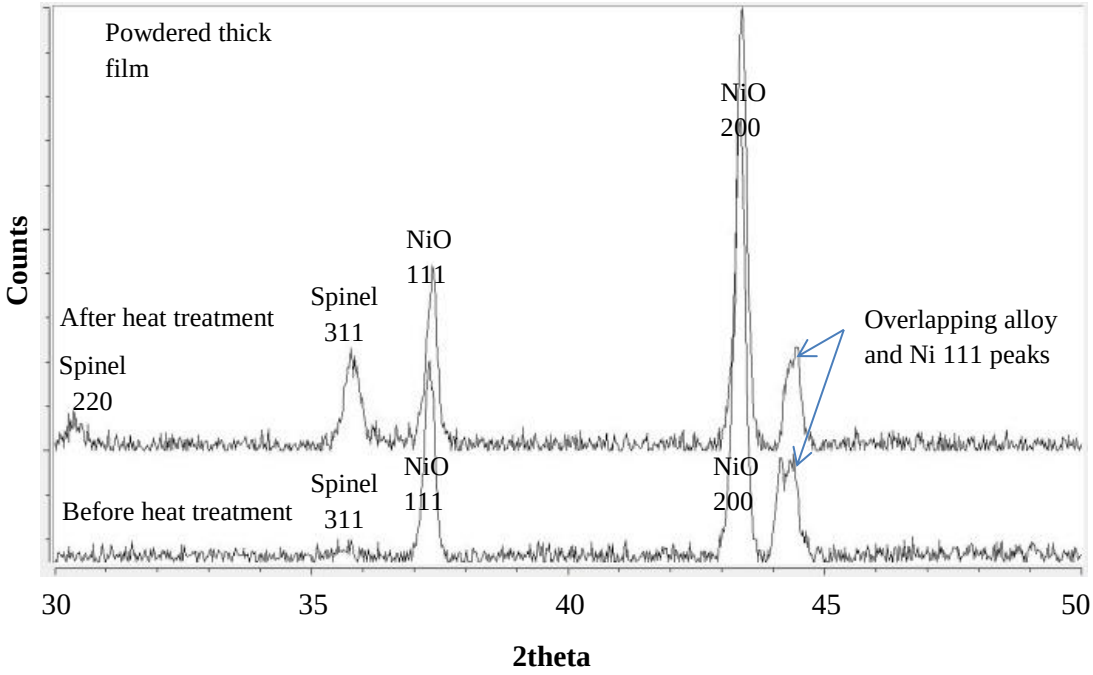

***Figure 6.2**: XRD diffraction patterns obtained before and after heat treatment of a thick film specimen.*

In agreement with the XRD results, SEM imaging of the doped NiO regions revealed a pronounced change in microstructure following heat treatment. Material that

originally looked homogenous (see figure 6.3a) developed a mottled appearance suggesting the presence of two phases (see figure 6.3b).

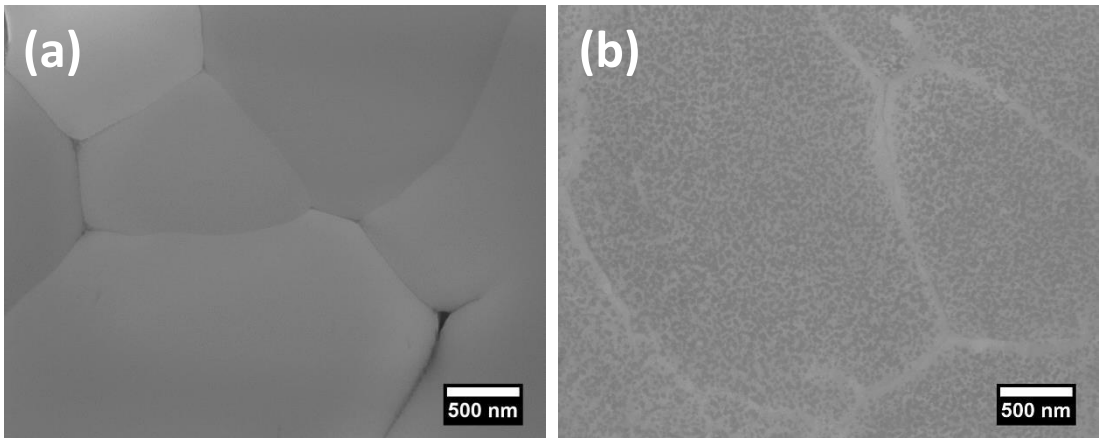

Figure 6.3*: SEM micrographs showing the doped NiO regions in (a) the original condition and (b) following 66h at 800˚C.*

When viewed at higher magnification, ordered arrangements of precipitates became discernible within the heat treated material (see figure 6.4). Given the homogenous nature of spinel nucleation within the doped NiO (see section 5.4.1), these precipitates were most probably the spinel particles in cross section. The alignment of these spinel particles indicates that the orientation relationship observed between spinel and NiO matrix is maintained following the heat treatment.

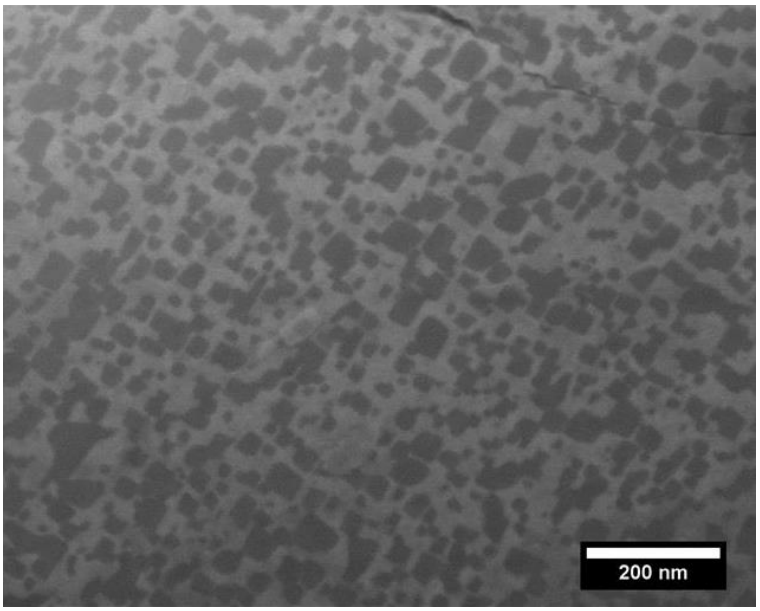

Figure 6.4*: SEM micrograph showing an array of precipitates within the heat treated doped NiO.*

6.1.2 Spinel growth rate at 800˚C

To investigate the growth rate of spinel at 800˚C, a series of 12 XRD readings were taken from a single thick film specimen over a 15h30m time period. Figure 6.5 displays these diffraction patterns, stacked in chronological order and normalised to the NiO 200 peak height. This comparison shows the height of the spinel 311 peak increasing relative to the 200 peaks over the course of the heat treatment.

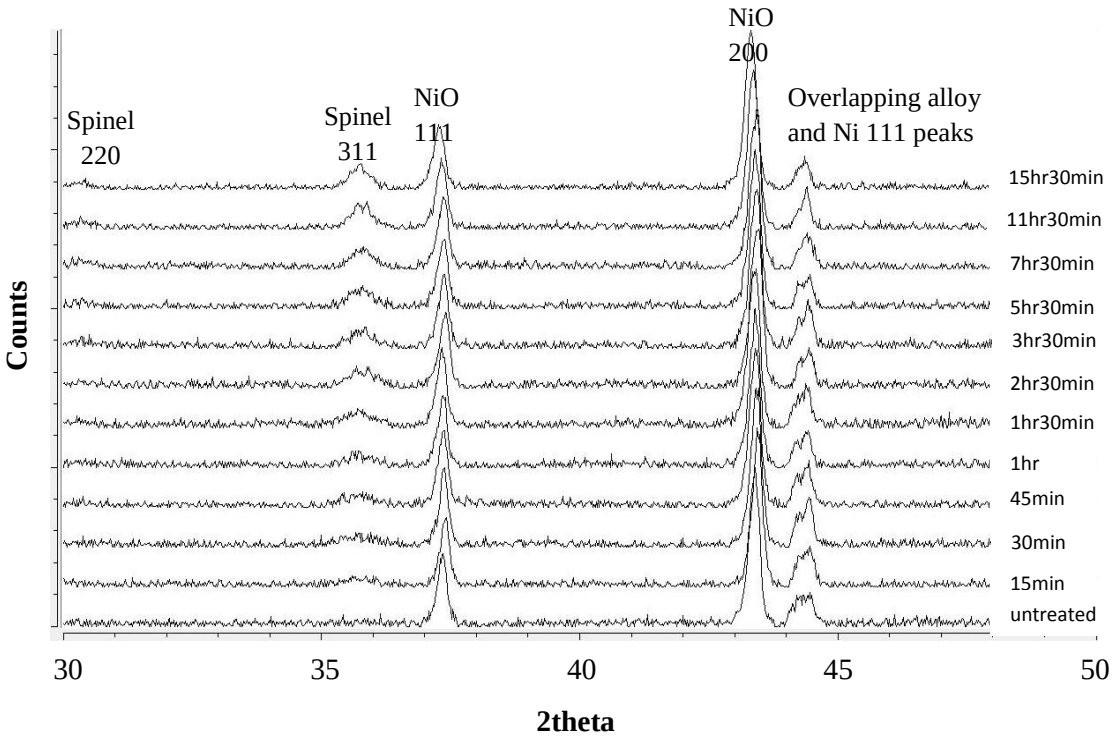

Figure 6.5*: A series of 12 diffraction patterns collected from a single thick film specimen over a 15h30m time period.*

To enable a more direct comparison of the diffraction data, the ratios of the areas beneath the NiO 200 and spinel 311 peaks were plotted against time. The resulting chart, displayed in figure 6.6, indicated that the spinel develops quickly within the first hour before slowing to a reduced growth rate after approximately 2hr30. Initially, while there is an abundance of doped NiO, the spinel growth rate is fastest; however, once diffusion rates and quantity of unreacted material become limiting factors, this growth rate begins to slow.

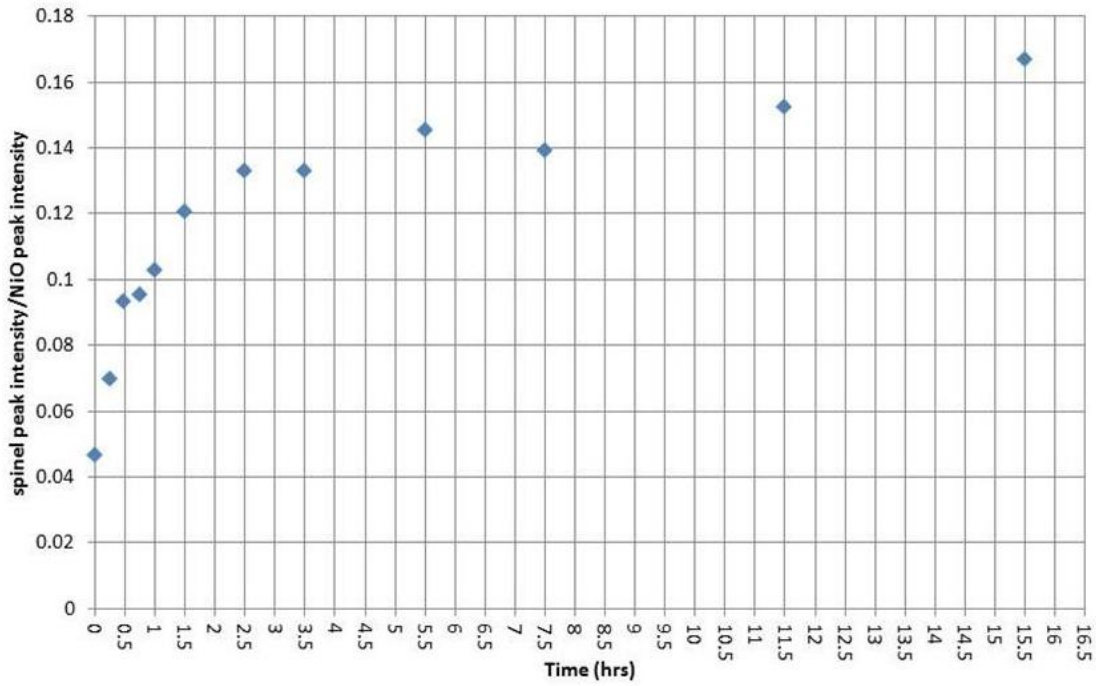

***Figure 6.6**: Graph plotting the ratios of areas underneath the NiO 200 and spinel 311 peaks against time.*

To help describe the kinetics of the phase transformation, the Avrami equation was used to fit a curve to the diffraction data.

$$X = 1 - exp(-Kt^n) \qquad \textit{Equation 6.1}$$

In this equation X is the fraction of material transformed at time *t*, K is the overall rate constant and *n* is the Avrami exponent. This may be rewritten as:

$$ln(-ln[1 - X(t)]) = ln K + n ln t \qquad \textit{Equation 6.2}$$

Which enables the constants *n* and K to be determined from a plot of ln(-ln[1-X]) vs ln(t), as figure 6.7a demonstrates. The Avrami exponent calculated from this plot reflects the nature of the transformation, with values between 1 and 4 representing the number of growth dimensions [143]. For three-dimensional growth an Avrami exponent of ~3-4 is expected; however, from the plot in figure 6.7a a value of 0.6 was calculated. Given that three dimensional spinel growth has been reported during the decomposition of both Fe and Cr doped NiO [82, 83], this model appears to be a poor fit for this particular data.

One possible reason for the inaccuracy of this model is the inhomogeneous nature of the doped NiO within the thick film. As noted in section 5.4.1, some of the doped NiO appeared of single phase while others contained spinel precipitates. During the heat treatment, this means that different regions of doped NiO will decompose at contrasting rates depending upon how much decomposition has previously occurred.

However, as discussed later in this chapter and in chapter 8, the most likely reason for the poor fit to the Avrami equation model is the nature of the transformation. The TEM results show that not all the doped NiO is available for transformation, since the diffusion of Cr and Fe takes place, leaving regions of almost pure NiO which do not transform into the spinel phase.

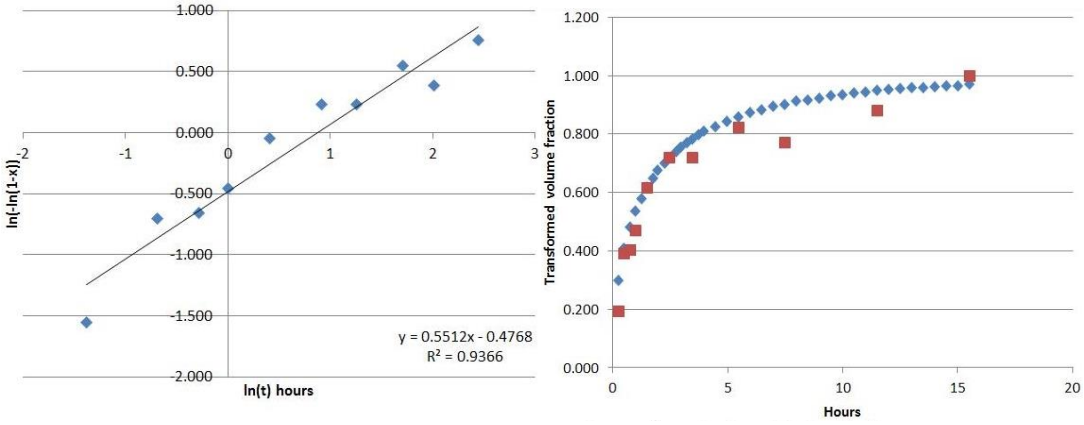

***Figure 6.7**: (a) plot of ln(-ln[1-X]) vs ln(t). (b) Curve fitted to the experimental data.*

To provide visual evidence of the spinel growth detected by the XRD, the SEM was used to examine 6 thick film specimens heated at 800˚C for time periods of 30m, 1h, 2h, 4h, 6h and 12h. In agreement with the XRD results, the mottled appearance characteristic of the phase change was observed in each of the heat treated specimens. As heat treatment time increased the spinel particles, which appear darker in the SE images below, appeared to coarsen. In an example of Ostwald ripening, numerous smaller crystals appeared to dissolve to fuel the growth of a smaller number of larger particles (see figure 6.8).

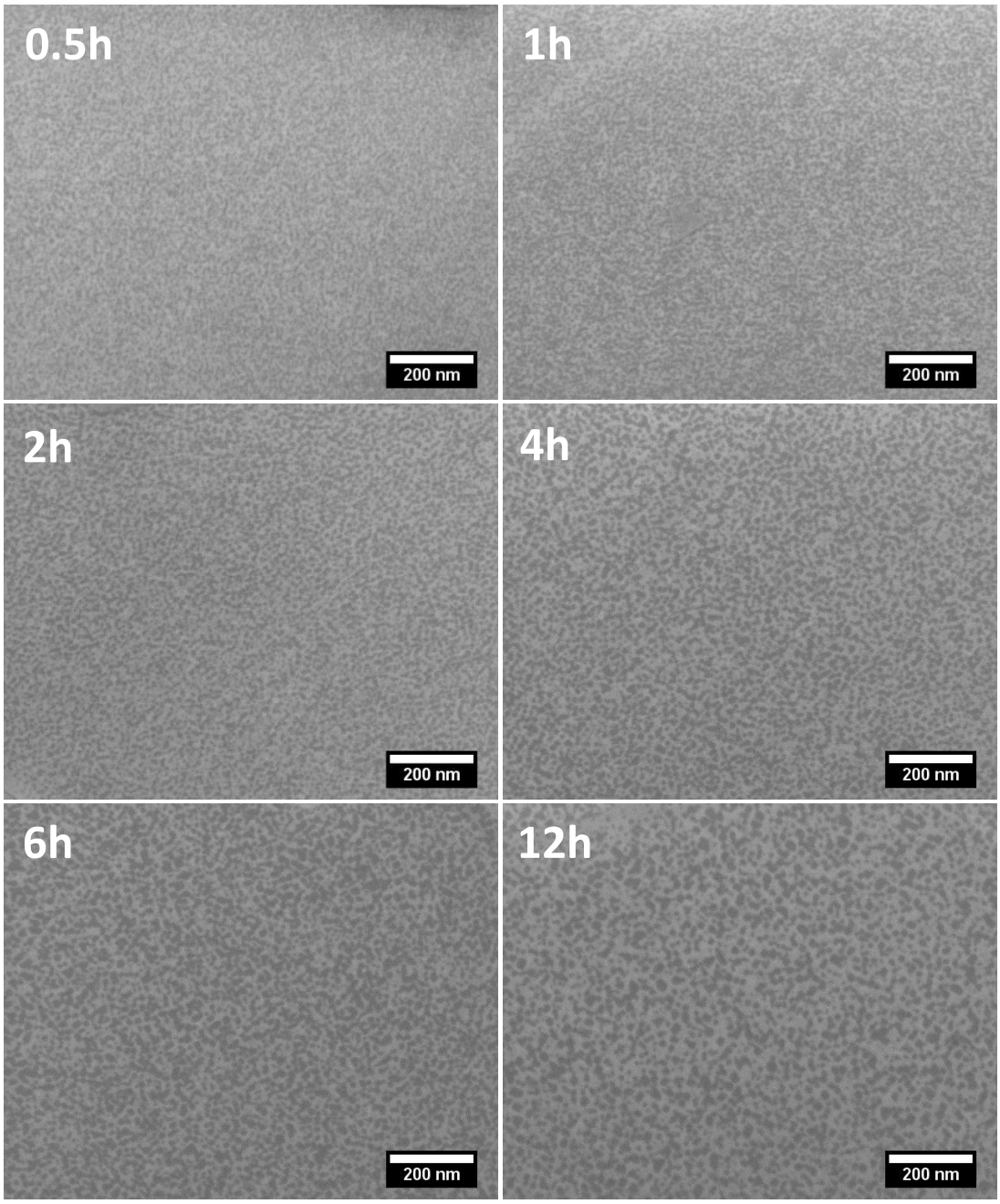

***Figure 6.8**: SEM micrographs displaying the coarsening of the spinel particles over the 15hr30m time period.*

6.1.3 Spinel growth between 400˚C and 700˚C

Typically, the thick film heating elements operate at temperatures of between 400 and 500˚C. To test whether spinel development could be linked to in-service resistance increases, spinel growth was investigated at a range of lower temperatures, again using a combination of SEM and XRD characterisation techniques.

After heating samples for 66h at 400 and 500˚C little evidence was found to indicate the decomposition of the oxidised material at these lower temperatures. Comparisons between XRD spectra obtained before and after the heat treatment showed no increase in spinel peak height, while SEM examination produced no evidence of the two phase microstructure (see figure 6.9).

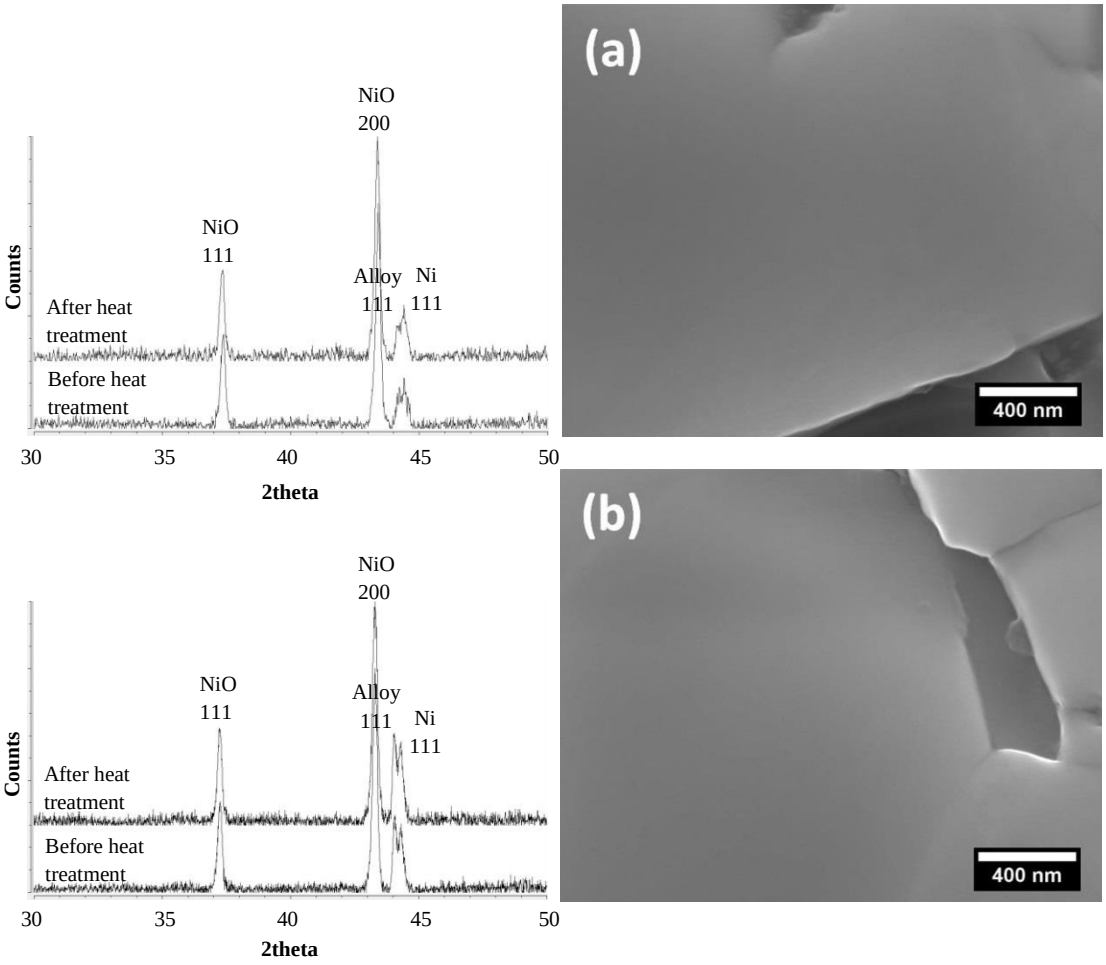

Figure 6.9*: Diffraction patterns and SEM imaging provide little evidence of doped NiO decomposition after 66h at (a) 400˚C and (b) 500˚C.*

As at the lower temperatures, the specimen heat treated for 66h at 600˚C produced little evidence of spinel growth; however once the temperature was increased to 700˚C, the decomposition of the doped NiO became detectable. Post heat treatment spinel peak height increased relative to the NiO peaks and a fine two phase structure was observable using the SEM (see figure 6.10 (b)).

These results indicate that when temperatures are below 600˚C, low rates of diffusion lead to limited decomposition of the doped NiO. As the thick film heating elements

typically operate below 600˚C, this suggests that decomposition is an unlikely cause of in-service resistance changes. However, as hot spots have been observed during heating element operation, temperatures conducive to spinel precipitation still remain possible in localised areas. For this reason, doped NiO decomposition may still be an influencing factor in heating element resistance increase.

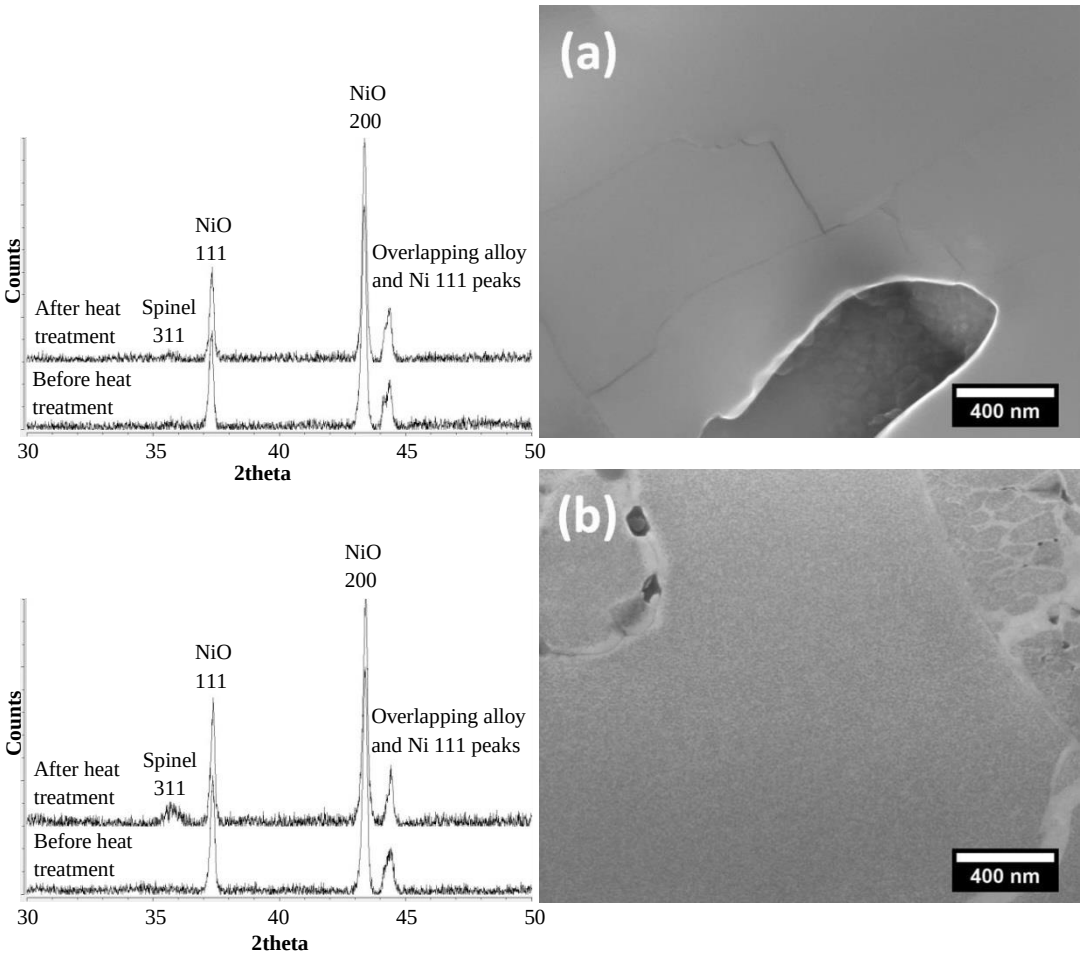

***Figure 6.10**: After 66h at (a) 600˚C, diffraction patterns and SEM micrographs displayed little evidence of NiO decomposition; however, following the same time period at (b) 700˚C, NiO decomposition became detectable.*

6.2 TEM/STEM analysis

After the SEM examination, TEM specimens were prepared from a sample of thick film, previously heated for 66h at 800˚C. In contrast to the as-deposited film (see section 5.4.1), the heat treated specimens displayed evidence of spinel growth in all the doped NiO grains. As the SEM results demonstrated, the high temperature caused an increase in spinel particle size. Prior to heat treatment the largest particles were

typically 20nm in width; however, after the 66h at 800˚C particles exceeding 40nm were observed.

6.2.1 Equiaxed grain – chemical and structural analysis

The TEM micrograph displayed in figure 6.11 shows a doped NiO grain from the heat treated specimen. As the grain was orientated for diffraction, the array of polyhedral particles present within appear darker than those in the surrounding material. These particles appeared to form preferentially in the centre of the grain, leaving a denuded zone immediately adjacent to the grain boundary. Possible mechanisms responsible for the formation of these denuded zones are discussed further in section 7.2.2.

Those spinel particles which were located on the grain boundaries appeared of similar size to those forming within the centre of the grain. This indicates that homogenous nucleation is relatively easy in this system.

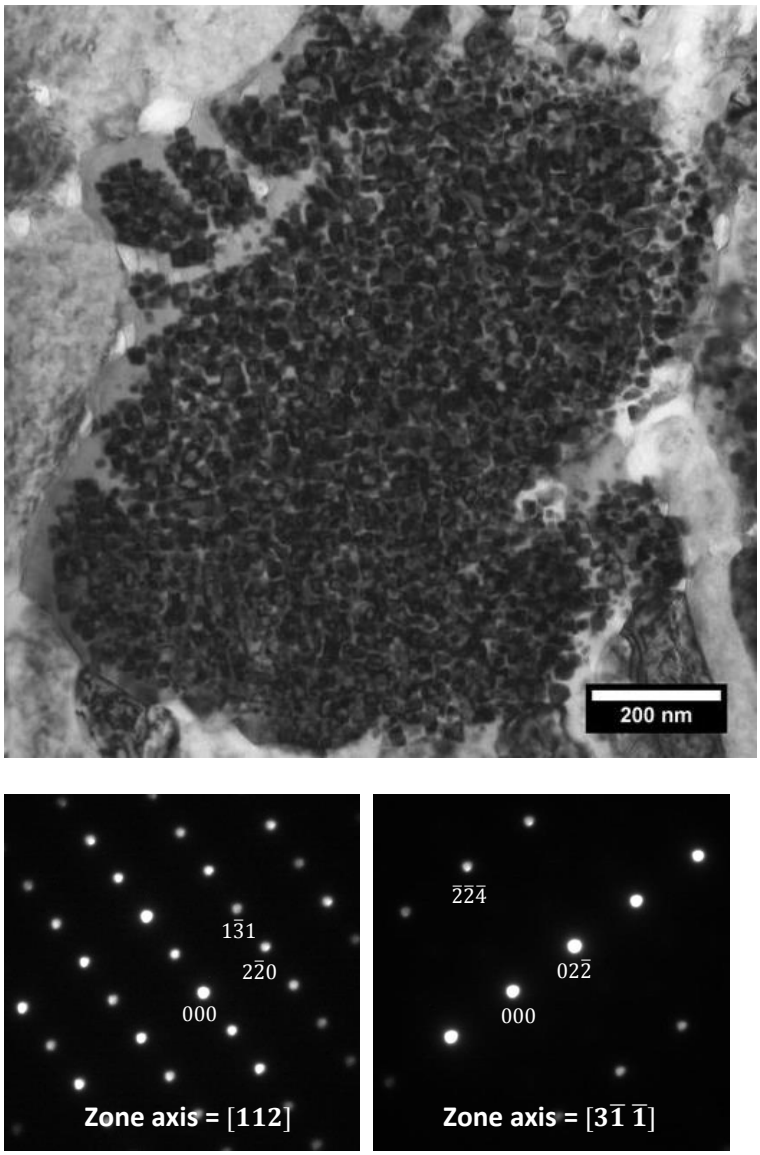

Figure 6.11*: After 66h at 800˚C, a BF TEM micrograph was obtained from a doped NiO grain, together with two SAD patterns.*

Due to the complimentary cubic structures of the spinel and NiO phases, spinel precipitates may grow topotactically within NiO. As a result of this close orientation relationship, diffraction patterns collected from the powder and untreated thick film consisted of a well-defined series of reflections, rather than a set of diffraction rings. When the heat treated material was examined using electron diffraction, the patterns acquired contained similarly ordered arrangements of reflections. These results show that the orientation relationship between the phases is maintained following the heat treatment.

Since the spinel lattice parameter is approximately twice that of the NiO, the spinel reflections have half the spacing of the equivalent NiO reflections. Therefore, diffractions patterns obtained from the two phase material contain isolated spinel reflections in addition to superimposed spinel and NiO reflections. An example of this superposition is the overlap between the $(2\bar{2}0)$ NiO and $(4\bar{4}0)$ spinel reflections in figure 6.11.

Comparing the diffraction patterns from the powder and as deposited film with those obtained from the heat treated specimen reveals a change in the intensities of the spinel and NiO reflections. Diffraction patterns collected from the unheated specimens contained isolated spinel reflections of much lower intensity than the superimposed NiO and spinel reflections (see figures 4.24 and 5.21). However, in those patterns acquired from the heat treated specimen, the isolated spinel reflections were much closer in intensity to the superimposed NiO and spinel reflections. This increase in the intensity of the spinel reflections relative to superimposed NiO and spinel reflections may be attributed to the higher spinel to NiO volume ratio produced by the heat treatment.

Using the SAD patterns displayed in figure 6.11, lattice parameters of 8.45Å and 4.20Å were calculated for the spinel and NiO structures respectively. These values were comparable with those determined by XRD, and electron diffraction examination of the powder and untreated thick film specimens.

Denuded zone

To help identify the crystal structure of the material, the denuded zone was further investigated using electron diffraction. In contrast to the regions containing precipitates, the CBED patterns collected from the denuded zone lacked spinel reflections and were comprised solely of NiO diffraction spots. As figure 6.12 demonstrates, the spinel reflections appearing at half intervals between the NiO reflections vanish as the electron beam is moved to the denuded zone, suggesting this region consists exclusively of NiO.

When the denuded zone was examined using EDS, the obtained readings indicated that this material contained significantly less Fe and Cr than the doped NiO

examined prior to heat treatment. As the Fe-Ni-O [56] and Cr-Ni-O [65] pseudo-binary phase diagrams predicted (see section 6.1.1), a more lightly doped NiO appeared to have developed during the growth of the spinel particles. EDS readings acquired from the central, spinel dominated regions had much higher concentrations Fe and Cr than the denuded zone, demonstrating the diffusion of these cations to the growing particles during the heat treatment (see below).

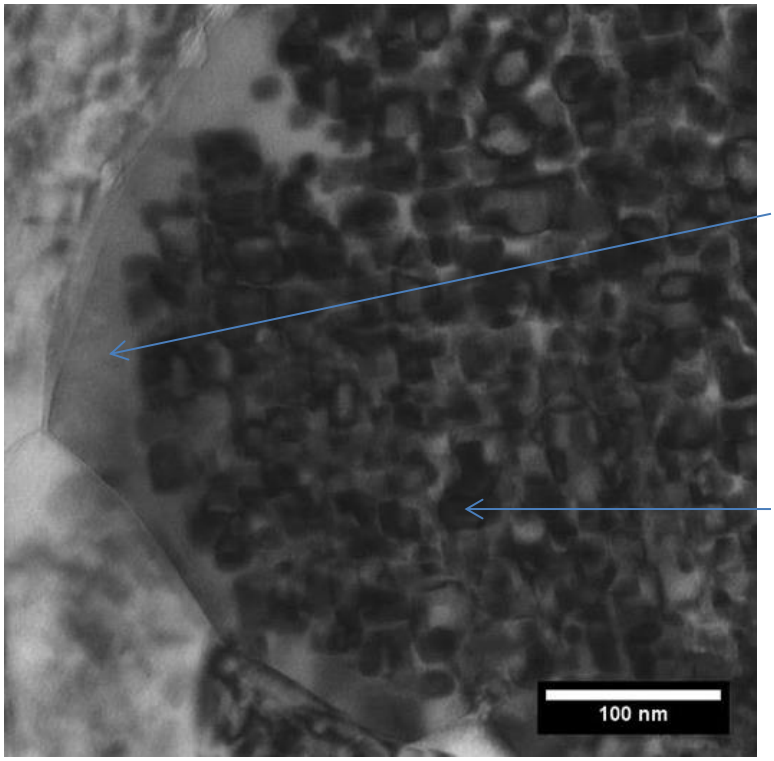

Element	Wt%	At%
O K	22	51
Cr K	1	1
Fe K	2	1
Ni K	75	47
Total	100	100

Element	Wt%	At%
O K	24	51
Cr K	13	10
Fe K	8	5
Ni K	55	34
Total	100	100

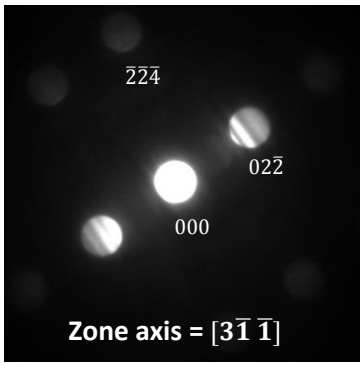

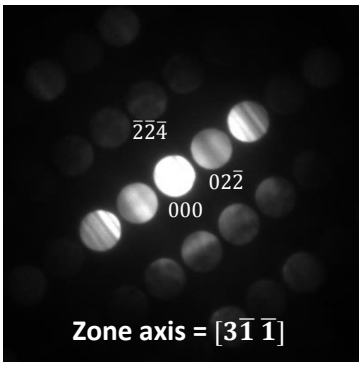

***Figure 6.12**: Combined EDS and electron diffraction analysis of the denuded zone near the edge of the grain and the central spinel-rich region.*

Elemental mapping

The concentration of Cr and Fe within the spinel particles was demonstrated more clearly by the EDS maps collected from a different two-phase grain within the heat treated specimen. In the Cr and Fe chemical maps displayed in figure 6.13, the regions of high intensity correspond with the positions of the spinel particles in the HAADF image. Conversely, the Ni concentration map appears the inverse of the Cr and Fe maps, with the regions of high intensity corresponding to the matrix rather than the spinel particles. In contrast to the other elements, the O concentration map remains relatively consistent, due to the shared O sublattice of the two phases.

During the FIB sample preparation, striations developed across the milled surface due to the film's uneven topography and varied chemical composition. As a consequence of this variation in sample thickness, the elemental maps in figure 6.13 contain a series of low intensity, diagonal lines. These regions of low intensity correspond to the bottom of the furrow, where the electron beam interacts with the lowest number of atoms, and excites fewest X-rays.

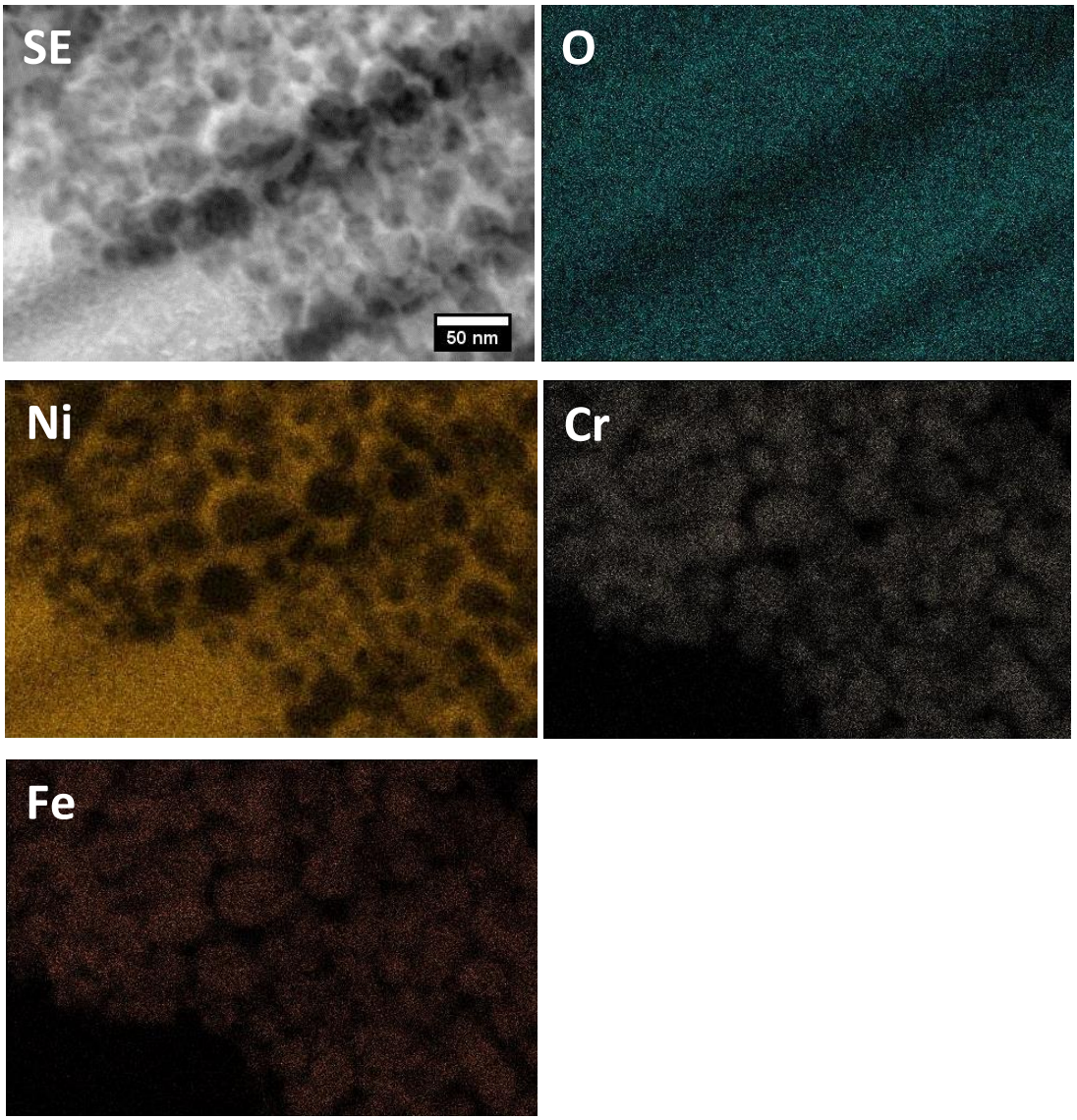

***Figure 6.13**: Elemental concentration maps collected from two-phase region, containing spinel precipitates within NiO matrix.*

The higher concentration of Ni within the matrix can be explained by considering the crystal structure of the NiO and spinel phases. Spinel, unlike NiO, contains trivalent cations, meaning that fewer cations are required per O atom to maintain charge neutrality. While a spinel unit cell has 32 O atoms, 8 divalent Ni atoms and 16 trivalent Cr/Fe atoms [91], the equivalent volume of NiO (8 NiO unit cells) contains 32 O atoms and 32 Ni atoms. In a sample size consisting of 8 NiO unit cells, estimates based on EDS readings obtained from the denuded zone NiO (see figure 6.12), indicate that approximately 1 Ni atom would be replaced by a Cr or Fe dopant atom. Therefore, the density of Ni within the NiO matrix is much greater than in the spinel, resulting in higher signal intensity during elemental mapping.

Similarly, the difference in cation density between the two phases explains the contrast between the spinel particles and NiO matrix in the HAADF image displayed alongside the elemental maps. Ni, Cr, and Fe are all of similar atomic masses; however, due the higher density of cations within the NiO, the matrix material scatters a higher proportion of electrons to high angles, causing it to appear brighter than the spinel particles in the HAADF image.

6.2.2 Columnar grains – chemical and structural analysis

Inspection of the columnar grains revealed the presence of faceted precipitates, similar to those observed in the equiaxed grains (see figure 6.14). These precipitates were of similar size and spread evenly throughout the grains, indicating homogenous nucleation. The denuded zone observed adjacent to the boundaries of the equiaxed grains, was less apparent in these finer, columnar grains.

The chemical makeup of the columnar grains was similar to the central, two-phase region of the equiaxed grains. A typical EDS reading is presented in figure 6.14.

Despite the polycrystalline character of the columnar grains, the CBED patterns collected displayed a regimented series of discs. This indicated a low strain, ordered relationship between precipitate and matrix, similar to that observed in the equiaxed grains. The d-spacings calculated from the pattern displayed in figure 6.14 were consistent with dual-phase material, containing both spinel and NiO. The spinel 220 d-spacing of 2.9Å matches values previously obtained by XRD. As it is twice the size of the 220 NiO d-spacing, the spinel 440 and NiO 220 reflections will overlap.

As discussed in section 5.4.1, the deposition of successive molten, doped NiO particles produced multi-layered, columnar grain formations. While studying these structures it was noted that some of the columnar grains exhibited a degree of epitaxy with the adjoining grains in the layer directly below. When the heat treated specimen was examined, columnar grains within similar layered formations were also found to display this epitaxial relationship. In the two layered structure displayed in figure 6.14, electron beam diffraction revealed matching orientations between grains on opposite sides of the interlamellar boundary (runs almost horizontally across the

centre of the image). The alignment of precipitates on either side of this boundary is visible in the high contrast grains in the middle of the micrograph.

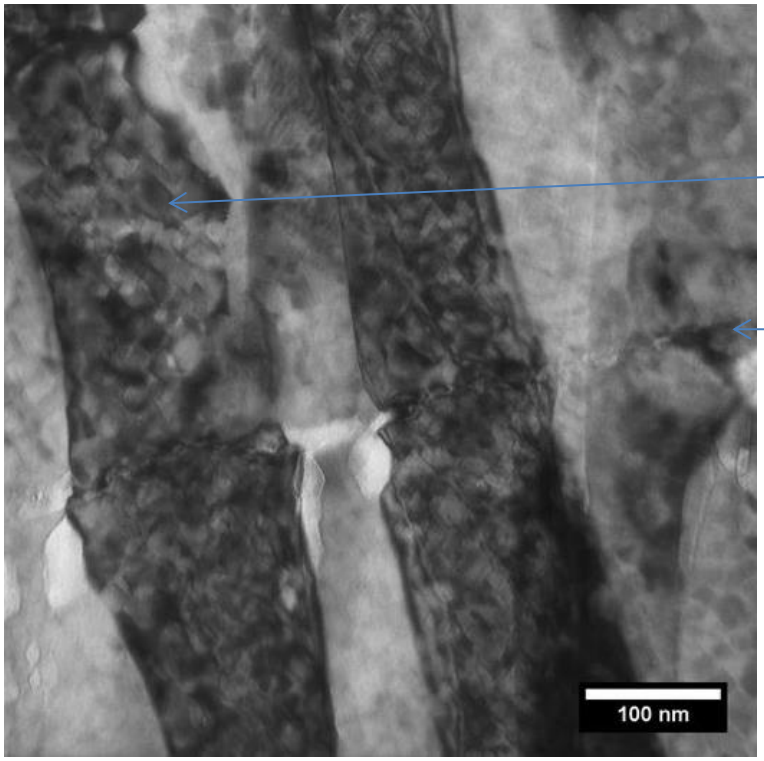

Element	Wt%	At%
O K	21	49
Cr K	14	10
Fe K	8	5
Ni K	57	36
Total	100	100

Interface between the layers.

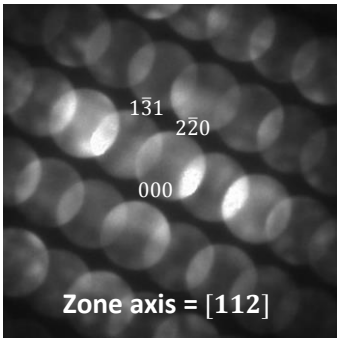

***Figure 6.14**: TEM micrograph displaying a two layered columnar grain structure, from which EDS readings and electron diffraction patterns were obtained.*

6.2.3 Spinel precipitate morphology

In contrast to the spinel particles within the powder and untreated thick film specimens, the precipitates within the heat treated sample were larger and more recognisably faceted. An example presented in figure 6.15, shows a diamond-shaped particle imaged from the [110] direction, with edges parallel to the ($\bar{1}$11) and ($\bar{1}1\bar{1}$) planes. Across the edge parallel to the ($\bar{1}1\bar{1}$) plane, the precipitate is approximately 33nm in width. In comparison, the diameters measured from the less faceted particles within the untreated thick film specimen typically fell within the 10-15nm range.

FFT image analysis of the TEM micrograph was used to calculate d-spacings from the precipitate and matrix materials. These values matched with the spinel and NiO d-spacings previously obtained during XRD examination of the heat treated thick film.

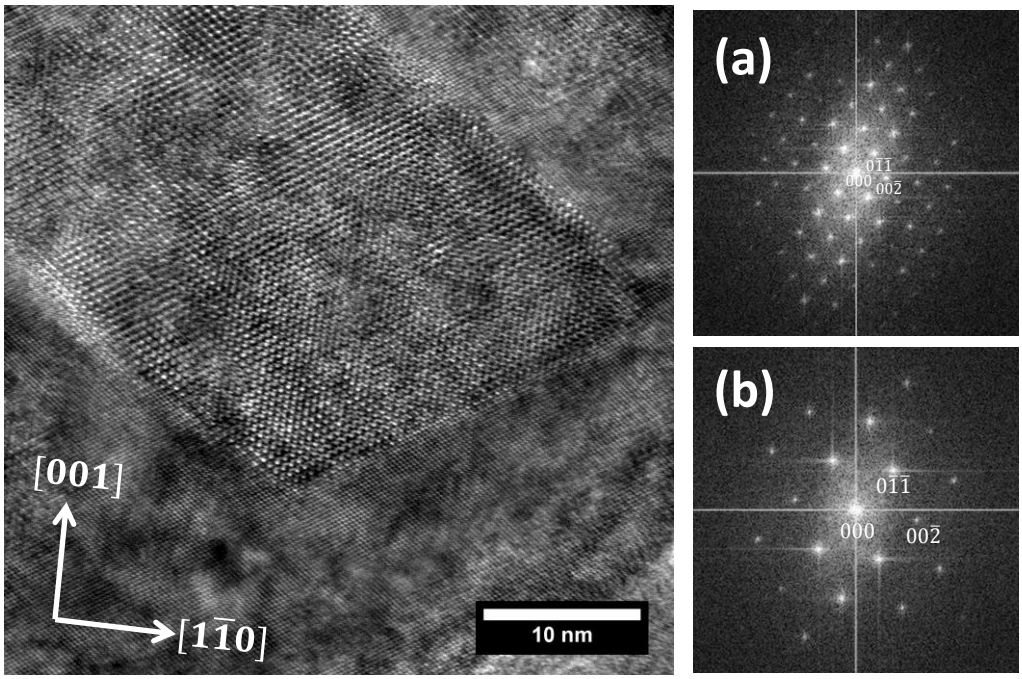

***Figure 6.15**: TEM micrograph displaying a faceted spinel precipitate surrounded by a NiO matrix, orientated on the [110] zone axis. Alongside the image are FFTs obtained from (a) the spinel particle and (b) the NiO matrix.*

Subsequent to the initial high resolution examination, a spinel particle within another grain was examined using electron energy loss spectroscopy. As the grain was similarly orientated on the [110] zone axis, this precipitate also appeared diamond-shaped. Mirroring the EDS results presented in section 6.2.1, EELS elemental mapping (see figure 6.16) indicated Cr and Fe concentrated within the particle, while the greatest density of Ni was within the matrix. Again, the O concentration map remained constant due to the shared O sublattice of the spinel and NiO phases.

Intensity variations within the Ni, Cr and Fe chemical concentration maps reflect the thickness of the [110] orientated spinel precipitate. In the Cr and Fe concentration maps, the intensity progresses smoothly from a minima beginning at the corners in the ±[001] directions, to a maxima located at the centre of the particle. Lines of constant intensity occur along the [110] directions. In the Ni concentration map, the positions of the maxima and minima are completely inverted. These results indicate that thickest region of the spinel particle lies centrally between the corners in the ±[110] direction.

As figure 6.16 demonstrates, these observations are consistent with an octahedral precipitate morphology. Similar octahedral precipitates, also bound by {111} planes, were previously reported in the $NiFe_2O_4$/NiO [82] and $MgFe_2O_4$/MgO [89] systems following particle coarsening.

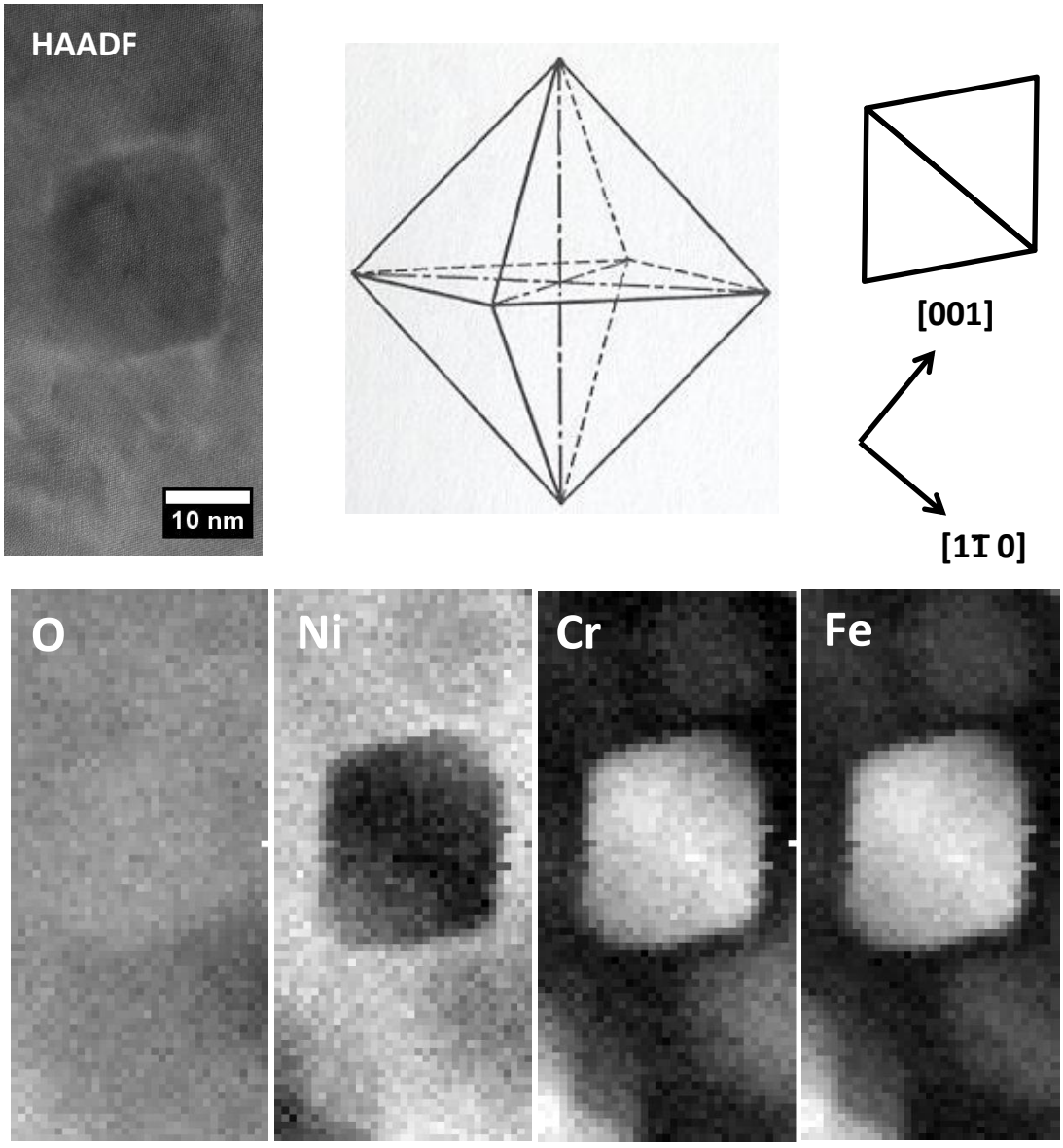

Figure 6.16*:EELS elemental intensity maps, presented alongside (a) a schematic diagram of an octahedron and (b)a projection from the [110] direction.*

6.2.4 Atomic scale electron energy loss spectroscopy

During the decomposition of doped NiO containing single dopants of Fe or Cr, the pseudo-binary phase diagrams (see figure 6.1) predict the precipitation of $NiCr_2O_4$

and $NiFe_2O_4$ respectively. $NiCr_2O_4$ is a normal spinel that has divalent ions (Ni^{2+}) located on the tetrahedral sites and trivalent ions (Cr^{3+}) positioned on the octahedral sites [69]. Conversely, $NiFe_2O_4$ is an inverse spinel with half the trivalent ions (Fe^{3+}) on tetrahedral sites, while the divalent ions (Ni^{2+}) and the remaining half of trivalent ions (Fe^{3+}) occupy the octahedral sites [70].

To investigate site occupancy within the spinel precipitating from the Cr and Fe doped NiO, the material was analysed on an atomic scale using electron energy loss spectroscopy. The spinel particles were orientated in the <110> direction, so that the atoms of the octahedral and tetrahedral sites were aligned into columns, as figure 6.17 demonstrates. This enabled the detection of any preferential distribution of Ni, Cr and Fe cations amongst the octahedral and tetrahedral sites.

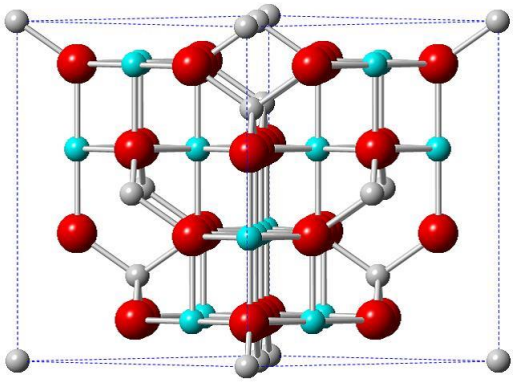

***Figure 6.17**: Near [110] projection of a spinel particle, showing atoms in the tetrahedral and octahedral aligned into columns.*

A HAADF image of spinel precipitate orientated in the [110] direction is displayed in figure 6.18 (a). As the intensity of the atomic columns in HAADF imaging is approximately proportional to the square of the atomic number (Z) [144], the image is dominated by high Z cation sites and the O columns are undetectable.

When the spinel crystal was viewed along the [110] direction, the atomic columns form a distinctive, reoccurring pattern in which ten closely spaced atomic columns formed a ring around a central atomic column. Examination of the [110] orientated spinel crystal using HAADF imaging showed that the octahedral columns within the outer ring produced lower intensity spots than those located in the centre of the ring. This may be attributed to a difference in the atomic density of the respective

octahedral columns. In the near [110] projection displayed in figure 6.18 (b), the octahedral columns of the outer ring (coloured blue), have lower density of atoms than the octahedral columns located at the centre of the ring (coloured green). This higher atomic density leads to increased scattering of the electron beam and therefore a greater intensity in the HAADF image.

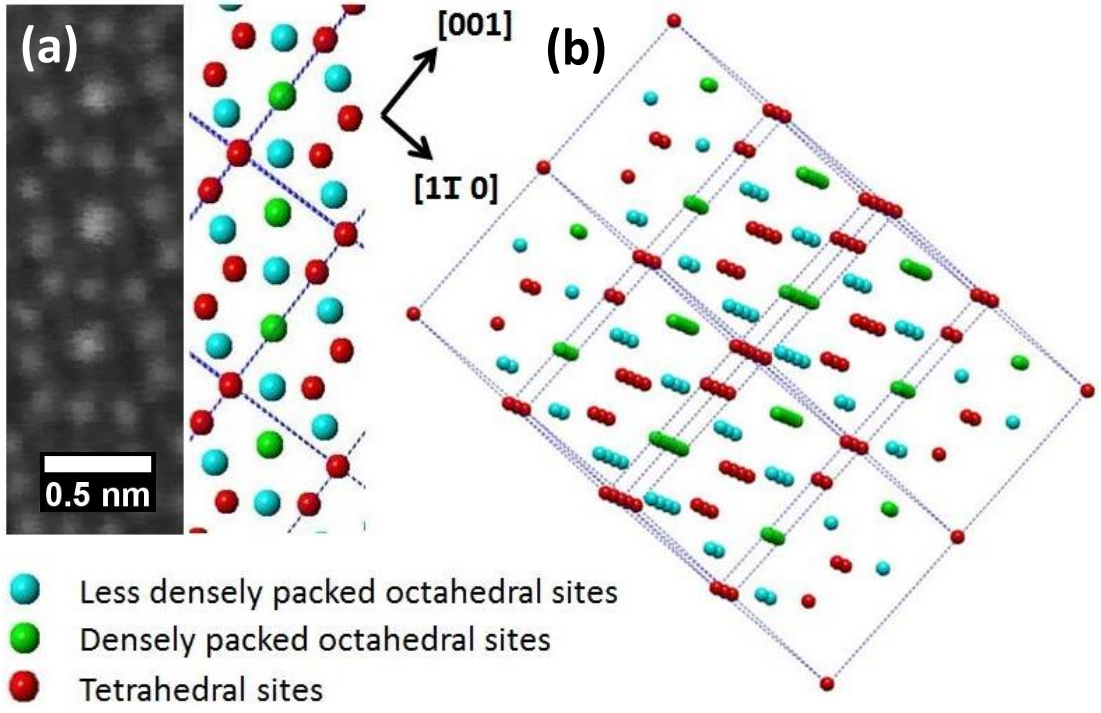

***Figure 6.18**: (a) HAADF image showing spinel precipitate orientated on the [110] zone axis. The tetrahedral and octahedral positions of the cations are highlighted in the accompanying model. (b) Near [110] projection demonstrating the difference in the cation ion density in the octahedral columns.*

Two-dimensional EELS was performed on the rectangular section of the [110] orientated spinel precipitate displayed in figure 6.19. The summed spectra from this analysed region were found to contain O, Ni, Cr and Fe edges. Using the spectroscopic signal from the Ni $L_{2,3}$, Cr $L_{2,3}$ and Fe $L_{2,3}$ edges, the composite map presented in figure 6.19 was constructed. This shows Fe occupying the tetrahedral sites, Cr positioned on the octahedral sites and Ni located on both the octahedral and tetrahedral sites.

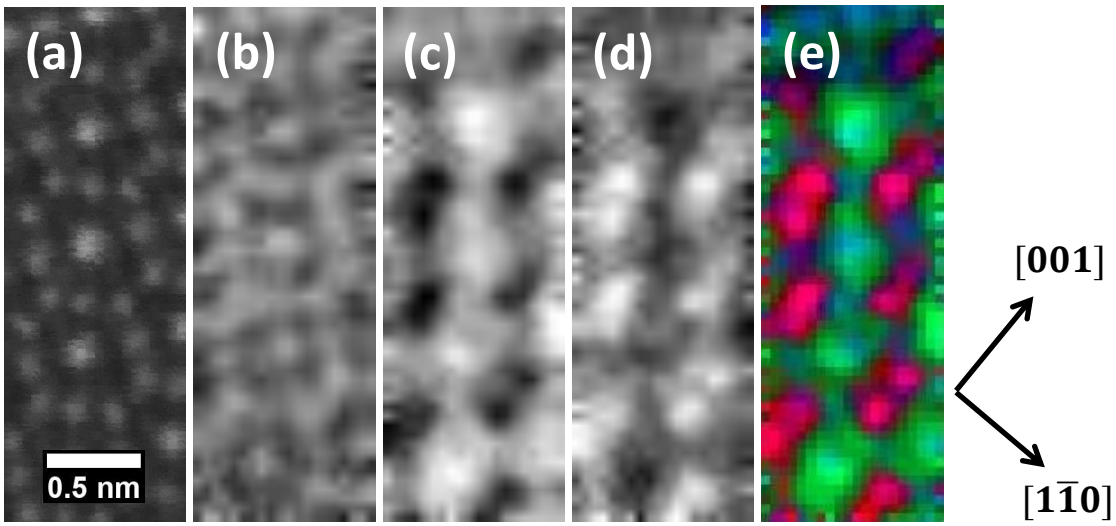

***Figure 6.19**: (a) HAADF image captured simultaneously with the EELS signal, alongside (b) Ni, (c) Cr and (d) Fe EELS elemental maps. Composite EELS map (e) in which Ni sites are indicated by blue, Fe sites by red and Cr sites by green.*

After the examination of the precipitate, EELS readings were also acquired from a rectangular section of the surrounding matrix (see figure 6.20). Due the orientation relationship between the phases, this material was also orientated on the [110] zone axis. In contrast with the readings from the spinel particle, the summed spectra obtained from the matrix material only displayed O and Ni edges. This lack of Cr and Fe is in agreement with the previous EDS analysis (see section 6.2.1), again indicating that the majority of the dopant atoms diffuse from the NiO matrix during the heat treatment.

The NiO has a NaCl crystal structure consisting of two interpenetrating O and Ni FFC lattices. When viewed along the [110] direction, the atoms align in either O or Ni columns. As the O atoms are light in comparison to Ni atoms, the O columns are not detected during HAADF imaging. However, using the Ni $L_{2,3}$ and O K edge signals, a composite map may be constructed showing the relative positions of the O and Ni columns (see figure 6.20).

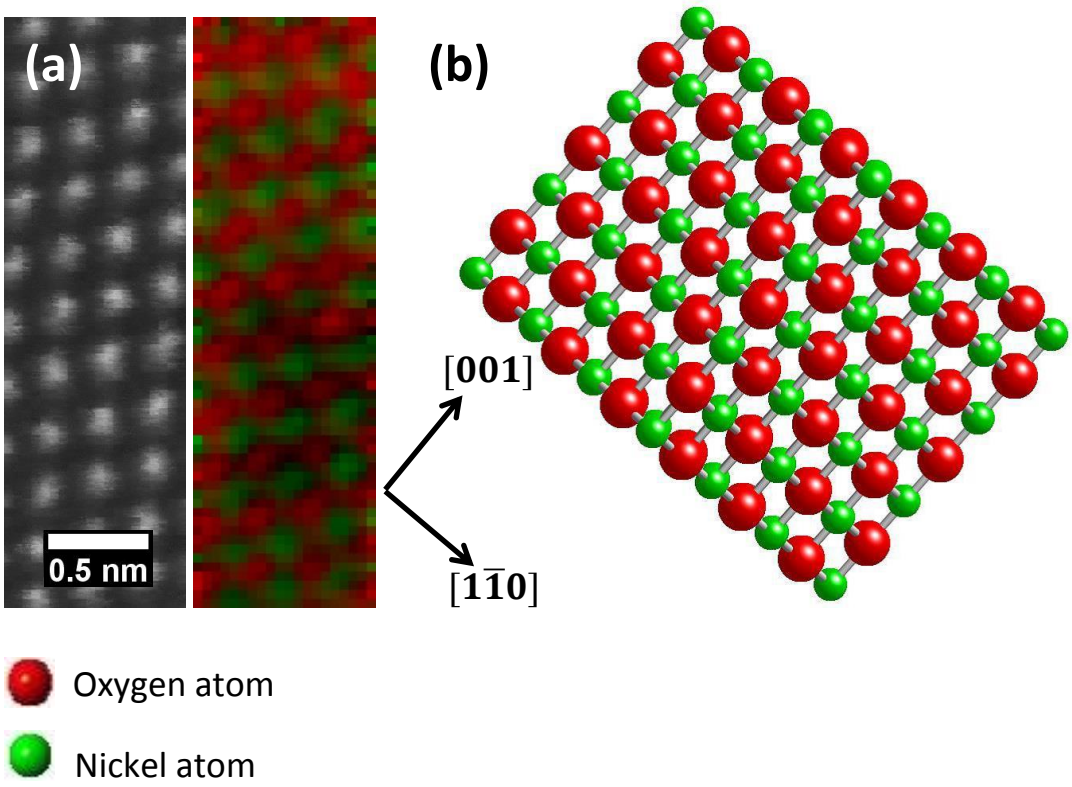

***Figure 6.20**: (a) HAADF alongside composite map produced from simultaneously captured EELS signal. (b) [110] orientated NiO lattice.*

To directly compare the two lattice structures, EELS analysis was conducted at the interface between the two phases. Spanning this interface, the section selected for investigation is displayed in figure 6.21. The summed spectra gathered from this rectangle contained edges from all the main constituent elements. Signals from the Ni $L_{2,3}$, Cr $L_{2,3}$ and Fe $L_{2,3}$ edges were used to construct the composite map, while O K edge signals were used to generate the O intensity map. Analysis was again conducted with the two phases positioned on the [110] zone axis.

The close coherency between the spinel and NiO structures is demonstrated by the EELS elemental maps presented in figure 6.21. In the Ni, Cr, Fe composite map, Ni atoms occupying octahedral sites within NiO matrix align with Ni atoms positioned upon octahedral sites within the spinel structure. Similarly, in the corresponding O intensity map, the planes of O atoms run uninterrupted through the interface, demonstrating the shared O sublattice of the two phases.

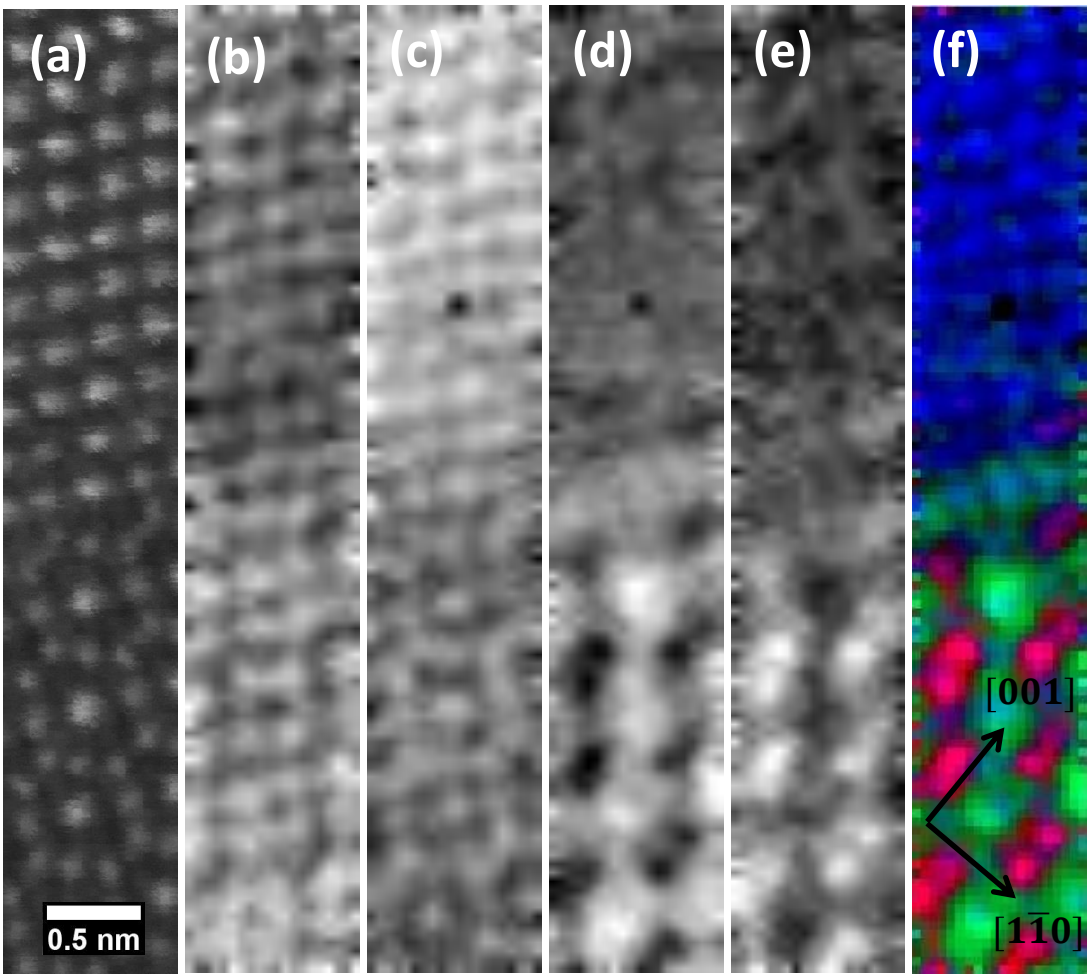

***Figure 6.21**: (a) HAADF image of spinel-NiO interface presented alongside (b) O, (c) Ni, (d) Cr, and (e) Fe EELS elemental maps. Composite EELS map (f) in which Ni sites are indicated by blue, Fe by red and Cr sites by green.*

All the data presented in this section was collected using the aberration corrected, 100keV Nion UltraSTEM, housed at the superSTEM facility in Daresbury. Dr Hernandez-Maldonado is kindly thanked for his microscopy and subsequent analysis which produced the EELS elemental maps displayed in sections 6.2.4 and 6.2.5.

Chapter 7

Discussion

7.1 Introduction

TEM analysis of FIB cross-sections produced from the oxidised powder specimens revealed the presence of spinel particles formed topotactically within a Cr and Fe doped NiO. These particles were non-faceted in appearance with diameters ranging from approximately 5-15nm. In the thin foil prepared from the as-deposited film, some oxide grains contained similar spinel particles, while other grains displayed a homogenous single-phase structure. This variation was attributed to the difference in heat exposure experienced by the doped NiO during the two-stage flame spray heat treatments.

While investigating a possible link between doped NiO decomposition and heating element resistance change, a thick film specimen was subjected to 66h at 800˚C. In agreement with the Ni-Fe-O and Ni-Cr-O binary phase diagrams, this produced an increase in the spinel volume fraction. Contrasting with the as-deposited film, TEM analysis of the heat treated material revealed evidence of spinel growth in all the doped NiO grains. The spinel precipitates shared a topotactic relationship with the parent material and were generally faceted in appearance. Their sizes ranged from approximately 30-40nm.

In this chapter, section 7.2 focuses upon the role of vacancies in spinel precipitation, discussing their influence upon the mechanism of phase transformation, and the formation of the precipitate-free grain boundary regions. Section 7.3 examines spinel morphology before and after heat treatment, and how this is influenced by nucleation rate. Finally, section 7.4 discusses site occupancy within the spinel and how this affects the type of spinel structure formed.

7.2 Influence of vacancies on spinel precipitation

The growth of the spinel particles within the Cr and Fe doped NiO seems only to involve the relocation of cations, if a shared O sublattice is assumed. However, since spinel contains trivalent cations, preserving charge neutrality requires less cations per O anion in the spinel than in the NiO. Therefore vacancies are also necessary in the growth of the spinel phase [87]. This relationship may be represented by the following equation which uses Kroger-Vink notation:

$$Ni^{x}_{Ni} + 2M^{\bullet}_{Ni} + V''_{Ni} + 4O^{x}_{O} = NiM_2O_4 \qquad \textit{Equation 7.1}$$

In this equation M represents the trivalent Fe and Cr cations.

The formation of spinel therefore requires some divalent cations to be replaced by vacancies and trivalent cations. For one unit cell of spinel to replace the equivalent volume of 8 NiO unit cells (spinel lattice parameter is almost exactly twice that of the NiO lattice parameter) 16 trivalent cations and 8 vacancies must be substituted for 24 divalent cations.

Changes to both the temperature and O activity influence the valance state of the Fe and Cr dopant atoms. This affects the vacancy concentration within the doped NiO, which must adjust to preserve charge neutrality. As environmental conditions cause the divalent cations to adopt a trivalent state, the additional positive charge is balanced by a cation vacancy. Therefore, assuming the vacancy concentration is in equilibrium with the local atmosphere, the concentration of vacancies will be half that of the trivalent cations.

While investigating the thermodynamics of the Ni-Fe-O system, Schneider and Schmalzried [55] used coulometric titration to measure vacancy concentration in Fe-doped NiO. During the study, samples doped with 1-10 at% Fe were held at temperatures of between 900 and 1030˚C, at a variety of O partial pressures. Results showed that vacancy concentration rose with increasing Fe concentrations, decreasing temperatures or a reduction in oxygen partial pressure. For each of the compositions tested, measurements suggested that all Fe in the doped NiO had become trivalent before spinel precipitation began.

Another study conducted by Greskovich [80], suggests that the Cr within Cr-doped NiO exists predominantly in a trivalent state when heated in air between the temperatures of 1330˚C and 1580˚C. During this research single crystals of NiO were heated in contact with Cr_2O_3 tablets in order to examine the kinetics of $NiCr_2O_4$ formation in NiO. Subsequent XRD measurements indicated that the NiO lattice parameter decreased following the heat treatment as smaller Cr^{3+} ions substituted for the larger Ni^{2+} ions.

The studies conducted by Greskovich, and Schneider and Schmalzried, suggest that a Cr and Fe doped NiO cooled under equilibrium conditions, would contain Cr and Fe cations in a mainly trivalent state. As the intrinsic vacancy concentration of NiO [55] is negligible in comparison to the number of dopant cations, the vacancy concentration would be approximately half that of the dopant concentration. A NiO containing 9 at% Cr and 4 at% Fe (as measured during the current work) would therefore contain a vacancy concentration of approximately 6.5%. However, as heat treatment varied according the particle flight path, and involved rapid rates of cooling, the vacancy concentration within the investigated doped NiO likely differs from the value predicted under equilibrium cooling conditions.

7.2.1 Mode of spinel precipitation

In the Ni-Fe-O system, the precipitation of spinel within Fe-doped NiO has been shown to occur by the local reordering of Fe and Ni cations with pre-existing cation vacancies [82]. Similar spinel particles, highly oriented with the NiO matrix, have also precipitated by internal oxidation, which requires the long-ranged diffusion of vacancies from the surface [84].

These contrasting modes of precipitation can be attributed to a difference in the valence state of the dopant atoms prior to nucleation. In the former investigation [82] Fe-doped NiO samples were cooled slowly to just above the solvus temperature, enabling the majority of the Fe to form Fe^{3+} as vacancy concentration reached equilibrium. As cooling continued and spinel precipitation became favourable, phase change occurred by the local rearrangement of cations and cation vacancies.

In the latter study [84] Fe-doped NiO was held at low oxygen partial pressure where most of the dopant cations were in a divalent state. Spinel precipitation was then induced by a rapid increase in oxygen activity. During this process vacancies diffused from the surface, enabling the divalent Fe cations to form trivalent Fe cations and spinel to precipitate topotactically within a nearly pure NiO matrix. The thickness of the two phase NiO-spinel layer varied parabolically with time, suggesting that the diffusion of vacancies from the surface was a rate limiting factor.

SEM examination of the heat-treated, cross-sectioned thick film indicated that spinel precipitation occurred by the local rearrangement of cations and cations vacancies rather than internal oxidation. While imaging samples heated for 30m, 1h, 2h, 4h, 6h and 12h at 800˚C (see section 6.1.2) spinel precipitation appeared relatively uniform within the ~100μm thick specimens. The internal reaction front reported by Ostyn et al [84], was not observed, while precipitates close to the sample surface did not appear to be significantly larger than those near the centre of the film.

These observations suggest that an influx of vacancies was not required for spinel precipitation. As manufacture of the thick film involves high temperatures followed by rapid rates of cooling, vacancies occurring due to thermal vibrations are likely to be frozen-in. This means a vacancy excess may well exist within the Cr and Fe doped NiO.

7.2.2 Grain boundary denuded zones

Following the heat treatment of the thick film at 800˚C, TEM analysis revealed the presence of precipitate-free zones immediately adjacent to the grain boundaries of the NiO-spinel grains (see section 6.2.1). EDS readings obtained from the precipitate-free zones revealed a near 1:1 ratio of O to Ni, indicating the formation of a near pure NiO. D-spacings calculated from convergent beam diffraction patterns were consistent with this assumption.

Within literature, the formation of denuded zones adjacent to grain boundaries during the heat treatment and quenching of age-hardenable alloys have been attributed to the localised depletion of either vacancies or solute atoms [93]. During the vacancy depletion mechanism, an alloy is heated above a critical temperature that requires

excess vacancies for homogenous nucleation. As the grain boundaries act as vacancy sinks, the necessary quantity of excess vacancies required for nucleation falls below the critical concentration in the material close to the grain boundary. In the solute depletion mechanism, solute concentrations fall below the minimum value required for homogeneous nucleation near the grain boundary. This may be due to the segregation of solute atoms to the grain boundary or the heterogeneous nucleation of particles at the grain boundary.

When precipitate free zones were examined in the TEM, heterogeneously nucleated particles were not observed along the grain boundaries adjacent to the denuded zones. Additionally, EDS analysis of the grain boundaries failed to detect concentrations of Cr and Fe. This lack of evidence for the solute depletion mechanism seems to indicate that vacancy depletion is the more likely means by which the denuded zones form. If this mechanism is responsible, it would appear that low vacancy concentrations impede spinel nucleation next to grain boundaries but remain sufficient for Cr and Fe to diffuse to growing particles nearer the grain's centre. This is one possible explanation for the near pure NiO discovered in the precipitate-free grain boundary regions.

Another factor that could also influence the formation of the grain boundary denuded regions is the distribution of Cr and Fe atoms prior to the heat treatment. In section 5.4, EDS mapping revealed that Cr accumulated at the centre of the grains while Fe concentrated around the grain boundaries. If these different dopant concentrations affect the temperature at which spinel precipitates, then the right heat treatment could cause limited decomposition in a region rich in one particular dopant atom. At 800˚C, if the Fe rich NiO retained its NaCl crystal structure while the Cr rich NiO decomposed, then this might also contribute to the formation of the precipitate-free zones located adjacent to the grain boundaries.

7.3 Shape transformation of spinel precipitates

7.3.1 Introduction

In the as-deposited thick film, TEM analysis revealed the presence of non-faceted spinel particles that were approximately 5-10nm in diameter, and shared a topotactic

relationship with the surrounding doped NiO matrix. After heating specimens for 66h at 800˚C, spinel volume fraction increased, and the individual particles become more faceted in appearance. When viewed from the [110] direction these particles were typically diamond shaped in appearance (see figure 7.1), with edges parallel to the $(\bar{1}11)$ and $(\bar{1}1\bar{1})$ planes. Across the edge parallel to the $(\bar{1}1\bar{1})$ plane, precipitates generally measured between 30 and 40nm. EDS readings obtained after the aforementioned heat treatment suggest a roughly 2:1 ratio of Cr:Fe exists within the spinel particles.

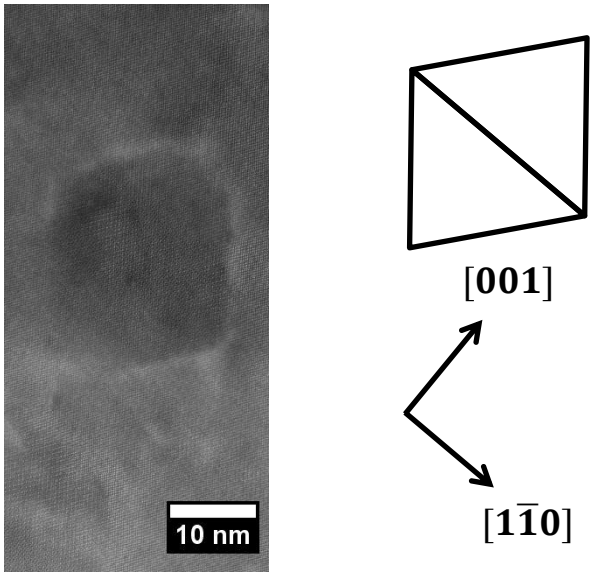

Figure 7.1*: HAADF image displaying a spinel precipitate within a heat treated specimen, viewed from the [110] direction.*

EELS elemental mapping (see section 6.2.3) showed that Cr and Fe accumulated within the precipitates, while Ni concentrated within matrix. Due to the shared O sublattice of the two phases, the O concentration map remained constant. The intensity of Ni, Cr and Fe concentration maps varied in relation to the thickness of the spinel precipitate. In the Cr and Fe concentration maps, intensity progressed smoothly from a minima at the corners in the ±[001] directions, to a maxima located at the centre of the particle. Intensity remained constant along the lines parallel to the [110] direction. As Ni accumulated within the matrix rather than the precipitate, the maxima and minima positions were completely inverted in the Ni concentration map. These results suggested that the particle's thickest region was located centrally,

between the corners in the ±[110] directions. This would be consistent with an octahedral morphology.

Previous studies into the $NiFe_2O_4$/NiO and $NiCr_2O_4$/NiO systems, have reported a range of different precipitate morphologies. Octahedrons bound by the {111} planes have been reported in the $NiFe_2O_4$/NiO system [82]. Similarly, faceted precipitates have also been observed while studying the $NiCr_2O_4$/NiO system [83]. Common to both systems are dendritic precipitates, with protrusions extending along the six <100> axes [83, 91]. Conversely, coherent ellipsoids lying on the {100} planes, appear to be unique to the $NiCr_2O_4$/NiO system [83]. The diversity of morphology reported within both systems indicates that the kinetics of phase transformation play an important role in controlling precipitate shape.

7.3.2 Precipitate morphology

Precipitate morphology within the powder and as-deposited thick film specimens

During the formation of the thick film, differences in the cooling rate of the Cr and Fe doped NiO material occurs due to variations in the flight-path of particles through the oxy-acetylene flame. Consequently, single phase material, typical of the high temperature state, exists alongside spinel-NiO grains within the as-deposited thick film specimens (see section 5.4.1). Within the grains that had experienced decomposition, particles of roughly spherical shape were observed, with diameters of approximately 5-10nm.

In the related $NiCr_2O_4$/NiO system, Chen et al [83] examined the influence of cooling rates on spinel precipitation within Cr-doped NiO, cooled from above solvus temperature using N_2-quenching and air quenching. TEM examination revealed that the more rapidly cooled N_2-quenched specimens experienced no precipitation, while the air-quenched specimens developed arrays of fine, spherical precipitates, similar to those observed during the current work.

The formation of these spherical particles is energetically favourable when the particles are small, and the free energy is dominated by the surface energy term, as this shape has the lowest surface area to volume ratio. A factor that may prevent

spherically shaped precipitates forming is the strain caused by a large misfit between precipitate and matrix materials [83]. However, in the current system, where the misfit between the NiO and spinel lattices is very small, the fine spinel precipitates were able to adopt this particular morphology.

Precipitate morphology following heat treatment of the thick film

Observations made using the SEM and TEM confirmed a dramatic increase in the volume fraction of precipitates following 66h at 800˚C. In contrasted with the fine, spherical precipitates previously observed within the powder and thick film prior to heat treatment, precipitates within the heat treated specimen were larger (approximately 30-40nm) and generally faceted. Examination of these particles using the TEM and EELS techniques (presented in section 6.2.3) suggested that the precipitates had adopted an octahedral morphology.

Though not readily discernible during qualitative analysis, a bimodal distribution of precipitates may have formed within some grains, due to populations of precipitates existing prior to heat treatment. A further investigation examining precipitate size distributions in different grains may help identify which material contained precipitates prior to the heat treatment.

Similar octahedral precipitates, as well as unidentified faceted shapes have been reported in the $NiFe_2O_4$/NiO [82] and $NiCr_2O_4$/NiO [83] systems respectively. In a study conducted by Summerfelt [87], dendritic $NiFe_2O_4$ precipitates were shown to develop octahedral morphologies when heated at temperatures ranging from 700-920˚C. These particles remained stable during successive heat treatment indicating that this was the equilibrium morphology. In a comparable study [83] carried out by Chen et al, $NiCr_2O_4$ precipitates heated at 950˚C transformed from spherical particles into faceted particles, before eventually forming coherent ellipsoids. This final morphology proved stable and was identified as the low energy shape.

As the precipitates within the Cr and Fe doped NiO samples were only examined after a single heat treatment (66h at 800˚C), the stability of the octahedral precipitates cannot be confirmed by comparisons with results obtained from previous heat treatments. Therefore, there remains the possibility that the octahedral

morphology is not the equilibrium shape, and longer heat treatments may result in further transformation. In this scenario, considering that the spinel particles contain an approximate Cr to Fe ratio of 2:1, and that $NiFe_2O_4$ and $NiCr_2O_4$ are completely miscible at 800˚C [71], the development of ellipsoidal precipitates, such as those reported in the $NiCr_2O_4$ system, could be a possibility. However, for the following reasons it seems more likely that octahedral precipitates have adopted the equilibrium morphology after the 66hr heat treatment:

1. At similar temperatures, precipitates in the $NiCr_2O_4$ [83] and $NiFe_2O_4$ [91] systems established their equilibrium morphology over time periods almost equal to, or less than 66h.

2. EDS and EELS results obtained from the heat treated thick film indicated the matrix material was almost pure NiO, as expected under equilibrium conditions (see Ni-Fe-O [56] and Ni-Cr-O [65] pseudo binaries).

Through the formation of the equilibrium morphology, the sum of the surface energy and strain energy are minimised. It has been suggested that the relative surface energies between the $NiFe_2O_4$/NiO and $NiCr_2O_4$/NiO systems are similar, meaning that the differences in the equilibrium morphologies are determined by the magnitude of the strain energy [91] (at room temperature the misfit between the $NiFe_2O_4$ and $NiCr_2O_4$ precipitates and the NiO lattice is 0.2% [87] and 0.4% [83] respectively). As $NiFe_2O_4$ and $NiCr_2O_4$ are completely miscible at high temperature, it was speculated that doping $NiCr_2O_4$ with increasing quantities of Fe would reduce lattice misfit, causing a gradual transition in the equilibrium morphology from ellipsoid to octahedron. However, considering that the precipitates within the current system have a Cr to Fe ratio of approximately 2:1, evidence suggests that this gradual transformation is not occurring. Rather than adopting an intermediate shape somewhere between an ellipsoid and an octahedron, the precipitates were octahedral in appearance, suggesting that Fe stabilises the octahedral morphology at relatively high Cr concentrations.

7.3.3 Influence of nucleation rate on spinel morphology

Another factor affecting precipitate morphology is the rate of nucleation within the parent material. When doped NiO is cooled slowly from above the solvus temperature into the two phase field, low undercooling causes a slow rate of nucleation. Under these circumstances $NiFe_2O_4$ and $NiCr_2O_4$ precipitates have been shown to develop dendritic morphologies with protrusions extending along the six <100> axes [79, 83].

When the doped NiO is heated at temperatures several hundred degrees Celsius below the solvus temperature, the high undercooling increases the driving force for phase change and the nucleation rate is much higher. Under these conditions octahedral precipitates of a high density have been observed within the $NiFe_2O_4$/NiO system [82], as well as during the current work.

The reason morphology changes with nucleation rate can be determined by considering the conditions necessary for solid-state dendritic precipitation. These requirements have been summarised by Doherty [88] as follows:

1. Low mismatch between the precipitate and matrix phases.
2. A low rate of solute diffusion within the precipitate.
3. Almost isotropic surface energy.
4. A wide spacing between the precipitates.

Under slow nucleation rates all the requirements for dendritic growth were fulfilled in the $NiFe_2O_4$/NiO and $NiCr_2O_4$/NiO systems; however, at high nucleation rates this was no longer true. As a higher nucleation rate causes the formation of a greater density of spinel particles, a reduction in the separation of the precipitates is the likely reason for the change in morphology.

Due to the close relationship between the current system and the $NiFe_2O_4$/NiO and $NiCr_2O_4$/NiO systems it is likely that the conditions for dendritic growth can be fulfilled in Cr and Fe doped NiO. Since octahedral precipitates were observed after

66h at 800˚C, this would indicate that nucleation rates were too high, and therefore precipitate separations too low for dendritic growth.

7.4 Site occupancy within the spinel precipitates

7.4.1 Introduction

Site occupancy within the spinel that precipitating from the Cr and Fe doped NiO was studied at an atomic scale using electron energy loss spectroscopy (see section 6.2.4). The spinel particles were orientated in the <110> direction, so that the atoms located on the octahedral and tetrahedral sites were aligned in columns. This allowed the detection of preferential site occupation by the constituent elements upon either the octahedral or tetrahedral sites.

When two-dimensional electron energy loss spectroscopy was performed upon a spinel precipitate, the summed spectra from the analysed area contained O, Ni, Cr and Fe edges. Using the spectroscopic signal from the Ni $L_{2,3}$, Cr $L_{2,3}$ and Fe $L_{2,3}$ edges a composite map (presented in figure 6.19) was produced. It showed that Fe occupied the tetrahedral sites, Cr was positioned upon the octahedral sites and Ni was located on both tetrahedral and octahedral sites.

7.4.2 General formula of spinel precipitate

Under equilibrium cooling conditions Cr [80] and Fe [55] cations within the NiO lattice favour a valency of +3, when the temperature is reduced to the solvus point in air. As previously discussed, the Cr and Fe doped NiO formed during the current study did not experience these same equilibrium cooling conditions. However, upon heat treatment, precipitation appeared to occur uniformly throughout the doped NiO grains, indicating that the spinel particles formed due to a local rearrangement of cations and cation vacancies. It would therefore appear that the majority of Cr and Fe cations within the doped NiO existed in a trivalent state prior to heat treatment.

If during thermal decomposition, Ni cations are divalent, while Fe and Cr cations are in a trivalent state, this would suggest the formation of a spinel with the general formula $Ni(CrFe)_2O_4$. The spinel's unit cell contains 8 divalent Ni cations, 16

trivalent Fe/Cr cations and 32 divalent O anions. Quantitative TEM-EDS point analysis (see section 6.2.1) of the heat treated thick film sample indicated that ratio of Cr to Fe was approximately 2:1 near the centre of the grain, where density of spinel precipitates was greatest. As both EDS analysis and EELS indicated that dopant levels within the matrix were very low following the heat treatment, the 2:1 Cr to Fe ratio may be considered as an approximation of the Cr to Fe ratio within the spinel particles. This would give the spinel precipitates a formula of $NiCr_{1.375}Fe_{0.625}O_4$.

7.4.3 Spinel structure

According to the Ni-Fe-O and Ni-Cr-O phase diagrams, the decomposition of Cr or Fe doped NiO results in the formation of $NiCr_2O_4$ or $NiFe_2O_4$ respectively. $NiCr_2O_4$ is a normal spinel in which Ni^{2+} cations are located on the tetrahedral sites and Cr^{3+} ions are positioned on the octahedral sites [69]. On the other hand, $NiFe_2O_4$ is an inverse spinel that has half the Fe^{3+} cations situated on the tetrahedral sites, while the other half of the Fe^{3+} cations occupy the octahedral sites, alongside the Ni^{2+} cations [70].

As the spinel precipitates formed within the Cr and Fe doped NiO specimens contain Cr^{3+} and Fe^{3+} ions, the perfect inverse and normal spinel particles located at opposite ends of the $NiFe_2O_4$ – $NiCr_2O_4$ binary cannot form. Instead, a mixed spinel develops with a combination of divalent and trivalent cations on both octahedral and tetrahedral sites.

When Fe^{3+} replaces Cr^{3+} in $NiCr_2O_4$, Ni^{2+} ions initially fill the octahedral sites vacated by the Cr^{3+} ions, while the substituting Fe^{3+} ions position themselves on the tetrahedral sites. As replacement of the Cr^{3+} ions continues, the Fe^{3+} carry on filling tetrahedral positions until the Cr^{3+} and Fe^{3+} concentrations reach parity. At this point all the Fe^{3+} ions occupy tetrahedral sites while the Ni^{2+} ions are located upon octahedral sites. Any further increase in Fe^{3+} at the expense of Cr^{3+} causes the Fe^{3+} ions to replace the Cr^{3+} ions at the octahedral sites [71].

Assuming the observed precipitates correspond approximately to the formula $NiCr_{1.3}Fe_{0.7}O_4$, the spinel composition is closer to that of the normal spinel $NiCr_2O_4$,

than the inverse spinel $NiFe_2O_4$. The work of previous researchers suggests that a spinel with this distribution of elements should have Fe^{3+} ions positioned on tetrahedral sites, Cr^{3+} ions located on octahedral sites and Ni^{2+} ions occupying both tetrahedral and octahedral sites. When the spinel precipitates were examined using atomic scale EELS analysis, the chemical maps obtained (see section 6.2.4) revealed that the constituent transition metal cations were located at the expected positions on the spinel lattice.

The chemical maps presented in section 6.2.4, were obtained at the interface between the spinel particle and the NiO matrix. With the roughly octahedral precipitate orientated on [110] zone axis, spectra obtained from regions close to the particle's edge likely contain contributions from the NiO matrix lying beneath. Consequently, the chemical maps produced from these spectra could falsely indicate the presence of Ni in spinel lattice positions which are devoid of Ni.

To maximise the signal from the spinel phase, a spectrum was obtained from another region near the centre of the precipitate, where interference from underlying NiO would be less. The resulting composite map (displayed in figure 7.2) showed a similar distribution of elements to the map acquired close to the edge of the spinel precipitate. As observed previously, Cr was located at the octahedral sites, Fe occupied the tetrahedral sites, and Ni cations were shared amongst both tetrahedral and octahedral lattice positions.

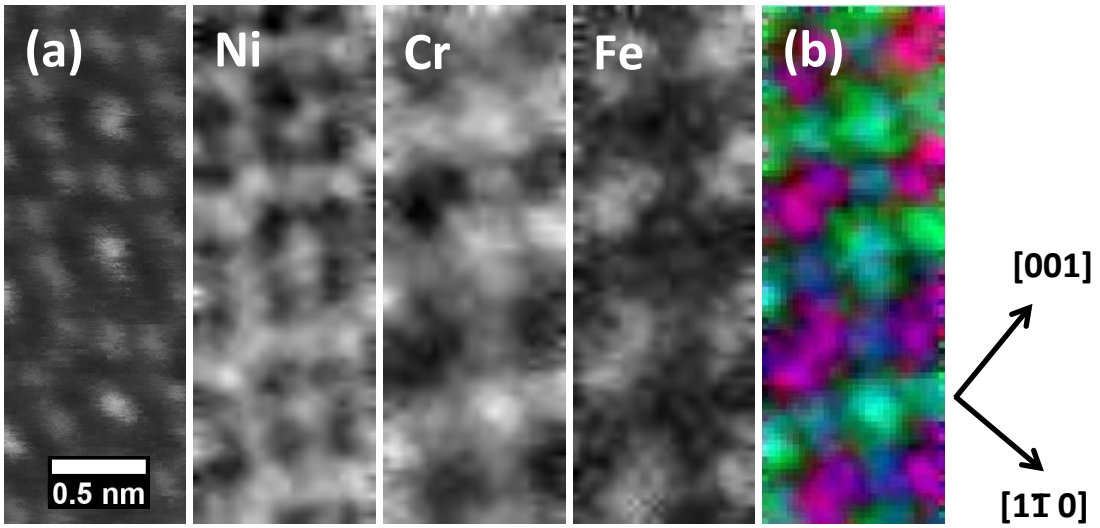

***Figure 7.2**: (a) HAADF image captured simultaneously with the EELS signal, alongside elemental maps. (b) Composite EELS map in which Ni sites are indicated by blue, Fe sites by red and Cr sites by green.*

The mixed spinel ferrite may be represented by the formula $(Ni_{1-y}Fe_y)[Ni_yCr_xFe_{2-x-y}]O_4$, where the round brackets signify that an ion is positioned on tetrahedral site, while the square brackets indicate that an ion is situated upon an octahedral site [76]. Qualitative observations suggest Cr occupies octahedral sites, Fe is located at tetrahedral sites, and Ni is present at tetrahedral and octahedral sites. As EDS results suggest the spinel composition is roughly $NiCr_{1.3}Fe_{0.7}O_4$, the cation distribution within the spinel may therefore be represented approximately by the formula $(Fe_{0.7}Ni_{0.3})[Cr_{1.3}Ni_{0.7}]O_4$.

The ordering of cations in the $NiCr_2O_4$ – $NiFe_2O_4$ has been explained by considering octahedral site stabilisation energy. Calculations carried out by Gismelseed and Yousif [74] suggest that the Cr^{3+} and Ni^{2+} ions exhibit a greater preference for octahedral sites than the Fe^{3+} ions. This would help explain why Fe was detected solely upon the tetrahedral sites during the EELS analysis.

Chapter 8

Conclusions

8.1 Introduction

2DHeat Ltd have developed a novel thick film technology for the manufacture of energy efficient, electric heating elements. Their two-step procedure utilizes existing flame spray technology to partially oxidise a powdered Ni-Cr-Fe alloy (approximately 75wt% Ni, 15wt% Cr, 10wt% Fe) and subsequently deposit it upon an enamelled substrate.

During the initial flame spray oxidation, individual powder particles take differing flight paths through an oxyacetylene flame, causing a variation in heat exposure, which leads to differences in the degree of powder particle oxidation. Particles are cooled from high temperature by directing the spray into an aluminium quenching bath filled with water. In the second stage of the production process, the partially oxidised powder is deposited by another flame spray gun onto an enamelled substrate. Electrical Cu contacts strips are then flame-sprayed onto the thick film deposits in appropriate positions.

The primary objective of this project has been to evaluate the phase formation and microstructural evolution that occurs during the flame spray processing of a gas atomised Ni-Cr-Fe alloy. Material has been examined using combination of optical, structural and chemical characterisation techniques, at the various stages of the manufacturing procedure. Additionally, the thick film has been studied following heat treatment (400˚C-800˚C), to assess possible phase changes occurring heating element operation.

8.2 Gas atomised Ni-Cr-Fe alloy

The initial focus of the project was the characterisation of the gas atomised alloy provided by manufacturer ECKA granules. XRD examination indicated that the powder was primarily composed of a crystalline solid with an FCC crystal structure.

Its lattice parameter of 3.56Å proved consistent with values reported for the Inconel 600 parent material.

The powder particle size distribution was calculated by analysing a series of low magnification SE micrographs. Particle diameters ranged from 4μm to 51μm, with a mean diameter of 25μm. Despite the sample size limitations of the image analysis method, the results showed fair agreement with the manufacturer's sieve gradation test for powder size distribution.

After cross-sectioning the powder particles, SEM examination revealed that the majority of particles displayed evidence of either cellular or dendritic growth. Despite these differences in microstructure, EDS analysis indicated the particle compositions were similar, and in agreement with ECKA Granules' chemical analysis. Though the bulk of examined particles appeared to be to specification, a small percentage contained elevated levels of Si. In contrast to those particles of typical composition, those of higher Si content had much smoother, more spherical exteriors and displayed no obvious grain structure. EDS used in combination with SEM image analysis indicated that Si-rich material accounted for 4.5% of the total volume of the powder particles tested. When a particle of high Si content was analysed using TEM, neither imaging nor diffraction techniques could provide any evidence of crystal structure. This indicated that these particles were likely amorphous.

8.3 Flame-sprayed powder

After flame-spray oxidation of the gas atomised alloy, the particle size distribution within the resultant powder was examined by means of SEM image analysis. These results indicated that the oxidising heat treatment caused the average particle diameter to increase to from 25μm to approximately 36μm.

When the heat treated powder was studied in cross-section, the heat treated powder was found to contain particles with varying degrees of oxidation. While the majority were almost completely oxidised, a small percentage either escaped oxidation or retained a substantial amount of metal. EDS conducted in combination with SEM

image analysis suggested that metallic particles accounted for approximately 2.9% of the powder's total volume.

Viewed in cross section, the oxidised particles appeared relatively dense near the exterior of the particle, but porous near the centre. Within these porous regions dendritic incursions were visible, which seemed to have grown inwards from the surface. This central porosity was attributed to volumetric contractions occurring as solidification progressed from the surface to the centre of the particles.

SEM examination of the oxidised particles suggested they were formed of a single phase oxide, which EDS readings indicated contained significant amounts of Ni,Cr and Fe. The Ni:Cr:Fe ratio was similar to that observed within the original alloy, while the ratio of metal to O atoms was approximately 1:1.

Elemental mapping was used to investigate the distribution of the four main constituent elements within an oxidised particle. Across the dendritic formations, the Ni and O concentrations appeared to remain constant. Conversely, the intensity maps indicated that Cr dominated near the centre of the dendrites, while Fe accumulated nearer the edges.

XRD analysis of the heat treated powder indicated that the dominate phase had NaCl crystal structure comparable to NiO. The calculated lattice parameter (4.17Å) was just 0.2% lower than that of the standard NiO data file with which it was compared. Agreeing with the SEM compositional analysis, the XRD patterns also indicated the presence of the original alloy and low alloyed Ni. Additionally, weak spinel peaks were also visible within the XRD pattern.

While the XRD results suggested that the majority of the powder had a NaCl crystal structure comparable to that of NiO, EDS readings acquired from the bulk oxide indicated the presence of significant amounts of Fe and Cr. This may be explained by the incorporation of Fe and Cr atoms into the NiO lattice structure during the formation of the oxide. Pseudo-binary Ni-Fe-O [56] and Ni-Cr-O [65] phase diagrams suggest that NiO can integrate appreciable quantities of Fe and Cr at high temperature. As the oxidised powder particles experience rapid cooling, this high temperature state can be maintained at room temperature.

To study the relationship between the spinel and doped NiO phases at high resolution, thin foil specimen were prepared from oxidised powder particles, and analysed using TEM/STEM techniques. When the oxide grains were examined at lattice resolution, arrays of commonly orientated particles were revealed, embedded within a matrix phase. Using FFT image analysis, d-spacings were calculated from the particles and the surrounding matrix. These values correlated with those previously obtained for the spinel and NiO phases during XRD analysis. The 111 spinel d-spacing (4.93Å) was approximately twice that of the 111 NiO d-spacing (2.44Å). This high degree of coherency between the two phases suggested that the oxygen sublattice was common to both phases and only the cations need to rearrange in order for the spinel precipitate to grow.

8.4 Flame-sprayed thick film

The thick film heating element, produced by flame spray deposition of the metal-metal oxide powder mixture, was initially studied in cross section using an optical microscope. This examination revealed the thick film was relatively porous and contained substantial quantities of metallic material embedded within an oxide matrix. Image analysis of the optical micrographs suggested that the film was approximately 62% oxide, 17% metallic, and 21% porous.

After removal from the substrate, a sample of thick film was analysed using XRD. The diffraction patterns suggested that the phases detected within the partially oxidised powder remained present after flame spray deposition. However, an increase in the intensity of the alloy 111 and Ni 111 peaks relative to the NiO 200 peak indicated that the metallic material accumulated preferentially on the substrate during flame spray deposition.

SEM examination of the cross-sectioned thick film revealed that the doped NiO existed in both columnar and equiaxed grain structures. This was attributed to the differences in the temperature of the impinging material. Molten particles that flattened upon impact formed columnar grain formations, orientated roughly parallel to the substrate surface. Conversely, particles that were deposited in a solid or semi-

molten state, deformed less during the deposition process, and presented a more equiaxed grain structure.

Variability in the particle temperature and velocity also influenced the levels of deformation experienced by the impinging metallic material. The particles that collided with the target surface at relatively low temperatures retained a more spherical shape and bonded less effectively with the surrounding material. However, those particles that were molten upon impact formed well-flattened splats, and appeared to develop better bonds with the material nearby.

The metallic splats that experienced the higher temperatures reacted with the ambient O and developed more complex microstructures. Two common features of these formations were oxide particles distributed within the metal, and metallic particles dispersed within an outer oxide shell.

After the fabrication of thin foil specimens using a FIB, the thick film was inspected at high resolution during TEM/STEM analysis. Examination of the oxide grains revealed variations in the degree of spinel precipitation. In some grains the lattice resolution imaging revealed a homogenous single phase structure. D-spacings calculated from these images proved consistent with the values previously obtained for doped NiO. In contrast to this single phase structure, other grains were found to contain arrays of coherent particles similar to those observed in the oxidised powder. FFT image analysis confirmed that the d-spacings from the precipitate and matrix phases were in agreement with values previously obtained for the spinel and doped NiO respectively.

The compositional variation between the spinel precipitates and the matrix was confirmed using EDS line scans. As the scan line passed over the spinel particle, Cr and Fe intensities were found to peak, while the Ni fell and the O remained fairly constant.

8.5 Heat treated thick film

The pseudo-binary Ni-Fe-O and Ni-Cr-O phase diagrams indicated that a Cr and Fe doped NiO should decompose to form more energetically favourable NiO and spinel phases during the correct heat treatment. To induce this effect, thick film specimens that had been removed from the substrate, were heat treated for 66h at 800˚C. The XRD and SEM characterization techniques were then employed to search for evidence of thermal decomposition.

A comparison between X-ray diffraction patterns, obtained before and after heat treatment, showed the spinel 311 peak height increased relative to the NiO 111 and 200 peaks, following 66h at 800˚C. These results were supported by SEM imaging, which showed that doped NiO regions developed a mottled, two-phase appearance after the heat treatment.

To investigate whether spinel development could be linked to the heating elements' in-service resistance increases, samples of the thick film coating were heat treated for 66h at a range of lower temperatures (400˚C, 500˚C, 600˚C and 700˚C). Decomposition of the doped NiO was not detected by XRD or SEM until a temperature between 600˚C and 700˚C was reached. As the heating elements typically operate at temperatures between 400˚C and 500˚C, widespread decomposition of the doped NiO was viewed as an unlikely cause of in-service resistance changes.

These results indicated that when temperatures were below 600˚C, low rates of diffusion led to limited decomposition of the doped NiO.

To study decomposition of the doped NiO at high resolution, FIB cross sections were extracted from a thick film sample, heated for 66h at 800˚C, and then analysed using TEM/STEM. As observed in the powder and as-deposited thick film specimens the spinel precipitates shared a topotactic relationship with the parent material. However, rather than appearing roughly spherical, these particles were generally faceted in appearance, and occupied a greater volume. TEM imaging used in conjunction with EELS elemental mapping indicated that the spinel particles were octahedral in appearance and bound by the {111} planes.

After heat treatment, both EELS and EDS elemental mapping showed that Cr and Fe accumulated in the spinel particles, while Ni concentrated in the matrix. In contrast to the other elements, O intensity remained constant across the concentration map. An equal concentration of O within both phases is consistent with a shared O sublattice.

During the heat treatment, spinel precipitation appeared to occur preferentially in the centre of the doped NiO grains, leaving a denuded zone immediately adjacent to the grain boundaries. CBED patterns collected from these regions lacked spinel reflections and were comprised solely of NiO reflections. EDS readings indicated that this material contained very low concentrations of dopant atoms. The formation of these denuded zones may be attributed to vacancy depletion next to the grain boundary inhibiting spinel precipitation.

Site occupancy within the spinel precipitates was studied at an atomic scale using electron energy loss spectroscopy. The spinel particles were orientated in the <110> direction to enable the preferential site occupancy at tetrahedral and octahedral positions to be detected. Using the spectroscopic signal from the Ni $L_{2,3}$, Cr $L_{2,3}$ and Fe $L_{2,3}$ edges, maps were produced showing that Fe occupied the tetrahedral sites, Cr was positioned upon the octahedral sites and Ni was located on both the tetrahedral and octahedral sites.

Chapter 9

Future work

While investigating site occupancy within the Cr and Fe doped NiO and spinel structures, EEL spectra were collected over a broad range of energy losses at a relatively low energy resolution. This meant that the fine structure on the O K edge was lacking features which could have been used to investigate the bonding and coordination states of the O anions. During a future investigation, a narrower range of energy losses could be scanned at higher resolution, enabling more features of the O K fine edge structure to be retained. By comparing spectra obtained from the doped NiO matrix with those collected from the spinel precipitates, differences in the O-cation bonding in the two phases could be analysed.

When the Cr and Fe doped NiO was heated for 66h at 800˚C, dense arrays of octahedral spinel particles formed, indicating relatively high rates of nucleation. At low nucleation rates, researchers investigating the $NiFe_2O_4$/NiO [82] and $NiCr_2O_4$/NiO [83] systems, reported dendrite spinel growth. To restrict the driving force for nucleation, undercooling was kept low, by slowly cooling doped NiO from above the solvus temperature into the two phase region. As part of future work, the Cr and Fe doped NiO could be subjected to a similar heat treatment, to discover whether dendritic growth would also occur.

It has been demonstrated that flame spray processing of the Ni-Cr-Fe powder produces a highly inhomogeneous thick film. However, the influence that the various phases and microstructures exert on the heating element behaviour during operation still requires further investigation. An in-depth examination of the thick film's electrical characteristics could be conducted during a future study.

References

[1] F. Hermanek, “Thermal spraying: what it was and what it has become,” *The International Journal of Powder Metallurgy,* vol. 38, no. 7, pp. 35-44, 2002.

[2] Advanced Coatings, “Flame spray process,” [Online]. Available: http://www.advanced-coating.com/english/spraying-flame.htm. [Accessed 15 11 2016].

[3] ASM International and the Thermal Spray Society, Handbook of Thermal Spray Technology, ASM International , 2011.

[4] A. Rabiei and A. Evans, “Failure mechanisms associated with the thermally grown oxide in plasma-sprayed thermal barrier coatings,” *Acta Materialia,* vol. 48, no. 15, pp. 3963 - 3976, 2000.

[5] P. Rodrigo, M. Campo, B. Torres, M. Escalera, E. Otero and J. Rams, “Microstructure and wear resistance of Al-SiC composites coatings on ZE41 magnesium alloy,” *Applied Surface Science,* vol. 255, no. 22, pp. 9174-9181, 2009.

[6] K. Tao, X. Zhou and H. Cui, “Oxidation and hot corrosion behaviours of HVAF-sprayed conventional and nanostructured NiCrC coatings,” *Transactions of Nonferrous Metals Society of China,* vol. 19, no. 5, pp. 1151-1160, 2009.

[7] M. Uusitalo, P. Vuoristo and T. Mantyla, “High temperature corrosion of coatings and boiler steels below chlorine-containing salt deposits,” *Corrosion Science,* vol. 46, no. 6, pp. 1311-1331, 2004.

[8] M. Martena, D. Botto, P. Fino, S. Sabbadini, M. Gola and C. Badini, “Modelling of TBC system failure: stress distribution as a function of TGO thickness and thermal expansion mismatch,” *Engineering Failure Analysis,* pp. 409-426, 2006.

[9] C. Hackett and G. Settles, “Research on HVOF gas shrouding for coating oxidation control,” in *Advances in Thermal Spray Science and Technology*, Houston, pp. 21-29, 1995.

[10] J. A. Gan and C. C. Berndt, “Review on the oxidation of metallic thermal sprayed coatings: a case study with reference to to rare-earth permanent magnetic coatings,” *Journal of Thermal Spray Technology,* vol. 22, no. 7, pp. 1069-1091, 2013.

[11] A. Vardelle, P. Fauchais and N. Themelis, “Oxidation of metal droplets in plasma sprays,” in *Advances in Thermal Spray Science and Technology*, Houston, pp. 175-180, 1995.

[12] D. Robertson and A. Jenkins, “The reaction of liquid iron and its alloys in pure oxygen,” in *Heterogeneous Kinetics at Elevated Temperatures*, New York, Plenum Press, 1970, pp. 369-385.

[13] S. Deshpandi, S. Sampath and H. Zhang, “Mechanisms of oxidation and its role in microstructural evolution of metallic thermal spray coatings: case study for Ni-Al,” *Surface and Coating Technology,* vol. 200, no. 18-19, pp. 5395-5406, 2006.

[14] P. Fauchais, G. Montavon and G. Bertrand, “From powders to thermally sprayed coatings,” *Journal of thermal spray technology,* vol. 19, no. 1, pp. 56-80, 2009.

[15] M. Hill, “On a spherical vortex,” *Philosophical Transactions of the Royal Society A,* vol. 55, pp. 213-245, 1894.

[16] G. Espie, P. Fauchais, J. Labbe, A. Vardelle and B. Hannoyer, “Oxidation of iron particles during APS: effect of the process on formed oxide wetting of droplets on ceramic substrates,” in *Thermal Spray 2001: New Surfaces for a New Millennium*, Materials Park, ASM International, 2001, pp. 821-827.

[17] Q. Wei, Y. Zhiyong and H. Li, “Oxidation control in plasma spraying NiCrCoAlY coating,” *Applied Surface Science,* vol. 258, no. 12, pp. 5094-5099, 2012.

[18] A. Syed, A. Denoirjean, P. Denoirjean, J. Labbe and P. Fauchais, “In-flight oxidation of stainless steel particles in plasma spraying,” *Journal of Thermal Spray Technology,* vol. 14, no. 1, pp. 117-124, 2003.

[19] H. Ageorges and P. Fauchais, “Plasma spraying of stainless-steel particles coated with an alumina shell,” *Thin Solid Films,* vol. 370, no. 1-2, pp. 213-222, 2000.

[20] G. Espie, A. Denoirjean, P. Fauchais, J. Labbe, J. Dubsky, O. Schneeweiss and K. Volenik, “In-flight oxidation of iron particles sprayed using gas and water stabilized plasma torch,” *Surface Coatings and Technology,* vol. 195, no. 1, pp. 17-28, 2005.

[21] A. Scrivani, U. Bardi, L. Carrafiello, A. Lavacchi, F. Niccolai and G. Rizzi, “A comparative study of high velocity oxygen fuel, vacuum plasma spray, and axial plasma spray for the deposition of CoNiCrAl bond coat alloy,” *Journal of Thermal Spray Technology,* vol. 12, no. 4, pp. 504-507, 2003.

[22] P. Fauchais, J. Heberlein and M. Boulos, “Introduction,” in *Thermal Spray Fundamentals: From Powder to Part*, New York, Springer, 2014, pp. 4-6.

[23] P. Fauchais, J. Heberlein and M. Boulos, “Combustion at equilibrium,” in *Thermal Spray Fundamentals: from Powder to Part*, New York, Springer, 2014, pp. 74-76.

[24] C. Hackett and G. Settles, “Turbulent mixing of the HVOF thermal spray and coating oxidation,” in *Proceeding of the 7th national spray conference*, Materials Park, Ohio, 1994.

[25] L. Moskowitz and D. Lindley, “High density thermal spray coating”. U.S. Patent 5151308, 29 September 1992.

[26] K. Dobler, H. Kreye and R. Schwetzke, “Oxidation of stainless steel in the high velocity oxy-fuel process,” *Journal of Thermal Spray Technology,* vol. 9, no. 3, p. 407–413, 2000.

[27] X. Wang, J. Heberlein, E. Pfender and W. Gerberich, “Effect of nozzle configuration, gas pressure, and gas type on coating properties in wire arc spray,” *Journal of Thermal Spray Technology,* vol. 8, no. 4, pp. 565-575, 1999.

[28] K. Voleník, F. Hanousek, P. Chráska, J. Ilavský and K. Neufuss, “In-flight oxidation of high alloy steels during plasma spraying,” *Materials Science and Engineering: A,* vol. 272, no. 1, pp. 199-206, 1999.

[29] C.-J. Li and W.-Y. Li, “Effect of sprayed powder particle size on the oxidation behaviour of MCrAlY materials during high velocity oxygen-fuel deposition,” *Surface and Coatings Technology,* vol. 162, no. 1, pp. 31-41, 2003.

[30] Z. Zeng, S. Kuroda, J. Kawakita, M. Komatsu and H. Era, “Effects of some light alloying elements on the oxidation behavior of Fe and Ni-Cr based alloys during air plasma spraying,” *Journal of Thermal Spray Technology,* vol. 19, no. 1, pp. 128-136, 2010.

[31] D. Seo, K. Ogawa, T. Shoji and S. Murata, “Effect of particle size distribution on isothermal oxidation characteristics of plasma sprayed CoNi and CoCrAlY coatings,” *Journal of Thermal Spray Technology,* vol. 16, no. 5, pp. 954-966, 2007.

[32] V. Sobolev and J. Guilemany, “Oxidation of coatings in thermal spraying,” *Materials Letters,* vol. 37, no. 4-5, pp. 231-235, 1998.

[33] N. Ahmed, M. Bakare, D. McCartney and K. Voisey, “The effects of microstructural features on the performance gap in corrosion resistance between bulk and HVOF sprayed Inconel 625,” *Surface and Coatings Technology,* vol. 204, no. 14, pp. 2294-2301, 2010.

[34] M. Bakare, K. Voisey, M. Roe and D. McCartney, “X-ray photoelectron spectroscopy study of the passive films formed on thermally sprayed and wrought Inconel 625,” *Applied Surface Science,* vol. 257, no. 3, pp. 786-794, 2010.

[35] J. Tuominen, P. Vuoristo, T. Mäntylä, M. Kylmälahti, J. Vihinen and P. Andersson, “Improving corrosion properties of high-velocity oxy-fuel sprayed inconel 625 by using a high-power continuous wave neodymium-doped yttrium aluminum garnet laser,” *Journal of Thermal Spray Technology,* vol. 9, no. 4, p. 513–519, 2000.

[36] Z. Liu, J. Cabrero, S. Niang and Z. Al-Taha, “Improving corrosion and wear performance of HVOF-sprayed Inconel 625 and WC-Inconel 625 coatings by high power diode laser treatments,” *Surface and Coatings Technology,* vol. 201, no. 16-17, pp. 7149-7158, 2007.

[37] R. González, M. Cadenas, R. Fernández, J. Cortizo and E. Rodríguez, “Wear behaviour of flame sprayed NiCrBSi coating remelted by flame or by laser,” *Wear,* vol. 262, no. 3-4, pp. 301-307, 2007.

[38] A. Dent, A. Horlock, D. McCartney and S. Harris, “Microstructure formation in high velocity oxy-fuel thermally sprayed Ni–Cr–Mo–B alloys,” *Materials Science and Engineering: A,* vol. 283, no. 1-2, pp. 242-250, 2000.

[39] C. Lee and K. Min, “Effects of heat treatment on the microstructure and properties of HVOF-sprayed Ni–Cr–W–Mo–B alloy coatings,” *Surface and Coatings Technology,* vol. 132, no. 1, pp. 49-57, 2000.

[40] C. Giacovazzo, H. Monaco, G. Artioli, D. Viterbo, M. Milanesio, G. Gilli, P. Gilli, G. Zanotti, G. Ferraris and M. Catti, “Symmetry generalisation,” in *Fundamentals of Crystallography*, Oxford, Oxford University Press, 1992, p. 63.

[41] S. Mrowec and Z. Gresik, “Oxidation of nickel and transport properties of nickel oxide,” *Journal of Physics and Chemistry of Solids,* vol. 65, no. 10, pp. 1651-1657, 2004.

[42] J. Keem and J. Honig, “Selected electrical and thermal properties of undoped nickel oxide,” Center for Information and Numerical Data Analysis and Synthesis, Lafayette, 1978.

[43] V. Biju and M. Khadar, “Dielectric properties of nanostructured nickel oxide,” *Journal of Materials,* vol. 38, p. 4055 – 4063, 2003.

[44] H. Sato, T. Minami, S. Takata and T. Yamada, “Transparent conducting p-type NiO thin films prepared by magnetron sputtering,” *Thin Solid Films,* vol. 236, no. 1-2, pp. 27-31, 1993.

[45] P. Lunkenheimer, A. Loidl, C. Ottermann and K. Bange, “Correlated barrier hopping in NiO films,” *Physical Review B ,* vol. 44, no. 11, pp. 5927-5930, 1991.

[46] N. Birks, G. H. Meier and F. S. Pettit, "High-temperature oxidation of metals", Cambridge: Cambridge University Press, 2006.

[47] A. Atkinson, R. Taylor and P. Goode, “Transport processes in the oxidation of Ni studied using tracers in growing NiO scales,” *Oxidation of Metals,* vol. 13, no. 6, pp. 519-543, 1979.

[48] C. Wagner and K. Zimens, “Rate of oxidation of nickel with small additions of chromium and manganese; theory of the tarnishing process,” *Acta Chemica Scandinavica,* vol. 1, pp. 547-65, 1947.

[49] R. Haugsrud, “On the high-temperature oxidation of nickel,” *Corrosion Science,* vol. 45, no. 1, pp. 211-235, 2002.

[50] R. Herchl, N. Khoi, T. Homma and W. Smeltzer, “Short-circuit diffusion in the growth of nickel oxide scales on nickel crystal faces,” *Oxidation of Metals,* vol. 4, no. 1, pp. 35-49, 1972.

[51] M. Graham and M. Cohen, “On the mechanism of low-temperature oxidation (23°-450°C) of polycrystalline nickel,” *Journal of the Electrochemical Society,* vol. 119, no. 7, pp. 879-882, 1972.

[52] A. Atkinson, “Transport processes during the growth of oxide films at elevated temperatures,” *Reviews of Modern Physics,* vol. 57, no. 2, pp. 437-470, 1985.

[53] M. Rhamdhani, P. Hayes and E. Jak, “Subsolidus phase equilibria of the Fe-Ni-O system,” *Metallurgical and Materials Transactions B,* vol. 39, no. 5, pp. 690-701, 2008.

[54] R. Luoma, “A thermodynamic analysis of the system Fe-Ni-O,” *Calphad,* vol. 19, no. 3, pp. 279-295, 1995.

[55] F. Schneider and H. Schmalzreid, “Thermodynamic investigation of the system Ni-Fe-O,” *Zeitschrift für Physikalische Chemie,* vol. 166, no. 1, pp. 1-18, 1990.

[56] V. Raghavan, “Fe-Ni-O (iron-nickel-oxygen),” *Journal of Phase Equilibria and Diffusion,* vol. 31, no. 4, pp. 369-371, 2010.

[57] J.-W. Yoon, H.-J. Kim, I.-D. Kim and J.-H. Lee, “Electronic sensitization of the response to C_2H_5OH of p-type NiO nanofibers by Fe doping,” *Nanotechnology,* vol. 24, no. 44, p. 444005, 2013.

[58] S. Liu, J. Jia, J. Wang, S. Liu, X. Wang, H. Song and X. Hu, “Synthesis of Fe-doped NiO nanofibers using electrospinning method and their ferromagnetic properties,” *Journal of Magnetism and Magnetic Materials,* vol. 324, no. 13, pp. 2070-2074, 2012.

[59] A. Mishra, S. Bandyopadhyay and D. Das, “Structural and magnetic properties of pristine and Fe-doped NiO nanoparticles synthesized by the co-precipitation method,” *Materials Research Bulletin,* vol. 47, no. 9, pp. 2288-2293, 2012.

[60] S. Manna, A. Deb, J. Jagannath and S. De, "Synthesis and room temperature ferromagnetism in Fe doped NiO nanorods," *The Journal of Physical Chemistry C,* vol. 112, no. 29, pp. 10659-10662, 2008.

[61] H.-J. Kim, K.-I. Choi, K.-M. Kim, C. Na and J.-H. Lee, "Highly sensitive C_2H_5OH sensors using Fe-doped NiO hollow spheres," *Sensors and Actuators B: Chemical,* Vols. 171-172, pp. 1029-1037, 2012.

[62] R. D. Shannon, "Revised effective ionic radii and systematic studies of interatomic distances in halides and chalcogenides," *Acta Crystallographica,* vol. A32, pp. 751-767, 1976.

[63] P. Mallick, C. Rath, R. Biswal and N. Mishra, "Structural and magnetic properties of Fe doped NiO," *Indian Journal of Physics,* vol. 83, no. 4, pp. 517-523, 2009.

[64] J. Taylor and A. Dinsdale, "A thermodynamic assessment of the Ni-O, Cr-O and Cr-Ni-O systems using the ionic liquid and compound energy models," *Z. Metallkde,* vol. 81, pp. 354-366, 1990.

[65] L. Kjellqvist, M. Selleby and B. Sundman, "Thermodynamic modelling of the Cr-Fe-Ni-O system," *Computer Coupling of Phase Diagrams and Thermochemistry,* vol. 32, no. 3, pp. 577-592, 2008.

[66] H.-J. Kim, J.-W. Yoon, K.-I. Choi, H. W. Jang, A. Umar and J.-H. Lee, "Ultraselective and sensitive detection of xylene and toluene for monitoring indoor air pollution using Cr-doped NiO hierarchical nanostructures," *Nanoscale,* vol. 5, pp. 7066-7073, 2013.

[67] J. Cao, Z. Wang, R. Wang and T. Zhang, "Electrostatic sprayed Cr-loaded NiO core-in-hollow-shell structured micro/nanospheres with ultra-selectivity and sensitivity for xylene," *CrystEngComm,* vol. 16, pp. 7731-7737, 2014.

[68] P. Elumalai, J. Zosel, U. Guth and N. Miura, "NO_2 sensing properties of YSZ-based sensor using NiO and Cr-doped NiO sensing electrodes at high temperature," *Ionics,* vol. 15, no. 4, pp. 405-411, 2009.

[69] H. Ishibashi and T. Yasumi, "Structural transition of spinel compound $NiCr_2O_4$ at ferrimagnetic transition temperature," *Journal of Magnetism and Magnetic Materials,* vol. 310, no. 2, pp. 610-612, 2007.

[70] V. Ivanov, M. Abrashev, M. Iliev, M. Gospodinov, J. Meen and M. Aroyo, "Short-range B-site ordering in the inverse spinel ferrite $NiFe_2O_4$," *Physical Review B,* vol. 82, no. 2, p. 024104, 2010.

[71] S. Ziemniak, A. Gaddipati and P. Sander, "Immiscibility in the $NiFe_2O_4$–$NiCr_2O_4$ spinel binary," *Journal of Physics and Chemistry of Solids,* vol. 66, no. 6, p. 1112–1121, 2005.

[72] S. Singhala and K. Chandra, “Cation distribution and magnetic properties in chromium-substituted nickel ferrites prepared using aerosol route,” *Journal of Solid State Chemistry,* vol. 180, no. 1, p. 296–300, 2007.

[73] M. Gabal and Y. Al Angari, “Effect of chromium ion substitution on the electromagnetic properties of nickel ferrite,” *Materials Chemistry and Physics,* vol. 118, no. 1, p. 153–160, 2009.

[74] A. Gismelseed and A. Yousif, “Mössbauer study of chromium-substituted nickel ferrites,” *Physica B: Condensed Matter,* vol. 370, no. 1-4, pp. 215-222, 2005.

[75] M. Fayek and S. Ata-Allah, “^{57}Fe Mössbauer and electrical studies of the (NiO)–$(Cr_2O_3)_x$–$(Fe_2O_3)_{2-x}$ system,” *Physica Status Solidi (a),* vol. 198, no. 2, p. 457–464, 2003.

[76] S. Lee, S. Yoon, G. Lee, H. Kim, C. Yo, K. Ahn, D. Lee and K. Kim, “Electrical and magnetic properties of $NiCr_xFe_{2-x}O_4$ spinel (0≤x≤0.6),” *Materials Chemistry and Physics,* vol. 61, pp. 147-152, 1999.

[77] G. Allen, J. Jutson and P. Tempest, “Characterization of nickel-chromium-iron spinel-type oxides,” *Journal of Nuclear Materials,* vol. 158, pp. 96-107, 1988.

[78] W. Callister, “The kinetics of phase transformation,” in *Materials science and engineering an introduction*, New York, John Wiley & Sons, 2007, pp. 313-324.

[79] S. Summerfelt and C. Carter, “Kinetics of $NiFe_2O_4$ precipitation in NiO,” *Journal of the American Ceramic Society,* vol. 75, no. 8, pp. 2244-2250, 1992.

[80] C. Greskovich, “Kinetics of NiCr2O4 formation and diffusion of Cr^{3+} ions in NiO,” *Journal of the American Ceramic Society,* vol. 53, no. 9, p. 498–502, 1970.

[81] K. Hauffe, “Disorder appearances and exchange processes in electrically conducting mixed phases,” *Annalen der Physik,* vol. 8, pp. 201-210, 1950.

[82] S. Summerfelt and C. Carter, “Morphology of $NiFe_2O_4$ precipitation in NiO,” *Acta Metallurgica et Materialia,* vol. 40, no. 5, pp. 1051-1067, 1992.

[83] C.-H. Chen, M. R. Notis and D. B. Williams, “Precipitation and solid solubility in the system NiO-Cr2O3,” *Journal of the American Ceramic Society,* vol. 66, no. 8, pp. 566-571, 1983.

[84] K. Ostyn, C. Carter, M. Koehne, H. Falke and H. Schmalzried, “Internal reactions in oxide solid solutions,” *Journal of the American Ceramic Society,* vol. 67, no. 10, p. 679–685, 1984.

[85] W. Luecke and D. Kohlstedt, “Kinetics of the internal oxidation of (MgFe)O solid solutions,” *Journal of the American Ceramic Society,* vol. 71, no. 3, p. 189–196, 1988.

[86] D. Ricoult and H. Schmalzried, “Internal reactions in the (Mg,Me)O system,” *Journal of Materials Science,* vol. 22, no. 6, p. 2257–2266, 1987.

[87] S. Summerfelt and C. Carter, “Coarsening and shape transformation of $NiFe_2O_4$ precipitates in a NiO matrix,” *Philosophical Magazine A,* vol. 65, no. 6, pp. 1503-1519, 1991.

[88] R. Doherty, “Roles of interfaces in kinetics of internal shape changes,” *Metal Science,* vol. 16, no. 1, pp. 1-14, 1982.

[89] G. Groves and M. Fine, “Solid solution and precipitation hardening in Mg-Fe-O alloys,” *Journal of Applied Physics,* vol. 35, no. 12, pp. 3587-3593, 1964.

[90] P. Hing and G. Groves, “The microstructure and fracture properties of MgO crystals containing a dispersed phase,” *Journal of Materials Science,* vol. 7, no. 4, p. 422–426, 1972.

[91] Summerfelt, "Precipitation of nickel ferrite in a nickel oxide matrix", New York: Cornell University, 1990.

[92] M. Jacobs and D. Pashley, “The factors controlling the width of precipitate-free zones at grain boundaries in Al-Zn,” in *The mechanism of phase transformations in crystalline solids*, London, The Institute of Metals, 1969, pp. 43-48.

[93] E. Starke, “The causes and effects of "denuded" or "precipitate-free" zones at grain boundaries in aluminum-base alloys,” *Journal of Metals,* vol. 22, no. 1, pp. 54-63, 1970.

[94] J. Martin, “Grain boundaries,” in *Micromechanisms in particle-hardened alloys*, Cambridge, Cambridge University Press, 1980, pp. 30-32.

[95] ASM International, “Corrosion of nickel and nickel-based alloys,” in *ASM Handbook*, 2005, pp. 228-251.

[96] S. Reyntjens and R. Peurs, “A review of focused ion beam applications in microsystem technology,” *Journal of Micromechanics and Microengineering,* vol. 11, no. 4, pp. 287-300, 2001.

[97] C. Volkert and A. Minor, “Focused ion beam microscopy and micromachining,” *MRS Bulletin,* vol. 32, no. 5, pp. 389-399, 2007.

[98] M. Kanouff, R. Neiser and T. Roemer, “Surface roughness of thermal spray coatings made with off-normal spray angles,” *Journal of Thermal Spray Technology,* vol. 7, no. 2, pp. 219-228, 1998.

[99] L. Giannuzzi and F. Stevie, “A review of focused ion beam milling techniques for TEM specimen preparation,” *Micron,* vol. 30, no. 3, pp. 197-204, 1999.

[100] D. Tomus and H. Pang, “In situ lift-out dedicated techniques using FIB-SEM system for TEM specimen preparation,” *Micron,* vol. 44, pp. 115-119, 2013.

[101] J. Mayer, L. Giannuzzi, T. Kamino and J. Michael, “TEM sample preparation and FIB-induced damage,” *MRS Bulletin,* vol. 32, no. 5, pp. 400-407, 2007.

[102] D. Dickensheets, “Introduction,” in *Encyclopedia of Optical Engineering*, CRC Press, 2003, p. 1738.

[103] C. Schneider, W. Rasband and K. Eliceiri, “NIH Image to ImageJ: 25 years of image analysis,” *Nature Methods,* vol. 9, no. 7, pp. 671-675, 2012.

[104] P. Goodhew, J. Humphreys and R. Beanland, “How it works,” in *Electron Microscopy and Analysis*, London, Taylor and Francis, 2001, pp. 122-124.

[105] P. Goodhew, J. Humphreys and R. Beanland, “Obtaining a signal,” in *Electron Microscopy and Analysis*, London, Taylor and Francis, 2001, pp. 124-129.

[106] G. Lloyd, “Atomic number and crystallographic contrast images with the SEM: a review of backscattered electron techniques,” *Mineralogical Magaine,* vol. 51, no. 1, pp. 3-19, 1987.

[107] P. Echlin, C. Fiori, J. Goldstein, D. Joy and D. Newbury, in *Advanced Scanning Electron Microscopy and X-Ray Microanalysis*, New York, Plenum Press, 1986, p. 88.

[108] Australian microscopy and microanalysis research facility, “Characteristic X-rays,” 12 June 2014. [Online]. Available: http://www.ammrf.org.au/myscope/analysis/eds/xraygeneration/characteristic/. [Accessed 12 09 2016].

[109] P. Goodhew, J. Humphreys and R. Beanland, “Detection and counting X-rays,” in *Electron Microscopy and Analysis*, London, Taylor and Francis, 2001, pp. 174-183.

[110] V. Scott and G. Love, "Quantitative Electron-probe Microanalysis", New York: Ellis Horwood, 1983.

[111] University of Oklahoma, “Samuel Roberts Noble Microscopy Laboratory,” [Online]. Available: http://www.microscopy.ou.edu/. [Accessed 6 5 2016].

[112] H. Jeong, S. Seo, H. Hong and Y. Yoo, “Characteriation of the parameters relating adjacent grains using transmission electron microscopy,” *Journal of Applied Crystallography,* vol. 43, pp. 1495-1501, 2010.

[113] D. Williams and C. Carter, “Centered dark-field operation,” in *Transmission Electron Microscopy*, New York, Springer, 1996, pp. 155-156.

[114] D. Williams and C. Carter, “Scattering and diffraction,” in *Transmission Electron Microscopy*, New York, Springer, 1996, pp. 23-36.

[115] M. Vijayalakshmi, S. Saroja and R. Mythili, “Convergent beam diffraction - a novel technique for materials characterization at sub-microscopic levels,” *Sadhana,* vol. 28, no. 3-4, p. 763–782, 2003.

[116] Oxford Instruments , “EDS in TEM explained,” [Online]. Available: https://www.oxford-instruments.com/?src=tn. [Accessed 21 02 2016].

[117] S. Pennycook, A. Lupini, M. Varela, A. Borisevich, Y. Peng, M. Oxley, K. Van Benthem and M. Chisholm, “Introduction,” in *Scanning Transmission Electron Microscopy for Nanostructure Characterization*, New York, Springer, 2006, pp. 152-191.

[118] D. Muller, “Structure and bonding at the atomic scale by scanning transmission electron microscopy,” *Nature Materials,* vol. 8, pp. 263-270, 2009.

[119] P. Goodhew, J. Humphreys and R. Beanland, “Electron energy loss spectroscopy (EELS),” in *Electron Microscopy and Analysis*, New York, Taylor and Francis, 2001, pp. 205-212.

[120] Gatan Corporate, “What is EELS?,” [Online]. Available: http://www.eels.info/about/overview. [Accessed 09 December 2016].

[121] M. Bosman, M. Watanabe, D. Alexander and V. Keast, “Mapping chemical and bonding information using multivariate analysis of electron energy-loss spectrum images,” *Ultramicroscopy,* vol. 106, p. 1024–1032, 2006.

[122] N. Bonnet, N. Brun and C. Colliex, “Extracting information from sequences of spatially resolved EELS spectra using multivariate statistical analysis,” *Ultramicroscopy,* vol. 77, pp. 97-112, 1999.

[123] University of Liverpool, “Scanning transmission electron microscopy,” [Online]. Available: www.matter.org.uk/tem/. [Accessed 12 02 2016].

[124] Wikipedia, “X-ray crystallography,” [Online]. Available: https://en.wikipedia.org/wiki/X-ray_crystallography. [Accessed 29 04 2016].

[125] B. Fultz and J. Howe, “Diffraction and the X-ray powder diffractometer,” in *Transmission Electron Microscopy and Diffractometry of Materials*, New York, Springer, 2013, pp. 1-59.

[126] F. Azarmi, J. Saaedi, T. Coyle and J. Mostaghimi, “Microstructure characterization of alloy 625 deposited on nickel foam using air plasma spraying,” *Advanced Engineering Materials,* vol. 10, no. 5, p. 459–465, 2008.

[127] K. Wua, G. Liua, B. Hu, F. Li, Y. Zhang, Y. Tao and J. Liu, “Solidification characterization of a new rapidly solidified Ni–Cr–Co based superalloy,” *Materials Characterization,* vol. 73, p. 68–76, 2012.

[128] D. West and N. Saunders, “Selected case studies of ternary systems,” in *Ternary Phase Diagrams in Material Science*, London, Maney Publishing, 2002, pp. 129-136.

[129] Special Metals, “Inconel alloy 600,” 20 September 2008. [Online]. Available: http://www.specialmetals.com/documents/Inconel%20alloy%20600%20(Sept%202008).pdf. [Accessed 8 April 2013].

[130] S. Ochiai, Y. Mishima and T. Suzuki, “Lattice parameter data of Ni, Ni_3Al and Ni_3Ga solid solutions,” *Acta Metallurgica,* vol. 33, no. 6, pp. 1161-1169, 1985.

[131] S. Pattnaik, D. Karunakar and P. Jha, “Developments in investment casting process—A review,” *Journal of Materials Processing Technology,* vol. 212, no. 11, p. 2332–2348, 2012.

[132] R. Molins, B. Normand, G. Rannou, B. Hannoyer and H. Liao, “Interlamellar boundary characterization in Ni-based alloy thermally sprayed coating,” vol. A351, no. 325-333, 2003.

[133] J. Huang, H. Fang, X. Fu, F. Huang, H. Wan, Q. Zhang, S. Deng and J. Zu, “High-temperature oxidation behavior and mechanism of a new type of wrought Ni–Fe–Cr–Al superalloy up to 1300°C,” *Oxidation of Metals,* vol. 53, no. 3, p. 273–287, 2000.

[134] J. Rouquette, J. Haines, G. Fraysse, A. Al Zein, V. Bornand, M. Pintard, P. Papet, S. Hull and F. Gorelli, “High-pressure structural and vibrational study of $PbZr_{0.40}Ti_{0.60}O_3$,” *Inorganic Chemistry,* vol. 47, no. 21, pp. 9898-p9904, 2008.

[135] ASM International, “Introduction to thermal spray processing,” in *Handbook of Thermal Spray Technology*, ASM International, 2004, pp. 3-13.

[136] S. Sasaki, K. Fujino and Y. Takeuchi, “X-ray determination of electron-density distributions in oxides, MgO, MnO, CoO, and NiO, and atomic scattering factors of their constituent atoms,” *Proceedings of the Japan Academy,* vol. 55, pp. 43-48, 1979.

[137] J. Pina, A. Dias and J. Lebrun, “Study by X-ray diffraction and mechanical analysis of the residual stress generation during thermal spraying,” *Materials Science and Engineering: A,* vol. 347, no. 1-2, p. 21–31, 2003.

[138] R. McPherson, “On the formation of thermally sprayed alumina coatings,” *Journal of Materials Science,* vol. 15, no. 12, pp. 3141-3149, 1980.

[139] M. Prates and H. Biloni, “Variables affecting the nature of the chill zone,” *Metallurgical Transactions,* vol. 3, no. 6, p. 1501–1510, 1972.

[140] S. Matthews and M. Schweizer, “Optimization of arc-sprayed Ni-Cr-Ti coatings for high temperature corrosion applications,” *Journal of Thermal Spray Technology,* vol. 22, no. 4, p. 538–550, 2013.

[141] G. Chin, W. Hosford and D. Mendorf, “Accommodation of constrained deformation in f.c.c. metals by slip and twinning,” *Proceeding of the Royal Society A,* vol. 309, no. 1499, pp. 433-456, 1969.

[142] S. Pandit, Theory of the Pearlite Transformation in Steels, Cambridge: University of Cambridge, 2011.

[143] P. Kalu and D. Waryoba, “A JMAK-microhardness model for quantifying the kinetics of restoration mechanisms in inhomogeneous microstructure,” *Materials Science and Engineering: A,* vol. 464, no. 1-2, pp. 68-75, 2007.

[144] J. Allen, E. Hemesath, D. Perea, J. Lensch-Falk, Z. Li, F. Yin, M. Gass, P. Wang, A. Bleloch, R. Palmer and L. Lauhon, “High-resolution detection of Au catalyst atoms in Si nanowires,” *Nature Nanotechnology,* vol. 3, pp. 168 - 173, 2008.

[145] H. Schmalried and M. Backhaus-Ricoult, “Internal solid state reactions,” *Progress in Solid State Chemistry,* vol. 22, pp. 1-57, 1993.

[146] G. Espie, P. Fauchais, B. Hannoyer, J. Labbe and A. Vardelle, “Effect of metal particles oxidation during the APS on the wettability,” *Annals of the New York Academy of Sciences,* vol. 891, pp. 143-151, 1999.